Author:
Gregson, Florence K. A.

Title:
Evaporation Kinetics and Particle Formation from Aerosol Solution Microdroplets

Evaporation Kinetics and Particle Formation from Aerosol Solution Microdroplets

---

by

Florence K. A. Gregson

A dissertation submitted to the University of Bristol in accordance with the requirements of the degree of Doctor of Philosophy in the Faculty of Science, School of Chemistry.

March 2020

72,000 words

Abstract

The evaporation of liquid droplets is an important problem across a range of industries, such as spray drying and respiratory drug delivery. Droplet drying can be highly complex, and the literature lacks a detailed understanding of how evaporation kinetics can affect the process of morphology development and particle formation, and the resulting dried particle properties.

This thesis presents experimental results of evaporation measurements performed using an electrodynamic balance (EDB). Single aqueous droplets were levitated in the instrument and light scattering methods were used to measure the radius throughout evaporation, as well as to detect crystal nucleation induced by a rising solute concentration during drying.

The evaporation of binary droplets containing two volatile solvents (ethanol and water) under a range of different conditions was studied. By comparing the evaporation profiles of droplet size vs. time to various numerical models, including a modified Maxwell model and a binary Kulmala model, the time-dependent composition and temperature of the droplet was studied. These studies elucidated the impacts of the coupling of heat and mass transfer during rapid evaporation.

The evaporation of aqueous droplets containing a range of inorganic solutions was studied using the EDB. The time that crystal nucleation occurred in an evaporating droplet was recorded. A numerical diffusive transport model was compared to the experimental data to provide insight into the evolving gradients in concentration during drying. Aqueous NaCl and $NaNO_3$ droplets were shown to undergo high levels of solute enrichment at the droplet surface as water evaporated, allowing predictions of homogeneous nucleation rates and reconciliation with the measured phase behaviour. Electron microscopy images of dried particles were recorded, collected from drying streams of droplets in a falling droplet column (FDC) under identical evaporation conditions to the EDB. Thus, experimentally measured drying rates, modelled concentration profiles and microscopy images were compared to demonstrate how varying the drying conditions can control the final particle phase and morphology in inorganic aqueous solutions.

Finally, the evaporation of droplets containing mixtures of solutes was studied. The propensity for an inorganic solute (e.g. $NaNO_3$) to undergo crystal nucleation was shown to vary depending upon the presence of other inorganic solutes, organic solutes that affect the droplet surface composition, and SiO_2 nanoparticles that act as heterogeneous nucleation sites. This represents a study into the ability to predict and control crystal nucleation in rapidly evaporating aerosol droplets.

Acknowledgements

First, I must express utmost thanks to my supervisor Prof. Jonathan Reid for providing support and guidance throughout my project. Thanks to Prof. Colin Bain and Prof. Andrew Bayly for the advice and collaboration over the years. Thanks also must go to the EPSRC for the funding that allowed me to perform this research, and to the members of the Industry Club for travel funding during my project.
Thanks are due to various collaborators, Dr. Josh Robinson, Dr. Paddy Royall, Mani Ordoubadi and Prof. Reinhard Vehring for the useful discussions and the models that elucidated my data.
To all the gang at BARC, thank you for all the help and the fun (see Fig. 0-1). Nat (EDBuddy), Lara, Mara, Rose, Stephen and the crossword chaps Dan, Henry, Malcolm: thanks for all the office banter, noodles and pub trips. Thanks to the brilliant Post-Docs and fellows in BARC through the years: Dr. Jim Walker, Dr. Allen Haddrell, Dr. Bryan Bzdek, Dr. Justice Archer and Dr. Grazia Rovelli. Special thanks to Dr. Rachael Miles for the guidance and encouragement on my project right the way through.
At the time of writing, I still hold the movie rights to this thesis, and thank you to Henry for agreeing to take on a lead role if it were ever to be made into a feature film.

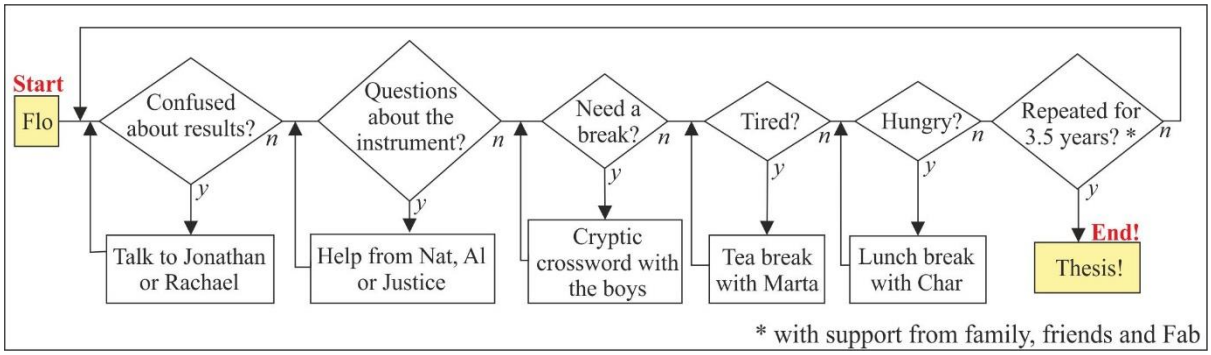

Figure 0-1: Flo chart of some of the processes involved in writing this thesis.

To Marta, (my morning tea buddy!) thank you for your constant positivity and martavation!
Outside of the department I've been lucky to have some super friends who have been there all the way through. To the members of Diracula House: Gemma, Matt, Lara, Cormac, and honorary members Becky and James – I don't know what I would have done without you lot. Thank you, Laurie, for your humour, encouragement and fridge-wine. Thanks to the brilliant friends in my softball teams for the endless fun. To Rebecca, Alice and Hollie, thank you for always being there.
Thank you to Mum, Dad and Ed for your continued support and for the ridiculously intellectual dinner-time chat. Tennessee, you certainly deserve thanks for all the impromptu meals and cakes! Also, special thanks to lovely Char, you've been more help than you could know.
Finally, Fabian, thank you for all your support and for your infinite positivity. I couldn't have done this without you. Danke, dass du immer für mich da bist!

Author Declaration

I declare that the work in this dissertation was carried out in accordance with the requirements of the University's *Regulations and Code of Practice for Research Degree Programmes* and that it has not been submitted for any other academic award. Except where indicated by specific reference in the text, the work is the candidate's own work. Work done in collaboration with, or with the assistance of, others, is indicated as such. Any views expressed in the dissertation are those of the author.

SIGNED: ..... DATE: .....

Table of Contents

List of Figures

List of Tables

List of Symbols and Abbreviations

Symbols

a – Activity

a_w – Water activity

A – Correction for Stefan flow

c – Concentration

c_p – Specific heat capacity

$\bar{c}$ – mean molecular gas speed

d - diameter

D – Diffusion coefficient

f - Frequency

F - Force

H – Henry's law constant

I – Mass flux

k – Evaporation rate

K – Thermal conductivity

L – Latent heat of vaporisation

J – Crystal nucleation rate

m – Mass

M – Molar mass

n – refractive index

p – Pressure

P – Probability of crystal nucleation

q - Charge

r – Radius

R_i – Molar refraction of a component

S - Saturation

T – Temperature

v – Gas speed

V – Volume

$V_{DC/AC}$ – Voltage of DC or AC

Greek Alphabet symbols

α – accommodation coefficient

β_M – Transitional correction factor for mass transfer

β_T – Transitional correction factor for mass transfer

σ – Surface tension

λ – Wavelength

υ_k – kinematic viscosity

η - viscosity

ϑ - angle

ρ – density

μ - Chemical potential

γ – Activity coefficient

Subscript

a – Property at a droplet surface

e – Property of a mixture

i – Property of one component

∞ - Gas phase property far from the droplet

Fundamental Constants

R - Molar gas constant – 8.314 J mol^{-1} K^{-1}

k_B - Boltzmann constant – 1.38 × 10^{-23} J mol^{-1}

g – Gravitational acceleration – 9.81 m s^{-1}

Acronyms

AC – Alternating Current
AIOMFAC-web – Aerosol Inorganics-Organics Mixtures Functional Groups Activity Coefficient web
API – Active pharmaceutical ingredient
ASD – Amorphous solid dispersion
CCD – Charged coupled device
CERS – Cavity enhanced raman scattering
CFC – Chlorofluorocarbon
CFD – Computational fluid dynamics
DC – Direct Current
DPI – Dry powder inhaler
DRH – Deliquescence RH
E-AIM – Extended Aerosol Inorganic Model
EDB – Electrodynamic balance
ERH – Efflorescence RH
FDC – Falling droplet column
GF – Growth factor
HFA - Hydrofluoroalkane
HFC – Hydrofluorocarbon
Kn – Knudsen number
MDI – Metered-dose inhaler
MFS – Mass fraction of solute
MODE – Millikan's oil drop experiment
Nu – Nusselt number
RH – Relative humidity
Re – Reynolds number
RSD – Relative standard deviation
Pe – Péclet number
Pr – Prandtl number
Sc – Schmidt number
Sh – Sherwood number
SEM – Scanning Electron Microscopy
SHEL – Standard Hyperboloidal Electrodynamic Levitator
SOA – Secondary organic aerosol
WGMs – Whispering gallery modes
XRD – X-Ray diffraction

Chapter 1

Introduction to the Evaporation of Liquid Aerosol Droplets

The evaporation of liquids is a process that touches every aspect of our lives, from the food we eat to many pharmaceutical products, paper, wood, coatings and textiles. Industrially, drying is an enormous global operation and a highly energy intensive process. The conversion of liquid to vapour requires a latent heat of vaporisation. A study calculated that in the U.K approximately 350×10^{15} J is used in drying processes, accounting for a staggering 17.7% of the nation's total energy consumption.[1] Drying is reported to be a relatively inefficient process; for example, in industrial spray drying the evaporation load often makes up as little as 50% of the energy supplied to the process, with significant energy consumption going to heat losses and additional equipment such as fans and pumps.[2] Thus, there is an increased drive to better understand the drying process as a whole.

This thesis focuses on the drying processes of free droplets, liquids that are not on a flat surface but rather take the form of levitated droplets on the micrometre-scale. The physical chemistry processes occurring in such droplets are fundamental to the spray drying industry. Understanding how a droplet containing a certain formulation will evaporate to leave a solid product is an active area of research because the drying processes control the resulting properties.[3,4] In crop-spraying, the dynamics of liquid agricultural sprays affect how the product ultimately interacts with the leaves. In the pharmaceutical sector, hundreds of millions of people inhale liquid droplets from inhalers for asthma treatment every day.[5] The transport of such droplets through the lungs is dependent upon the rate of drying, which controls the pharmacokinetics of the drug and the resulting efficacy of the therapy.

We are continuously surrounded by free liquid droplets, the multitude of liquid aerosol particles that we breathe in every day and that make up clouds. Such droplets are in a constant state of flux; water and organic semi-volatile components continuously evaporate and condense, partitioning between the droplet and gas phase. The process of how liquid aerosol droplets dry and crystallise affects the way that light interacts with aerosols in the atmosphere.[6] The effect that aerosols have on the climate is the largest source of uncertainty in our understanding of the radiative balance of the Earth and on the continued rise in average global temperatures.[7,8] Hence, the processes occurring in free-droplet drying are a problem of broad importance.

This thesis presents experimental measurements on the mass and heat transfer from liquid aerosol droplets under a range of different environmental conditions, to demonstrate the importance of single-droplet measurements in improving our understanding of the evaporation processes occurring in more complex industrial applications. This chapter introduces the challenges associated with studying droplet drying to provide context for the experimental results presented in later chapters. First, Section 1.1

introduces the industries for which droplet-drying is a fundamental aspect, with more attention focused on spray drying and respiratory drug delivery for which the work presented in this thesis is of more relevance. In Section 1.2 the principles and history of experimental techniques that are used to study droplet drying are discussed. The aims of this thesis are listed in Section 1.3.

1.1. Industrial Applications with Relevance to Droplet Drying

In the following sections, a range of industries will be discussed, for which droplet drying makes up an important process. This list is not intended to be exhaustive. First, the process of spray drying will be introduced.

1.1.1. Spray Drying

Spray drying is an industrial technique that has wide-reaching applications in the production of food, biochemical, nanotechnological and pharmaceutical products.[9] It is typically a single step process, turning liquid formulations into solid powdered products. Its attraction for many applications stems from the relatively narrow size distribution of the dried particles, and the ability to work with thermally sensitive materials, such as many drug compounds.[3]

The basic principle of spray drying is the conversion of a feed liquid into solid powdered particles by fine-spraying droplets of the solution into a stream of hot gas, causing rapid evaporation of the droplets in-flight. Typically operated as a continuous process, the feed solution, emulsion, melt or slurry of interest goes through four key stages: i) atomisation into droplets; ii) combination of the spray with the drying gas; iii) evaporation into dried particles; and iv) product collection and separation from the gas. A schematic diagram of a conventional spray dryer and the process is shown in Fig. 1-1.

The liquid feed solution is pumped into an atomiser to form a spray of droplets. Various atomisation techniques exist, generating droplets through a high pressure nozzle, using centrifugal energy in a rotary atomiser or using kinetic energy with a two-fluid nozzle.[10] The initial droplet size varies according to processing parameters such as the atomisation method, liquid flow rate, viscosity of the feed solution and its surface tension. Typically, a droplet size distribution will range between diameters of 20 and 150 µm. The droplets enter the drying chamber where the solvent rapidly evaporates to form solid particles with specific characteristics.[11] The drying chamber size varies according to the application, and can range from commercial bench-top spray dryers to industrial-scale spraying towers that are 30 m in height.[12] The gas used for drying is typically atmospheric air, but some process for drying organic solvents use nitrogen as a reusable drying gas.[13] Inlet air temperatures are typically in the region of 200 – 250 °C, but can be higher for thermally insensitive products.[14] The droplets or dried particles typically

follow the streamlines of the gas to the bottom of the chamber where they are separated from the gas flow using a cyclone.[15] Spray dryers are commonly open cycle, which means that the humidified gas containing the moisture that is removed from the droplets is only used once. Some closed-cycle dryers exist, wherein the drying gas undergoes a scrubbing operation to extract the moisture and is then is recirculated back into the dryer.[16] Closed-cycle dryers are less common and are used typically for systems that use nitrogen as the inlet gas, to keep an oxygen-free atmosphere for oxidation-sensitive products or flammable solvents.[13]

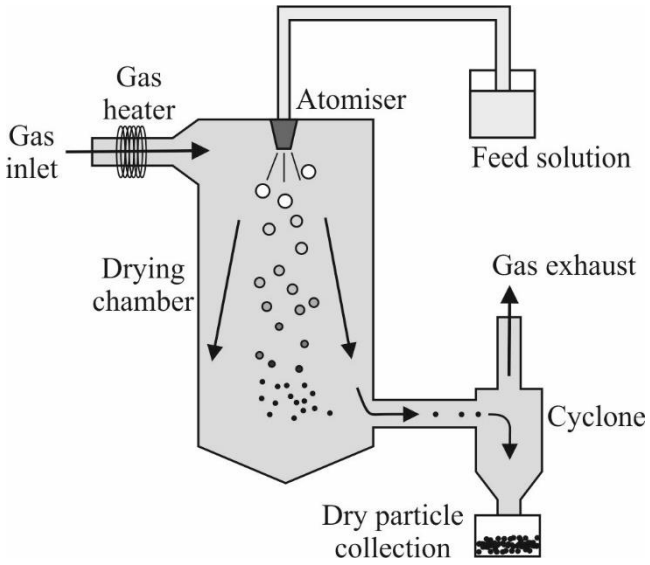

Figure 1-1: Schematic of the apparatus of a conventional co-current spray dryer. Figure is based on a schematic from Sosnik and Seremeta.[10]

The production rate of spray drying depends upon the dryer dimensions and the processing parameters. For example, for a factory-scale spray dryer with a chamber height of ~ 5 m, initial solid content of feed solution of 20% by weight, and inlet temperature of 200 °C, roughly 50 kg of water evaporates per hour, resulting in 12.5 kg of powdered product per hour.[17]

Spray drying is often preferred over other drying processes to produce powdered products such as fluid bed drying because it is a continuous operational process, which makes it applicable for large volumes of product. It can also serve a wide variety of solvents, including those that are flammable organics, explosive or toxic. However, a large disadvantage to spray drying is that it is thermally inefficient compared to other types of drying. The thermal inefficiency arises from the large size of the spray drying chamber for a small product volume, and because a lot of liquid needs to evaporate as the inlet solution needs to be fluid enough to pump and atomise.[2]

1.1.1.1. Different Types Spray Dryers and their Application to Industry

The gas trajectory compared to the spray can be co-current, counter-current or mixed flow, and the choice of arrangement depends upon the feed solution.[18] Schematic figures showing examples of the gas and droplet trajectories are shown in Fig. 1-2. Heat-sensitive products tend to be dried in co-current dryers (panel *a*). The hottest region of the spray dryer is the top, with negative temperature gradients going down. The heated gas passes over the solution droplets at the top of the chamber where they have the greatest water content. Rapid solvent evaporation is a cooling process, so even though the inlet drying temperature in a co-current dryer can be very hot, the droplets rarely reach such a high temperature. The solvent evaporation means the droplets maintain a temperature cooler than the gas temperature, which is known as the wet-bulb temperature.[19] This evaporative cooling effect renders co-current spray dryers suitable for products that can degrade at high temperatures such as those in the food or pharmaceutical industries.

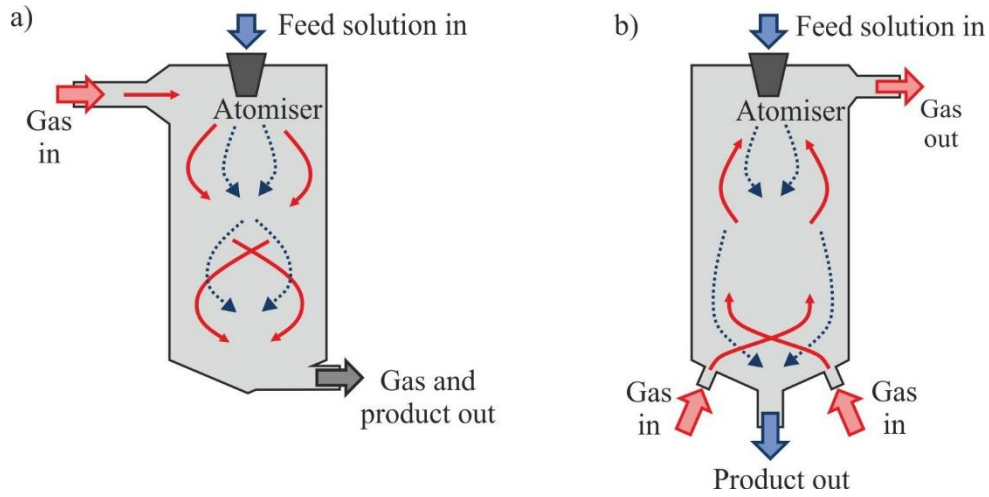

Figure 1-2: A general depiction of the different formats of gas trajectory in a spray dryer. Liquid flow is depicted in blue and gas flow in red, for a) Co-current, b) counter-current spray dryers.

Spray drying is highly popular in the food and drink industry, suppressing the growth of microorganisms such as bacteria, yeast or mould by removing water. One of the largest applications of spray drying is to the dairy industry for improved milk storage, transport and the addition of probiotics and vitamins.[20] The infant formula milk powder market size was estimated to be worth $45.12 billion worldwide in 2018, with expectations for it to surpass $100 billion by 2026.[21]

Challenges in the spray drying of food involves the retention of flavours and aromas during drying, properties which have been shown to be affected by the drying operating conditions.[22] Another regular complication with spray drying dairy products or those that are rich in sugar, for example fruits, honey or starches, is that the droplets become overly sticky and can agglomerate with other droplets to form undesirable clusters.[23] Also, droplets sticking to the dryer wall leads to problems with hygiene, product loss, processing difficulties and fire risks.[24] Whether particles stick to walls in the dryer, pipes or

cyclone often depends upon the drying kinetics that occur after a droplet forms a crust at the surface, and this aspect remains one of the greatest challenges in spray drying.[25]

Examples of pharmaceutical products that are processed with co-current spray drying include antibiotics, vaccines and enzymes. Many pharmaceutically active molecules suffer from poor aqueous solubility, which reduces the possibility of oral administration.[26] A popular route to overcome this limitation is to form an amorphous solid dispersion (ASD), where an active pharmaceutical ingredient is combined with a soluble polymer excipient. Spray drying the mixture to form solid particles of ASD greatly improves the aqueous solubility and efficacy of the drug without the need for any chemical alteration.[27]

Dry powder inhalers (DPIs) are devices that administer drugs through inhalation of a very fine powder. Since the Clean Air Act following the Montreal Protocol, metered-dose inhaler (MDI) formulations containing ozone-depleting chlorofluorocarbon propellants (CFCs) have been phased-out and replaced by hydrofluorocarbons (HFCs).[28] HFCs are more expensive, so there is a drive to increase the use of DPIs where there is no need for a propellant. The vast majority of marketed DPIs rely on jet-milling and micronization to form the drug powders. However, micronizing can lead to highly hydrophobic surfaces which cause agglomeration in storage and can lead to poor aerosolization performance.[29] DPI particles can be produced through spray drying, which can result in a smaller average particle size (hence a larger respirable fraction) with a narrower size distribution.[30] Spray drying allows some control over the product morphology (density and shape) which affect the transport properties of the powdered drug within the lung. Particle engineering is an emerging field focused on producing bespoke particles that satisfy a range of purposes, be it carrying and stabilising the active pharmaceutical ingredient (API), targeting specific lung regions or controlled release.[13] Different regions of the lung can be targeted for deposition depending upon the size of the inhaled particle.[31]

Counter-current spray dryers (Fig. 1-2b) have the heated gas flow applied in the opposite direction to the sprayed droplets, meaning that there is a large temperature difference between the liquid phase and the gas phase for most of the drying chamber. This arrangement provides more thermal efficiency, but it is only suitable for thermally stable products, the most common example being detergent powders.[32] Detergent products need to have a long shelf life, good flowability and fast dissolution for a variable degree of water hardness. To design products that meet such needs requires a deeper understanding of the powder structure.[33] Understanding the drying kinetics can be challenging because the counter-current trajectory can lead to highly complex swirling flows that can lead to particle recirculation and agglomeration of semi-dried material, which can affect the resulting size distribution.[34]

1.1.1.2. Product Morphologies and Properties from Spray Drying

There is a wide range of possible morphologies that can be created through evaporation of free droplets in a spray dryer, and the particle size and morphology are fundamental for the properties of the resulting solid product. The morphology development inside a drying droplet can be strongly affected by the processing parameters in the spray dryer, such as the gas inlet temperature, the number of atomiser nozzles and their arrangement, the initial droplet size, the solution feed temperature, flow rate, and the gas pressure. In addition, the properties of the feed solution are important, such as the concentration, viscosity, rheology and additives such as surfactants.[4]

The final particle structure after drying spherical free droplets has been shown to vary from solid, dense spheres to hollow, buckled, flat or doughnut shaped, with surfaces that can be smooth, porous, rough or spiky.[35–38] In addition, the phase of the dried solid after spray drying can be crystalline[39,40] or amorphous, where molecules in the particle are packed in a way that features no long range order.[41,42]

An example of the range of possible morphologies accessible through spray drying of spherical liquid droplets is shown in Fig. 1-3.

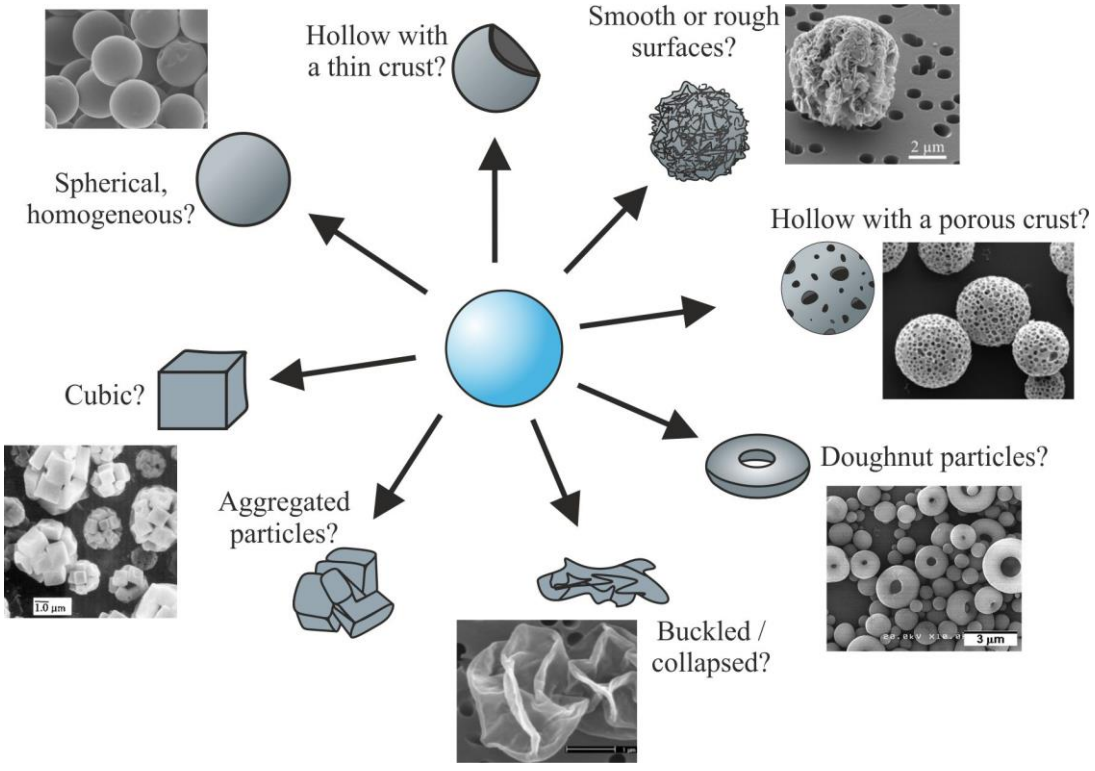

Figure 1-3: Examples of the possible final particle morphologies that can be accessed through spray drying of spherical liquid droplets. Inset images are reprinted with permission from Refs. [35,43–45]

Regardless of the application for the spray dried product, the final particle morphology and size are usually highly important. For solid particles that are inhaled for respiratory drug delivery, the size and density of the particles directly influence the transport properties in the lung and hence, the lung region

of drug deposition.[31] The extent of crystalline order in a particle, or whether it is an amorphous solid, control how soluble the product is, which is important for applications in the food industry. Understanding the particle formation process in a spray dryer to predict and control product morphology is, hence, the subject of active research.

1.1.1.3. Challenges in Studying Droplet Evaporation in Spray Drying

Spray drying appears a simple concept: the conversion of liquid free droplets into solid powders through the removal of water. In reality, there is multitude of competing kinetic processes occurring during drying, and whilst spray drying is such a commonly used technique, there is still a limited understanding of morphology development during drying.[9] In one single droplet, there is strong coupling between heat and mass transfer, as well as phase transitions, potential rheological changes, internal flows and mechanical instabilities. Considering that in the drying chamber there is a spray plume of billions of droplets with polydisperse sizes, each that can interact with one another through collisions, coalescence or with the wall of the chamber, makes the picture even more complicated. In addition, the drying chamber itself is likely to have unpredictable temperature gradients, with turbulent and swirling flows.[18]
The residence time of droplets in a spray dryer can vary, but generally it is a very rapid process with the drying step over in a matter of seconds. This, with the enormous quantity of droplets present, makes it very difficult to study the drying process *in situ*.[24] Experiments involving industrial spray dryers can be difficult to interpret due to the large size and complexity of the instrumentation.[46]
The success of a spray drying operation usually depends upon the experience of the engineer and on previous experiments in pilot-scale dryers. Scaling-up from pilot-scale to the size of the large spray drying towers can often be a challenge because of the difference in length and gas speed scales between the two cases.[47] Modelling can reduce the number of design steps required for planning spray drying processes, and multiple models exist for spray drying at a broad range of complexities. There are computational fluid dynamics (CFD) models to track the particle and gas flows in a dryer, which provide insight into the droplet residence time.[48] Simple single droplet drying calculations are used to predict the time required for solvent loss and psychrometric charts can identify potential "sticky-points" in the drying step.[49] However, a comprehensive model that can couple the flow patterns inside a spray dryer with the morphology changes from droplet to particle, including the complexities of shell formation, has not yet been developed.[25]
In view of the difficulties associated with *in situ* studies of the internal microphysics of droplets in a spray drying process, much recent work has looked to simplify the picture with single-droplet experiments. Building an understanding of the kinetics of droplet drying means moving away from the 'cook and look' approach that has historically dominated much of the spray-drying literature.[4]

1.1.2. Respiratory Drug Delivery

Droplet drying is of fundamental importance to the field of respiratory drug delivery using metered dose inhalers. Inhalation therapy is rapidly becoming a popular choice for drug delivery, not only for lung syndromes but a range of diseases such as circulatory system diseases and cancer.[50] There are promising results from administering insulin with metered dose inhalers (MDIs)[51] and inhalable insulin has been approved for use in Europe and America.[52]

The human lung can contain up to 600 million alveoli, each with only a single cellular layer (0.2–0.7 μm thick),[53] so the immense epithelial surface area and rich blood supply amounts to a fast rate that drug molecules can be taken up into the systemic circulation.[54] Behind intravenous therapy, inhalation provides the fastest method of drug delivery than any other administration technique, with less degradation to the drug molecules than if taken orally.[50] However, with the developments in inhalable medicines comes the need for consistency in the dose delivered by different inhaler devices.[55]

Typical studies of aerosol lung delivery only address the drug formulation and the pharmacokinetics of uptake on the lung surface, or the device used to produce the aerosol spray. Studies often neglect the kinetic processes occurring at the aerosol droplet level in the time period between when the droplets are generated and when they deposit at the lung surface.[31] Indeed, to advance inhalation therapy there needs to be an improved understanding of the amount of drug deposition in different areas of the lung, to ultimately control where this deposition occurs.[53] Aerosol droplets are highly dynamic and can rapidly respond to environmental conditions with changeable diameters, concentrations and phases. The transport kinetics of inhaled droplets controls the region of delivered dose, which will ultimately depend upon the aerosol kinetic processes occurring in the humid lung, such as evaporation and condensation.

1.1.2.1. Evaporation and Condensation Processes Occurring in the Lung

Inhaler formulations for metered dose inhalers (MDIs) are typically stored in a pressurised canister that contains the active pharmaceutical ingredient (API) dissolved in a solvent which is commonly ethanol, and a propellant, such as a hydrofluoroalkane (HFA). Some MDIs are used in conjunction with a spacer unit, which increases the length of time from aerosol generation to lung deposition. The aerosol kinetic processes that can take place in the aerosolised drug formulation are initial rapid evaporation of the propellant, either in the spacer, mouth or in the lungs, and evaporation of the other solvent in the formulation. Evaporation leads to an increase in concentration of the API, which could segregate out of solution and form an amorphous or crystalline dried particle. The phase state of the API upon deposition could strongly affect the pharmacokinetics of the drug uptake, because dissolution must occur at the lung surface first and this process could be accelerated for an amorphous particle.[55]

In addition, the humid environment of the lung could lead to water condensation and aerosol droplet growth, affecting the phase state of the particles further.[31] Hygroscopicity is the ability of a substance

to absorb water under increases in the gas phase relative humidity (RH). In the aerosol phase this water absorption leads to an increase in size of the droplet. The RH in the lung can reach levels as high as 99.5% [56] so, if droplets that are inhaled from MDIs are hygroscopic, this size change can lead to dramatic differences in the transport properties of the droplets and the resulting deposition region in the lung. Hygroscopic water uptake can also alter the droplet phase state; API solubility in water could be very different to that in the MDI cosolvent, which is typically ethanol.

1.1.2.2. The Relationship Between Droplet Size and Expected Lung Deposition Region

Certain regions of the lung may be specifically targeted for drug deposition depending on the treatment strategy, such as the upper airways for asthma therapy or the deep lung for alveolar diseases.[53] The region of the lung in which inhaled particles are deposited is critically dependent upon the aerosol size (Fig. 1-4). The majority of particles with diameter larger than 5 µm typically do not penetrate far into the lung and are deposited in the mouth, nose or throat through impaction and sedimentation. Smaller particles within the range of 2 to 5 µm tend to enter the lung region but losses of particles occur around the bronchi through sedimentation. The fraction of particles that are in the submicron range tend to be able to penetrate the deep lung, with losses of particle less than 0.1 µm by diffusion.[31,57]

The size and phase state of inhaled MDI droplets depend upon microphysical processes such as solvent evaporation, water condensation and precipitation. As the size is highly important for the region of lung deposition, and the phase state is critical for the pharmacokinetics of the drug, an improved understanding of these kinetic processes is vital for improving patient outcomes for respiratory drug delivery.

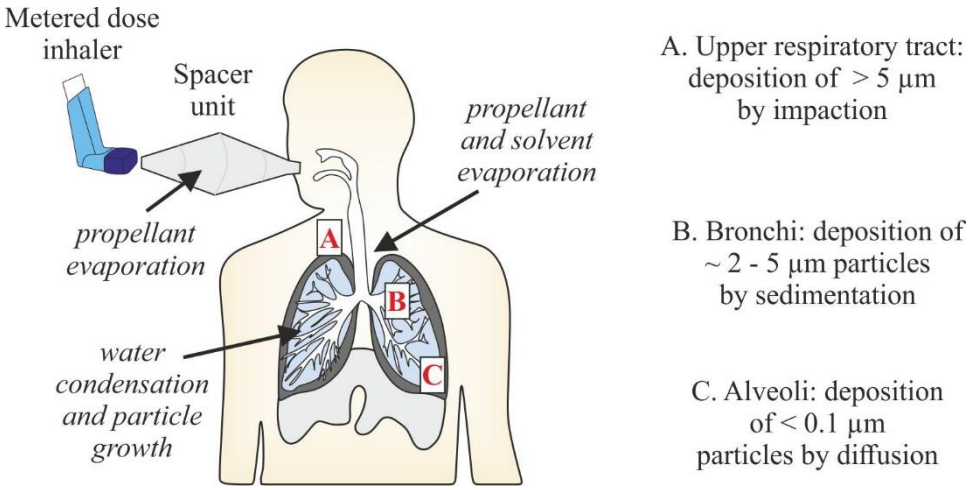

Figure 1-4: Schematic figure demonstrating the microphysical processes occurring to liquid droplets that are inhaled from an MDI into the lung. The predicted particle size to deposit in different regions is shown.

1.1.3. Crop-Spraying

Much of modern farming relies on efficient application of fertilisers and pesticides to plants. A common method to administer such chemicals is through sprays (foliar application), which typically contain dilute aqueous solutions.[58] There are environmental concerns about large-scale spraying techniques, such as aerial crop spraying, due to the impacts of pesticide drift to nearby areas on human health, ecological balance and water supplies. Research is ongoing to identify more effective methods of atomizing the product into droplets and applying this to the leaves, as well as investigating new agricultural compounds.[59] Hence, studies to understand droplet evaporation rates as well as spray dynamics are fundamental.[60]

In agricultural spraying, a solution is continuously mixed to keep all products in a suspension whilst a stream is atomised into a liquid sheet using hydraulic spray nozzles, that rapidly destabilises into droplets that are sprayed out onto leaves. Evaporation can occur in-flight as well as once the droplets impact the leaves. The remaining solid deposit is then taken-up by pores of the plant.[61] If the droplets are still in liquid-form after leaf impact, the degree of spreading of a product on the leaf surface relates to the solution viscosity and the surface tension of the sprayed solution,[58] both of which are liquid properties that can change drastically during evaporation as the concentration of a solute rises.[62,63] In addition, the size distribution of deposited droplets strongly affects the area of leaf coverage. Evaporation kinetics of the product in free space prior to deposition would affect the resulting droplet size, and droplet coalescence occurring in the sprays would have an impact on the breadth of the size distribution and the spray drift.

1.1.4. Ink-Jet Printing

Inkjet printing is an industrial process on a global scale, providing cost-effective patterning of products in precise positioning. Aside from the well-known application in document preparation, inkjet printing has been developed into a deposition method for resolved patterning of functional, rare or delicate materials.[64] It has been shown to produce high resolution patterns when producing transparent conducting film,[65] organic semiconductors,[66] LEDs,[67] solar cells[68] and sensors.[69] In addition, inkjet printing is used in the pharmaceutical industry for the production of drug microcapsules.[70,71]

It is a challenging task to control the drying of inkjet droplets into the desired morphology with precision. The general concept of inkjet printing is to deposit liquid inks from thin nozzles, typically in picolitre droplet volumes, onto defined positions on a treated surface.[66] The droplets dry, sometimes under the action of heating the substrate, to leave the patterned material. For most inkjet applications, a uniform homogeneous film is required for the dried material, however the evaporation of sessile

droplets, i.e. droplets on a flat surface, can be subjected to internal flow mechanisms that can lead to non-uniform drying deposits.[72]

Sessile droplets dry in similar mechanisms to free droplets but with the added complexity of the supporting substrate beneath the droplet. This surface causes deviation from the 3D-spherically symmetric shape of an aerosol droplet, as well as introducing a three-phase contact line between the droplet, the surface and the vapour phase. Drying may not be symmetric across the droplet surface due to the non-spherical shape causing spatial gradients in the composition of the drying droplet. Such gradients can lead to diffusive flow as well as Marangoni flow, which is that arising from surface tension gradients.[4] To address these challenges, single-droplet drying studies are an active area of research to understand the process that govern the spatial evolution of components inside a droplet and the morphology of the final deposit.

1.2. History and Principles of Experimental Techniques used to Study Droplet-Drying

1.2.1. Overview of Single Particle Techniques

The use of single droplet experiments to study how different solutions evaporate dates back to 1952 with a publication from Ranz and Marshall.[73] They studied the rate of evaporation from pure liquid droplets and those containing solutes and suspensions, in droplets of 0.6 – 1.1 mm in diameter, up to temperatures of 220 °C. They suspended a spherical droplet of solution from a micropipette in a vertical stream of heated air and measured the evaporation rate by recording the rate of feed solution from the pipette into the droplet to maintain a constant droplet diameter. Using a balance to record the mass transfer in evaporation led to radical work on the study of skin formation during rapidly drying droplets and the observation of different morphologies developing in different drying conditions.[74] Since then, there have been significant developments in the instrumentation available for studying single droplets at smaller size range.[9] The most common single-droplet experiments that can be used to study evaporation are summarised in Fig. 1-5 and described in the following sections.

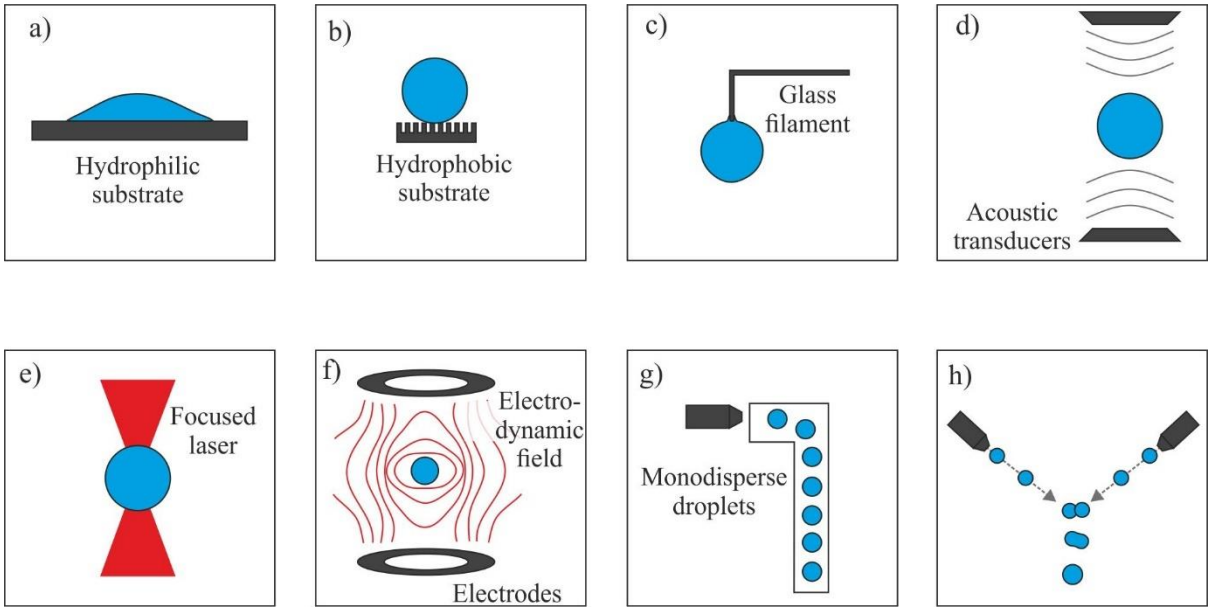

Figure 1-5: Schematic showing the varying experimental methods to study droplet drying. a) and b) Sessile droplet studies on hydrophilic and hydrophobic substrates, respectively, i.e. intrusive droplet studies, c) intrusive levitation (pendant droplet studies), d) acoustic levitation, e) optical levitation, f) electrodynamic levitation g) free-falling droplet column, h) coalescence experiments.

1.2.2. Sessile Droplet Studies

Sessile droplets are those that are deposited on a flat surface and are perhaps the simplest droplet systems to study in terms of the experimental equipment required. The surface properties can be varied to study the evaporation, spreading and morphology of the remaining deposition of different solutions for applications such as ink-jet printing (Fig. 1-5a).[72,75] Tracer particles can be included as a suspension in the initial droplet formulation, to study internal Marangoni flows [76,77] or thermal convective flows.[72] However, such work is not reflective of the drying behaviour in a free droplet, where there is no three-phase contact line. However, if hydrophobic surfaces are used (Fig. 1-5b) the spherical shape of a free droplet can be closely replicated and the contact point between the droplet and the surface can be minimised, to closely present the conditions in spray dryer.[78] Xu and Choi made a superhydrophobic silicon surface using a photolithography and etching processes to roughen the surface with various structures (pillars, lines and wells), so that they could study the evaporation rate of colloidal sessile droplets in the millimetre size range.[79]

A benefit of using sessile droplets to study the drying processes occurring in free droplets is that it can be much simpler to image droplets on surfaces as they are easier to locate and to image with focused optics.[80] Multiple sessile droplets can be isolated and dried simultaneously, with varying residence times to study how droplets of different ages interact with one another when in close proximity.[81] Most evaporation experiments of droplets deposited on a surface use different optical techniques to image the

droplet shape while it dries, such as high-frame rate cameras, interferometry [82] or optical coherence tomography,[83] with a microbalance underneath the substrate to monitor changes in mass throughout drying.

There are significant disadvantages to using sessile droplet experiments to investigate free droplet drying in applications such as spray drying. Even if droplets have a large contact angle with the surface, the droplet shape is still distorted from spherical, and the droplets in sessile experiments (~ mm in size) are generally larger than those found in a spray dryer, where droplet sizes reach few hundred micrometres as a maximum. Sessile experiments have been criticised due to the contact area between the surface and the droplet, as the surface can act as a heat sink during evaporation and thus affect the heat and mass transfer by conduction.[84] The surface could also serve as a source of contamination to the liquid and could lead to heterogeneous nucleation of crystals of the solutes upon drying.

1.2.3. Intrusive Levitation

Intrusive levitation experiments are those where a droplet is suspended from a filament or needle (Fig. 1-5c). They have the advantage of being able to record the mass loss, either from a microbalance attached to the suspension filament, or by determining the mass from the deviation in the position of the filament from the equilibrium point using a calibration curve. The filament that suspends the droplet can also attach a thermocouple wire to the droplet, to measure the droplet temperature suppression during drying. The coupling of heat and mass transfer is a complex microphysical problem in rapid droplet drying, and intrusive levitation enables both to be measured simultaneously.[85] Like sessile droplets, the position of a suspended droplet in multiple repeat experiments can be highly reproducible and so imaging with a focused camera to record the droplet diameter throughout drying is facile.

A limitation in suspended droplet drying is that it can be difficult to use droplets smaller than a few hundred micrometers,[73,85,86] so experiments can only access the upper end of droplet radii typical in spray drying. In addition, often the droplets cannot freely rotate. Applying a heated gas in a spherically symmetric direction can be challenging so typically one side of the droplet experiences slightly different conditions to the other. The contact between the droplet and filament can also have inherent effects. For example, contact can lower the activation barrier for nucleation of inorganic crystals and act as a templating surface for heterogeneous nucleation.[87] This means that suspended droplets cannot reach as high supersaturations as if they were contact-free. However, suspended droplets are very practical experiments to undertake and morphological changes in a drying droplet can be readily observed in a range of experimental conditions, making it a popular method for studying spray drying.[88,89]

1.2.4. Aerodynamic Levitation

Non-intrusive methods of levitation are advantageous in that there is not contact between the drying droplet and any external surface. Some non-intrusive levitation methods, notably electrodynamic and optical levitation, can access small droplet sizes, down to the micron and even sub-micron range. In fact, smaller radii are favoured as less force is required to counteract the gravitational force acting upon the droplet. The forces acting upon the droplet (drag, buoyancy and gravitational forces) may change whilst the droplet shrinks in size and loses mass, so maintaining a steady position using contact-free methods can be a challenge in non-intrusive levitation. Methods for non-intrusive levitation use aerodynamic, acoustic, optical or electrodynamic forces, which will be reviewed in this and the following sections, starting with aerodynamic levitation.

Droplets can be levitated in a gas stream that is directed vertically upwards, known as aerodynamic levitation. For a diverging gas flow there is a decreasing level of drag force acting upon the droplet with increasing height, so an equilibrium vertical position will be achieved when the drag acting on the droplet or particle is equivalent to the gravitational force acting downwards.[90] There have been instrumental designs that achieve axial stability by having restoring forces surrounding the droplet that stabilises it in a potential energy well.[91]

The simplicity of the setup required for aerodynamic levitation means that it can be incorporated into different kinds of experiments. For example, Hennet et al. combined aerodynamic levitation with a CO_2 laser to heat droplets of 3 mm in diameter, and could access temperatures up to 1000 K.[92] The gas flow rates required to hold up droplets in the millimetre size range need to be as high as several hundreds of $cm^3\ s^{-1}$, which can be a good representation of the turbulent flow of droplets in a spray dryer. However, the stability of an aerodynamically levitated particle can be poor, as minor fluctuations in the pressure field around the droplet, like morphological changes to the particle during drying, can make it fall out of the gas jet. Maintaining a steady position of the levitated droplet for focused imaging is challenging, and for this reason aerodynamic levitation to study the microphysics during droplet drying is not a popular technique.

1.2.5. Acoustic Levitation

Standing waves, generated by an ultrasound transducer, can provide sufficient radiation forces to manipulate solid objects without contact. Not needing a gas flow for droplet stabilisation means that the flow rate, RH and temperature of the gas flow can be explicitly tuned for the desirable droplet drying conditions. An example schematic of a simple acoustic levitator is shown in Fig. 1-6. The setup has an ultrasound transducer (comprising a piezocrystal with a vibrating plate) that generates the sound waves, mounted vertically opposite a reflector. An ultrasonic frequency in the range 20 to 58 kHz can typically

levitate droplets of radius 50 to 5000 μm.[24,90] Depending upon the acoustic field that is generated, there can be multiple ultrasound nodes in the trapping region where a droplet levitates stably. The acoustic levitation setup can then incorporate a method of heating, for example from a heated gas flow or from an external CO_2 heating laser, and a camera to study size changes and the morphological developments during drying. In addition, micrometre screws can allow adjustment of the acoustic nodes with respect to the camera focal point in three dimensions.

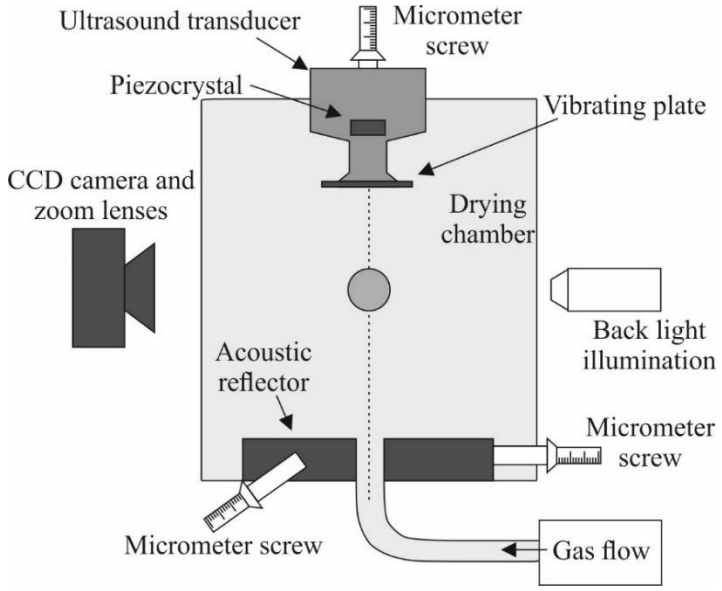

Figure 1-6: A schematic of a standard acoustic levitator for studying droplet drying in a gas flow. Schematic is based on a figure from Schiffter and Lee.[93]

The radiation forces acting on an acoustically trapped particle can be up to five orders of magnitude larger per unit power expended than particles held in optical traps (discussed in Section 1.2.6).[94] The high efficiency of acoustic trapping enables its use for the levitation of droplets containing biological materials such as proteins,[95] lipids [96] and cells,[97] where high power outputs could be damaging. In 2019, Marzo and Drinkwater developed an iterative backpropagation algorithm, which, when applied to two arrays each containing 256 transducers mounted opposite one another, could produce a holographic acoustic field that could be spatially manipulated in three dimensions in real time.[94] They were able to trap multiple particles that could be moved independently of one another, which was a significant step forward in acoustic trapping.

Acoustic fields can levitate a broad range of droplet sizes, from the submicron up to the centimetre scale, as well as being able to trap non-spherical particles,[94] making it a suitable technique for studying droplet drying. However, Schiffter and Lee [98] observed deviation from the expected evaporation rates, where typically isothermal evaporation should display a linear dependence in the temporal $radius^2$, which they cite as being a result of acoustic streaming. Due to the setup of an acoustic field inside the constraints of an experimental chamber, an array of doughnut-shaped vortices formed that surrounded the trapped particle.[99] This led to the trapping of solvent vapour in the vortex which increased the local

partial pressure of water in the gas surrounding the droplet and reduced the evaporation rate. They showed that acoustic fields can be used qualitatively to study droplet evaporation and resulting particle morphology but that there are complexities to obtaining quantitative kinetic data.

1.2.6. Optical Levitation

The radiation pressure of light can exert forces on matter, and this property is exploited in optical tweezers. In 1970, Arthur Ashkin demonstrated that micrometre-sized single particles can be freely suspended in both a liquid and gas phase surrounding medium by the radiation pressure (optical scattering) from an argon laser.[100] This concept was developed into a gradient-force optical trap using a tightly focused IR laser which allowed for stable 3D trapping of a range of particles, including single bacterial cells.[101] In 2018, Ashkin received the Nobel Prize in Physics for his work on optical traps, demonstrating the relevance of this technique even fifty years on from his original studies.[102] The technique is popular across a wide span of experimental fields as it enables stable trapping of individual objects across length scales from tens of nanometres up to a few hundred micrometres,[103] with forces on the order of picoNewtons.[104] Trapping aerosol droplets in optical tweezers has led to significant advances in the understanding of atmospheric processes such as hygroscopic response,[105,106] SOA condensation [107,108] and heterogeneous chemistry.[109]

In principle, there are two types of force exerted upon a particle interacting with a highly focused laser beam: the scattering force and gradient force. The balance between these two forces controls the mechanism by which a single particle is held in the trap. An induced dipole is generated inside the particle by the electric field in the light; the magnitude of the dipole is proportional to the difference between the refractive index in the particle and in the surrounding phase. The scattering force acts in the direction of the propagation of the laser, and the magnitude of this force is proportional to the intensity of the laser beam. The gradient force is present in the case of a spatially varying electric field, so is prevalent in the case of a highly focused laser. A net force acts in three dimensions on the induced dipole to draw the particle into an area of highest laser intensity. The equilibrium trapping position depends upon the droplet mass, as it relates to the balance between the gravitational force, vertical gradient forces and the scattering force, but it is typically just below the focus of a vertically propagating laser beam.[110] The gradient force is directly proportional to the spatial gradient in light intensity. A schematic of the forces acting upon a spherical liquid droplet in a vertically propagating optical trap is shown in Fig. 1-7. The scattering force acts upwards, counteracting the gravitational force on the droplet. In Fig. 1-7a the droplet is positioned at the laser focal point, so the gradient forces in three dimensions are equal and there is no net force. In Fig. 1-7b the droplet position is to the left and below the laser focus, so there is a net gradient force acting to the right and vertically upwards which pulls the droplet back into the equilibrium position.

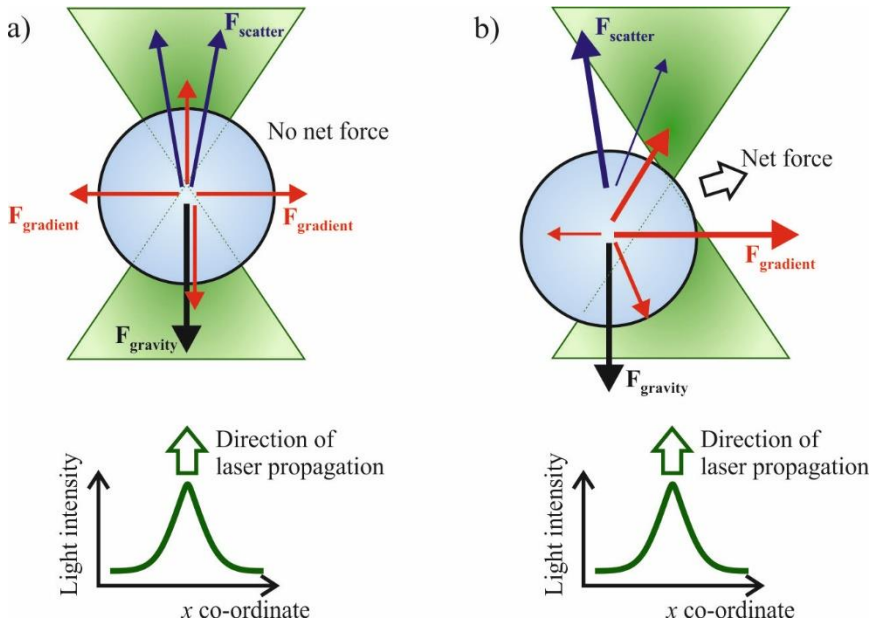

Figure 1-7: Schematic depicting the trapping of a liquid spherical droplet in optical tweezers. The vertically propagating incident laser beam is highly focused. a) The droplet is positioned slightly below the beam focus. The gradient forces (red) act equally in all directions, and the scattering force (blue) and vertical gradient forces are equivalent to the gravitational force (black), so there is no net movement of the droplet. b) The droplet is displaced in the trap, and there is a net force directing it back to the equilibrium trapping position due to the imbalance of the three-dimensional gradient forces.

A benefit to studying droplet drying with optical tweezers are that the droplet shape is typically not distorted by the optical forces. Droplets of a few micrometres in size retain a spherical shape due to the surface tension and capillary forces, and this is typical of a droplet in flight. In addition, the laser light used to trap the droplet can also be exploited for spectroscopic techniques. Raman spectroscopy can be applied to infer the presence of molecular components within a drying droplet, and the droplet can act as an optical cavity that enhances the scattering for stimulated raman scattering, which is known as Cavity-Enhanced Raman Spectroscopy (CERS). The CERS fingerprint of a liquid droplet held in an optical trap can provide the droplet size as well as refractive index, with indication to the droplet composition.[111]

A drawback to the use of optical tweezers to study droplet drying is that the potential gradient that draws a particle in to the trap only extends over a small area in space. Hence, it can be challenging to direct one single particle into the tweezers. Droplet generation in optical tweezer experiments is typically performed using nebulisers that flood the trapping cell with several millilitres of solution. Such droplets cause the RH in the chamber to be slow to equilibrate, hence, the timescale of water evaporation from trapped liquid droplets can have poor resolution. Optical tweezer experiments have been used to study slow isothermal evaporation processes of free droplets.[112,113] However, its use in studying rapid droplet drying is more challenging. Corsetti et al. were able to trap droplets of an ethanol-biofuel mixture for timescales of up to 1.5 s in optical tweezers. Whilst the evaporation rates were too rapid to use Raman scattering to size the droplets, the radius was recorded from a focused camera with sufficient precision

to show how the evaporation rate changed with varying starting ratios between the two liquids in the droplet.[114]

1.2.7. Electrodynamic levitation

1.2.7.1. Principles of Electrodynamic Levitation

Electrodynamic trapping is another example of contactless, non-intrusive levitation of particles. It has been a popular technique across many research groups studying droplet processes, from timescales occurring over a few seconds [114,115] up to many minutes or hours.[116–119] This is the method of droplet levitation used for the work in this thesis.

Electrodynamic levitation involves the use of electrodes with application of AC and DC fields. The levitated particle or droplet can be in the micrometre or sub-micrometre range,[120] but must be charged prior to entering the trapping region and this can be a challenge when studying non-polar liquids, such as organic solvents. There are various methods to get charged droplets into the chamber including nebulisation, coulombic break-up, vibrating charged needles or induction charging. Nebulisation can produce a cloud of droplets by bubbling N_2 gas through a solution.[121] Many of the droplets are charged, and by manually adjusting the field strength in the trapping cell, a single charged droplet can be isolated from those that settle out. This technique, whilst simple, involves a large number density of aerosol entering the trapping chamber which can lead to some vapour saturation in the carrier gas,[120] and hence, unreliable evaporation rates. Coulombic break-up of a larger solution drop suspended from a charged tip occurs when the charge density in the drop is increased above a threshold value. If the repulsive electrostatic forces surpass the surface tension, charged microdroplets will be produced through Coulombic explosion, and such droplets could enter the trapping cell and interact with the electrodynamic field.[122] Davis et al. demonstrated that solid particles, such as pollen, could be introduced into an electrodynamic balance (EDB) setup using an insulated hypodermic needle.[123] Charging the needle with a square wave, and vibrating the tip, induced particles to travel into the EDB trap. The experiments in this thesis employed an induction charged technique: the same technique as that used by Heinisch et al.[124] Single droplets are produced by a piezoelectric droplet-on-demand generator which is positioned in the presence of an induction electrode, leading to a net-charge accumulation on the droplet during formation.

A single charged droplet in only an AC field will oscillate around a central null point due to the gravitational force acting vertically upon the droplet. A combination of an AC field with a DC field to counteract the gravitational force leads to precise electrodynamic trapping at the centre of the instrument so that techniques can be employed to measure the size or mass of the trapped particle.[125]

1.2.7.2. History and Development of the Instrumentation for Electrodynamic Levitation

The principle of levitating charged particles using electrostatic forces can be dated back to the oil-drop experiment performed by Millikan in 1909.[126] Charged droplets of oil were fired into a chamber between two parallel metal surfaces (see Fig. 1-8a). The rate that the droplets fell depended upon the strength of the DC field applied to the metal plates, and measuring this ultimately led to their calculation of the charge on an electron to be 1.433×10^{-19} C. Millikan did not levitate any particles in a stationary position, but he suggested that such electrostatic forces could be made to suspend individually charged droplets for periods of time, and that this could be used to determine the mass of levitated objects down the order of picograms.[125] The addition of a central disk to one of the electrodes, known as a Fletcher disk,[127] exerted a horizontal restoring force onto a particle towards the centre of the instrument, which improved the stability of the measurement.

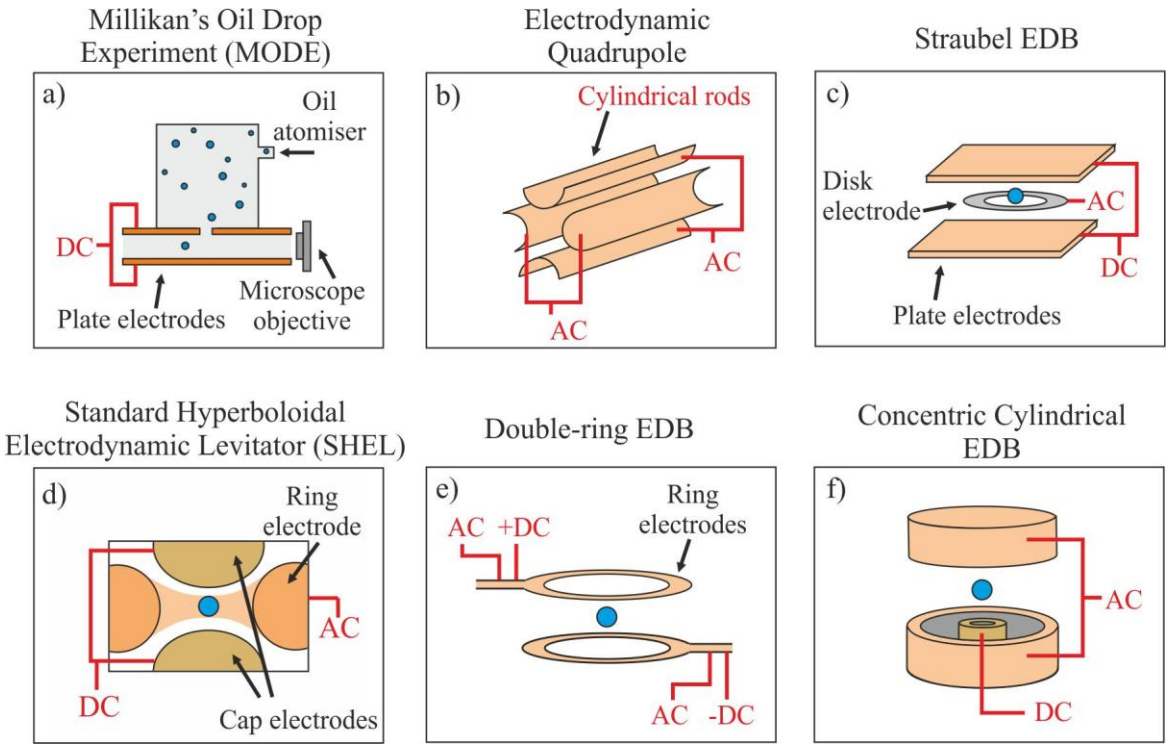

Figure 1-8: Schematic showing the electrode geometry in the different development stages of the electrodynamic balance. a) The original setup for Millikan's Oil Drop Experiment (MODE), for the early observations of electrostatic trapping. b) The electrodynamic quadrupole setup by Paul and Raether, [128] the electrodynamic principle from which was combined with the MODE geometry to make the Straubel EDB [129] in c). d) The Standard Hyperboloidal Levitator developed by Wuerker.[130] e) The double-ring EDB[131] and f) The Concentric Cylindrical EDB geometry as developed by Heinisch.[124]

Whilst the addition of the Fletcher disk added some lateral stability within the electrostatic forces imparted within the Millikan oil drop experiment (MODE) instrumentation, the real advance in steady trapping came through using an electrodynamic field rather than a static electric field. Paul and Raether observed that Rubidium ions could be stably held in place along the central axis between four cylindrical rods if a sinusoidal time-varying electrostatic force is applied to the rods (Fig. 1-8b).[128] Straubel applied this principle to the MODE setup by including an AC field as well as a DC field.[129] Straubel added a disk-shaped AC electrode around the centre of the trapping chamber, between the two DC MODE plate-electrodes, and could readily trap charged droplets of 10 μm using AC frequencies of ~ 100 Hz. This was the first electrodynamic balance (EDB), shown in Fig. 1-8c.

Wuerker et al. introduced the SHEL (Standard Hyperboloidal Electrodynamic Levitator) in 1959, which consists of two electrode caps and a central ring electrode, with a hyperboloidal shaped cavity (see Fig. 1-8d). A combination of AC and DC fields applied to the end-caps provides highly robust electrodynamic trapping, but very limited access for viewing the trapped particle.[130] The SHEL became an important apparatus in atomic spectroscopy, being developed into a mass spectrometer.[132] Dehmelt et al. found that by applying a radio frequency AC field to the electrodes, the chamber of a SHEL could act as an ion storage device,[133] leading them to receive the Nobel Prize for Physics in 1989.

Over the following decades, multiple variations of the electrodynamic balance have been presented. Wuerker et al. adapted the EDB arrangement to include three pairs of flat electrodes, i.e. the trapping chamber was at the centre of an enclosed cube.[134] The three opposite-facing surface-pairs had an applied AC field with a phase-difference to the other pairs, and DC fields could be applied additionally to any electrode to counteract the drag force imparted from a horizontal gas flow. This arrangement enabled the study of aerosol in a high flow rate. Müller greatly simplified the setup required for electrodynamic levitation by observing that charged particles can be trapped in an oscillatory mode above one simple disk that has an applied AC field.[135] An additional electrode, such as a plate with an applied DC field, is needed to trap particles in a non-oscillatory mode. Ray and Souyri took this further with double-rings;[131] this geometry has become widely popular as viewing and accessing the trapped particle is facile (Fig. 1-8e). Recently, such a setup has been adapted for use in studying the effect of evaporation on the viability of suspended droplets containing bacteria.[136] The EDB geometry that is employed in this thesis uses concentric cylindrical electrodes, which are mounted vertically opposite one another and use both AC and DC fields for stable trapping (Fig. 1-8f). This arrangement was developed by Heinisch et al.[124] and shown to be suitable for studying dynamic hygroscopic response of aerosol microdroplets.[116,137]

1.2.7.3. Studying Droplet Evaporation with Electrodynamic Levitation

Levitation with electric fields has developed into one of the most popular methods to study liquid droplet evaporation. However, the electrostatic trapping setup by Millikan (MODE) was initially developed to study fundamental properties or processes such as the charge of an electron, the Avogadro constant or Brownian motion.[138] Early into Millikan's experiments he switched from using water droplets to oil droplets, because of the errors in mass balancing arising from unwanted droplet evaporation. The concept of using the MODE apparatus to study droplet drying rates *in situ* was revisited in 1924 by Gudris and Kuikowa.[139] They recorded the evaporation rate of pure water in high RH conditions to study the Kelvin effect, whereby the vapour pressure over a curved surface is increased compared to a flat surface, which is an important concept in atmospheric chemistry.[140] The principle of MODE is to use the potential difference applied to the plates to maintain a constant droplet levitation-position, so the changing potential difference can track the droplet mass. However, this study, along with others in the 1930s that used MODE to study droplet evaporation,[141,142] had problems with poor reproducibility and results that disagreed with the theory.[125]

Significant advances in the study of droplet evaporation using electrostatic levitation came with the development of droplet sizing using light scattering during levitation, so that an optical radius could be retrieved in addition to the mass. Gucker and Rowell levitated a single droplet of dioctyl phthalate using a MODE apparatus with a Fletcher disk and collected the intensity of forward scattered light as a function of the angle.[143] They determined the radius of the droplet by fitting the angular intensity to a Mie simulation, and in doing so, validated Maxwell's theory about how electromagnetic radiation interacts with a homogeneous sphere. The light scattering technique is used widely to size droplets during evaporation, but it requires access to the central trapping chamber at specific angles for both laser illumination of the droplets as well as collection of the scattered light. Whilst this has been achieved for the hyperboloidal setup,[117] in general it is much easier to allow for optical sizing techniques with the double-ring setup [144] or concentric cylinder setup [119,137] where there is a large range of angles in the horizontal plane available for the optical instrumentation.

A disadvantage of using light scattering to provide a droplet radius during drying is that Mie theory relies on assumptions that droplets are homogeneous and spherical.[145] Thus, if a droplet becomes distorted in shape or inhomogeneous in refractive index, which could occur through processes such as crystallisation or phase-separation, the light scattering becomes erratic and cannot be used to provide information on the droplet size.[146] Using an EDB in a similar way to MODE, to measure the droplet mass using the DC required to maintain a stable trapping position does not carry requirements in the droplet shape or homogeneity, hence it can provide information on the droplet drying process after crystal nucleation. Using the double-ring geometry Ray and Souyri were able to combine both mass measurements, from recording the DC trapping voltage, with radius measurements from the light

scattering to study slow evaporation processes.[131] A detailed description about how an EDB was used to study droplet drying for the results presented in this thesis is provided in Chapter 3.

1.2.8. Multiple-Droplet Studies

Typically, single-particle techniques such as levitation and pendant studies require capture or stabilisation of the droplet after it has been generated. There is, hence, a delay between droplet generation and the measurement of evaporation rates. In some rapid evaporation processes the initial drying period is highly unsteady and challenging to predict with models.[147] Evaporating multiple droplets in free-falling chains carries the advantage that measurements can be made immediately after droplet generation.[148] In such experiments, the falling particles do not need to be spherical, homogeneous or charged, which is often a requirement for electrodynamic or optical levitation. In addition, directing falling chains of drying droplets onto a microscope slide or stub allows collection of the dried particles for further analysis, such as SEM imaging or XRD analysis to determine the crystalline content. The history and principles of studying evaporation with free-falling chains will be outlined in the following section. In addition, the process of how multiple evaporating droplets interact with one another through collisions is a common problem in understanding sprays, such as in spray drying,[149] crop-spraying,[58] and inhaler therapy applications.[150] In the final section, experimental techniques used to study droplet coalescence between multiple droplets will be briefly reviewed.

1.2.8.1. Free-Falling Droplet Chain Techniques

In 1960, Dlouhy and Gauvin performed a simple experiment of studying the evaporation of water sprays by directing plumes of droplets from an atomiser down a chamber, and sampling droplets at varying heights down the chamber to record the radius.[151] The main observation was that falling droplets within the micron-size regime soon reach a terminal velocity, with a relative velocity between the droplets and the downward gas flow of zero. In this trajectory, the evaporation rate of the liquid droplets is equivalent to that in a stationary droplet. This introduced the concept of wind factors, wherein a gas flow passing over a droplet can affect the evaporation rate. Hendricks and Babil developed the chamber setup to allow for collection of dried particles at the bottom, and studied changes in the final particle morphologies arising from changes in the drying temperature of aqueous solution droplets.[152] Over the 1980s there were numerous studies from King that employed the free-falling droplet chain technique with sampling ports at various points down a heated column to collect and image the liquid or semi-dried particles at different times in the evaporation process.[153–155] However, evaporation rates in such studies were only inferred from the changing morphology of collected particles. Significant advances in the free-falling droplet chain method came with the addition of laser techniques to build an

understanding of the evaporation kinetics. Using laser-induced fluorescence, the pH of free falling droplets could be calculated, which inferred the time-dependent composition of aqueous solution droplets.[156] In addition, cavity-enhanced Raman scattering (CERS) has been combined with falling droplet chains to measure the radius of rapidly evaporating droplets.[157] Like the use of CERS in optical levitation, falling spherical droplets can behave as optical cavities for light wavelengths equivalent to whispering-gallery modes (WGMs). Thus, stimulated Raman scattering can be collected at distinct wavelengths and the band can be compared to Mie scattering calculations to determine the droplet size. More recently, the evaporation of aqueous droplets in monodisperse droplet chains was studied using a sophisticated combination of real-time imaging techniques.[44] Vehring et al. produced monodisperse droplets using a droplet-on-demand generator with a high reproducibility in the time-interval between subsequent droplets in the chain.[148] Pulsing a laser with an equivalent frequency to the droplet-generator enabled stroboscopic imaging to be performed; the droplets appeared "frozen" in space at defined intervals through the evaporation process and a focused camera could record the particle geometric-diameter. In addition, the distance between subsequent "frozen" droplet positions could be measured to determine the aerodynamic-diameter, which gave to the particle density. Hence, this setup enabled detailed measurements of the evaporation and particle formation process, including after a crust had formed at the droplet surface.[158]

1.2.8.2. Coalescence Experiments

A detailed understanding of droplet evaporation kinetics, which can be gained from single-particle experiments, is important for building computational fluid dynamics (CFD) simulations for predicting particle formation in a spray dryer.[159] However, in spray drying, the collisions between multiple droplets is prevalent, and can lead to variations in the product morphology and size distribution.[160] Collisions occur in the initial dense spray-inlet region of the spray dryer and also further down in the recirculation regions. Predicting the outcome between collisions of droplets is critical to the success of spray dryer models.[161]

Over the last few decades, many experimental studies have focused on identifying the collision outcome of two particles when they come together in free space.[162] Typical experiments involve firing two separate streams of droplets such that a droplet from each stream will collide, and the relative angle and velocity between the droplets can be varied (Fig. 1-9a). The collision is monitored by two cameras; one camera is front-facing with a high frame rate to record the collision and determine the collision outcome (Fig. 1-9b). The other camera is side-facing to monitor that the droplets travel in the same plane, so that the angle between the two droplet trajectories can be calculated. The Weber number (*We*) represents the ratio between kinetic energy of collision and the surface energy of the droplets, where a higher *We* indicates a higher energy of collision. The impact parameter, *B*, relates to the angle of approach between

two droplets. Values of *B* vary between 0 and 1 where 0 is a head-on collision and 1 is a grazing collision.[163]

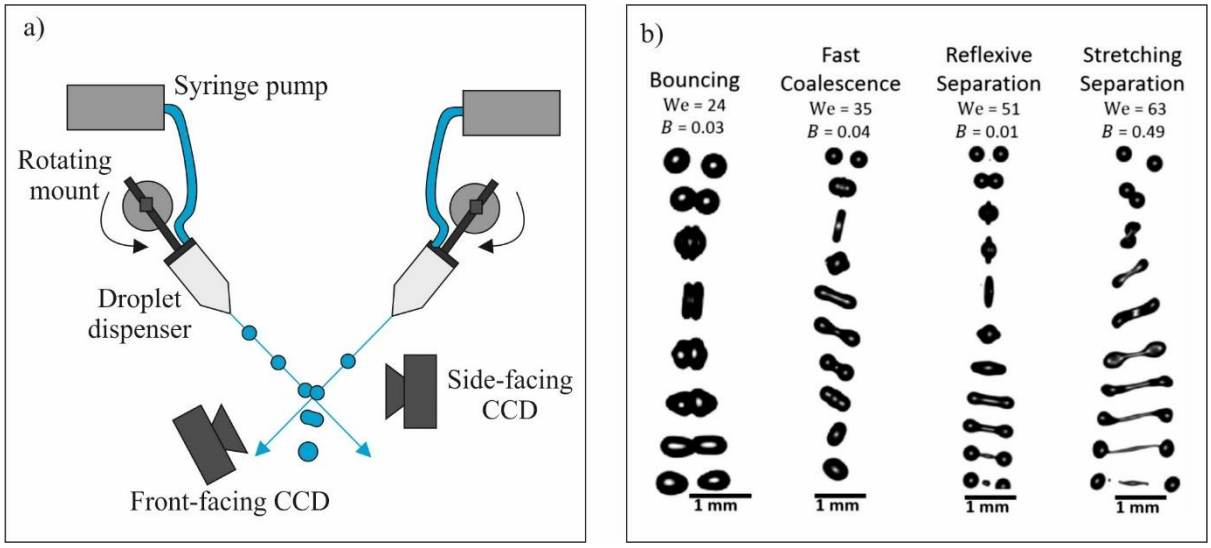

Figure 1-9: a) Schematic setup of a typical coalescence experiment to study the collision outcome of liquid droplets. b) Images of the collision outcome from two aqueous droplets of hydroxypropylmethyl cellulose colliding with varying Weber numbers (*We*) and impact parameters (*B*). Panel *b* is reprinted under the Creative Commons Attribution 4.0 License, copyright 2020 Al-Dirawi and Bayly.[163]

Coalescence experiments have been performed on a variety of droplets containing pure water,[164] pure-component hydrocarbons,[165] and polymers that are commonly used as spray drying excipients such as hydroxypropyl methyl cellulose.[166] Such coalescence experiments demonstrate how the collision proceeds between droplets of increasing viscosity and velocity, and even for two droplets of different sizes and liquid properties.[163] Typical droplet radii for such coalescence experiments are in the range of 100 – 200 µm, with the viscosity of studied liquid ranging from 10^{-2} Pa.s (pure water)[167] to ~ 0.3 Pa.s.[166,168] The results enable validation of collision simulations with the intention that spray drying CFD models can incorporate both drying kinetics and collision dynamics to accurately predict the size distribution of resulting products.

1.3. Thesis Aims

The aims of this thesis are to study the processes of evaporation and particle formation from liquid aerosol droplets, and to explore the relationship between the evaporation kinetics and the properties of the dried particles, such as morphology and degree of crystallinity. Performing experiments on single droplets enables the heat and mass transfer processes governing evaporation to be studied in detail. This allows a bottom-up approach to understanding the factors that affect particle formation during rapid droplet evaporation.

In this thesis, results of evaporation kinetics will be presented that have been retrieved from an electrodynamic balance instrument (EDB). The evaporation rates of droplets containing two volatile components, specifically water and ethanol, will be presented in Chapter 4. The results are compared to a range of different evaporation models, and the complexities arising from the coupling of heat and mass transfer during evaporation will be discussed. From Chapter 5 onwards, the presented results will focus on the evaporation of droplets containing aqueous inorganic salt solutions.

The emphasis of Chapter 5 is the evaporation of droplets containing aqueous sodium chloride solutions leading to crystal nucleation. Evaporation kinetics from EDB measurements will be compared to a numerical model that is employed to highlight the degree of spatial inhomogeneity in concentration of solute and solvent during rapid evaporation. In tandem, dried particles from a falling droplet column experiment are collected for imaging with a scanning electron microscope (SEM). SEM images will be compared with the experimental results, using sodium chloride solutions as a model system to study the morphology development in a drying droplet.

The concept of crystal nucleation in drying droplets will be developed in Chapter 6, focusing on the evaporation of aqueous alkali nitrate droplets under a range of different drying conditions. The viscosity of such solutions can rise greatly throughout evaporation; thus, the competition between crystallisation during evaporation and the formation of an amorphous particle can be observed and manipulated. The propensity for crystal nucleation will be compared for the alkali nitrate series (lithium, sodium, potassium and rubidium nitrate), reflecting trends in equilibrium properties such as the solute activity and hygroscopicity.

Finally, in Chapter 7, the evaporation of aqueous solution droplets with increasing compositional complexity will be studied. The nucleation behaviour during drying of mixed solution droplets will be investigated. Also, Chapter 7 will present studies on how the crystal nucleation of an inorganic salt can be manipulated by the presence of additives, such as inducing nucleation, delaying it or preventing it with added nanoparticles or organic components.

Overall, the key focus of this work is to study the evaporation kinetics of liquid aerosol solution droplets, the nucleation propensity of the inorganic solute during evaporation of the solvent, and how these two processes govern the final particle morphology.

Chapter 2

Droplet Evaporation: Thermodynamic Driving-Forces and Kinetic Processes

This chapter discusses the *why* and *how* of evaporation of liquid droplets. *Why* a droplet dries under certain conditions to form a solid particle is a result of the system's drive towards maintaining thermodynamic equilibrium. In Section 2.1, the underlying thermodynamic principles associated with liquids will be examined. Secondly, in Section 2.2, the question of *how* droplets evaporate will be considered. Evaporation is a combination of both heat and mass transfer, and they can be strongly coupled. Droplets that contain solutes have the additional complexity of how the solute behaves at high concentration as the solvent continues to evaporate. The kinetic basis behind crystal nucleation is discussed in Section 2.3, as well as the evaporation of solutions containing glass-forming solutes, and how this can affect the mass transport from drying droplets. Finally, the concepts of coupled heat and mass transfer with solute precipitation are brought together to discuss the particle formation process in a spray-dryer, and how a range of different particle morphologies can be produced through changes to the evaporation conditions.

2.1. Thermodynamic Driving Forces for Evaporation

2.1.1. Vapour Pressure

For a liquid held in a sealed container of its own vapour, molecules will continuously partition to and from the liquid and gas phases in microscopic processes of evaporation and condensation. If this system is at equilibrium, the pressure exerted by the vapour phase onto the condensed phase at a specific temperature is known as the vapour pressure. For a pure liquid, this vapour pressure is the saturation vapour pressure, and it increases in value as the temperature rises due to the liquid molecules having a greater thermal energy and so more molecules are able to partition to the gas phase. To derive the vapour pressure, it is helpful to consider the underlying thermodynamic principles, starting with the Gibbs energy, *G*:

$$G = H - T\,S \tag{2-1}$$

where *H* and *S* are the enthalpy and entropy of a substance, respectively, and *T* is the temperature. The change in Gibbs energy for a system can be represented in terms of changes in the temperature or pressure:

$$dG = V\,dp - S\,dT \tag{2-2}$$

where V is the volume and p is the pressure. For two phases in equilibrium with one another, such as a sealed volume containing both a liquid and its own vapour, the Gibbs energy change for the two phases are equivalent, i.e. $dG_{\text{liquid}} = dG_{\text{vapour}}$. Thus:

$$V_{\text{liquid}}\,dp - S_{\text{liquid}}\,dT = V_{\text{vapour}}\,dp - S_{\text{vapour}}\,dT \tag{2-3}$$

Rearranging Eq. 2-3 leads to the Clapeyron equation:

$$\frac{\mathrm{d}p}{\mathrm{d}T} = \frac{S_{\text{liquid}} - S_{\text{vapour}}}{V_{\text{liquid}} - V_{\text{vapour}}} = \frac{\Delta S}{\Delta V} \tag{2-4}$$

For the phase boundary between liquid and vapour, the entropy of vaporisation is equal to $\Delta_{\text{vap}}H / T$, so the Clapeyron equation at the boundary is:

$$\frac{\mathrm{d}p}{\mathrm{d}T} = \frac{\Delta_{\text{vap}}H}{T\,\Delta_{\text{vap}}V} \tag{2-5}$$

$\Delta_{\text{vap}}V$ is the change in molar volume during vaporisation. As the molar volume of a gas, $V_{\text{m,g}}$ is much larger than that of the liquid, we use the approximation that $\Delta_{\text{vap}}V \sim V_{\text{m,g}}$. Substituting the ideal gas equation for $V_{\text{m,g}} = RT/p$ into Equation 2-5, and using the approximation of $\mathrm{d}p/p \sim \mathrm{d}(\ln p)$, gives the Clausius-Clapeyron equation:

$$\frac{\mathrm{d}\ln p}{\mathrm{d}T} = \frac{\Delta_{\text{vap}}H}{R\,T^2} \tag{2-6}$$

The Clausius-Clapeyron equation shows that the gradient in the pressure-temperature phase diagram is related to the difference in molar enthalpy between the two phases. For a liquid-vapour phase boundary the enthalpy difference is the enthalpy of vaporisation (Fig. 2-1).

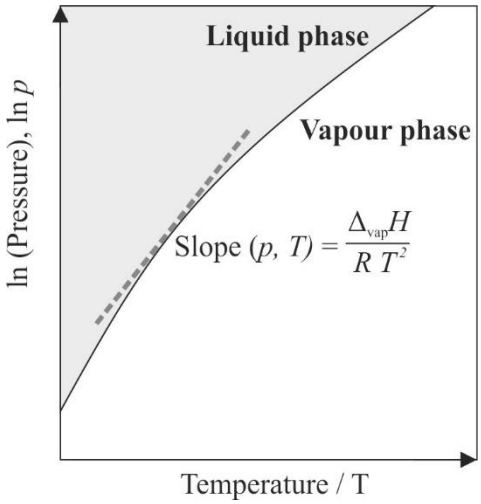

Figure 2-1: A typical liquid-vapour phase diagram with respect to pressure and temperature. The slope of such a phase boundary can be related to the difference in molar enthalpy between the two phases according to the Clausius-Clapeyron equation.

If it is assumed that the enthalpy of vaporisation is independent of temperature, then integrating Equation 2-6 between temperatures T and T^* leads to the derivation of the vapour pressure p_i:

$$p_i(T) = p_i^{\,0} \exp\left[\frac{\Delta_{\text{vap}}H}{R}\left(\frac{T - T^*}{T\,T^*}\right)\right] \tag{2-7}$$

where p_i^0 is a standard vapour pressure of substance *i* at a standard temperature *T**. The vapour pressure describes the volatility of a liquid and is a fundamental term for describing the evaporation of liquid droplets. A liquid with a higher vapour pressure has a greater driving force for evaporation than one with a lower vapour pressure and is, thus, more likely to exist in the vapour phase at a given temperature and pressure.

2.1.2. The Kelvin Effect

Liquids with a curved surface have a greater vapour pressure than those with a flat surface, which can be an important contribution to the Gibbs free energy term for small aerosol droplets that have a large curvature. The vapour pressure in a droplet, $p_{i,a}$ is greater than the vapour pressure p_i^0 in a bulk liquid according to the Kelvin equation:

$$p_{i,a} = p_i \exp\left(\frac{2\,\sigma\,M_i}{R\,T\,r\,\rho_i}\right) \tag{2-8}$$

where σ is the surface tension, M_i is the molar mass of component *i*, and ρ is the liquid density. As the exponential function in Eq. 2-8 is always positive, $p_{i,a}$ is always greater than p_i, however the effect of curvature on the vapour pressure is only significant for particles of radius < 0.1 μm. A consequence of Eq. 2-8 is that supersaturated humidities are required to prevent very small water droplets from evaporating, which is called the Kelvin effect. As the droplets in this thesis range from ~ 5 – 30 μm, the Kelvin effect is not considered when discussing the vapour pressures of liquids.

2.1.3. The Chemical Potential and Raoult's Law

So far, only the vapour pressure of pure liquids has been discussed. If a solute is dissolved in a liquid to make a solution, the vapour pressure of the liquid is reduced due to an effective reduction in the liquid concentration at the surface. This reduction is a function of the amount of dissolved solute.

The chemical potential, μ_i, is the partial molar Gibbs energy, i.e. it is the gradient of a line of Gibbs energy (*G*) with respect to the molar amount (*x*) of substance *i*, in a closed system of constant temperature and pressure:

$$\mu_i = \left(\frac{\partial G}{\partial x_i}\right)_{p,T,x} \tag{2-9}$$

The Gibbs energy of a binary mixture of components *a* and *b* is:

$$G = x_a\mu_a + x_b\mu_b \tag{2-10}$$

where μ_a and μ_b are the chemical potentials of *a* and *b*, respectively and *x* is the component mole fraction. Hence, the chemical potential of a substance is its molar contribution to the total Gibbs energy. The chemical potential of a liquid component in a mixture is:

$$\mu_a = \mu_a^0 + R\,T\,ln\frac{p_a}{p_a^0} \quad (2\text{-}11)$$

where $\mu_a{}^0$ is the chemical potential of *a* in a pure liquid state.

For an ideal solution, the ratio between the vapour pressure of *i* in a mixture and that in a pure liquid is the mole fraction, x_i, which is known as Raoult's law:

$$p_i = x_i\,p_i^0 \quad (2\text{-}12)$$

Raoult's law only applies for ideal solutions, but it holds closely for solutions that have structural similarity. An ideal solution mixture of *a* and *b* would have intermolecular attractions between *a*-*a*, *a*-*b* and *b*-*b* that are equal, so the enthalpy of mixing and volume of mixing are both zero.

In reality, many mixtures are not ideal, particularly when the solution is far from dilute. Henry's law serves to account for non-ideality at low concentrations of solute, where the solute vapour pressure is typically proportional to its mole fraction:[169]

$$p_i = x_i H_i \quad (2\text{-}13)$$

where *H* is the Henry's law constant for solute *i*, calculated by fitting a line tangential to an experimental data plot of vapour pressure against mole fraction at a low mole fraction of *i*. The vapour pressure of water and ethanol in a mixture are shown across the range of x_{EtOH} in Fig. 2-2. The vapour pressure of each component shows a deviation from ideality (Raoult's law) and the plot for Henry's law of ideal dilute solutions is shown for low concentrations of ethanol dissolved in water.

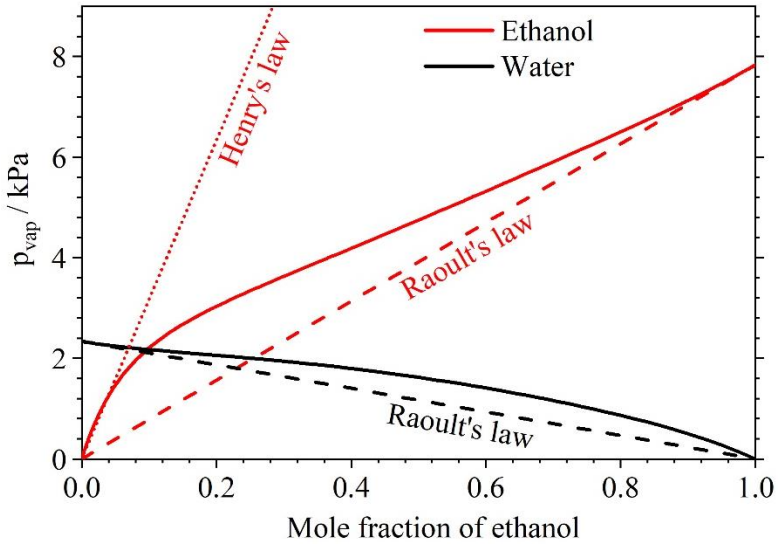

Figure 2-2: The vapour pressure of ethanol and water at 293 K in liquid mixture (solid lines), depicting the deviation from an ideal solution (Raoult's law, dashed line) and an ideal dilute solution of ethanol in water (Henry's law, dotted line). The solvent activity for ethanol and water are calculated using the AIOMFAC model.[170,171]

The deviation from ideality of components in a mixture is depicted in terms of an activity, a_i, which is the mole fraction multiplied by an activity coefficient, γ:

$$p_i = a_i\,p_i^0 = \gamma_i x_i\,p_i^0 \quad (2\text{-}14)$$

For water, the ratio between the partial pressure of water vapour in the gas phase and the saturation vapour pressure of water at that temperature is also known as the saturation ratio, S_w. This is often expressed as a percentage, known as the relative humidity (RH):

$$\frac{p_w}{p_w^0} \times 100 = S_w \times 100 = \text{RH} \quad (2\text{-}15)$$

The RH is a highly important gas-phase property in aerosol science as it strongly influences the size and phase state of aerosol droplets,[172,173] which will be discussed in more detail in the next section.

2.1.4. The Equilibrium Between Liquid and Vapour Phases

If water in an aqueous solution is in equilibrium with the gas phase, this means that the vapour saturation ratio just above the liquid surface (subscript *a*) is equal to that at a distance far from the liquid, i.e. $S_{w,a} = S_{w,\infty}$. This saturation at the liquid surface is described in thermodynamic literature as the water activity, a_w. Hence, for an aqueous aerosol droplet, the water in the droplet is in equilibrium with the vapour if a_w = RH. Evaporation occurs if there is a greater value of a_w than RH, and condensation is the reverse process. As discussed in Section 2.1.1, liquids in equilibrium with the vapour phase are constantly in a state of flux; microscopic evaporation and condensation occurs between the two phases. If a droplet is initially out of equilibrium such that a_w > RH, there will be a thermodynamic drive for a net increase in the number of molecules escaping through the phase boundary from the liquid to the vapour state, to reduces the vapour pressure at the droplet surface and re-establish equilibrium.

2.1.5. Hygroscopicity and the Solute Effect

The thermodynamic driving force behind the evaporation of water from aqueous solutions is governed by the aerosol hygroscopicity, which is the ability of an aerosol to take up (or give out) water vapour from (or to) the surrounding gas phase. Neglecting the Kelvin effect, a pure water aerosol droplet, by definition, has a_w = 1, i.e. the vapour pressure at the droplet surface is equivalent to the saturation vapour pressure. In an environment with RH < 1, evaporation from the pure water droplet will occur. The presence of any solute in the water will reduce the water activity according to Eq. 2-14, and this is known as the solute effect. The water in the aqueous droplet will evaporate until a new value of a_w is reached that is equal to the RH (Fig. 2-3).

The hygroscopicity of an aerosol solution droplet can be expressed in different ways. Commonly, the mass fraction of the solute (MFS) as a function of a_w is reported, to demonstrate the reduction by the solute to the vapour pressure of water in the droplet (Fig. 2-3b). In addition, hygroscopicity can be represented as a radial growth factor (GF_r) or mass growth factor (GF_m), which relate the size or mass

of the droplet under a certain RH to that of the dried particle with no water present.[174] Thus, it is a direct measure of the growth of an aerosol under different RHs.

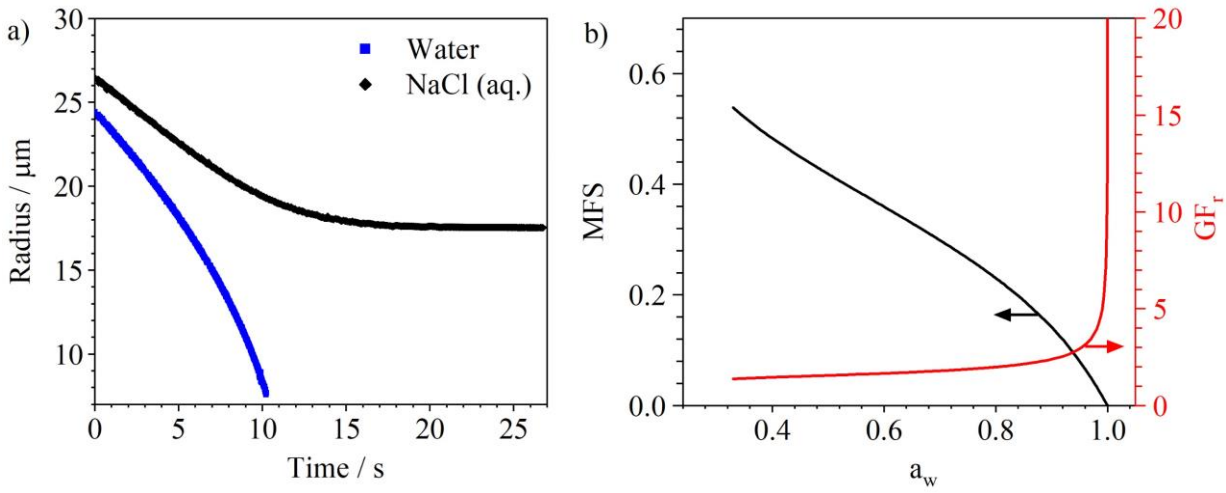

Figure 2-3: a) The evaporation process of a pure water droplet (blue squares) or an aqueous NaCl solution droplet (0.007 mass fraction NaCl, black diamonds) at 80% RH and 293 K. The data was collected on an EDB. b) The hygroscopicity of NaCl as predicted by the E-AIM model,[175] described in terms of the mass fraction of NaCl (MFS) and the radial growth factor (GF_r) across a range of water activity (a_w).

2.1.5.1 Thermodynamic Hygroscopicity Models

There are various thermodynamic models in the literature that predict the equilibrated concentration and sizes of aerosol droplets under different RHs. The Extended-Aerosol Inorganics Model (E-AIM) [176] is based on various papers from Clegg and Wexler [175,177] that use previously measured activity coefficients from the literature to determine the Gibbs free energy of an inorganic solution droplet in a closed system of defined volume, pressure and temperature. The model calculates the extent of partitioning between liquid and vapour phases and provides an output of equilibrium phase properties such as molality, molarity and partial pressures of volatile components in the gas phase. The E-AIM model is used in this thesis in Chapter 5 and 6 for predicting the composition of NaCl (E-AIM, model III) and $NaNO_3$ aerosol droplets (E-AIM, model IV) at varying RHs and temperatures.

The Aerosol Inorganic-Organic Mixtures Functional Groups Activity Coefficients (AIOMFAC-web) model uses a group contribution method to model the equilibrium concentrations of aerosol droplets containing various organic or inorganic solutes, as well as mixtures. [170,178] The user enters the chemical species that are present in the aerosol phase in terms of the functional groups in the organic species and any additional inorganic ions. A global optimisation algorithm minimises the Gibbs free energy of the condensed and vapour phases. The model can then predict the equilibrium mole fraction, molality, activity and vapour pressure for each component, for a user-defined temperature and RH. AIOMFAC-

web was used in this work to determine the activity coefficients of ethanol and water mixtures in Chapter 4.

2.2. Kinetics of Evaporation

For an aqueous droplet, the difference between the saturation ratio of water vapour far from the droplet and just above the droplet surface provides the thermodynamic driving force for evaporation. The rate at which evaporation occurs is governed by various transport processes. Evaporation involves, first, the diffusion of water molecules through the bulk of the droplet to reach the interface, followed by interfacial transport, and then diffusion in the vapour phase away from the surface (Fig. 2-4). Under different conditions, any of these steps could be the rate-limiting step that defines the rate of the evaporation process as a whole.

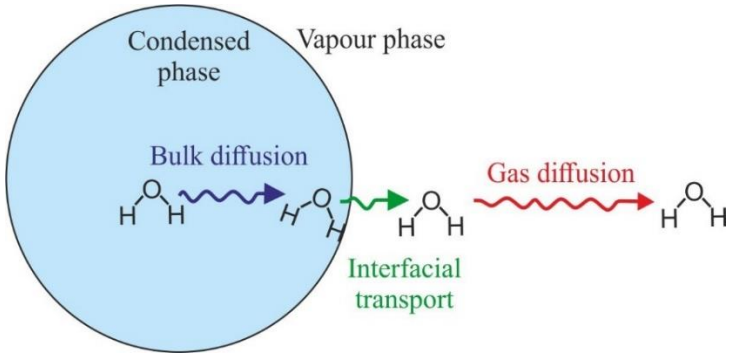

Figure 2-4: Three transport processes that could be rate-limiting steps in the evaporation of water from a liquid aerosol droplet. The direction of the processes would all be reversed for condensation of water from the vapour phase onto the droplet.

An important feature to consider for the rates of evaporation is the gas-kinetic regime, which depends upon the relative size of an aerosol and the molecular density of the gas phase. The kinetic regimes are discussed in the next section.

2.2.1. Aerosol Kinetic Regimes

The treatment of the evaporation kinetics of an aerosol droplet depend upon the droplet size compared to the relative distances between molecules in the vapour. The mean free path of a vapour, λ, is the average distance that a gas molecule will travel before undergoing a collision with another. The ratio of the mean free path to the radius of an aerosol droplet, r, is the Knudsen number:

$$Kn = \frac{\lambda}{r} \qquad (2\text{-}16)$$

Kn is a dimensionless number that defines which of two kinetic regimes applies to an aerosol droplet, the continuum regime or the free molecule regime (Fig. 2-5). Where the droplet size is larger than the mean free path of gas molecules, either by having a large droplet size or a high gas pressure, *Kn* tends to zero and the droplet is in the continuum regime. In the limit where $Kn >> 1$, the droplet is in the free-molecule regime.[123] The intermediate region can sometimes be referred to as the transition regime, where $Kn \sim 1$ and the droplet size is on the same order of magnitude as the mean free path. The treatment of the evaporation kinetics for these regimes will be briefly reviewed in the next sections.

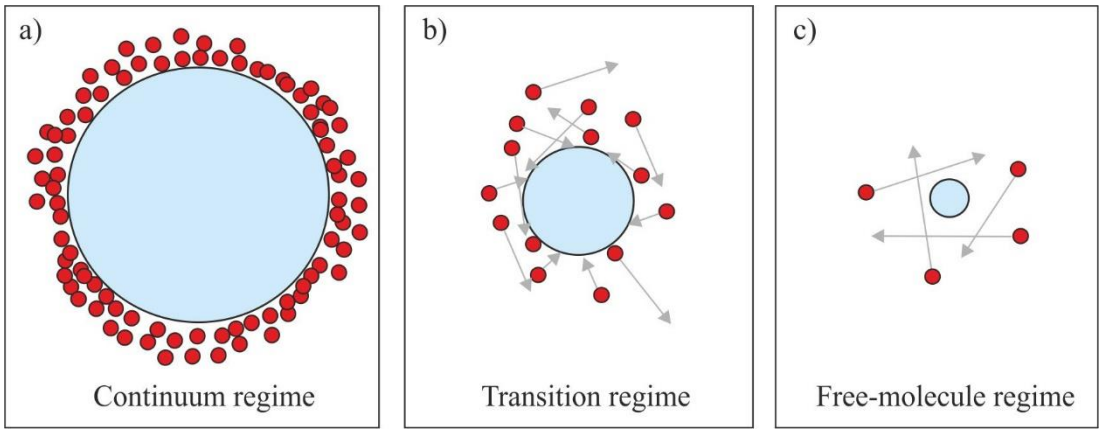

Figure 2-5: Schematic to demonstrate the kinetic regimes for an aerosol droplet (blue circle) surrounded by gas-phase particles (red circles), with gas-particle trajectories shown by the grey arrows. a) Continuum regime: the droplet radius is large compared to the mean free path, so $Kn \sim 0$. b) Transition regime: the droplet radius is comparable to the mean free path length so $Kn \sim 1$. c) Free-molecule regime: the droplet radius is smaller than the mean free path length, so $Kn >> 1$.

2.2.2 Mass Transport in the Continuum Regime

The work in this thesis focuses on evaporation in the continuum regime. The gas phase in the continuum regime has the properties of a continuous fluid, from the droplet perspective, and the evaporation rate is governed by the rate of mass diffusion of the evaporating component through the gas phase.[179] In 1855 Adolf Fick derived the laws of diffusions.[180] The first law of diffusion (steady diffusion) states that the diffusional flux, *J*, which is the amount of material flowing through a unit area per unit time, is related to the concentration gradient $\partial c/\partial x$, and a diffusion coefficient, *D*:

$$J = D\,\frac{\partial c}{\partial x} \tag{2-17}$$

For unsteady diffusion, where the rate of diffusion is not constant, Fick's second law of diffusion is used. Along the *x* direction, the change in concentration with time is proportional to a variable concentration gradient:

$$\frac{\partial c}{\partial t} = -D\,\frac{\partial^2 c}{\partial x^2} \tag{2-18}$$

Eq. 2-18 can be converted into three-dimensional diffusion:

$$\frac{\partial c}{\partial t} = -D\nabla^2 c \qquad (2\text{-}19)$$

Where ∇ is the Laplace operator, i.e. $\partial/\partial x + \partial/\partial y + \partial/\partial z$. In spherical co-ordinates, Eq. 2-19 becomes:

$$\frac{\partial c}{\partial t} = D\left(\frac{\partial^2 c}{\partial r^2} + \frac{2}{r}\frac{\partial c}{\partial r}\right) \qquad (2\text{-}20)$$

The diffusion equation in Eq. 2-20 can be applied to mass diffusion of vapour from a spherical droplet if the vapour concentration c_i is constant at an infinite distance from the droplet as well as above the surface of the droplet, which defines steady evaporation. Steady evaporation in the continuum regime was studied in depth by Maxwell in the nineteenth century.[181] He observed that the mass flux, *I*, during slow evaporation of single-component liquid droplets is proportional to the diffusion coefficient of the vapour through air, *D*, and the difference in vapour concentration, *c*, at the droplet surface and far from the droplet (subscript *a* and ∞, respectively):

$$I = \frac{d\,m}{d\,t} = -4\,\pi\,r\,D\,(c_a - c_\infty) \qquad (2\text{-}21)$$

where *r* is the droplet radius. We substitute $r = \sqrt[3]{m/\left(\frac{4}{3}\,\pi\,\rho\right)}$, where *m* and *ρ* are the droplet mass and density, and assume that the vapours are ideal with concentration $c_i = p_i(T)\,M_i/R\,T$. Integrating Equation 2-21 with respect to mass gives the r^2 law:

$${r_t}^2 = {r_0}^2 - \frac{2\,D\,M_i\,t}{\rho\,R\,T}\,(p_a(T) - p_\infty(T)) \qquad (2\text{-}22)$$

where M_i is the molar mass of the evaporating component, *t* is time, *ρ* is the liquid density, *R* is the molar gas constant, *T* is the temperature and *p*(*T*) is the temperature-dependent vapour pressure. This is diffusion-limited evaporation, wherein the rate that vapour travels away from the droplet surface contributes strongly to the evaporation rate. Such evaporation proceeds with a linear dependence in the r^2 with time, with a constant gradient from which the vapour pressure at the droplet surface can be determined.

A droplet evaporating in the continuum regime will be surrounded by a vapour concentration gradient (Fig. 2-6). Evaporation in the continuum regime becomes unsteady if the mass flux is large enough that the boundary of the droplet recedes faster than the vapour concentration above the droplet surface can relax; in such cases Eq. 2-22 cannot describe the evaporative mass transport. In addition, the evaporation process is not always fully dictated by the mass flux in Eq. 2-21, as the heat transport must also be considered. The droplet temperature is an important parameter in the evaporation rate and the flux of heat between a droplet and the gas phase will be discussed in the next section.

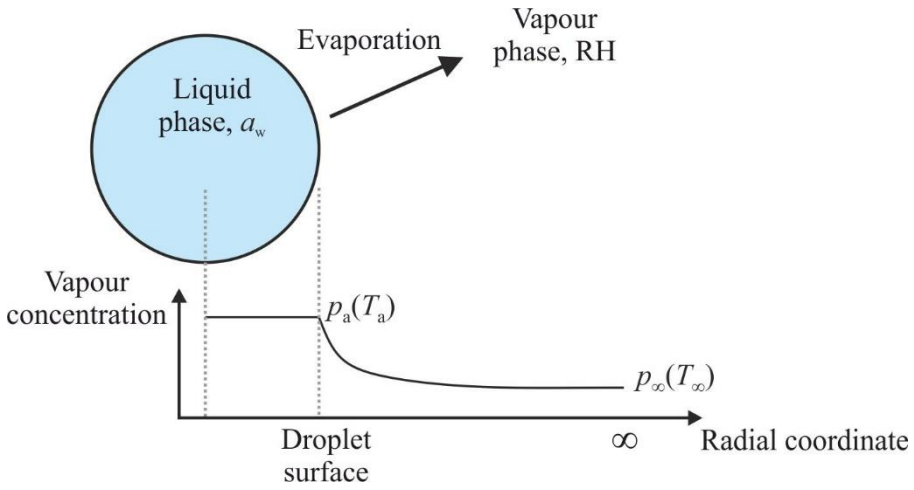

Figure 2-6: Schematic figure to describe the vapour concentration gradient surrounding a droplet evaporating in the continuum regime, if the gas phase RH is lower than the water activity at the droplet surface.

2.2.3. Heat Transport in the Continuum Regime

Evaporation of volatile liquids from a droplet is a cooling process. From a molecular viewpoint, molecules inside the droplet collide with the surface with speeds that form a Maxwell-Boltzmann distribution. Those with a large enough energy can escape the droplet through evaporation, which leads to a reduction in the average kinetic energy of molecules in the droplets, causing a reduction in droplet temperature. From a macroscopic perspective, the cooling of a droplet is quantified using the latent heat of vaporisation, *L*, which is the amount of energy required to convert a liquid into a vapour.

For an evaporating droplet that is cooler than the surrounding air, heat conducts from the gas to the droplet. The rate of unsteady heat conduction for a stationary droplet in air takes the same form as for the diffusive mass flux in Eq. (2-20):

$$\frac{\partial T}{\partial t} = \frac{K}{c_{p,gas}\ \rho_{gas}}\left(\frac{\partial^2 T}{\partial r^2} + \frac{2}{r}\frac{\partial T}{\partial r}\right) \qquad (2\text{-}23)$$

where K, $c_{p,gas}$ and ρ_{gas} are the thermal conductivity, specific heat and density of the gas phase, respectively.[179] A temperature gradient will surround the evaporating droplet, as for the vapour concentration in Fig. 2-6. There are two competing rates of heat transport; there is a rate that heat is conducted from the gas to the droplet, and there is a rate that heat is lost from the droplet through evaporation. For rapid evaporation processes, the latter rate may outcompete with the former, leading to a temperature suppression of the droplet compared to the gas phase. This decreased temperature causes a reduction in the vapour pressure of the evaporating component, $p_a(T_a)$. Thus, the rate of mass diffusion in Eq. 2-20 and the rate of heat flux in Eq. 2-23 must be solved simultaneously.[179]

2.2.4. Simulating the Coupled Heat and Mass Transport in The Continuum Regime

Kulmala derived an equation for the mass flux, *I*, of a solvent from a binary (one solute and one solvent) solution,[182] which couples both the heat and mass transport between a droplet and a gas phase:

$$I_i = -4\,\pi\,r\,\left(S_{i,\infty} - S_{i,a}\right) \times \left[\frac{R\,T_\infty}{M_i\,\beta_M\,D_i\,p_i{}^0(T_\infty)\,A} + \frac{S_a\,L_i{}^2\,M_i}{K\,R\,\beta_T\,T_\infty{}^2}\right]^{-1} \quad (2\text{-}24)$$

where S_∞ and S_a (anagolous to a_w) are the saturation of *i* in the vapour phase at infinity and above the droplet surface. *R* is the ideal gas constant, M_i is the molar mass of the evaporating liquid, D_i is the mass diffusion coefficient of the vapour *i*, $p_i{}^0(T_\infty)$ is the saturation vapour pressure of *i* at gas phase temperature T_∞. L_i is the latent heat of vaporisation of *i*, *K* is the thermal conductivity of the gas phase. *A* is a correction to account for Stefan flow, which is the effect of radial convection,[183] and is given by:

$$A = 1 + p_i{}^0(T_\infty)\,\frac{(S_{i,\infty} - S_{i,a})}{2\,p} \quad (2\text{-}25)$$

where *p* is the total gas pressure. β_M and β_T are transitional correction factors for the mass and heat transfer, respectively. This will be discussed in more detail in a later section (Section 2.2.6).

The Kulmala equation (Eq. 2-24) was derived to be first order with respect to mass flux by making an approximation for the temperature-dependent vapour pressure at the droplet surface.[182] The exponential form of the Clausius-Clapeyron equation in Eq. 2-7 for the vapour pressure, scaled by the saturation at the droplet surface, is approximated using a first-term Taylor expansion ($e^x \approx 1 + x$):

$$p_{i,a}(T_a) = S_{i,a}\,p_i{}^0(T_\infty)\exp\left[\frac{L_i M_i}{R}\left(\frac{T_a - T_\infty}{T_a T_\infty}\right)\right] \quad (2\text{-}26a)$$

$$p_{i,a}(T_a) \approx S_{i,a}\,p_i{}^0(T_\infty)\left[1 + \frac{L_i M_i}{R}\left(\frac{T_a - T_\infty}{T_a T_\infty}\right)\right] \quad (2\text{-}26b)$$

where subscript *a* indicates a property at the droplet surface, and ∞ is at an infinite distance from the droplet. This approximation holds when T_a and T_∞ are similar in value. However, if the droplet temperature T_a cools significantly during evaporation then the temperature-dependent vapour pressure at the droplet can be underestimated.[116] $p_{i,a}(T_a)$ as predicted by the Clausius-Clapeyron equation in Eq. 2-26a is compared to that predicted by the Taylor expansion in Eq. 2-26b for pure water evaporation at 0% RH and 293 K in Fig. 2-7. For ΔT = 3 K, the error in the vapour pressure at the droplet surface arising from the Taylor expansion approximation is 1.6%, which increases as the difference between the droplet temperature and gas temperature increases (Fig. 2-7).

In this thesis, the Kulmala model is only used to reasonably simulate evaporation kinetics if the magnitude of mass flux is sufficiently small to lead to ΔT < 3 K. The difference in the temperature of the droplet and the gas phase can be estimated from the magnitude of the mass flux:

$$T_a - T_\infty = -\frac{I_i L_i}{4\,\pi\,r\,K} \quad (2\text{-}27)$$

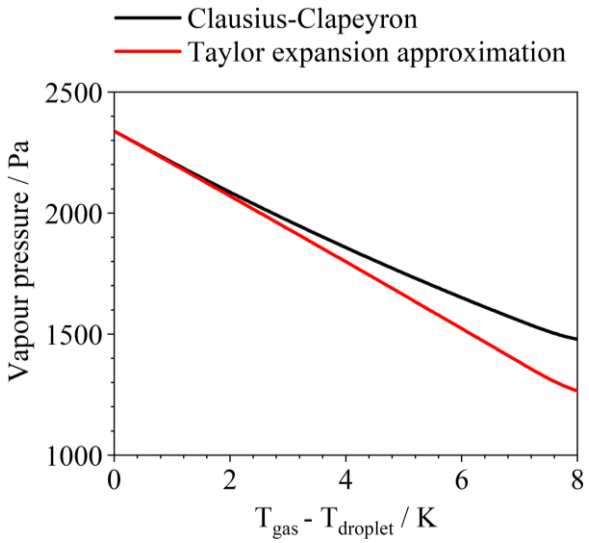

Figure 2-7: A comparison between the temperature-dependent vapour pressure of water at a droplet surface estimated using the Clausius-Clapeyron equation (Eq. 2-26a) and the Taylor series first-term approximation (Eq. 2-26b), for pure water evaporation at 0% RH and 293 K. The temperature-dependent vapour pressure of water is taken from Wagner and Pruss.[184]

The evaporation profiles of aqueous NaCl droplets (panel *a*) and water droplets (panel *b*) in varying RHs, as simulated using the Kulmala model, are shown in Fig. 2-8**.** The mass flux simulated by the Kulmala model is used to estimate the droplet temperature throughout evaporation using Eq. 2-27, shown in panels *c* and *d* for the aqueous NaCl droplets and water droplets, respectively.

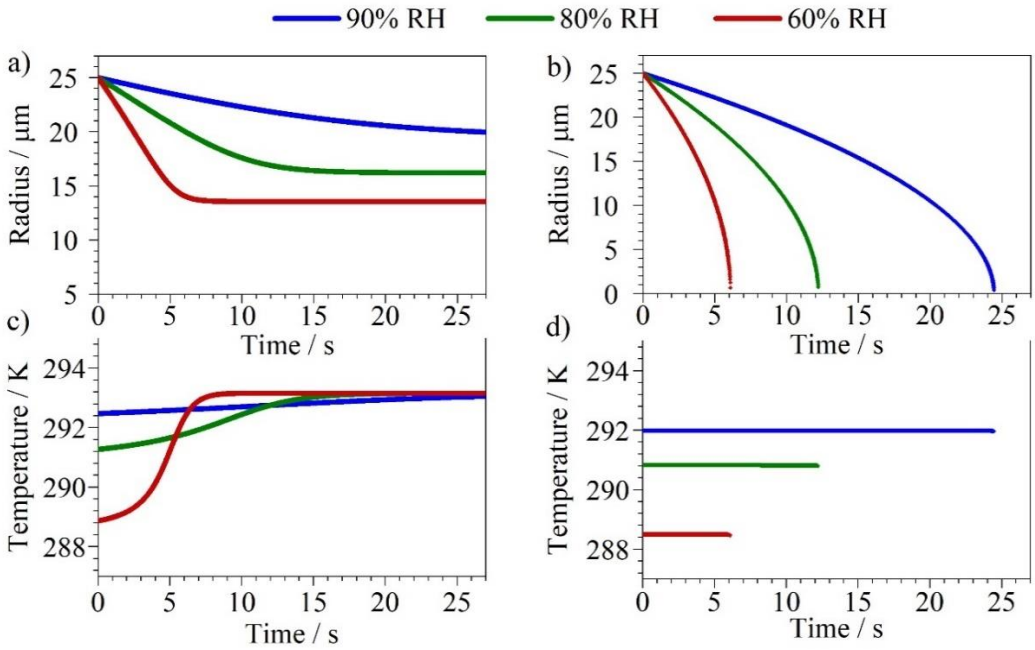

Figure 2-8: Simulations of the radius of evaporating aqueous NaCl droplets (0.07 MFS) (panel a) and pure water droplets (panel b) using the Kulmala model, in varying RHs at 293 K. Panel c) and d) show the droplet temperature, estimated using the mass flux and equation 2-27, for the aqueous NaCl droplets and water droplets, respectively.

The droplet temperature for the aqueous NaCl droplets has an initial temperature suppression that is greater when evaporating in lower RHs due to the larger mass flux. The aqueous NaCl droplet temperature steadily equilibrates with the gas phase temperature. On the other hand, the water droplets remain at a steady, suppressed temperature, which is the temperature at which the heat loss through evaporation is equivalent to the rate that heat is conducted from the gas to the droplet. This is known as the wet-bulb temperature. The droplet in 60% RH evaporates rapidly such that the droplet temperature becomes suppressed by more than 3 K below the gas phase temperature, so the Kulmala model cannot accurately model the mass flux. The evaporation rate in 60% RH for both the water and NaCl droplet in Fig. 2-8a and Fig. 2-8b is likely to be slower than experimental data, because the water vapour pressure at the droplet surface is underpredicted in Eq. 2-24.

2.2.5. Mass Transport in the Free-Molecule Regime

In the limit where *Kn* >> 1, the droplet is in the free-molecule regime,[123] within which the macroscopic picture of gas diffusion cannot be used to represent the mass transport from small droplets. Rather, the motion of individual gas molecules must be considered, using a Maxwell-Boltzmann treatment, which gives the rate of gas diffusion across an area A_g as:

$$\frac{\mathrm{d}m}{\mathrm{d}t} = \frac{A_g}{4}\rho_g\,\bar{c} \tag{2-28}$$

where ρ_g is the number-density of the gas molecules and $\bar{c}$ is the mean molecular speed, given by:

$$\bar{c} = \sqrt{8\,k_B\,T/\pi\,M_g} \tag{2-29}$$

with k_B as the Boltzmann constant and M_g as the gas molar mass. Hence, the rate of collisions of gas molecules with a surface per unit time and unit area is:

$$Z = \frac{\rho_g\,\bar{c}}{4} \tag{2-30}$$

The mass accommodation coefficient, α_M, is introduced, which describes the likelihood a gas molecule colliding with a surface is accommodated into the bulk of the droplet and is expressed as the successful fraction of all collisions. Evaporation is considered to be the exact reverse process of condensation,[185] hence, α_M is included in Equation 2-21 to describe the molecular flux from a droplet of radius *r*, in the region just above the surface, as:

$$I = \pi\,r^2\,\bar{c}\,\alpha_M\,(c_a - c_\infty) \tag{2-31}$$

2.2.6. Mass Transport in the Transition Regime

In the intermediate region, where *Kn* ~ 1 and the droplet size is on the same order of magnitude as the mean free path, the droplets falls within the transition regime. The mass transport is governed by a combination of diffusion and heat transport kinetics, like droplets in the continuum regime, as well as

governed by gas-molecule kinetics like in the free-molecule regime. There is no general solution for the mass transport under such conditions, and often an empirical correction is included in the continuum solution in Equation 2-24 that makes use of α_M to account for free molecule behaviour of the gas phase. Such a correction is known as a transitional correction factor and in this thesis the Fuchs-Stutugin method is used. The theory considers that there is a region surrounding the droplet, of thickness equal to one mean free path of the vapour molecules, within which the mass transport proceeds according to free molecule kinetics in Eq. 2-31, and outside of which the mass transport behaves as if in the continuum regime. The transitional correction factor for mass transfer, β_M, is:

$$\beta_M = \frac{1+Kn}{1+\left[\left(\frac{4}{3\,\alpha_M}+0.337\right)\times Kn\right]+\left[\left(\frac{4}{3\,\alpha_M}\right)Kn^2\right]} \quad (2\text{-}32)$$

The analogous transitional correction factor for heat transfer, β_T, takes the same form as Eq. 2-32 but uses the thermal Knudsen number, Kn_T, and thermal accommodation coefficient for heat transfer, α_T. In the continuum regime, where Kn tends to 0, β_M and β_T are equal to 1 and thus make no contribution to the mass flux equation in Eq. 2-24. However, for smaller droplet sizes, when a droplet is in the transition regime, the β correction factors allow the continuum regime mass flux equation to be used to simulate the evaporation kinetics. For example, a droplet of radius 1 µm evaporating in 50% RH at 293 K, will have Kn = 0.13 and a β_M of 0.9.

2.2.7. The Relative Motion of Particle and Gas Phases During Evaporation

If there is a relative velocity between the droplet and the surrounding vapour, for example, a droplet in a gas flow, the rate of evaporation increases. This is, in part, because the rate of heat conduction to the droplet increases, so the latent heat that is lost through drying is more readily replaced by the vapour. Thus, the droplet temperature is not suppressed to as low a temperature during evaporation compared to in static vapour. Secondly, the mass transfer from the droplet changes from being diffusive transport to convective transport.[179] There is no general solution to the heat and mass transfer problem for forced convective evaporation because the vapour field is highly dependent on the droplet diameter and gas speed.

We consider the dimensionless Reynolds number for a droplet of diameter d:

$$Re = \frac{v\,d}{\upsilon_k} \quad (2\text{-}33)$$

where v is the relative velocity between the vapour and droplet and υ_k is the kinematic viscosity of the vapour phase, sometimes referred to as the momentum diffusivity. Thus, Re is the ratio of inertial to viscous forces and is used to predict flow patterns; a low Re indicates laminar flow and a high Re indicates turbulent flow.

The Schmidt number is the dimensionless ratio between the kinematic viscosity and mass diffusivity in the vapour phase (D):

$$Sc = \frac{\upsilon_k}{D} \tag{2-34}$$

The analogous quantity for heat transfer, rather than mass transfer, is the Prandtl number:

$$Pr = \frac{\eta_{gas} \times c_{p,gas}}{K} \tag{2-35}$$

where η_{gas} is the viscosity of the vapour phase, $c_{p,gas}$ is its specific heat capacity and K is the thermal conductivity of the gas.

The Sherwood number, *Sh*, relates the rate of solely diffusive mass transfer to the rate of convective mass transfer and was correlated to the Reynolds and Schmidt numbers by Ranz and Marshall [73] for $Re < 200$ and $Sc < 250$:

$$Sh = 2 + 0.6\, Re^{1/2}\, Sc^{1/3} \tag{2-36}$$

where a value of $Sh = 2$ means that mass transfer is only diffusive, and no correction is required to simulate the mass flux.

In a similar way, the analogous comparison between convective heat transfer and diffusive heat transfer is described by the Nusselt number for $Re < 200$ and $Pr < 250$:

$$Nu = 2 + 0.6\, Re^{1/2}\, Pr^{1/3} \tag{2-37}$$

Droplets evaporating in the EDB instrument in BARC have starting droplet sizes of ~ 25 µm, with gas speeds of ~ 0.03 m s^{-1}, and this equates to a low *Re* of 0.097, and a *Sh* of 2.15. Such values indicate that the evaporation occurring in this vapour field can be approximated to being only diffusive mass transport rather than conductive, and that the presence of the gas flow does not significantly alter the evaporation rate of the droplets. Nevertheless, in this thesis the mass flux as provided by the Kulmala equation (Eq. 2-24) is corrected using the Sherwood number to be:

$$I = -4\, \frac{Sh}{2}\, \pi\, r\, \left(S_{i,\infty} - S_{i,a}\right) \times \left[\frac{R\, T_\infty}{M_i\, \beta_M\, D_i\, {p_i}^0(T_\infty)\, A} + \frac{S_a\, {L_i}^2\, M_i}{K\, R\, \beta_T\, {T_\infty}^2}\right]^{-1} \tag{2-38}$$

The Ranz and Marshall correlations for *Sh* and *Nu* only hold for low *Re* because the droplet is approximated to maintain a spherical shape under such conditions.

2.3. Droplets Containing Solutes and Evolving Particle Morphology During Evaporation

Solution droplets that evaporate become increasingly concentrated in the solute during drying. As described in Section 2.1.5, the presence of solutes can reduce the vapour pressure of the solvent and effect the evaporative mass transport. Solutes in aerosol droplets can typically reach supersaturated concentrations that cannot be accessed in a bulk solution,[6] but eventually a solid particle will form if all

of the solvent evaporates. The next sections will describe the processes of particle formation during the later stages of solvent evaporation.

2.3.1. Aerosol Efflorescence

In the bulk phase, solutes typically crystallise upon reaching saturation. However, in aerosol droplets metastable supersaturated solute states are prevalent, and crystallisation occurs at a higher solute concentrations and lower water activity than the bulk solubility limit.[140,186,187] This is a result of there being no solid surface in an aerosol droplet where heterogeneous nucleation can be induced. The process of crystal nucleation in the aerosol phase is often referred to as efflorescence. Ignoring the Kelvin effect on the water vapour pressure, the RH at which an equilibrated aerosol droplet is too concentrated to stay in solution, and homogeneous nucleation occurs, is known as the efflorescence RH (ERH).

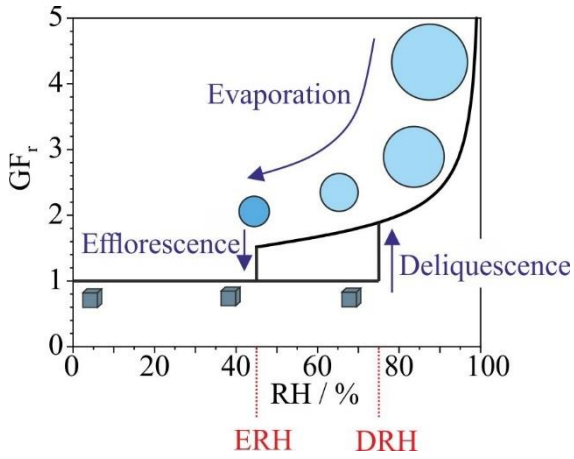

Figure 2-9: The radial growth factor for an aqueous NaCl droplet through a dehydration-rehydration process showing that, with a gradually reducing RH, the droplet effloresces at the ERH (45% for NaCl) [175] and re-dissolves at the DRH (75%).

For a crystalline particle after efflorescence has occurred, an increase in RH will lead to dissolution of the solute to form a liquid aerosol droplet only at RHs above the deliquescence RH (DRH), which is the water activity of the bulk solubility limit.[140] The radial growth factor and phase state through a dehydration and rehydration process is depicted for an aqueous NaCl aerosol droplet in Fig. 2-9. Many studies have investigated the ERH and DRH of both inorganic and organic solutes.[140,188] The efflorescence-deliquescence cycle demonstrated in Fig. 2-9 is not applicable to all solutes. Some solutes do not effloresce upon dehydration and instead dry to form amorphous particles, which continue to release and take up water in dehydration and hydration steps, respectively.

2.3.2. Crystal Nucleation Kinetics in Highly Concentrated Aerosol Droplets

Understanding and controlling the kinetics of crystallisation in evaporating droplets can be very important. The competition between the rate of crystal growth and the rate of solvent loss can dictate the degree of crystallinity in the dried particle,[158,189] the crystal size,[190] and even the crystal polymorph.[191,192] Whilst highly important for the spray-drying industry, crystal nucleation remains poorly understood due to the challenges associated with studying it.[193] The typical size of a crystal nucleus is estimated to be within the range 100 – 1000 ions,[194] so detection of such small nuclei can be challenging, as well as preventing impurities or container walls that could affect the process. In addition, crystal nucleation is a stochastic process,[195] so evaporation experiments typically need to be repeated multiple times for a statistically significant insight into the kinetics, which can be time consuming and requires accurate environmental control to keep the experimental conditions steady.

If a solution droplet evaporates to a high enough solute concentration, there will be a chemical potential drive to crystal nucleation. In a liquid, there may be the formation of microscopic crystal nuclei at any point in time, arising from thermal fluctuations.[196] Forming a crystal nucleus out of solution has an associated enthalpic change, ΔH_{cryst}, which is the reverse of the enthalpy of dissolution, ΔH_{diss}. The enthalpy of crystallisation in solution is made up of three parts. First, the solute-solvent interactions that had formed upon solvation must be broken. Second, any additional solvent-solvent interactions that had formed in the solution, such as hydrogen bonding, must also be broken. Both are endothermic processes. However, new solute-solute interactions are created that arise from the formation of an ordered crystal, which for an inorganic salt is the lattice energy.

Classical nucleation theory is often applied to consider nucleation of crystals out of solution.[196] The formation of a critical nucleus to begin the process has a low probability of occurring due to the high free energy of the cluster. The Gibbs free energy change brought about by the formation of a cluster of molecules, of number *n*, is:

$$\Delta G(n) = A_c\,\alpha - n_c\,V_c\,|\Delta\mu| \qquad (2\text{-}39)$$

where $\Delta\mu$ is the chemical potential change between solution and crystal, n_c is the crystal number density, A_c and V_c are the surface area and volume of the nucleation cluster, respectively and α is the surface free energy of a cluster in solution (Fig. 2-10). The first term on the right-hand side of Eq. 2-39, represents the free energy gain caused by the creation of a phase boundary between the cluster and the solution (green line in Fig. 2-10). However, the second term (blue line) has a negative free energy contribution due to the formation of energetically favourable solute interactions, as more solute ions are incorporated into the ordered cluster volume. The function of $\Delta G(n)$ is initially positive with increasing *n*, as the favourable solute interactions in the cluster are not sufficient to out-weigh the unfavourable formation of a surface boundary between cluster and solution. $\Delta G(n)$ goes through a maximum after which an increasing *n* leads to a decrease in Gibbs free energy and spontaneous crystal growth.

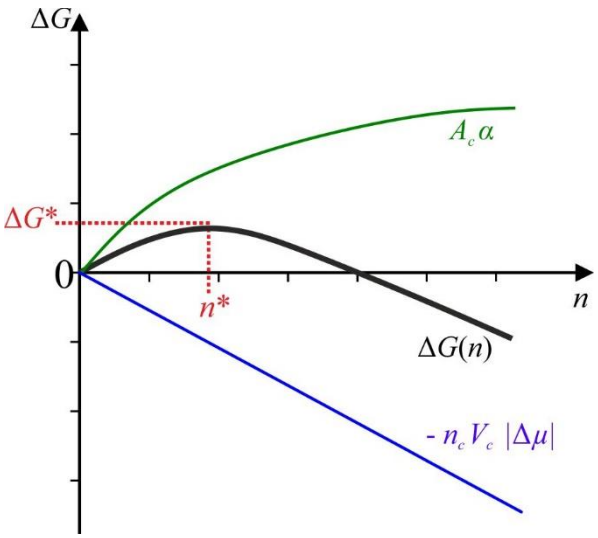

Figure 2-10: The contribution of different functions making up the Gibbs free energy change (*ΔG*) in going from a supersaturated solution to crystal nucleation, according to classical nucleation theory. Figure is based on Equation 2-39, where *n* is the number of molecules in a cluster, n_c and V_c are the number density and volume of a crystal cluster, *Δμ* is the chemical potential change between solution and crystal and α is the surface free energy of a cluster in solution.

Assuming that the ordered cluster forms a sphere, the maximum in Δ*G*(*n*) occurs at a critical radius, *r** of:

$$r^* = \frac{2\,\alpha}{n_c\,|\Delta\mu|} \tag{2-40}$$

Substituting *r** into Eq. 2-39 gives the barrier height, Δ*G**:

$$\Delta G^* = \frac{4}{3}\,\pi\,\alpha\,r^{*2} \tag{2-41}$$

The nucleation rate of crystals out of solution per unit volume per unit time, *J*, is typically expressed in the form of an Arrhenius equation:

$$J = n_I\,j\,Z\,\exp\left[\frac{-\Delta G^*}{k_B\,T}\right] \tag{2-42}$$

where k_B is the Boltzmann constant, *T* is the equilibrium temperature and the parameters in the pre-exponential factor n_I, *j* and *Z* are the number density of potential nucleation sites, the rate of attachment of monomers to these sites and the Zeldovich factor, respectively.[197] *Z* is related to the width of the free energy peak in Fig. 2-10, which links to the rate of diffusive transport of ions through the solution.

The chemical potential change between crystal and solution in Equation 2-39 can be expressed using the solute activity:

$$\Delta\mu = 2\,k_B T\,\ln\left(\frac{\gamma}{\gamma_0}\frac{m_s}{m_{s,0}}\right) \tag{2-43}$$

where γ and γ_0 are the mean activity coefficients in solution and at the value of saturation (subscript 0), respectively. m_s and $m_{s,0}$ are the solute molality in solution and at saturation.[198]

Homogeneous nucleation describes the process where the initial nucleus is made up of only a cluster of solute molecules. Heterogeneous nucleation occurs when there is an additional surface, such as a container wall or dust particles, and is usually the dominating process in crystal nucleation.[193,199,200]

A common nucleation study is to observe the probability of crystal formation at constant supersaturation.[201–203] Small volumes, such as solutions confined in capillaries or droplets, are favoured because only one nucleation event is needed to induce crystallisation in the whole volume and be detectable.[196] Commonly, through a long series of repeated measurements, the cumulative probability P that a crystal nucleus has formed in a solution of given volume as a function of time is plotted to give a decay-shaped curve. For a constant nucleation rate, P takes on an exponential function:

$$P(t) = \exp(-k\,t) \qquad (2\text{-}44)$$

Thus, a plot of the natural log of $P(t)$ takes a straight line with a constant negative gradient of k, which is the nucleation rate constant. An example of such a study in shown in Fig. 2-11, which is reprinted from Duft and Leisner's study on ice nucleation in supercooled water droplets. The linear fit to the temporal $\ln(P(t))$ is attributed to the constant nucleation rate of the ice crystals.

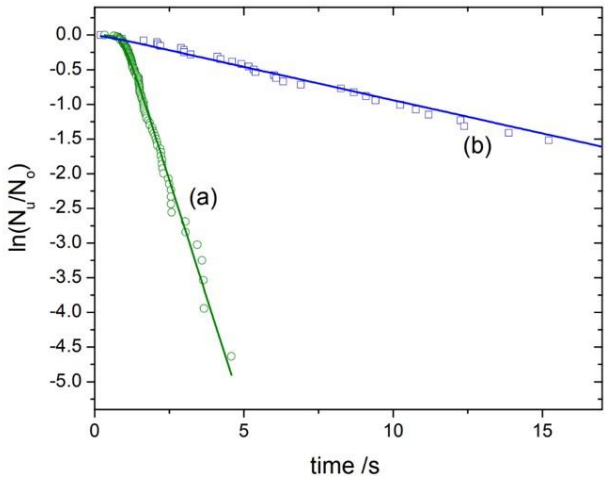

Figure 2-11: Natural log plot of the probability of supercooled water droplets remaining unfrozen as a function of experimental time, for two different starting radii: a) r_0 = 49 µm and b) r_0 = 19 µm. Droplets are cooled to a temperature of 237.1 K. Figure is reprinted under the Creative Commons Attribution 2.5 License, copyright 2004 Duft and Leisner.[202]

2.3.3. Viscous and Glass-Forming Solutes

Some solutes in the aerosol phase, particularly organic solutes, do not effloresce upon dehydration. Generally, if a solute has only weak aqueous solubility in the bulk phase, for example, succinic acid, the aerosol solution droplet tends to crystallise and has a defined ERH. Aerosol solution droplets with a solute that has a high solubility in water, such as malonic acid, are able to stay in the liquid phase without efflorescence occurring even down to very low RHs.[6] An implication of reaching very low RHs with no efflorescence occurring is that the substance can become viscous, and in some situations, glassy.[204] For example, at high RHs, sucrose solution aerosol droplets can readily undergo a radial response to changes in the gas phase RH, indicative of the water activity equilibrating with the RH. At

RHs < 40%, Zobrist et al.[205] showed that there are significant delays in the radial response to dehydration, with droplets still continuing to lose water over timescales of 10^5 s following step changes in RH down to 0%. This demonstrates that the high viscosity in concentrated sucrose solutions can cause a kinetic limitation to the evaporation rate. Such solution droplets undergo bulk-diffusion controlled evaporation.[112] Bones et al. studied the kinetic limitation to water transport from aerosol droplets exposed to RH changes, and correlated the time-scale for radial response to the bulk viscosity related to the Stokes-Einstein equation.[108]

Droplet-bulk kinetic limitations to evaporation can cause heterogeneities in the concentration and density of the solution inside a droplet, i.e. a core-shell morphology. Loss of solvent from the outer regions of a droplet can lead to a glassy surface that isolates the liquid interior from the vapour phase.[205] The evaporation kinetics of glass-forming solutions is typically characterised as initial loss of water from the droplet surface (gas-diffusion limited evaporation) until the surface becomes viscous and the evaporation rate slows significantly (bulk-diffusion limited evaporation).

Such bulk-diffusion limited evaporation can cause challenges in spray drying. Many formulations for spray drying in the food industry contain sugars like sucrose and lactose.[24] The rapid evaporation of water from the droplet surface can lead to glass-formation, with the high water retention leading to undesirable stickiness in the product.[206]

2.3.4. The Péclet Number in Droplet Evaporation

The ratio between the rate that a droplet evaporates and the rate that the solution inside the droplet undergoes diffusional mixing is called the Péclet number:

$$Pe = \frac{k}{D} \tag{2-45}$$

where k is the evaporation rate in terms of the droplet radius, dr^2/dt, from Eq. 2-22 and D is the binary diffusion coefficient for the droplet solution.[44] Evaporation processes with a $Pe < 1$ indicate that the diffusional mixing rate dominates over the rate of evaporation. Solvent vaporising at the surface is rapidly replaced with solvent from the bulk of the droplet, so the concentration of solute does not build up at the surface and the droplet maintains a radial homogeneous concentration profile of solute throughout the evaporation process. Such droplets generally dry to form a dense, homogeneous particle.[44] On the other hand, droplets with $Pe > 1$ have an evaporation rate that is greater than the rate that components in the droplet can redistribute. The evaporation process of such droplets generally proceeds with an enrichment of solute at the surface, as solvent from the droplet bulk cannot diffuse to the surface fast enough to replenish that which evaporates (Fig. 2-12).

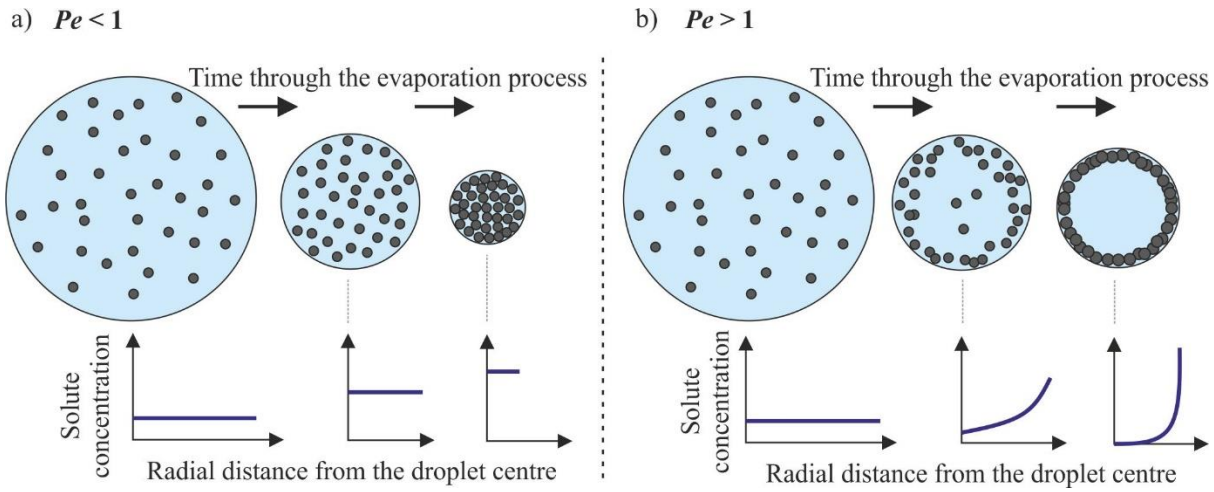

Figure 2-12: A schematic figure showing the development of morphology in evaporating droplets with a) *Pe* < 1 and b) *Pe* > 1. The concentration distribution of solute is indicated by the dark grey circles, and the graphs showing the radial concentration profile at different times into the evaporation process.

2.3.5. Morphology Development in Spray Dried Droplets

Droplets evaporating in a spray dryer typically have a very rapid evaporation rate, and the heat and mass transfer can be very strongly coupled. The temperature profile of a droplet evaporating in a spray dryer has an important effect on the resulting particle morphology and will be discussed in the next section.

2.3.5.1. The Droplet Temperature and Drying Stages in Spray Drying

The typical temperature profile of a droplet undergoing the spray drying process is shown in Fig. 2-13. The feed solution for spray dryers is typically much lower than the gas temperature, so upon entering the dryer the temperature of the droplets rises as heat is rapidly conducted from the gas phase, at point *A* in the figure. This is known as the initial drying period. Heat and mass transfer occur at the droplet surface simultaneously and the droplet soon reaches its wet bulb temperature (point *B*) at which time the heat transferred from the gas to the droplet is equal to that which sustains a constant mass flux.[4] At the wet bulb temperature, the droplet enters the constant rate period. The constant rate period is characterised by symmetric shrinking of the droplet and a relatively constant droplet temperature.[46] The surface of the droplet may start to become enriched with solute during this period, leading to a slight rise in temperature, indicated by the trajectory of the dashed line in Fig. 2-13. Eventually, the surface enrichment leads to crust formation (point *C*). The crust leads to internal resistance in mass transfer, so the droplet enters the falling rate period. The falling rate period is characterised by a rising droplet temperature, as the rate of heat conduction to the droplet from the gas outweighs the rate of latent heat

loss through evaporation.[4] The falling rate period proceeds as the crust thickens, eventually leading to a dried particle at point *D* in Fig. 2-13. By this point, the dried particle would be equilibrated in temperature to the outlet gas temperature.

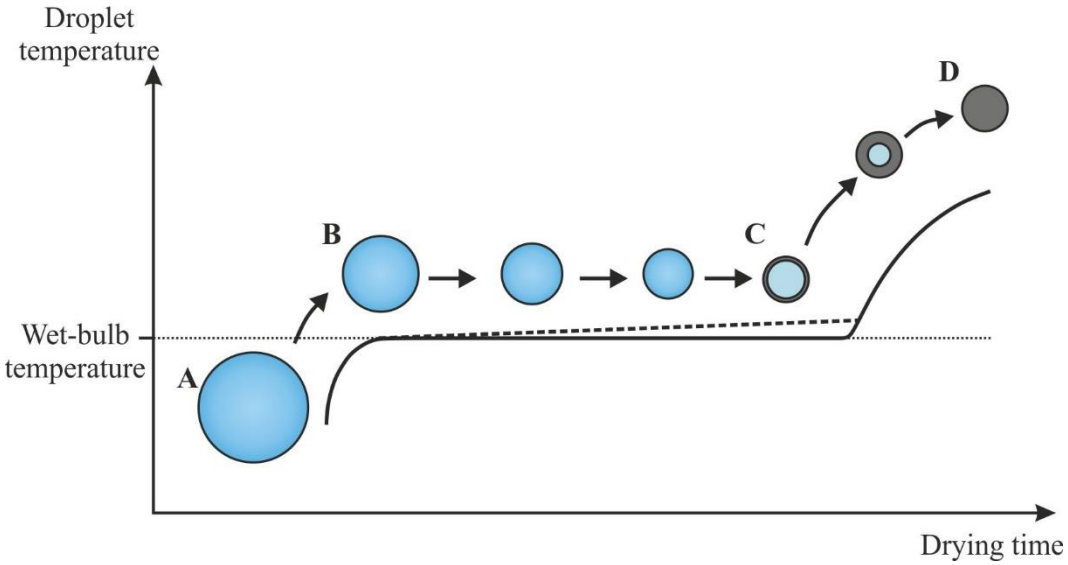

Figure 2-13: Schematic showing the typical droplet temperature profile during spray drying as it goes through the initial drying period (point A), the constant rate period (B), crust formation and the falling rate period (C) leading to particle formation (D).

2.3.5.2. Mechanical Properties of the Droplet Crust

Owing to the high gas temperatures in spray drying, Péclet numbers are typically high, so surface enrichment during drying is common. The constant rate period prior to crust formation can be very short in commercial spray drying because of the high contents of solids in the feed solution or slurry.[4] Crust formation can occur through either efflorescence or glass-formation of the solute at the surface, or agglomeration of suspended colloidal particles.[44] A thickening crust will eventually become rigid enough to resist further shrinkage, and a range of different particle morphologies can form depending on the mechanical properties of the shell/crust/film, and the evolving pressure within the droplet. Examples of structures that can arise following crust formation are shown in Fig. 2-14.

For an equivalent content of solid, a droplet that forms a crust earlier into the evaporation process will lead to a larger radius at the point of crust formation than one for which the crust forms later. Earlier crust formation also causes the shell to be thinner, which could make it more inclined to buckle and collapse.[88] In some cases, the rise in droplet temperature following crust formation at point *C* in Fig. 2-13 could cause the remaining solvent in the droplet to surpass the boiling temperature and lead to solvent boiling, which can cause significant droplet expansion due to the rapid pressure increase inside the

droplet.[207] This can cause inflation, rupture, bursting or collapse of the particle depending upon the elasticity or brittleness of the crust,[208] as shown in Fig. 2-14.

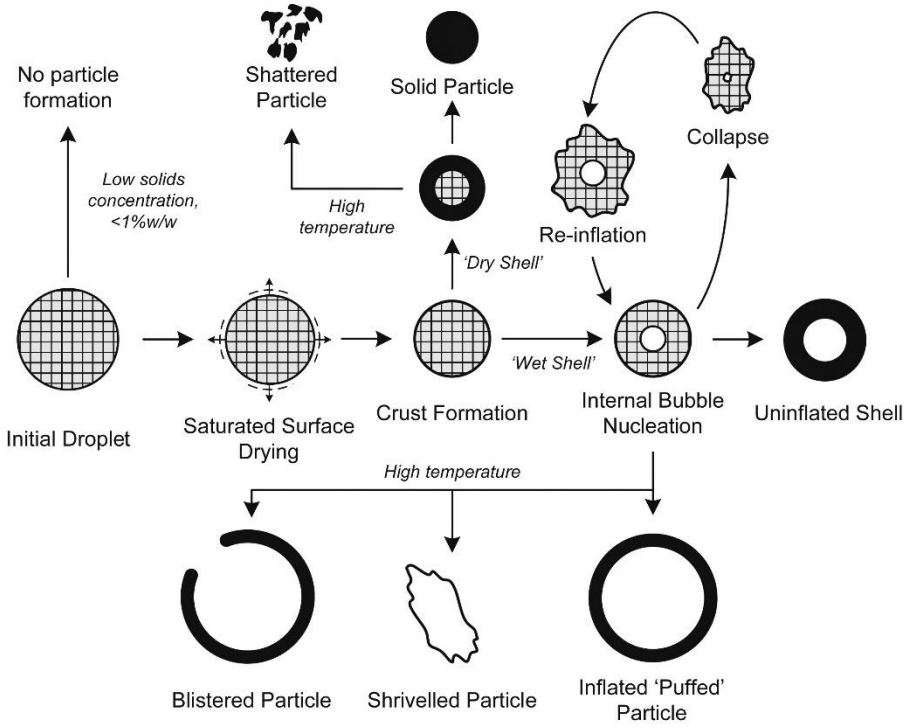

Figure 2-14: Examples of structures that can develop from spherical droplets containing dissolved or suspended during the spray drying process. Reproduced from Handscomb et al.[209] Reprinted with permission from Chemical Engineering Science, 65 (2), 713-725, Copyright 2010, Elsevier.

The final drying stage in the spray drying process can often be that which dictates the resulting product properties. The aerodynamic diameter of a particle, d_A, is the diameter of a sphere with standard density ρ^* (1 g cm^{-3}) that falls with the same settling velocity of that particle, and thus is strongly related to the particle density, ρ_p. In the continuum regime, the aerodynamic diameter is given by:

$$d_A = d_G\sqrt{\frac{\rho_p}{\rho^*}} \tag{2-46}$$

where d_G is the geometric diameter.[44] The aerodynamic diameter governs the transport properties of a dried particle, so is of particular importance to the spray drying of pharmaceutical products as it can dictate the location of deposition of inhaled products in the lung.[31] The competition between retaining a spherical ballooned shape and buckling of the crust during inflation influences whether a very low density puffed particle is formed, with a potentially higher solubility and smaller aerodynamic diameter, or a shrivelled particle as in the bottom of Fig. 2-14, which would have a higher density.

2.4. Chapter 2: Summary

This chapter has introduced the thermodynamic principles governing evaporation, discussing the vapour pressure of liquids and how the presence of a solute can influence the chemical potential of the solvent. The kinetics of mass transfer across different regimes of droplets size have been discussed. For the continuum regime, which includes the droplet sizes considered in this thesis, the concept of coupled heat and mass transfer have been examined. Building on this, the evolving temperature profile of a droplet in a spray dryer has been discussed and how this influences the mass flux through the varying stages of the spray drying. The equilibrium concept of the efflorescence RH has been introduced, leading into the kinetics of evolving solute concentration profiles in an evaporating droplet and the nucleation of solutes. The formation of a crust in a droplet and its mechanical properties can strongly influence the resulting particle morphology and density.

Chapter 3

Experimental Techniques and Methodology: The Electrodynamic Balance and The Falling Droplet Column

---

In this chapter, the experimental methodology for the work presented in this thesis will be discussed. Primarily, experiments were performed using the Electrodynamic Balance (EDB), which is an instrument that can stably levitate a single droplet of radius between 5 – 30 μm. The radius and particle phase state can be inferred from the elastic light scattering pattern of a droplet illuminated with light from a 532 nm laser. The EDB can be used to study evaporation kinetics of liquid droplets,[137,210] measure the vapour pressure of liquids [211] and study the equilibrium hygroscopicity of both inorganic and organic solutes.[116,212] In this work, the EDB is used to study rapid evaporation processes of aqueous inorganic solutions and mixtures under varying environmental conditions, as well as to present the hygroscopic growth curves of some solutes to discuss trends in evaporation kinetics. The EDB setup up will be described in Section 3.1 and the methodology for retrieving evaporation kinetics of droplets and the hygroscopicity will be discussed in detail in Section 3.2.

In addition to EDB data, the images of dried particles will be presented. The dried particles were collected using a falling droplet column (FDC) and imaged using a Scanning Electron Microscope (SEM). The techniques implemented to collect the dried particles for electron microscopy imaging are discussed in Section 3.3 and 3.4.

3.1. The Electrodynamic Balance Setup

The electrodynamic balance (EDB) setup is shown in Fig. 3-1. The instrument consists of two sets of concentric cylindrical electrodes, mounted vertically opposite one another. The central space between the two sets of electrodes is the trapping region; charged droplets levitate in this space. The cylindrical electrodes are positioned within an octagonal chamber, that is mounted ~ 20 cm above an optical bench. A 532 nm continuous wave laser is directed parallel to the bench through the centre of the instrument and into a laser beam block opposite. Four sides of the octagonal chamber contain circular transparent windows. Through two windows, scattered light from the centre of the chamber is focused through lenses onto a charged coupled device (CCD), as shown in the figure. The image from one CCD is used for sizing the droplet by collecting the out-of-focus phase function in the near-forward scattering direction. The other CCD collects the image of a focused droplet in the back-scattering direction such

that its vertical position in the trap can be monitored, and it can used to assist with alignment. Two sides at the front of the instrument have conducting rings mounted around the circular apertures as the induction electrodes. A chain of droplets is generated externally by a droplet-on-demand generator and the droplets travel through the side-opening into the centre of the instrument to be trapped. The droplets are charged through the action of the induction electrode, discussed in more detail in the next section.

The environmental conditions within the trapping chamber of the EDB can be controlled. The temperature in the EDB is adjusted by a circulating coolant of polyethylene glycol that passes over the electrodes, and the RH is regulated by flowing an N_2 gas through the chamber, of controllable humidity. These aspects are discussed in Section 3.1.3.

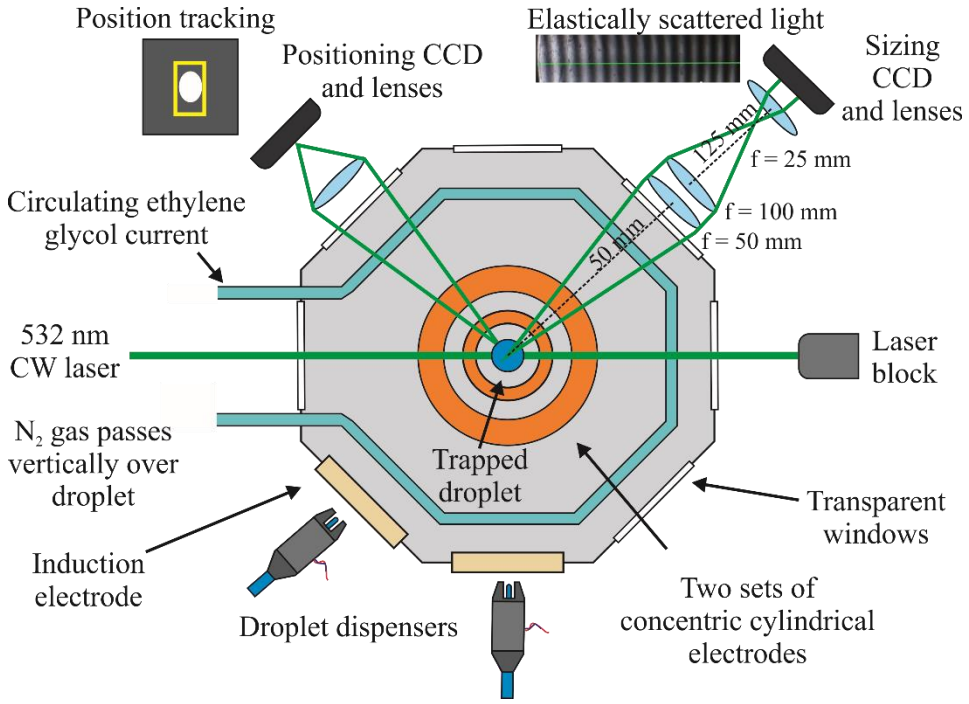

Figure 3-1: A birds-eye-view schematic of the Electrodynamic Balance (EDB).

3.1.1. Droplet Generation

Piezoelectric dispensers are used to produce the liquid droplets in this study. Piezoelectric dispensers are commonly used in inkjet printing applications and are advantageous over other atomization techniques such as nebulisers, due to the reproducibility in the size of the picolitre droplets produced by piezo dispensers, and the ability to produce one single droplet on demand. In this study we use MicroFab dispensers (MJ-APB-01) which have an orifice diameter of 30 µm. Whilst the droplet size produced is variable depending on the input settings, typically such dispensers produce droplets that are ~ 25 µm in radius.

Droplets are produced outside of the EDB using the dispenser and directed into the trapping chamber. A thin plastic tube of ~ 2 cm in length is attached to the back of the dispenser as a liquid feed acting as a reservoir for the solution of interest. First, 20 µL of a solution of known concentration is injected into the back of the dispenser reservoir using a micropipette (Pipetman, Gilson). After filling the dispensers, they are attached to a voltage supply, which is controlled by in-house LabView software via a DAQ card. An electric pulse in the form of a square waveform is applied to the droplet dispenser. A piezoelectric crystal in the dispenser turns this electric pulse into a mechanical wave through the liquid in the dispenser, which causes a jet through the dispenser tip that subsequently breaks up into droplets. Commonly, a principal droplet is formed at the front followed by small satellite droplets, as shown in Fig. 3-2.

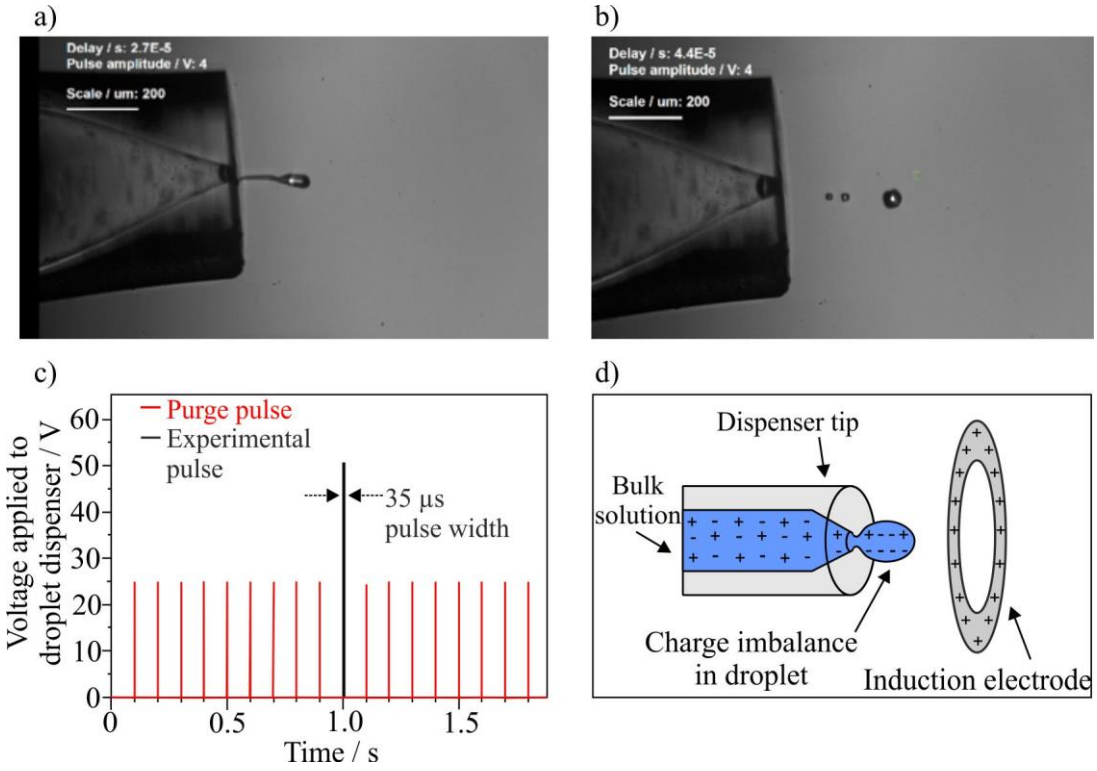

Figure 3-2: A droplet of water produced by a MicroFab droplet on demand generator using a pulse of 50 V amplitude and 35 µs width at a) 27 µs and b) 45 µs after the pulse is received by the dispenser. The water is initially a liquid jet that breaks up into a principal droplet followed by smaller satellite droplets. Scale bar is 200 µm. c) The sequence of pulses applied to the dispenser in order to produce a droplet at t = 1.0 s. d) A schematic of the positioning of the tip of the droplet dispenser near to the induction electrode ring, inducing a charge-imbalance in the droplet as it is formed.

The distance between the centre of the EDB and the dispenser is approximately 5 cm; the square waveform applied to the dispenser must be large enough in amplitude that the droplet produced reaches the trapping area. Aligning the dispenser into the chamber is performed with the dispenser in "continuous" mode, with electric pulses of 30 - 80 V and ~35 µs width applied at a rate of 10 Hz. The droplet dispenser is positioned such that the continuous stream of droplets can be seen to enter the EDB and fall into the centre of the cylindrical electrodes. To perform experiments, the "automatic" mode for

the dispensers is used. The signal of light scattering registered by the CCD determines whether a droplet is currently trapped and, when a droplet is no longer levitated, a pulse to automatically produce one single droplet is sent to the droplet dispenser to reload the trap. Throughout an experiment a continuous pulsed wave of lower amplitude is applied at a rate of 10 Hz to the dispensers to continuously purge the dispenser tip of fresh solution; an example of the pulse sequence is shown in Fig. 3-2c. The amplitude of the "continuous pulse" is sufficiently high to produce a constant jet of droplets but not large enough that such droplets would reach the centre of the EDB and hence interfere with the experiment. The initial flight speed of dispensed droplets increases with increasing amplitude of the pulse, but on average it takes 0.1 s for droplets to travel the ~ 5 cm distance to the centre of the instrument to become trapped. The LabView software records the time that the electric pulse was applied to the dispenser to produce each droplet; hence, the precise time of droplet generation can be known. The instrument can only record the radius of the droplet once it is trapped in the instrument, so the radius at t=0 s can only be determined by extrapolating back through the first 0.1 s.

3.1.2. Droplet Confinement

Droplets are charged upon generation by an induction electrode, which comprises a conductive ring wired to the side of the EDB. Droplets are produced directly in front of the induction electrode and pass through the electrode once dispensed. The induction electrode is charged to a voltage of 500 – 700 V, which induces a mirror charge on the droplet while it forms at the dispenser tip (Fig. 3-2d). Thus, when the single droplet is produced it has a charge imbalance, for example, arising from OH^- and H_3O^+ ions, leading to an overall charge on the droplet. Previous work has estimated that droplets charged in this way have an overall charge on the order of fC.[213] An alternating current (typically 500 – 1000 V) is applied to the inner rings in the sets of upper and lower electrodes in the EDB, whilst maintaining the outer rings at 0 V, which produces an electrodynamic field inside the chamber that causes a droplet to become trapped in the centre. The instrument design used in this study is similar to that in the work of Heinisch et al., who calculated the magnitude of the electric field in the region around the cylindrical electrodes (Fig. 3-3).[124]

Levitation of a single droplet arises from a balance between forces. An AC field periodically exerts a force on the droplet, both vertically and radially, towards the centre of the trap where the magnitude of the electric field tends to zero. The force is proportional to the distance between the droplet and the centre of the trap, z_0. A gravitational force, F_g, acts on the droplet arising from its mass, m. In addition, as a gas flow passes over the droplet (Section 3.1.3), the droplet also experiences a drag force, F_{drag}. The influence of the gravitational and drag forces will induce oscillation in a droplet that is trapped in a field produced by only an AC current. Thus, an additional DC (typically 100 V) is applied to the lower electrodes only to counteract F_g and F_{drag}.

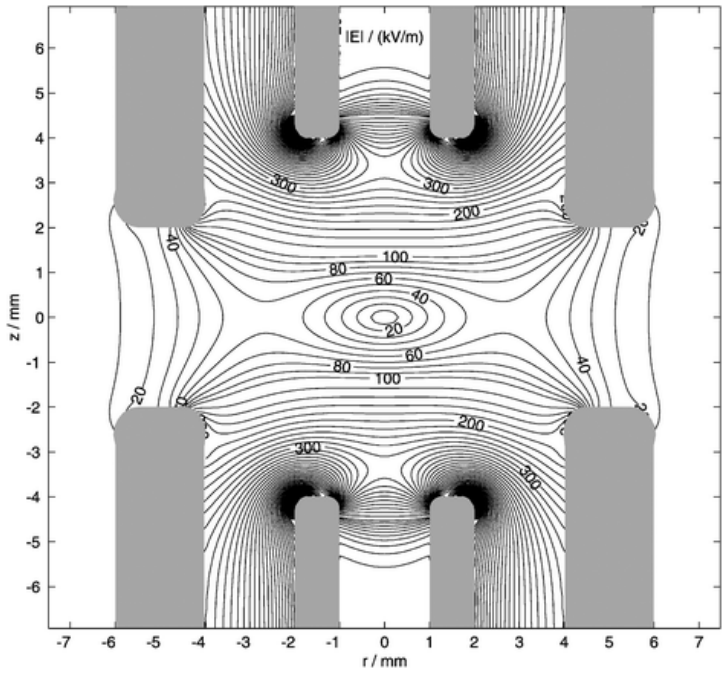

Figure 3-3: The magnitude of the electrodynamic field produced in a concentric cylindrical EDB when a potential of 1 kV is applied to the inner electrode and 0 V to the outer electrode. Reprinted with permission from the Royal Society of Chemistry from Heinisch et al., Physical Chemistry Chemical Physics, 2009, 42, 9720.[124]

The net vertical force acting upon a droplet located a vertical distance of *z* from the centre of the EDB trap is:

$$F_{net} = -F_g + F_{drag} + F_{DC} + F_{AC} \tag{3-1}$$

Thus, the vertical motion of a droplet of radius *r*, at time *t*, can be described by:

$$m\,\frac{d^2 z}{d\,t^2} = -mg + 6\pi r\eta v + qC_0\frac{V_{DC}}{z_0} - z\left(2qC_1\frac{V_{AC}}{{z_0}^2}\cos(2\pi f t)\right) \tag{3-2}$$

where *m* is the droplet mass and *g* is gravitational acceleration, η is the dynamic viscosity of the gas that passes over the droplet at a gas speed of *v*. *q* is the droplet charge and V_{DC} and V_{AC} are the voltages of the AC and DC, respectively. *f* is the frequency of the AC field. C_0 and C_1 are constants relating to the geometry and positioning of the electrodes in the EDB.[214] Heinisch et al. characterised the position of trapped water droplets in such a trapping chamber and reported that combining AC and DC fields led to stable trapping with droplets not moving further than 1 µm from the equilibrium position within the centre of the instrument.[124]

As droplets evaporate, they rapidly lose mass, so the magnitude of the electrodynamic field required to keep the droplet trapped in position decreases during an experiment. For a constant AC field, an evaporating droplet would fall out of the trap when its mass decreased below a threshold value. The in-house LabView software decreases the amplitude and increases the frequency of the AC field according to the measured radius according to:

$$V_{AC}(r) = V_{AC,0} - \frac{\mathrm{d}V}{1-\frac{r}{r_0}} \tag{3-3}$$

$$f_{AC}(r) = f_{AC,0} + \frac{\mathrm{d}f}{1-\frac{r}{r_0}} \quad (3\text{-}4)$$

where $V_{AC,0}$ and $f_{AC,0}$ are the initial AC voltage and frequency, and dV and df are constants, manually set to vary V_{AC} and f_{AC} according to the radius, r, that changes relative to the initial radius, r_0. Using Eq. 3-3 and 3-4, with typical values of dV and df of 0 – 200 V and 0 – 300 Hz, respectively, it is possible to keep droplets trapped in the EDB down to a radius of ~ 4 µm.

3.1.3. Controlling Environmental Conditions in the Electrodynamic Balance

The temperature and RH within the trapping chamber of the EDB can be controlled such that the evaporation of liquid droplets can be studied under a range of different environmental conditions. The temperature is controlled by circulating a polyethylene glycol current across the electrodes to act as a coolant; the temperature of the polyethylene glycol is controlled using a commercial chiller (F32-ME, Julabo). Both the upper and lower electrodes are thermally conductive and the N_2 gas flow passes through the electrodes, which allows the temperature inside the trapping chamber to equilibrate to that set with the chiller. The temperature is recorded using a thermocouple (National Instruments, NI-USB-TC01 with K-type probe) that hangs in the airflow next to the upper electrode and can be read-out on the PC to ± 1 K. The temperature can be controlled between 273 and 323 K.

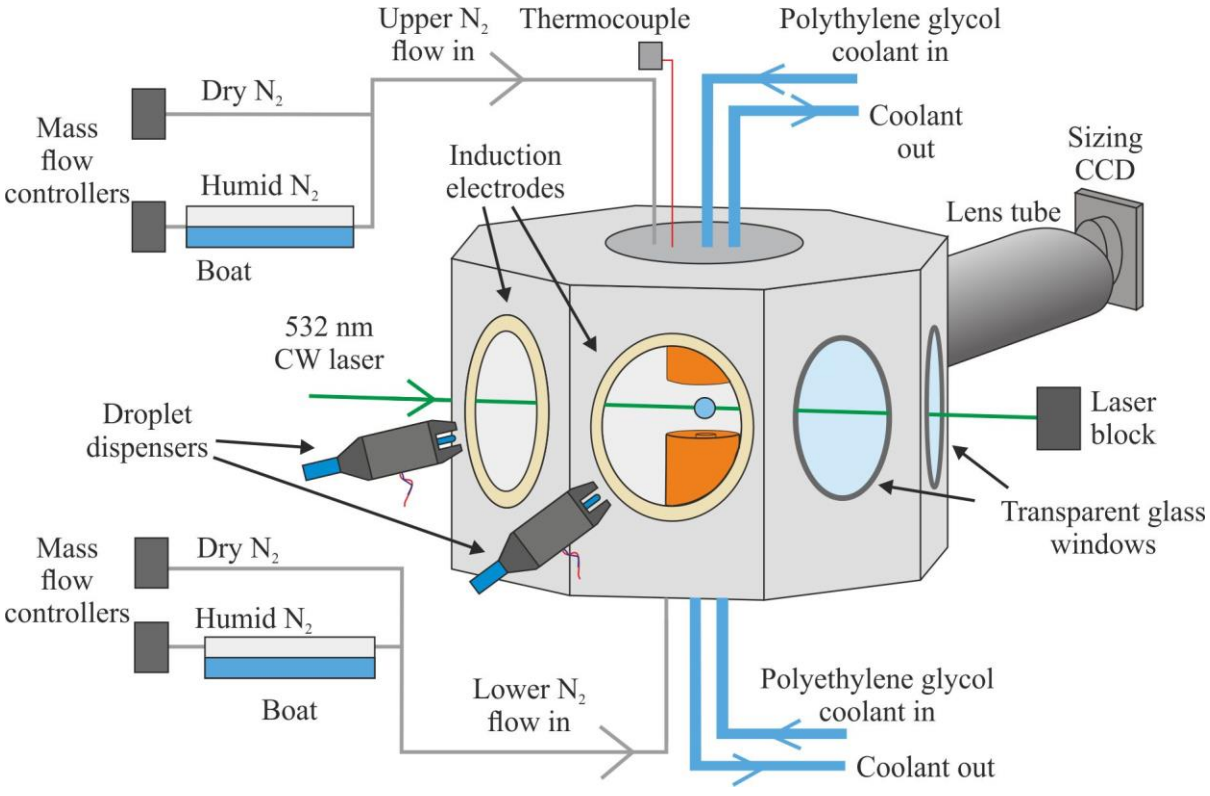

Figure 3-4: Schematic to depict the side-on view of the EDB, demonstrating how the RH and temperature is controlled within the chamber through the use of N_2 gas flows and polyethylene glycol coolant, respectively.

The RH inside the chamber is controlled by flowing N_2 gas of controllable degree of humidification through the outer electrode and across the droplet trapping position. The N_2 gas can either be introduced into the EDB through the top or bottom electrodes. Each supply (upper or lower flow) is a combination of two gas-flows, one dry N_2 gas supply and one that has passed through a water boat and has become humidified. These are combined into one single flow prior to entering the trapping chamber (Fig. 3-4). Adjusting the ratio between the wet and dry N_2 gas flows controls the RH. If the upper and lower supply are set to different ratios between their dry and wet gas flows, then the RH in the chamber can be rapidly changed by switching between the upper and lower supply. This enables a rapid switch in the RH, which typically occurs over < 0.1 s.[215] An example of an RH switch performed during the evaporation of a pure water droplet in the EDB is shown in Fig. 3-5. This switching feature of the EDB can be useful in simulating inhalation, wherein an inhaled aerosol experiences a rapid increase in RH when it enters the lung. In the experiments performed in this thesis, the gas flow was set to 200 cm^3 min^{-1}. Previous work in the group calibrated this flow-rate on the EDB to be equivalent to a gas-speed of 3 cm s^{-1} across the trapping region.[213]

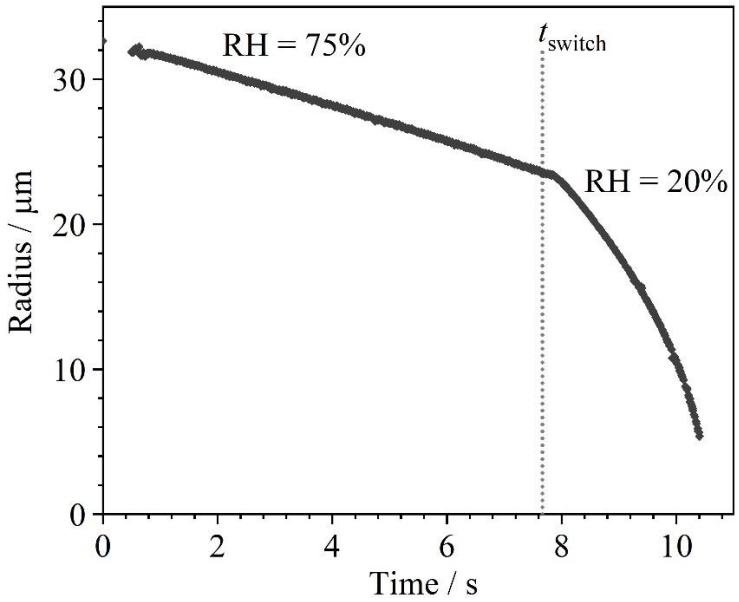

Figure 3-5: The radius during evaporation of a pure water droplet in the EDB at 293 K. The RH is switched at t_{switch} from 75% to 20%, showing the increase in evaporation rate of the water droplet after the switch.

Capacitance RH probes (e.g. Vaisala) can typically be used to record the RH to an accuracy of ± 2%. The RH in the EDB is recorded to greater accuracy by studying the evaporation kinetics of a probe droplet. This will be discussed in greater detail in a later section. Briefly, the evaporation kinetics of a droplet of either water or aqueous NaCl of known concentration are measured directly before the sample droplet of interest. The evaporation kinetics of the probe droplet can be used to estimate the RH in the chamber. The accuracy of the RH retrieval depends upon whether a pure water droplet or an aqueous NaCl droplet is used but is typically less than ± 1% RH as described in more detail in Section 3.2.6. Whilst the probe droplet is produced using a different dispenser to the sample droplet, the equilibrium

trapping position inside the EDB is in the same place; hence, it can be assumed that the RH experienced by a probe droplet is the same as for the sample droplet immediately afterwards.

Most of the experimental data collected in this thesis is performed at a gas temperature of 293 K. The wet and dry N_2 gas flows are combined at room temperature, which is typically close to 293 K, so the RH that is recorded is often very close to that intended with the mixing ratio. For example, a mix of 80% wet N_2 to 20% dry N_2 will result in an RH that is very close to 80%. However, if an EDB experiment is performed at a different temperature to 293 K, the ratio of wet to dry N_2 required to give a certain RH must change, because the mixing of the gas flows still takes place at 293 K. This is related to the temperature-dependent saturation vapour pressure of water vapour, which is shown in Fig. 3-6a. Fig. 3-6b plots the ratio of wet to dry N_2 to set on the mass flow controllers to achieve a desired RH at a range of temperatures, if the mixing of wet and dry N_2 occurs at 293 K. As the temperature-dependent vapour pressure of water decreases at lower temperatures, less of the wet flow of N_2 is required in the gas mixture, which is combined at 293 K, to produce a certain RH. For example, at 283 K the vapour pressure is 1.23 kPa, so to achieve an 80% RH environment in the EDB, a partial pressure of 0.98 kPa is required, which is a ratio of 42% wet N_2 to 58% dry N_2 at room temperature.

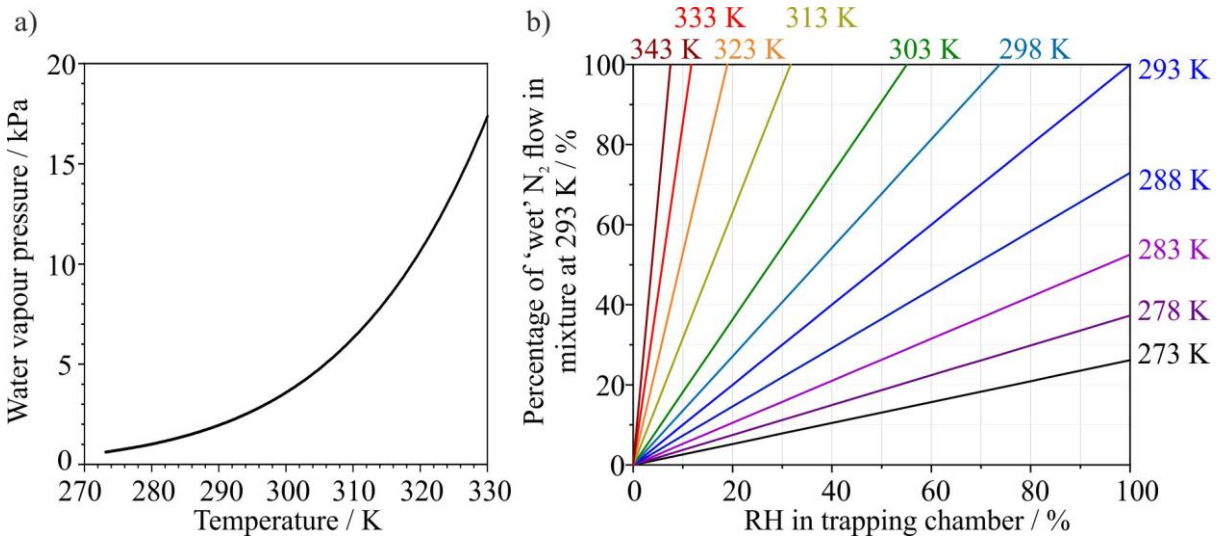

Figure 3-6: a) The temperature-dependent vapour pressure of water at atmospheric pressure, plotted from Wagner and Pruss.[184] b) The ratio of wet and dry N_2 flows required to produce varying RHs in the EDB at different temperatures given that the mixing of flows occurs at 293 K.

3.2. Analysis of Data Collected using the Electrodynamic Balance

3.2.1 Determination of Droplet Size and Inferring the Particle Phase State

The beam from a 532 nm continuous-wave laser is aligned to the centre of the electrodynamic trap, such that trapped droplets are illuminated. The reflection and refraction of the laser on passing through and around the droplet lead to a scattering pattern formed from constructive and deconstructive interference. A charged coupled device (CCD) collects the scattering pattern at 45 ° to the laser in the forward direction, over an angular range of ~ 27 °. The approximate arrangement of the lenses used to focus the forward scattered light, and the focal lengths, is shown in Fig. 3-1.

The way that aerosol particles interact with radiation depends on the relative sizes of the light wavelength λ, and the particle radius, r. Particles significantly smaller than the wavelength ($r < \lambda/20$) fall within the regime for which Rayleigh theory can be used to interpret the scattering pattern. Radiation scattering of particles with r significantly greater than λ can be described by geometric optics. Mie theory provides an exact solution to scattering of light for all size ranges, but it is commonly used for the regime wherein $r \sim \lambda$.

The droplets in this study range in size from 5 – 30 μm, so r/λ = 10 – 60. A spherical, homogeneous, liquid droplet within this size range will produce a scattering interference pattern from 532 nm wavelength radiation that takes the form of a phase function of regularly spaced fringes, whose intensity decays monotonically across the angular range. An example of the phase function (PF) collected from a droplet in the EDB is shown in Fig. 3-7a. The intensity across the angular range along the indicated green line is collected to form a plot of intensity vs. angular range (Fig. 3-7b).

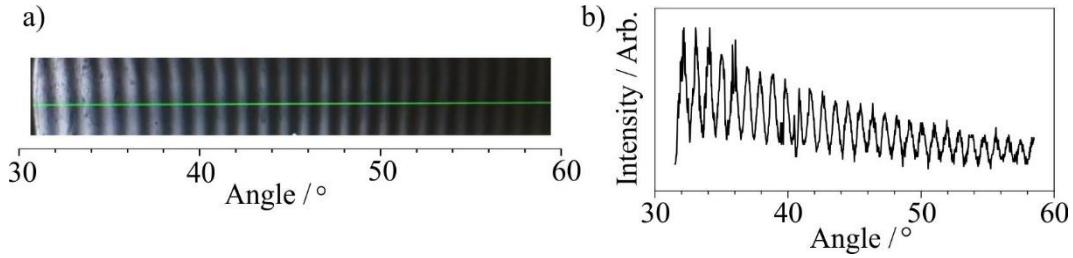

Figure 3-7: a) An example of the phase function (PF) in the light scattering collected from a homogeneous liquid droplet in the EDB in the forward scattering direction. b) An example of the intensity plot of light scattering with respect to angle.

Collected PFs such as in Fig. 3-7 can be compared to a library of simulated scattering patterns from Mie theory, with the best match providing both the droplet radius and the refractive index.[105] However, Mie theory is computationally expensive, and for the droplet sizes in this study, the geometric optics approximation to Mie theory is used as it can provide the radius of droplets in real-time during evaporation to a reasonably high accuracy.[137]

The spacing between the peaks in the scattering pattern, $\Delta\vartheta$, is used to calculate the droplet radius, *r*, using the geometric optics approximation equation:

$$r = \frac{\lambda}{\Delta\vartheta}\left(\cos\left(\frac{\vartheta}{2}\right) + \frac{n\sin\left(\frac{\vartheta}{2}\right)}{\sqrt{1+n^2-2\,n\cos\left(\frac{\vartheta}{2}\right)}}\right)^{-1} \quad (3\text{-}5)$$

where λ is the laser wavelength, *n* is the real part of the droplet refractive index and ϑ is the central viewing angle. This approximation can allow the determination of the droplet radius with an accuracy of ± 100 nm.

The radius is estimated in real-time by the EDB software and output in the form of radius vs. time for the evaporation process of a droplet. During data acquisition the software assumes the refractive index is equal to that of water at 532 nm, i.e. 1.335. Thus, for droplets that are not pure water, the output data must be corrected for a different refractive index. In the case of an aqueous solution droplet, the refractive index changes throughout evaporation as the solution becomes more concentrated in solute. Thus, the radius as inferred from the geometric optics equation (Eq. 3-5) becomes increasingly inaccurate as the evaporation proceeds and this must be accounted for in a post-processing step.

The refractive index of the droplet at all times can be calculated from the concentration using the molar refraction mixing rule.[216] The mixing rule has been to shown to provide the most accurate model for treating the refractive index of mixtures across a range of inorganic solutions.[217] The mixing rule states that the molar refraction of a solution, R_e, is a mole-fraction (x_i) weighted sum of the molar refraction of each component in the mixture, for example for water and a solute *i*:

$$R_e = x_i R_i + x_{water} R_{water} \quad (3\text{-}6)$$

where the molar refraction R_i of one component *i* is defined as:

$$R_i = \frac{(n_i^2-1)\,M_i}{(n_i^2+2)\,\rho_i} \quad (3\text{-}7)$$

where n_i is the pure component refractive index, M_i is the compound molecular mass and ρ_i is the pure component melt density.

The refractive index, *n*, of a solution can be solved from:

$$R_e = \frac{(n_e^2-1)\,M_e}{(n_e^2+2)\,\rho_e} \quad (3\text{-}8)$$

where *M* is a molar-weighted molecular mass, ρ is the density of the solution and *R* is the molar refraction of the solution, where the subscripts *e* denotes a property of the mixed solution. Rearranging Equation 3-8 yields:

$$n_e^2 = \frac{\left(\frac{2\,\rho_e\,R_e}{M_e}\right)+1}{1-\frac{\rho_e\,R_e}{M_e}} \quad (3\text{-}9)$$

Multiplying the top and bottom of Equation 3-9 by $\frac{M_e}{\rho_e}$, and cancelling, leads to:

$$n_e = \sqrt{\frac{2\,R_e+\frac{M_e}{\rho_e}}{\frac{M_e}{\rho_e}-R_e}} \quad (3\text{-}10)$$

Thus, the refractive index of a mixture of components can be inferred across the concentration space. We consider the implementation of this treatment in interpreting the optical measurements in the following section.

3.2.2. Parameterising the Density of Mixtures and Calculation of the Pure Component Density

To use Eq. 3-10 to calculate the refractive index of a solution, one also needs an accurate parameterisation of the density of aqueous solutions of water and solute *i,* ρ_e, across the concentration range. The method used to obtain such a parameterisation depends upon the solubility of the solute.[216] If bulk solutions of concentrations greater than 0.4 mass fraction of solute (MFS) can be made, the density of a range of bulk solutions up to the solubility limit are recorded using a density meter (Mettler, Toledo). The bulk density measurements are fitted with a 3rd order polynomial fit in the square root of the MFS. The square root of MFS is chosen for the fit over the MFS because it spreads the bulk data further across the accessible range, which decreases the extent of extrapolation to calculate the pure component density at MFS=1.

If the bulk solubility limit of the compound is smaller than 0.4 MFS, then the pure component melt density of a solute, ρ_s, can be calculated using an ideal mixing treatment:

$$\frac{1}{\rho_e(1-\mathrm{MFS})} = \frac{\mathrm{MFS}}{(1-\mathrm{MFS})\times \rho_s} + \frac{1}{\rho_w} \qquad (3\text{-}11)$$

where ρ_e and ρ_w are the density of the aqueous solution and of pure water, respectively. By plotting bulk density data in the form of $\frac{1}{\rho_e(1-\mathrm{MFS})}$ against $\frac{\mathrm{MFS}}{(1-\mathrm{MFS})}$ on the *y* and *x* axes, respectively, and constraining the intercept to be $\frac{1}{\rho_w}$, the data forms a straight line with the inverse gradient being equal to the pure component density of the solute. For low solubility compounds, this pure component density value has a much smaller error than that retrieved from extrapolating the density data in a polynomial function.

An example of the density treatment for the determination of the pure component melt density (ρ_s) of KNO_3 is shown in Fig. 3-8a. KNO_3 has an aqueous solubility of 0.242 MFS at 293 K.[218] Bulk density values (grey datapoints) are extrapolated in a 3rd order polynomial function in terms of the $MFS^{1/2}$, which gives a value of ρ_s = 1.70 ± 0.08 g cm^{-3}. This large error in melt density converts into an error of ± 0.007 in the calculated pure component refractive index of 1.490. Alternatively, when the ideal mixing equation (Eq. 3-11) is plotted for the same data, as in Fig. 3-8b, a straight line can be fitted with a gradient of 0.424 ± 0.003 $cm^3\ g^{-1}$, which yields a value ρ_s = 2.36 ± 0.01 g cm^{-3}. The smaller error envelope in this treatment converts into an error of ± 0.001 in the refractive index of pure melt KNO_3, determined to be 1.548.

It is not possible to know which method to retrieve ρ_s is more accurate, as the sub-cooled melt of KNO_3 cannot be accessed experimentally, so ρ_s cannot be measured. However, we can compare these values to the pure KNO_3 crystalline density of 2.105 g cm^{-3},[218] which is closer in value to the melt density estimated using ideal mixing.

This demonstrates that, due to the low solubility of KNO_3 at 20 °C, the extrapolation of the measured density datapoints provides not only an underprediction of the pure component density and refractive index, but also a much greater error envelope. Most of the inorganic salts used in the work in this thesis have an aqueous solubility of < 0.4 MFS at 293 K, so the ideal mixing method was used to produce a parameterisation of the pure component density and refractive index.

Once a parameterisation of the density and the refractive index has been obtained for the solution of interest across the entire concentration range, the raw data collected by the EDB can be corrected to account for the increasing density and refractive index during evaporation. A post-processing in-house LabView software iterates through the timesteps in the experimental raw data to calculate the MFS at each point, to then determine the refractive index at every point using a refractive index vs. concentration parameterisation. The steps behind this process are outlined in the next section.

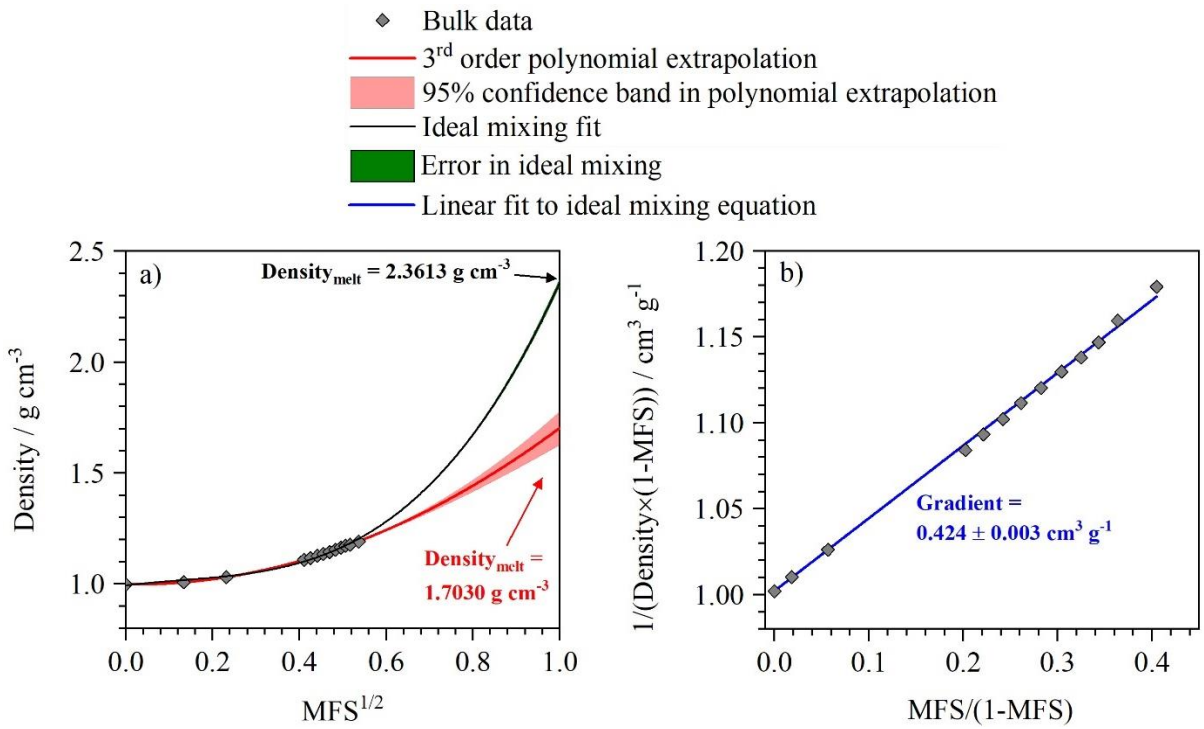

Figure 3-8: a) The density of aqueous solutions of KNO_3, measured using a density meter. The red line shows a 3rd order polynomial extrapolation, with a 95% confidence band. This is compared to the ideal mixing fit (grey line) with a melt density that is retrieved using the inverse of the gradient in panel b).

3.2.3. Correcting Raw Electrodynamic Balance Data for a Changing Refractive Index

At t = 0 s, the initial radius from the raw data, $r_{0,raw}$, is known. The initial concentration in terms of MFS is known, so the initial refractive index n_0 is known, as well as the density ρ_0 and hence the mass m_0. Thus, the initial radius $r_{0,raw}$ is corrected using Equation 3-5 and n_0, to yield $r_{0,corr}$. At the next timestep, t_1, there is a new raw radius, $r_{1,raw}$, and some water mass has been lost. To estimate the new mass, $m_{1,guess}$, the density of the step before, ρ_0, is used because the timesteps are very small in the data recorded from the EDB (typically < 0.01 s). With $m_{1,guess}$ the new MFS at t_1 can be calculated given that water is the only evaporating component, so any mass loss is attributed to an increase in solute concentration. The new MFS can yield a better estimate of the density at t_1, which leads to a better estimate of the mass, $m_{1,guess}$. A second attempt at the calculation of the mass loss during that first timestep provides an even better estimation of the MFS, and hence an improved determination of the concentration, density and refractive index at t_1. Following two iterations in estimates of the density at each timestep, an accurate value of the refractive index is calculated, and the radius at that timestep is then corrected from the raw data. Evaporation of water leads to an increase in the solute concentration, and for a solute that has a pure component refractive index greater than that of water, the correction process will increase the values of the measured radius compared to the raw data. An example of raw and corrected data of an aqueous NaCl droplet with initial concentration of 0.0777 MFS evaporating in the EDB at 293 K and 52% RH is shown in Fig. 3-9a. The water evaporates so an increase in refractive index occurs (see panel *b* of the figure) as the NaCl concentration increases (panel *c*).

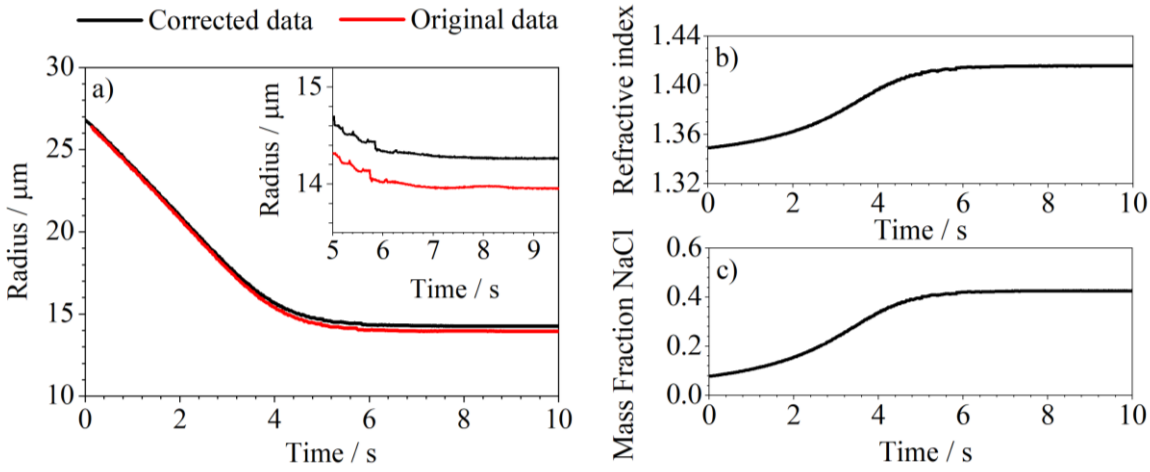

Figure 3-9: a) The evaporation of a droplet of aqueous NaCl (initial MFS of 0.0777) as it evaporates in the EDB in 52% RH at 293 K. The original data as recorded by the EDB is shown in red and once corrected for the changing refractive index. The inset shows the image focused on the equilibrated radii of the two datasets. b) and c) show the refractive index of the droplet and mass fraction of NaCl, respectively.

3.2.4. Density and Refractive Index Parameterisations for Solutions Containing Mixtures of Multiple Inorganic Solutes

In Chapter 7 of this thesis, the evaporation of droplets containing mixtures of different solutes is studied. The correction of raw data collected from the EDB of such droplets requires a parameterisation of density and refractive index of a mixture of solutes. This is performed using similar methods to the above section and will be outlined here.

For a droplet that contains two involatile solutes *i* and *j*, as water evaporates from the droplet, the ratio of *i* to *j* will remain the same throughout the drying process. Density and refractive index parameterisations can be produced for a specific ratio of *i* and *j*, as if a single solute is present.

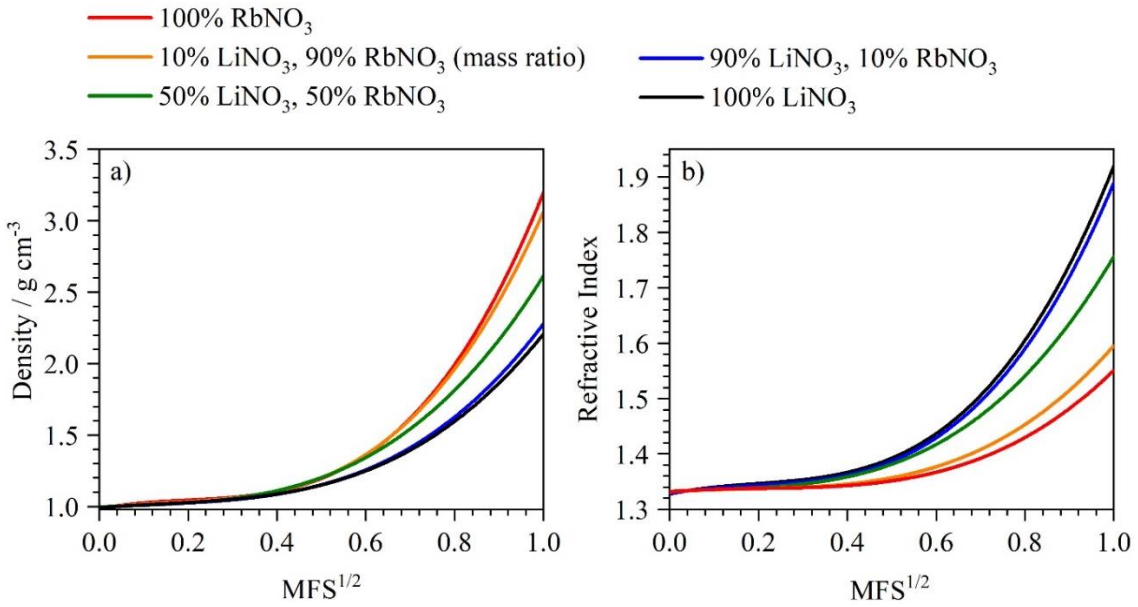

Figure 3-10: a) The density of aqueous solutions of mixtures of $RbNO_3$ and $LiNO_3$ in varying ratios (by mass), as determined using ideal mixing. b) The refractive index of mixed aqueous $RbNO_3$ and $LiNO_3$ solutions.

Provided the single component melt density of solutes *i* and *j* are known, the density of a multi-solute solution can be calculated across the concentration range using an ideal mixing approach. Equation 3-11 becomes:

$$\frac{1}{\rho_e} = \frac{\mathrm{MFS}_i}{\rho_i} + \frac{\mathrm{MFS_j}}{\rho_j} + \frac{1-(\mathrm{MFS}_i + \mathrm{MFS}_j)}{\rho_w} \qquad (3\text{-}12)$$

For a parametrisation of the refractive index of a multi-solute solution, the molar refraction mixing rule in Equation 3-10 still applies, with the only difference being that the molar-weighted molecular mass, M_e, is now weighted across three components and the sum of the molar refraction in Equation 3-6 becomes:

$$R_e = x_i R_i + x_j R_j + x_{water} R_{water} \qquad (3\text{-}13)$$

Examples of density and refractive index parameterisations for such multi-solute mixtures are shown in Fig. 3-10 panels *a* and *b*, respectively, for aqueous mixtures of $LiNO_3$ and $RbNO_3$. The red and black lines show the parameterisations of solutions of only aqueous $RbNO_3$ or aqueous $LiNO_3$, respectively, and the mixtures all fall between these outer limits.

3.2.5. Assessment of the Particle Phase State

The elastic light scattering from a droplet is used to estimate the radius, but it can also be used to infer the phase state of the trapped droplet or particle. This method is outlined in a recent publication by Haddrell et al.[210] When a liquid spherical droplet is suspended in the EDB, the beam from a 532 nm laser will interact with the droplet through reflection and refraction at the droplet surface, and the constructive and deconstructive interference of the resulting light surrounding the droplet will produce the regularly space fringes depicted in Fig. 3-11a in the forward direction with decreasing intensity of fringes with increasing scattering angle. Such a pattern forms a phase function that can be described by Mie theory, and the radius of the trapped droplet can be retrieved using the geometric optics approximation in Eq. 3-5, or comparing the phase function to a library of Mie theory simulations.[110,217] The components inside a droplet may not be homogenously distributed and this could disrupt the phase function, which no longer then shows the regularly spaced fringes; the underlying assumptions in Mie theory are not met. Whilst irregular fringes in the light scattering collected by a particle may not enable the radius of the particle to be retrieved, the morphology can sometimes be inferred, and this is described in the next section.

3.2.5.1. Different Particle Morphologies that are Identifiable from the Light-Scattering

There are several different particle morphologies that a levitated particle in the EDB may have that can be identified by the light scattering. For example, there may be a strong gradient in refractive index or even a core-shell morphology. Qualitatively, such a core-shell structure would show regularly spaced fringes, as in the case of a homogeneous sphere, but with a secondary regular structure superimposed in the scattering pattern that takes the form of a modulation in intensity, (Fig. 3-11d). Also, a droplet may contain inclusions, which are internal objects randomly scattered inside the host droplet that have a different refractive index to the continuous medium in the droplet. Such inclusions can lead to random enhancement or suppression to the light intensity at certain angles. The overall phase function shows peaks in the light scattering similar to the PF in Fig. 3-11a, but with a random variation in the intensity of such peaks and a less regular pattern (Fig. 3-11c).

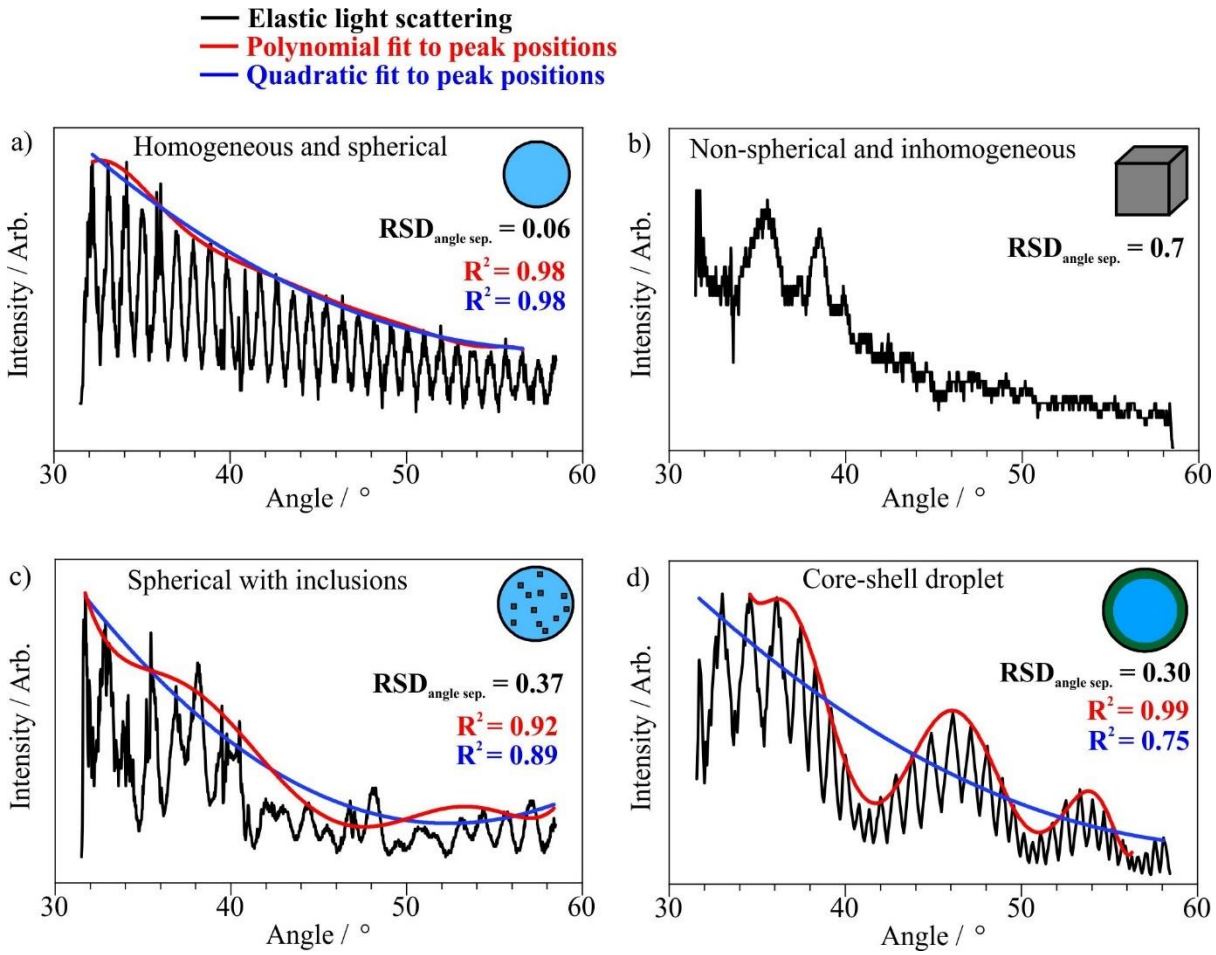

Figure 3-11: Examples of the elastic-scattering collected from droplets/particles exhibiting different morphologies when trapped in the EDB. a) A homogeneous phase-function caused by a pure water droplet. b) The elastic scattering pattern caused by a crystalline NaCl particle that has been dried fully in the EDB. c) The inclusions phase function shown by a $NaNO_3$ droplet that has nucleated small nuclei but has not undergone complete crystallisation, d) a dodecanol-water droplet, data of which is plotted from Haddrell et al.[210] The fit to the peak positions using a quadratic or polynomial function is shown in blue and red, respectively.

Trapped particles in the EDB that are either non-spherical, opaque to the laser light or that are completely inhomogeneous typically show highly erratic light scattering patterns such as dried salt particles that have formed crystalline structures (Fig. 3-11b).

3.2.5.2. Assigning the Particle Morphology from the Elastic Light Scattering

The morphology of a trapped particle can be inferred at specific time-points from the PF, using both the consistency in the angular spacing between the peaks, and the relative amplitudes of the peaks. The algorithm (as outlined in Haddrell et al.[210]) used to differentiate between the different particle morphologies is summarised in the flow-chart in Fig. 3-12 and will be described briefly here.

The spacing between the peaks in a PF is described using the relative standard deviation (RSD) from the average separation, and this value is the initial criterion distinguishing the particle from being either

unspherical/crystalline (for RSD > 0.4) or all other morphologies for RSD < 0.4, i.e. spherical/homogeneous, spherical with inclusions, core-shell/concentration-gradient.

The second criterion for the algorithm to assign the morphology to a specific PF is the goodness of fit of the angular variation in the amplitude of the peaks in the PF to either a polynomial or quadratic dependence. The order of a polynomial chosen for the fit to the peak points in the elastic scattering is chosen based on how many peaks there are in the PF. A polynomial function of 6th order is used for PFs with fewer than 18 peaks, and for more than 18 peaks, then the order parameter is one third of the number of peaks. For example, for the PF in Fig. 3-11a, there are 28 peaks, so a 9th-order polynomial equation is fit to the peaks. If the polynomial fit to the positions of the peaks is not good (quantitatively, R^2 < 0.98) then the droplet is labelled as being spherical with inclusions. Such randomly dispersed amplitudes of peaks that have reasonably consistent peak spacings is a characteristic scattering pattern for a droplet containing internal inclusions. Inclusions are readily detected if the relative volume is greater than 0.04% of the droplet.

The remaining two morphologies, spherical-homogeneous and core-shell, both have a low RSD for peak separation and a good match to a polynomial fit in the peak positions. However, the goodness of quadratic fit is used to separate these morphologies, with a spherical-homogeneous droplet showing much closer fit to a quadratic function (R^2 < 0.945) than a core-shell droplet. If there are fewer than 10 peaks in the elastic light scattering, which typically corresponds to a radius of ~ 6 μm or smaller, then there are not enough features to resolve the morphology between core-shell and spherical-homogeneous, so in such situations the algorithm automatically assigns the latter as the droplet morphology. The R^2 threshold values used to identify droplets as homogeneous, core-shell or those containing inclusions were chosen by correlating the fits to the peak positions from over one million experimental phase functions for particles of known morphology.[210] In a droplet evaporation experiment, an increase in background noise or droplet movement in the trap could lead to misassignment in the droplet morphology for one phase function. Hence, the PF is recorded in the shortest possible time-interval in the experiment, which is typically ~0.01 s. The morphology assignments are averaged (mode) over several datapoints into time-bins, and this method improves the accuracy.

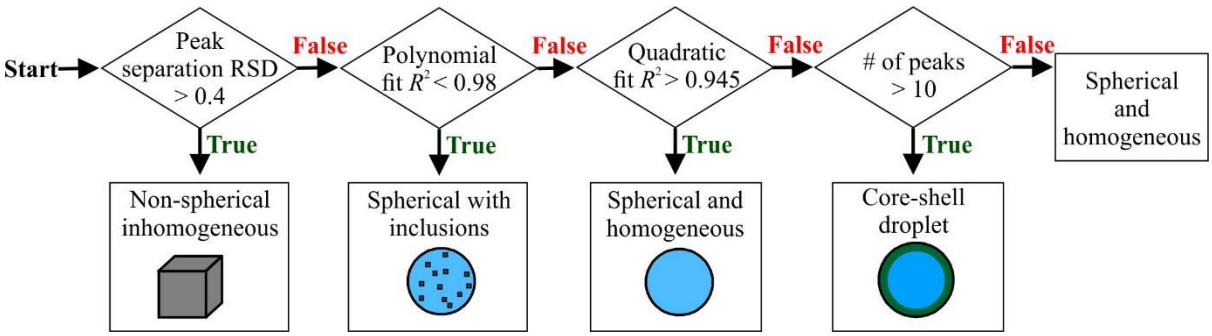

Figure 3-12: Flowchart outlining the algorithm presented in Haddrell et al.[210] that is used to identify the particle morphology from the peaks in intensity in the elastic light scattering.

3.2.6. Measurement of the Hygroscopicity of Solutes in the Electrodynamic Balance

The hygroscopicity of a compound is its ability to absorb water vapour, and for aerosol droplets this is characterised by a size and mass change in response to changes in the relative humidity. Evaporation data of aerosol droplets in the EDB can be used to determine the hygroscopicity of droplets, by using the comparative-kinetics capability of the instrument. Two droplet dispensers can be used simultaneously in an experiment, such that the evaporation kinetics of a sample droplet can be compared to those of a probe droplet with well-established drying rates.[116] This method has been validated for determining accurate hygroscopicity data for a range of inorganic compounds.[212,219] A typical hygroscopic measurement will involve evaporating a series of droplets, alternating between using the probe dispenser to produce a probe droplet and the sample dispenser immediately afterwards. Such a droplet sequence is shown in Fig 3-13, where the RH at the time of evaporation of the first sample droplet, s_1, is calculated using the kinetics of evaporation of the first probe droplet, p_1. This is described in more detail in the next section.

3.2.6.1. Determining the RH of the Gas Phase using a Probe Droplet

The evaporation of a probe droplet is compared to the Kulmala model to retrieve the environmental RH that is assigned to a sample droplet immediately afterwards.

The mass flux from a droplet of radius r is:

$$I = -2\,Sh\,\pi\,r\,(S_\infty - a_\mathrm{w}) \times \left[\frac{R\,T_\infty}{M\,\beta_\mathrm{M}\,D\,p^0(T_\infty)\,A} + \frac{a_\mathrm{w}\,L^2\,M}{K\,R\,\beta_\mathrm{T}\,{T_\infty}^2}\right]^{-1} \qquad (3\text{-}14)$$

where S_∞ is the saturation ratio of water in the gas phase, i.e. the RH, and a_w is the droplet water activity. R is the ideal gas constant, M is the molar mass of water, D is the mass diffusion coefficient of water vapour, $p^0(T_\infty)$ is the saturation vapour pressure of water at gas phase temperature T_∞. Sh is the Sherwood number, A is a correction for Stefan flow, L is the latent heat of vaporisation of water, K is the thermal conductivity of the gas phase, and β_M and β_T are the transitional correction factors for mass and heat transfer, respectively.

A simulation of the evaporation of a probe droplet is performed using Eq. 3-14, with the RH iterated until the simulation matches the experimental data (Fig. 3-13).

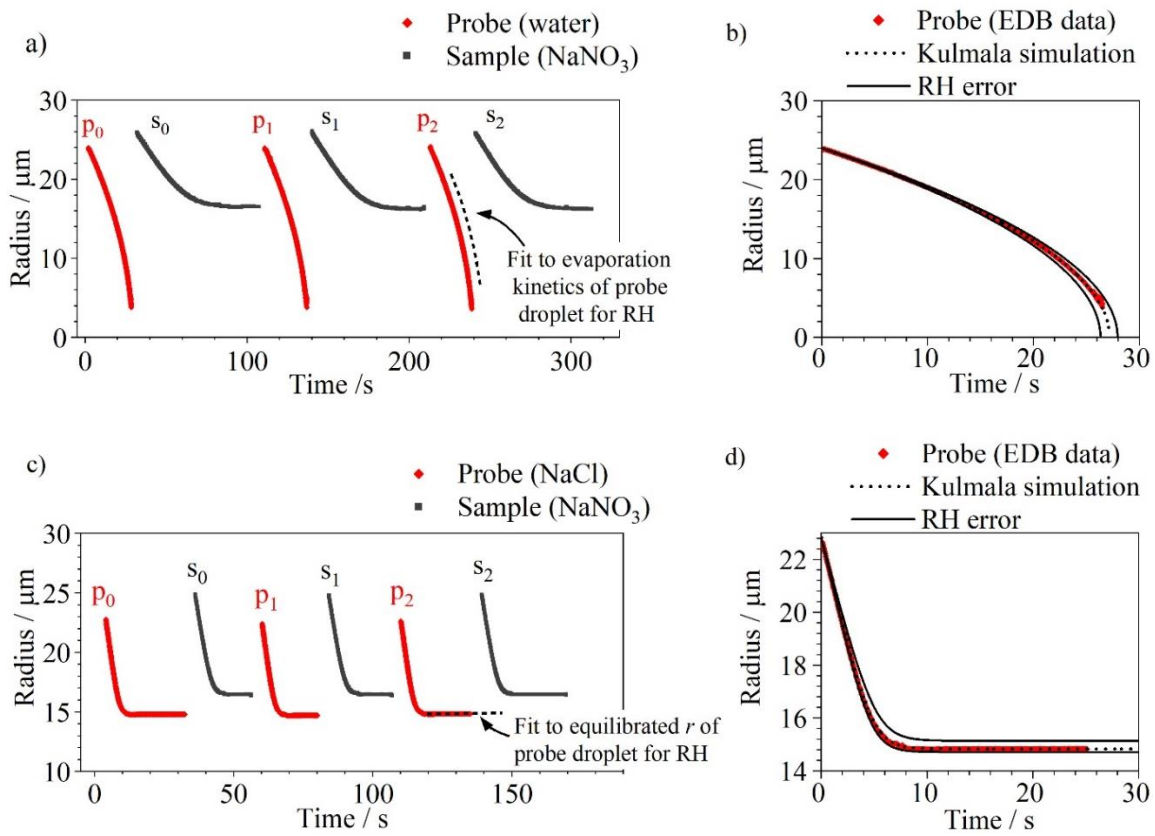

Figure 3-13: An example of the sequence of probe and sample droplets evaporated in the EDB, used to measure the hygroscopicity of $NaNO_3$. In a) The RH is 92% at 293 K, so the probe droplet consists of water, and an example of the Kulmala simulation to fit to the probe droplet evaporation data is shown in panel b) as the dotted line, with the filled line showing the ± error in the RH retrieval. In c) the RH is 68% at 293 K so an aqueous NaCl solution is used for the probe droplets, with the comparison between the Kulmala simulation and the EDB data shown in panel d).

For measurements at 293 K, the probe droplet used is pure water if the RH is above 80% RH, as shown in Fig. 3-13 panels *a* and *b* for 92% RH. Aqueous NaCl is used as a probe droplet for experiments in RHs lower than 80%, as in panels *c* and *d*. The reasons for this selection are as follows. The Kulmala model in Eq. 3-14 can accurately replicate the mass flux of droplet evaporation under quasi-isothermal conditions, i.e. slow evaporation when the droplet temperature remains relatively constant. An approximation to the temperature-dependent vapour pressure at the droplet-surface in the Kulmala model relies on the assumption that the droplet temperature remains close to the gas phase temperature, i.e. within 3 K. If aerosol droplets evaporate rapidly, the droplet temperature cools due to the latent heat loss during the conversion of water from liquid to vapour at the droplet surface.

The droplet temperature can be estimated from the mass flux:

$$T_{droplet} - T_{gas} = \frac{-I\,L}{4\,\pi\,\beta_T\,K\,r} \qquad (3\text{-}15)$$

At 293 K, the Kulmala equation of mass flux can only be used to accurately the model the evaporation of pure water above 80% RH,[220] as such conditions lead to a minimum droplet temperature of 290 K, i.e. within 3 K of 293 K. Lower RHs than 80% at 293 K lead to the water droplet cooling to a temperature that is below that which can be accurately modelled with the Kulmala equation. In this

case, rather than comparing an evaporation *rate*, the radius (r_{wet}) of an equilibrated aqueous NaCl droplet is used to estimate the RH (Fig. 3-13c). Given that the probe NaCl droplet is produced with known initial radius and concentration, the dry radius of pure NaCl in the droplet can be calculated, r_{dry}. The ratio between r_{wet} and r_{dry} is the radial growth factor:

$$GF_r = \frac{r_{wet}}{r_{dry}} \tag{3-16}$$

The GF_r of the equilibrated probe droplet can be used to determine the RH using the E-AIM model, which accurately correlates these parameters for a range of inorganic aerosol, including NaCl.[175]

The use of a water or an aqueous NaCl probe droplet to determine the RH in the EDB is a well-established method that has been validated by comparing experimental hygroscopicity data retrieved through this technique with other hygroscopic measurements.[221,222] Errors associated with determining the RH from a water probe droplet arise from the error in the radius retrieval from the geometric optics approximation of ± 100 nm, and the back extrapolation in the r^2 to determine the initial size. For an aqueous NaCl droplet, the hygroscopic growth of NaCl for varying RHs, and the density of NaCl solutions, both also contribute to the error in the RH retrieval. These quantities are taken from the E-AIM model,[175,176] and previous work in the BARC group showed very close agreement between EDB hygroscopic data and the E-AIM model. It was determined that the overriding source of error in the RH determined from an NaCl probe droplet also stemmed from the radius retrieval.[221] The upper and lower errors from determining the RH from a water probe droplet are:[116]

$$RH_w{}^{+\,\text{error}} = \left(0.169\, RH_w{}^2\right) - 0.364\, RH + 0.194 \tag{3-17}$$

$$RH_w{}^{-\,\text{error}} = -0.02\, RH + 0.21 \tag{3-18}$$

For an aqueous NaCl probe droplet the upper and lower errors in determining the RH are:[116]

$$RH_{NaCl}{}^{+\,\text{error}} = \left(-0.0199\, RH_{NaCl}{}^2\right) + 0.0130\, RH + 0.0063 \tag{3-19}$$

$$RH_{NaCl}{}^{-\,\text{error}} = \left(-0.0266\, RH_{NaCl}{}^2\right) + 0.0086\, RH + 0.0017 \tag{3-20}$$

The absolute uncertainty in estimating the RH in the EDB chamber using a probe droplet (water or aqueous NaCl) is shown in Fig. 3-14.

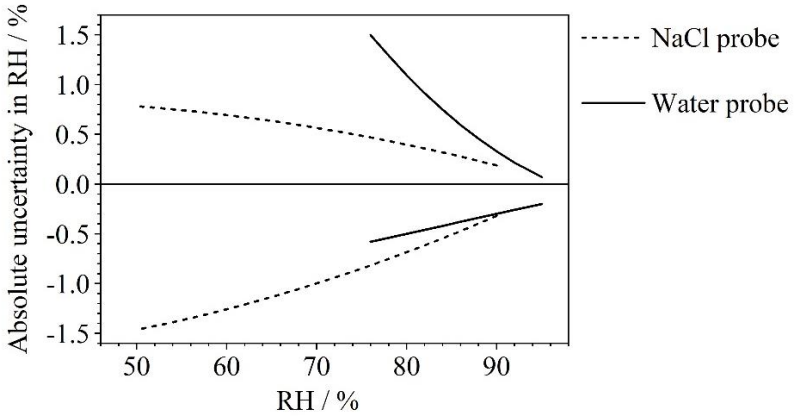

Figure 3-14: The absolute uncertainty in the estimation of the RH in the EDB chamber, using a water probe droplet (filled line) or aqueous NaCl probe droplet (dashed line), as a function of RH.

3.2.6.2. Inferring the Hygroscopic Response of a Solute

The mass fraction of solute (MFS) in a droplet for every timestep in the experiment is calculated using the method described in Section 3.2.3, where the density and mass of the droplet during evaporation is iterated through estimates based on the previous timestep. For a droplet of aqueous $NaNO_3$ with an initial MFS of 0.25, the radius during its evaporation in shown in Fig. 3-15a, and using the parameterisation for the density of aqueous $NaNO_3$, the MFS with respect to time is retrieved and shown in panel *b*.

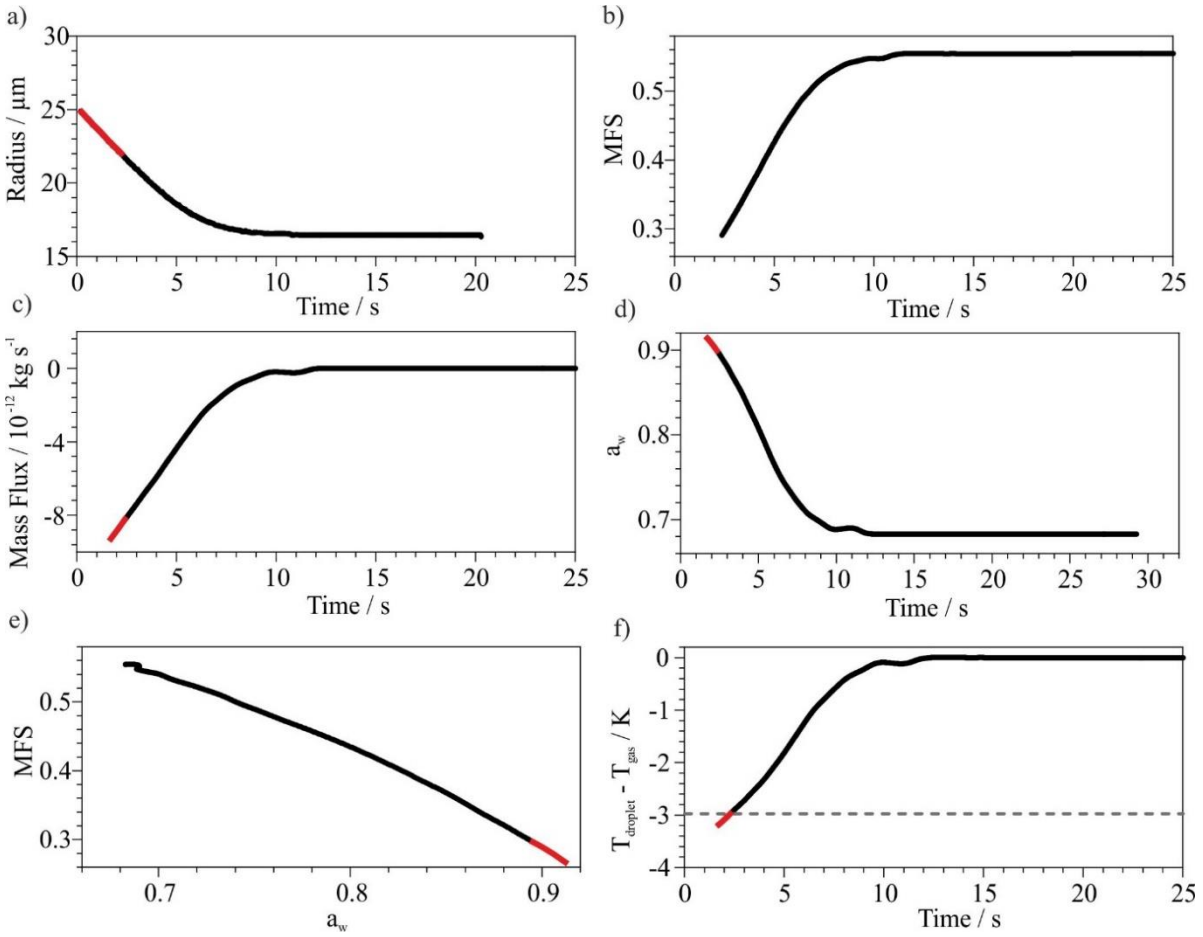

Figure 3-15: a) EDB data of an aqueous droplet of 0.25 MFS $NaNO_3$ evaporating at 68% RH and 293 K. b) The MFS throughout the evaporation process. c) The mass flux, which is used to calculate the droplet a_w in d). e) The hygroscopic response of the $NaNO_3$ droplet. f) The droplet temperature throughout evaporation, where the dashed line shows which datapoints (in red) have a ΔT greater than 3 K and will not be used in calculating the hygroscopic response of the solid.

With knowledge of the MFS throughout the experiment, the mass-flux can also be retrieved, which is shown in panel *c*. The gas-phase RH (i.e. S_∞) is determined from the drying kinetics of the probe-droplet. Equation 3-14 can be rearranged to solve for a_w:

$$a_w = S_\infty - \left[\frac{I\,R\,T_\infty}{2\,Sh\,\pi\,r\,M\,\beta_M\,D\,p^0(T_\infty)A}\right] \times \left[1 + \frac{I\,L^2\,M}{K\,R\,\beta_T\,{T_\infty}^2}\right]^{-1} \qquad (3\text{-}21)$$

Thus, if the gas phase RH is known then the mass flux of the evaporating sample-droplet can be used with Equation 3-21 to retrieve the water activity, a_w, at the droplet surface at each timestep in the experiment (Fig. 3-15d).

Once the MFS vs. time has been retrieved, as well as the a_w vs. time, the MFS vs. a_w relationship can be determined, which is the aerosol hygroscopic response. The hygroscopicity for $NaNO_3$ within the a_w range covered in Fig. 3-15 is shown in panel *e*.

The droplet temperature is estimated using Equation 3-15, and in general, for evaporating aqueous solutions, the droplet temperature shows an initial suppression compared to that of the gas phase, followed by a steady increase up to the gas phase temperature as the mass flux decreases. The temperature of the droplet in Fig. 3-15 is shown in panel *f*. As discussed in the previous section, the Kulmala model can only accurately retrieve the water activity from the mass flux if the droplet temperature remains within 3 K of the gas phase temperature. Thus, depending upon how rapidly a droplet evaporates, some datapoints are discarded and are not used to calculate the hygroscopicity of the solute. In Fig. 3-15 the datapoints that are collected when $\Delta T > 3$ K, shown by the dashed line in panel *f*, are coloured red. These points from this dataset are discarded and not used when compiling several datasets together for determining the hygroscopic response of a solute across a large a_w range.

Typically, one evaporation experiment that involves a droplet evaporating from a high a_w, i.e. a low solute concentration, into low RHs to reach low a_w conditions will lead to too rapid evaporation and substantial droplet cooling beyond the 3 K threshold of accuracy of the Kulmala model. Hence, several separate evaporation experiments are performed, going from low starting MFS at a high RH, to a high starting MFS at lower RHs. Each experiment can target a particular a_w range, and the data can be amassed to retrieve the hygroscopic response for the whole a_w curve (Fig. 3-16).

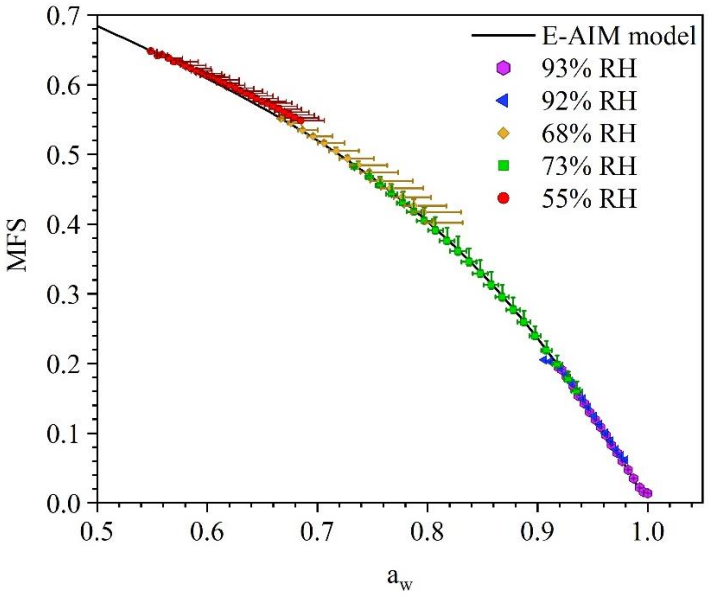

Figure 3-16: The hygroscopicity of aqueous $NaNO_3$ as measured using four separate datasets using the method shown in Fig. 3-15, at varying RHs in the EDB at 293 K. The data is compared to the E-AIM model for $NaNO_3$.[175]

3.3. The Falling Droplet Column

In typical EDB experiments only one droplet is evaporated at a time, and the system is closed with glass windows, so it is not possible to collect dried particles from this instrument. A falling droplet column (FDC) is used in conjunction with the EDB to collect sufficient sample of dried particles such that they can be imaged using a Scanning Electron Microscope. For an experiment that is performed in the EDB, the environmental conditions can be replicated on the FDC, such as drying temperature, initial droplet radius and concentration, to combine dried particle images with kinetic data from the EDB.

The FDC technique has been shown to provide insight into droplet evaporation and the particle formation process for spray-drying[148,223] and microfluidics.[224] Recently, work from Baldelli and Vehring [148,158] demonstrated that a monodisperse falling chain of droplets can be imaged with a vertically propagating laser beam and if the column is long enough, different stages in the evaporation and particle formation process can be observed at different points vertically down the column. In this study the FDC was used only for producing a monodisperse chain of droplets to collect dried particles on a coverslip.

3.3.1. The Falling Droplet Column Setup

The setup for the FDC is shown in Fig. 3-17. The FDC consists of a vertically mounted glass rectangular column, 500 mm long and 25 × 25 mm in width. There is a side opening near the top of the column through which the droplet dispenser can be inserted. Both the droplet dispenser and the method for producing droplets are identical to those in Section 3.1.1 for the EDB. However, where the dispenser for the EDB produces one single droplet to study, with the FDC the dispenser operates on continuous mode and produces a highly reproducible stream of droplets at a defined frequency (usually 10 – 100 Hz). The droplets enter the column through the opening and fall vertically through the column. As the column is made of transparent glass, the droplets can be observed for the duration of the fall. The pulse amplifier is also connected to the power switch of a vertically propagating 532 nm continuous-wave laser which illuminates the falling droplets to assist with aligning the stream down the column. The pulsing of the laser and droplet dispensing is synchronised such that the droplets can be seen stroboscopically; they appear frozen in position to the observer.

3.3.2. Controlling Environmental Conditions in the Falling Droplet Column

Inside the outer glass column there is an internal glass column, 20 mm × 20 mm in width, within which the droplets fall. A heated filament wire, approximately 1 mm thick, is wrapped around the outside of the internal column such that it spirals clockwise for the length of the column. The wire is connected to a power supply and can vary in temperature from room temperature (~ 293 K) to 393 K by increasing

the potential supplied to the wire. The temperature inside the column is recorded by two thermocouples: one hanging in free air inside the internal column at the top, just above where the droplet chain enters the column; the second is inserted in the column at the bottom near the gas outlet. Having two thermocouples enables the temperature gradient down the column to be known.

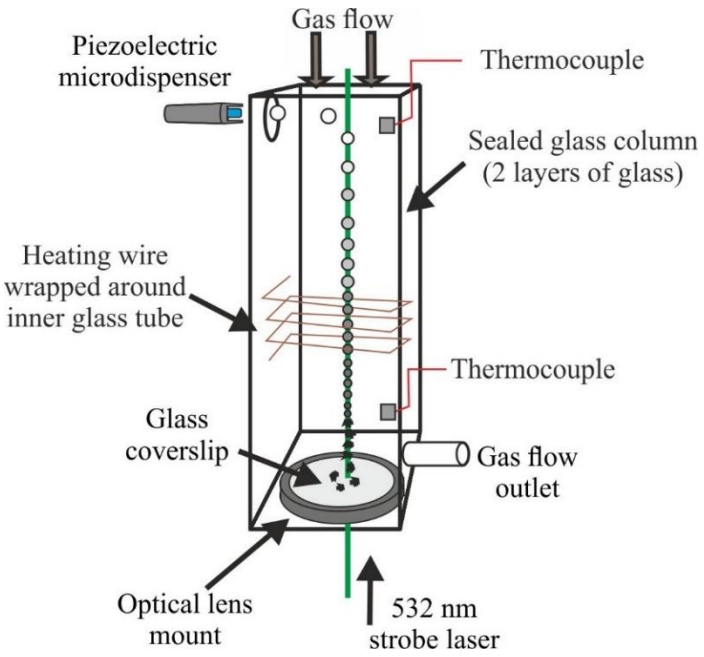

Figure 3-17: A schematic image of the setup for the falling droplet column. The heating wire is only shown for a small section of the column for clarity in the figure; it extends for the entire length of the column.

A dry N_2 gas flow is directed vertically downwards into the inner column via the top, the speed of which can be varied using a valve. Having a strong gas flow ensures that the temperature gradient in the column is evenly distributed, maintaining a 0% RH environment. However, it can cause turbulence in the column and thus disrupt the chain of droplets. Hence, a light gas flow of < 500 cm^3 min^{-1} is typically used as it does not appreciably disturb the position of droplets in the column, but it allows the two temperature probes to read the same temperature to ± 2 K.

3.4. Scanning Electron Microscopy on Dried Particles

Dried particles are collected on a glass coverslip (Chance glass, spherical 25.4 mm diameter, borosilicate) that is mounted at the bottom of the column next to the gas outlet. The collected sample and coverslip are stored inside a desiccator in the 24 hours prior to being used at the imaging facility. For imaging, first, the coverslip is attached to a metal sample holder using conductive tape, to ensure electrical conductivity between the instrument and the coverslip. Then the sample and coverslip are treated with a silver coating of ~ 15 nm using a sputter deposition process (sputter coater, Agar

Scientific**)**. A Jeol IT300 scanning electron microscope (SEM) is used to image the particles, using a 15 mm working distance, 15.0 kV acceleration voltage and magnification of 100 – 2000×.

3.5. Chapter 3: Summary

This chapter has described the setup of the instruments used to collect the experimental data presented in this thesis, and the methods behind analysing the raw data. The EDB can levitate single liquid droplets of known concentration, and by collecting the elastic light scattered from a laser by the droplet, the size and particle phase state can be determined. This chapter has discussed how this instrument can be used to measure the evaporation kinetics of liquid droplets as well as measure the hygroscopicity of solutes. In addition, the process of collecting dried particles on the FDC and perform imaging with SEM has been described.

Chapter 4

The Evaporation of Multiple Volatile Components from a Binary-Component Aerosol Droplet

Chapter 4 is based on a publication in Physical Chemistry Chemical Physics, entitled: *Studies of Competing Evaporation Rates of Multiple Volatile Components from a Single Binary-Component Aerosol Droplet*, Phys. Chem. Chem. Phys. 2019, **21,** 9709–9719, for which I am the first author,[225] and a publication in Pharmaceutical Research: *Multi-Solvent Microdroplet Evaporation : Modeling and Measurement of Spray-Drying Kinetics with Inhalable Pharmaceutics*, Pharm. Res., 2019, **36**, 100, for which I am the second author.[43] I collected, analysed and interpreted all experimental data presented in both manuscripts. I discuss a model that was developed by Mani Ordoubadi, a PhD candidate at the University of Alberta.

The evaporation of droplets containing multiple volatile liquids is a problem that is prevalent in a range of industries. For example, formulations used in industrial spray drying will typically contain a mixture of inorganic and organic components so more than one solvent may be required for a homogeneous solution prior to drying. The evaporation step in a spray-drying tower may involve liquids with varying volatilities, that would be expected to evaporate at different rates. The relative concentration of the different solvents may strongly affect the time it takes for droplets to form solid particles, and hence affect the product morphology and properties. In addition, the solution inside metered-dose inhalers for respiratory drug delivery commonly contain a propellant, such as HFA-134, along with a co-solvent, such as ethanol. Such liquids have vastly different volatilities and thus, a detailed understanding of how the different liquids evaporate upon aerosolization and in the lung is vital for drug-delivery applications to improve the dose delivery of products. Also, how multicomponent fuels evaporate during the delivery into an engine is an important area of research for the automotive industry. In this chapter I will discuss how single droplet drying can be used to study the evaporation of droplets containing two volatile liquids, here ethanol and water.

4.1. Overview of the Literature on the Evaporation of Multiple Volatile Components

The evaporation of droplets containing more than one volatile liquid has been studied in millimetre-sized droplets suspended from filaments, wherein the evaporation occurs over several minutes.[226] For the micrometre regime (droplet size range of ~ 1 – 100 µm), there have been previous studies on the evaporation rates of aerosols that contain a mixture of volatile and semi-volatile components. For example Ingram et al. studied the dehydration of aqueous sucrose droplets that contained maleic acid or malonic acid as an additional semi-volatile liquid, by observing the radius response of optically trapped droplets to step-changes in the relative humidity.[112] The evaporation processes were isothermal and occurred over some thousands of seconds as the maleic acid or malonic acid component had a much lower volatility than water; but the study highlighted the need to consider a non-homogeneous concentration profile in a drying droplet in a Maxwell-Stefan framework.[227]

There have been previous studies using the cavity-enhanced Raman scattering (CERS) technique on monodisperse falling droplet streams to measure the evaporation rates of ethanol-methanol,[228] and water-methanol systems.[229] CERS allows the measurement of both the droplet size and refractive index, giving insight into the time-evolving composition as well as the droplet temperature. In mixed component droplets of varying initial composition, the evaporation rate lies between that of the pure-component droplets, as shown in Fig. 4-1, and such studies were able to observe unsteady evaporation with temperature suppression of the droplets compared to the gas phase. Hopkins and Reid also performed such evaporation experiments with ethanol-water droplets, to study the effect of surrounding gas pressure on drying rates. A high N_2 gas flow-rate (5000 cm^3 min^{-1} compared to the 200 cm^3 min^{-1} in this work) and low gas pressures (7-77 kPa compared to 101 kPa in this work) led to rapid evaporation with total drying times on the order of milliseconds,[157] which is two orders of magnitude faster than the evaporation rates studied in this thesis. In addition, as the CERS technique probes only the near-surface composition of the droplets, the measurements were sensitive to concentration gradients that may occur in multicomponent systems during drying.

Kulmala et al. introduced a model for droplet evaporation and condensation,[182] that can account for either one or two volatile components and has been validated with numerous experimental datasets.[115,116,212,230] However, such experiments often involve slow droplet drying and can be assumed to proceed isothermally, enabling the quasi-steady-state mass and heat flux to be uncoupled in the model. Rapid evaporation of solvents with high volatility would typically be unsteady and the differential equations for the rates of mass and heat transfer must be solved simultaneously as they are strongly coupled.

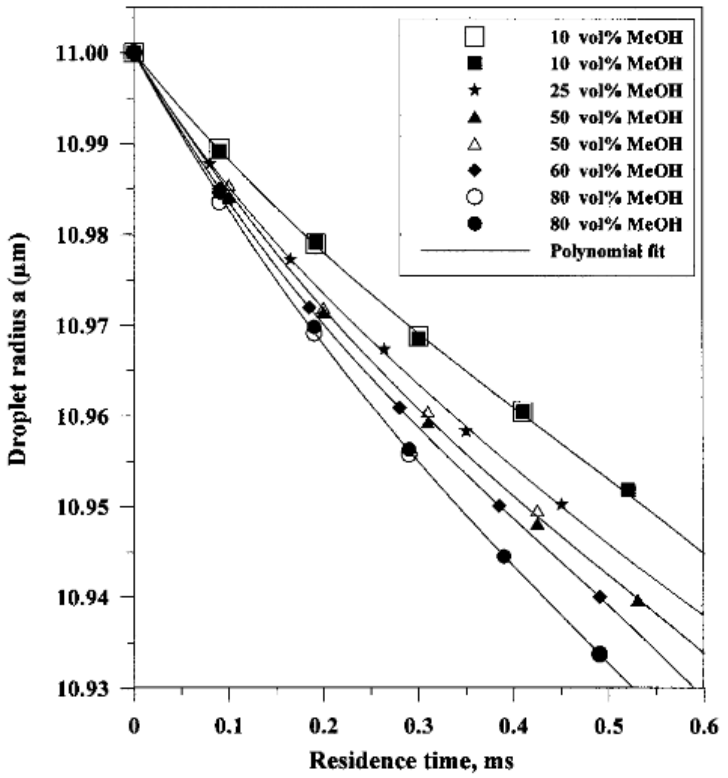

Figure 4-1: The evaporation of binary droplets containing varying ratios of ethanol and methanol, from Devarakonda and Ray.[228] Methanol has a higher volatility and the evaporation rate of the binary droplet decreases as the initial composition tends to ethanol-rich. Reprinted with permission from The Journal of Colloid and Interface Science, 221 (1), 104-113, Copyright 2000, Elsevier.

This chapter aims to build upon the concepts introduced in the previous studies on multiple volatile components, but with residence times that more closely reflect the evaporation of droplets in spray driers and in respiratory lung delivery (seconds). In addition, the evaporation of droplets containing multiple volatile components at non-zero RHs will be studied, which is important for applications where the surrounding gas phase is humid. In such situations, mass flux may occur in two directions: evaporation of one component may occur concurrently with the gas-particle condensation of another.

4.2. The Evaporation of a Pure Ethanol Droplet in Dry N_2

Before studying the complex situation of two volatile components, it is helpful to start by considering the evaporation of just pure ethanol droplets. With a higher vapour pressure than water at 293 K (5.7 kPa for ethanol [231] compared to 2.34 kPa for water [184]) it is expected that ethanol would evaporate faster that water. The evaporation of a pure ethanol droplet of starting radius 23.77 µm was recorded using the EDB (Fig. 4-2a, grey squares). The evaporation profile proceeds in a straight line when plotted in terms of $radius^2$.

The evaporation of single component droplets can be simulated using the Maxwell equation:[232]

$$I_m = 4\,\pi\,D_v\,r\,(C_a - C_\infty) \qquad (4\text{-}1)$$

where I_m is the mass flux, D_v is the mass diffusivity of the vapour component in the gas-phase, r is the droplet radius and C_i is the vapour concentration at the droplet surface (subscript a) or far from the droplet (subscript ∞). C_i, with units kg.m^{-3}, is calculated from the vapour pressure at the gas phase temperature, $p(T)$ using Clapeyron's gas law:

$$C_i = \frac{n\,M}{V} = \frac{p(T)\,M}{R\,T} \qquad (4\text{-}2)$$

where n is the number of moles of the volatile species in a volume V in the gas phase, M is the molar mass, R is the molar gas constant and T is the gas temperature.

The simulation of ethanol evaporation using the Maxwell equation is compared to the experimental data in Fig. 2a. The vapour pressure at the droplet surface is calculated using the temperature-dependent vapour pressure of ethanol assuming that the droplet temperature is equivalent to the gas phase temperature. The evaporation rate obtained from the EDB experiment, which was performed at 293 K, is not well represented by the Maxwell simulation that uses 293 K as the input temperature. The simulation shows an evaporation rate that is much larger than the experimental data. Reducing the temperature in the simulation reduces the evaporation rate, and the figure shows that the temperature in the Maxwell equation must be reduced to a temperature of 275 K to provide a good fit to the measurement of the evaporaton rate.

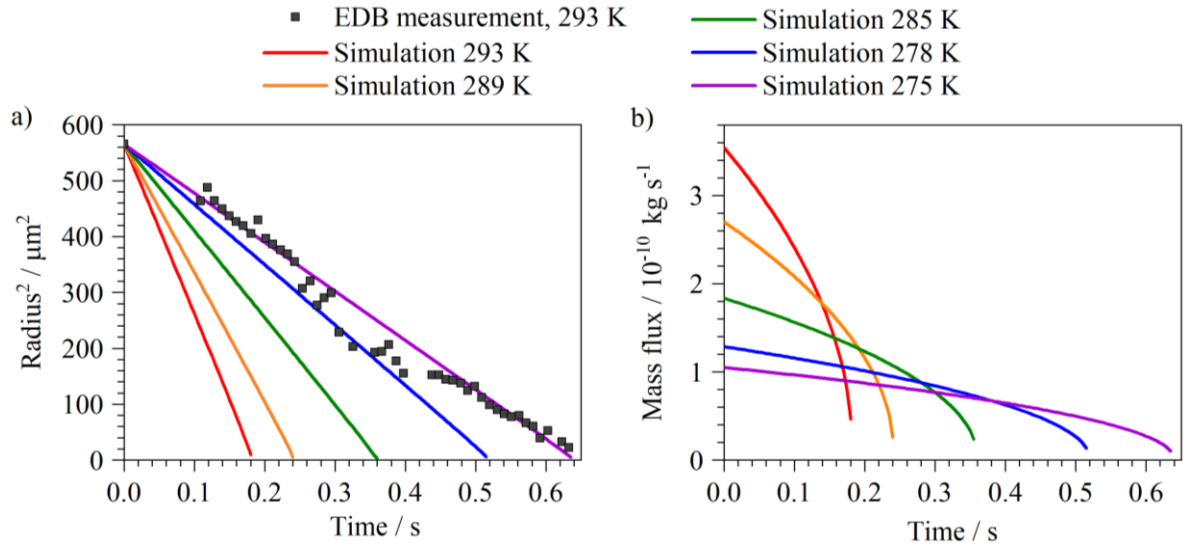

Figure 4-2: a) The evaporation of a pure ethanol droplet at 293 K in 0% RH (datapoints) compared to a Maxwell simulation from Eq. 4-1 using different temperatures, assuming that the droplet temperature is equivalent to the gas temperature. b) The mass flux from the Maxwell simulations in panel *a*.

In many spray drying models, the gas temperature may be used to calculate the vapour pressure and the drying time in a spray drying tower, and the data in Fig. 4-2a shows that this method could drastically overpredict the magnitude of the evaporation rate. The magnitude of the mass flux throughout

evaporation for each simulation in Figure 4-2 is shown in panel *b*. Where the evaporatation rate for each simulation is constant in the r^2, the mass flux decelerates throughout the evaporation process. It can be concluded that the occurrence of evaporative cooling by 18 K leads to a magnitude of mass flux that is initially only a third of that expected from the vapour pressure at the gas phase temperature.

4.3. The Evaporation of Mixed Ethanol-Water Droplets in Dry N_2

The evaporation of a droplet containing an ethanol-water mixture (with 0.7-0.3 mass fractions, respectively) in dry N_2 at 293 K is compared in Fig. 4-3 (blue diamonds) to that of a pure ethanol droplet (grey squares) and a pure water droplet (green circles) in the same conditions.

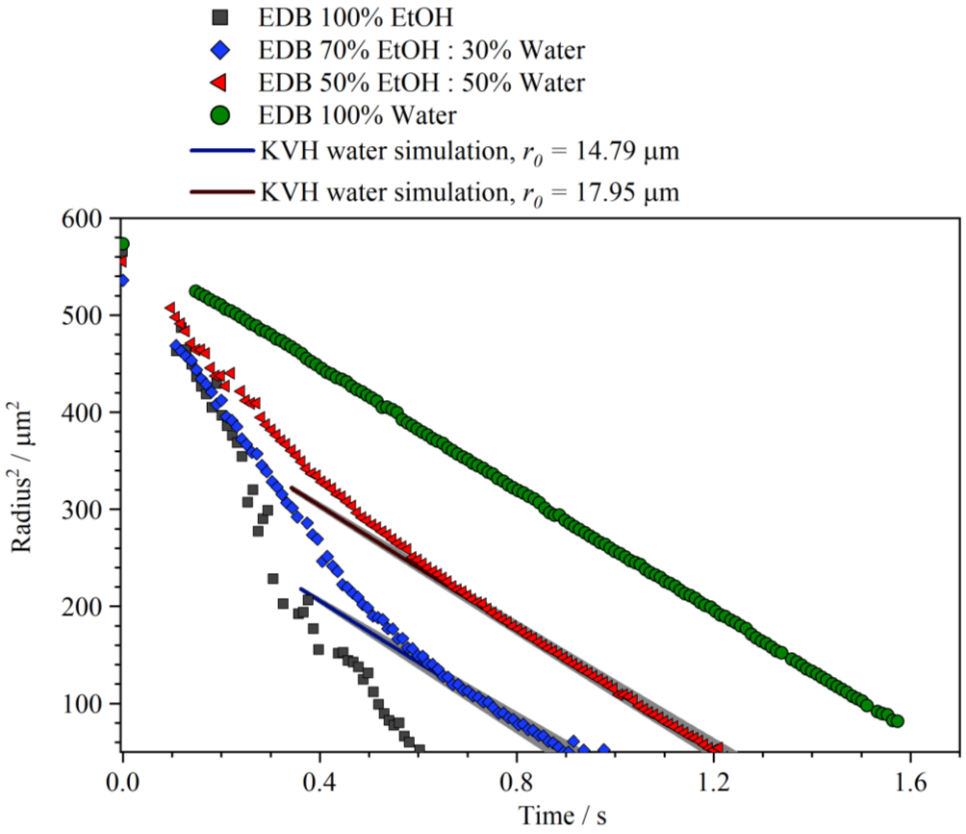

Figure 4-3: The evaporation of a droplet containing ethanol-water mixture (0.7-0.3 mass fraction, respectively) in 0% RH at 293 K (blue squares) compared to that of a 0.5-0.5 mass fraction mixture. The theoretical evaporation of a droplet of pure water of equivalent volume to that present in the droplets are shown by the blue and brown lines, respectively. The water evaporation simulation was performed using the K-V-H model.[115] Also shown are the evaporation profiles of a pure ethanol droplet (black squares) and pure water droplet (green circles), at 293 K in dry nitrogen.

When water is present in the ethanol-rich droplet there is a variable evaporation rate, with an inflexion point occurring at t ~ 0.5 s, contrasting with the constant evaporation rate of both pure-component

droplets in the same conditions. The initial evaporation rate of the mixed droplet is lower than the pure ethanol droplet, and faster than in the pure water droplet. Initially, it is likely to be preferentially ethanol evaporating, but the presence of water reduces the vapour pressure of the ethanol component in the mixture.

The reduction in partial pressure, p_i, of a component in a mixture compared to its pure component vapour pressure, p_i^0, can be described in terms of its activity, a_i:

$$p_i = a_i\, p_i^0 = \gamma_i x_i\, p_i^0 \qquad (4\text{-}3)$$

where x_i is the mole fraction and γ_i is the activity coefficient. The activities of ethanol and water in a mixture at 293 K, as calculated using the AIOMFAC model,[171] are show in Fig. 4-4, as well as the temperature dependency upon the pure-component vapour pressures.[184,231]

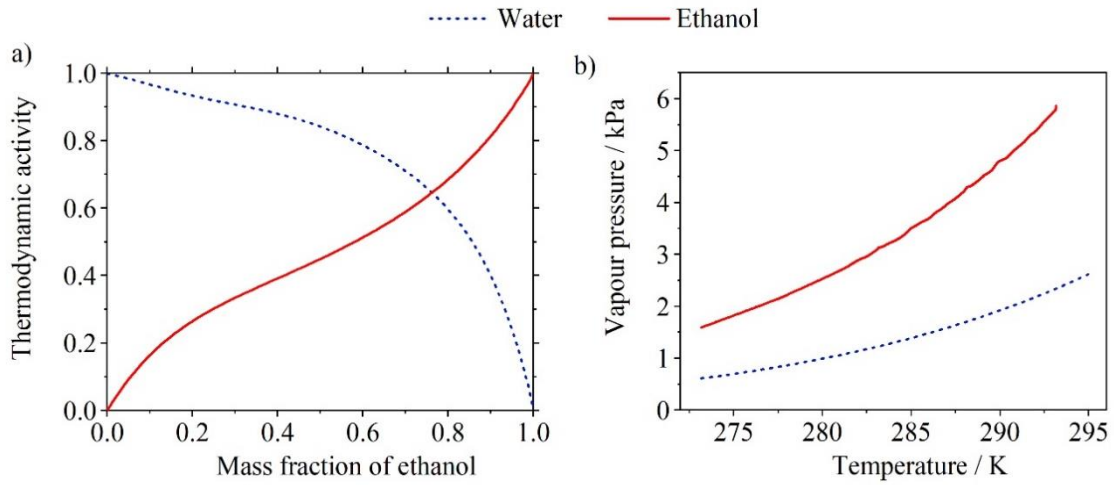

Figure 4-4: a) The thermodynamic activity (the activity coefficient multiplied by the mole fraction) for ethanol and water in a binary mixture as determined by the AIOMFAC model[170,171] at 293 K. b) the pure-component saturation vapour pressure of ethanol [231] and water [184] at varying temperatures.

In a 0.7-0.3 (mass fraction) mixture of ethanol-water, the activities are 0.59 and 0.71, respectively, which means that the vapour pressure of ethanol in the droplet initially is 3.46 kPa compared to the 5.7 kPa for pure ethanol. The water vapour pressure is reduced by the presence of the ethanol from 2.34 kPa in a pure droplet to 1.66 kPa in the mixed droplet. Thus, both components in the mixed droplet in Fig. 4-3 have a lower vapour pressure than if they were evaporating in a pure droplet, but ethanol is more volatile and evaporates faster. The evaporation rate decreases in a smooth transition over the inflexion point and then reaches a constant gradient that is very similar to the slope in the pure water droplet. This indicates that, by this point, all of the ethanol has evaporated and only pure water remains. The smooth transition in gradient suggests that there is no single period of pure ethanol evaporation

followed by pure water evaporation; rather, there is co-evaporation of both liquids in the region ~ 0.4 s to 0.7 s, with a gradual decrease in ethanol concentration until the droplet is pure water.

A simulation of a pure water droplet evaporating in 0% RH at 293 K (solid blue line) is compared to the data in Fig. 4-3. The simulated droplet has the same mass of water as that present initially in the 0.7-0.3 (mass fraction) mixed droplet. The simulation is performed using the K-V-H model presented by Su et al.,[115] which can model pure water droplets with a consideration of the evaporative cooling caused by the coupling of heat and mass transfer. This simulation line has been moved forward by 0.36 s to demonstrate the very close match in the gradient to that of the evaporation data of the mixed ethanol-water droplet. A grey error overlap is included with the simulation, which takes into account the uncertainty in the volume of water from the extrapolation of the initial droplet radius, and the experimental temperature and RH uncertainty (± 0.5 K and ± 1%, respectively).

The evaporation data from a droplet containing a 0.5-0.5 (mass fractions) ethanol-water mixture in an EDB experiment is also shown in Fig. 4-3 (red triangles). It shows the same feature as the 0.7-0.3 (mass fraction) mixture (blue diamonds) in that there are two evaporation regimes: an initially fast period followed by a smooth reduction in gradient to another constant-gradient period that closely matches the gradient of a pure-water simulation (dark-red line). The activities for the 0.5-0.5 composition are 0.45 and 0.84 for ethanol and water, making the vapour pressures 2.56 kPa and 1.97 kPa, respectively. This explains the much smoother transition in gradient over the inflexion point in the red data in Fig. 4-3; whilst ethanol is still more volatile in the 0.5-0.5 mixture, the volatilities are closer in value so there is likely to be a longer period of coevaporation in this dataset than for the 0.7-0.3 mixture.

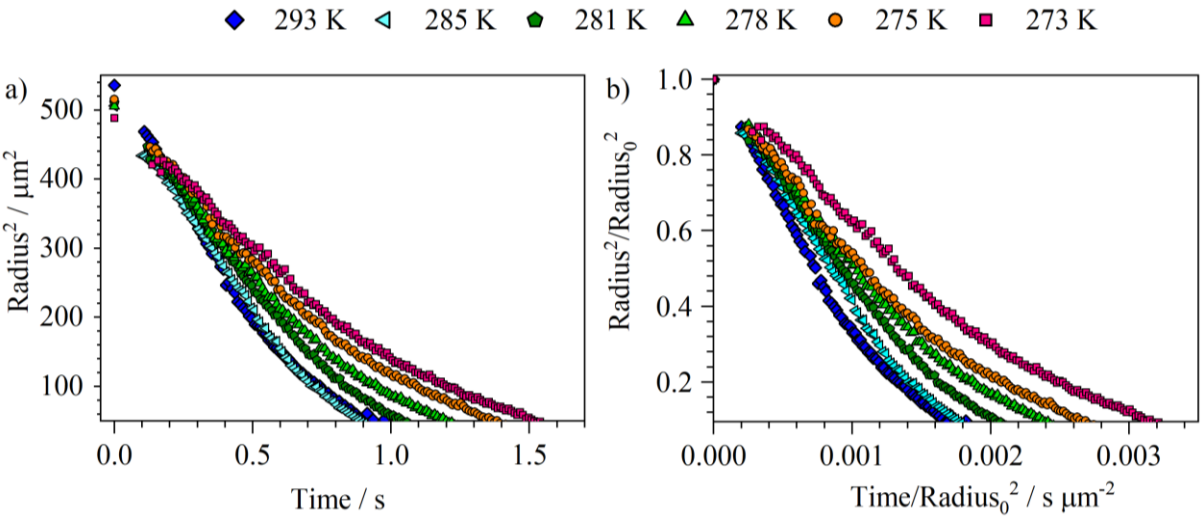

Figure 4-5: a) The evaporation profiles of droplets containing a mixture of 0.7-0.3 ethanol-water (mass fraction, respectively) in 0% RH over a range of gas phase temperatures. b) The same data as in a) but normalised with respect to the initial droplet radius.

To explore the influence of temperature upon the evaporation rate of binary-component droplets, the evaporation of a droplet containing a mixture of 0.7-0.3 (mass fractions) ethanol-water was repeated at

a range of gas phase temperatures from 293 K down to 273 K, in 0% RH. The evaporation rates are compared in Fig. 4-5a. The vapour pressures of both ethanol and water decrease as the temperature decreases. Comparing the two extreme cases in Fig. 4-5a, 293 K and 273 K, the inflexion point appears to occur over a smoother transition when the temperature is lower, and the mass flux is slower. This can be attributed to the vapour pressures of ethanol and water being closer in value at colder temperatures than at 293 K. Although it appears that the evaporation of the ethanol-water droplet was at a similar rate at 285 K to that at 293 K, this is a consequence of different initial droplet sizes. The datasets have been normalised with respect to the initial r^2 in Fig. 4-5b and thus the trend of decreasing evaporation rate with decreasing temperature is more apparent.

The data in Fig. 4-3 and 4-5 show that, even for 'simple' evaporation experiments of pure ethanol, pure water or mixed ethanol-water droplets drying in 0% RH at ambient temperatures, the evaporation kinetics can be highly complicated due to the time-evolving composition and the coupling of heat and mass transfer causing evaporative cooling. We will now move on to consider similar compositions of droplets evaporating in humid environments.

4.4. The Evaporation of Mixed Ethanol-Water Droplets in Humid N_2

The evaporation of droplets containing an ethanol-water mixture (0.5-0.5 mass fraction, respectively) at 293 K in atmospheres of varying RH are compared in Fig. 4-6a in terms of the *radius*^{2} as a function of time.

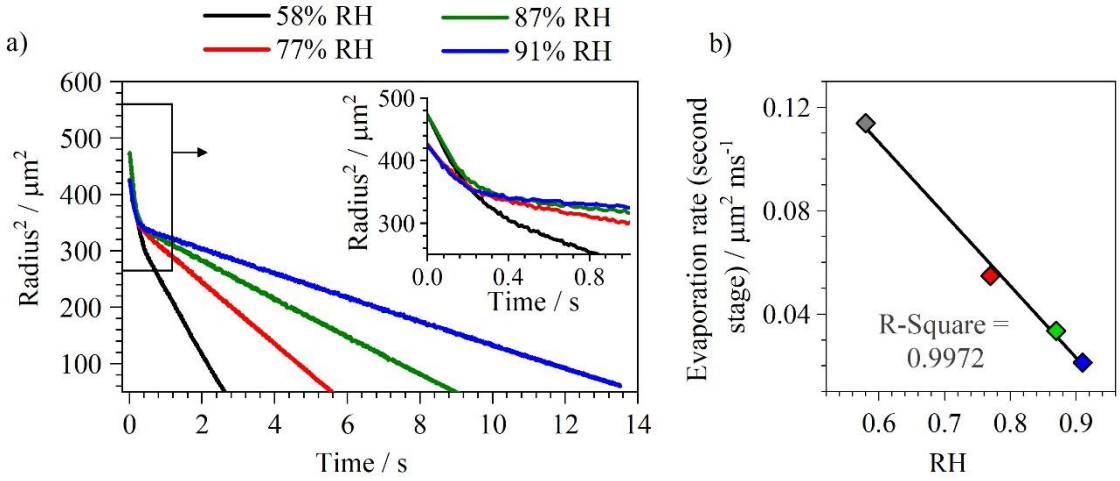

Figure 4-6: a) The time-dependent radius^2 of droplets containing an ethanol-water mixture (0.5-0.5 initial mass fractions, respectively) as they evaporate into environments of different RH at 293 K. b) The correlation between the evaporation rate of the second regime in the evaporation curve and the RH.

As for the evaporation at 0% RH, there are two distinct evaporation periods separated by an inflexion point. However, in the humid atmospheres the decrease in evaporation rate is more pronounced. Prior to the inflexion point there is a large evaporative flux, which can be assumed to be the ethanol evaporation and is largely independent of the gas phase RH. The second stage of evaporation is likely to be that of water because the gradient of this stage is strongly dependent upon the RH, typical of water droplets evaporating in varying RHs. The linear relationship between the evaporation rate of the second stage of the evaporation and the RH is shown in Fig. 4-6b.

4.4.1. Water Condensation onto Aerosol Droplets

There is an N_2 gas flow in the EDB that passes over the droplet surface at a rate of 0.03 m s^{-1}, and this leads to the general assumption that any component that evaporates from the droplet surface is carried away as the volume of gas surrounding the surface is replenished with dry N_2. Thus, the volume surrounding the droplet can be considered as infinite with no possibility of an evaporating species remaining in the droplet vapour-field and re-condensing back onto the droplet. However, in atmospheres of a non-zero RH, there is the possibility of condensation of water from the humidified gas flow onto the droplet surface. Such condensation is possible if a droplet has a lower water activity than the surrounding gas phase. A pure water droplet has a water activity of 1, so condensation from the gas-phase with a sub-saturated humidity (RH < 100%) onto the droplet will not occur. Condensation of water onto existing water droplets can occur in supersaturated conditions, a process prevalent in cloud physics. Warm air has a higher saturation point than cold air, and hence a greater capacity for holding water vapour. If a volume of saturated air reduces in temperature, water will condense from the gas-phase. This change in temperature is key to the gas-particle partitioning process.

In the mixed ethanol-water droplets in Fig. 4-6a, the ethanol evaporates rapidly, ~ 1×10^{10} kg s^{-1}, and this is sufficiently rapid to cause evaporative cooling of the droplet. Thus, the saturation vapour pressure at the droplet surface is significantly lower than the partial pressure of water in the surrounding 293 K gas, driving water vapour to condense at the droplet surface concurrently with ethanol evaporation. This condensation step is consistent with prior work that observed that a small amount of water condensed onto much larger droplets, such as ethanol sessile droplets [233] or millimetre-sized droplets held in an acoustic trap.[234] To build an understanding of the evolving droplet composition and temperature in such droplets, we model the coupling between mass and heat transfer, and the results are presented in the next section.

4.4.2. Simulating the Evaporation of Ethanol-Water Droplets with a Modified Maxwell Model

We employ a quasi-steady model, developed by Mani Ordoubadi, which is a modified form of the Maxwell equation to account for multiple components in a droplet.[43] The model considers the fact that ethanol-water systems show non-ideality in density and activity coefficients. It employs an energy-balance and mass-balance approach to superimpose the effects of changes to the droplet temperature and mass caused by water and ethanol separately, so that is can consider simultaneous evaporation and condensation of the different components.

The droplet evaporation rate, in the form of a mass flux, is calculated using the Maxwell equation (Eq. 4-1). The rate of mass diffusion of ethanol or water in the gas phase is assumed to be independent of the other, so the mass transfer rate of each component is summed to a total mass flux:

$$I_m = \sum I_{m,i} = \sum_i \; 4\,\pi\, D_{v,i}\, r\, (C_{a,i} - \; C_{\infty,i}) \qquad (4\text{-}4)$$

The vapour concentration at the droplet surface, $C_{a,i}$, can be calculated as in Eq. 4-2 but now taking into account the activity coefficient of each species, γ_i, as well as using the droplet surface-temperature, T_a:

$$C_{a,i} = x_i\, \gamma_i\, \frac{P^0{}_i(T_a)\, M_i}{R\, T_a} \qquad (4\text{-}5)$$

where x_i is the mole fraction of species i, $P^0{}_i$ is the pure-component saturation vapour pressure and M_i is the molar mass. The droplet temperature, T_a, is calculated from:

$$\rho\, C_p\, \frac{r^2}{3}\, \frac{\mathrm{d}\, T_a}{\mathrm{d}\, t} = \; -K\, (T_a - \; T_\infty) - \sum L_i D_i (C_{a,i} - \; C_{\infty,i}) \qquad (4\text{-}6)$$

where ρ is the droplet density, C_p is the specific heat capacity of the droplet, K is the thermal conductivity of the gas phase at the intermediate temperature surrounding the droplet (T_∞), L_i is the latent heat of vaporisation of substance i, and D_i is the mass-diffusivity of component i in the gas phase. Temperature-dependent values for the latent heat of vaporisation for pure water [235] and ethanol [236] and for the gas phase mass diffusivity values of both solvents [237,238] are used independently, with the effects summed to solve the droplet's energy equation, whereas values for the density,[239] specific heat capacity [240] and thermal conductivity [240] are determined from temperature-dependent correlations for the ethanol mixture as a whole. The temperature-dependent parameterisations used in the models presented in this chapter are reported at the end of this section in Table 4-2.

The experimental data of droplets of ethanol-water mixtures evaporating into varying RHs at 293 K are compared in Fig. 4-7 to the simulation using the modified Maxwell model. The shaded area represents the effect on the model from various experimental uncertainties, such as those in the gas phase temperature (± 0.5 K), the retrieval of the RH (~ ± 1%) and in determining the initial droplet radius from extrapolating the experimental datapoints back to t = 0 s. The model is consistent with the experimental data in that there are two clear regions of evaporation processes for the initial evaporation of ethanol followed by the slower loss of water, with the data and the model agreeing on the time that

the inflexion point occurs when there is a reversal in the direction of the water mass flux. Whilst the model shows reasonably good agreement to the EDB data in Fig. 4-7a (58% RH), 4-7c (87% RH) and 4-7e (71% RH), there is a disparity between the model results and the experimental data for Fig. 4-7b (77% RH) and 4-7d (91% RH). The reasons behind such discrepancy between the model and the data will be discussed in a later section.

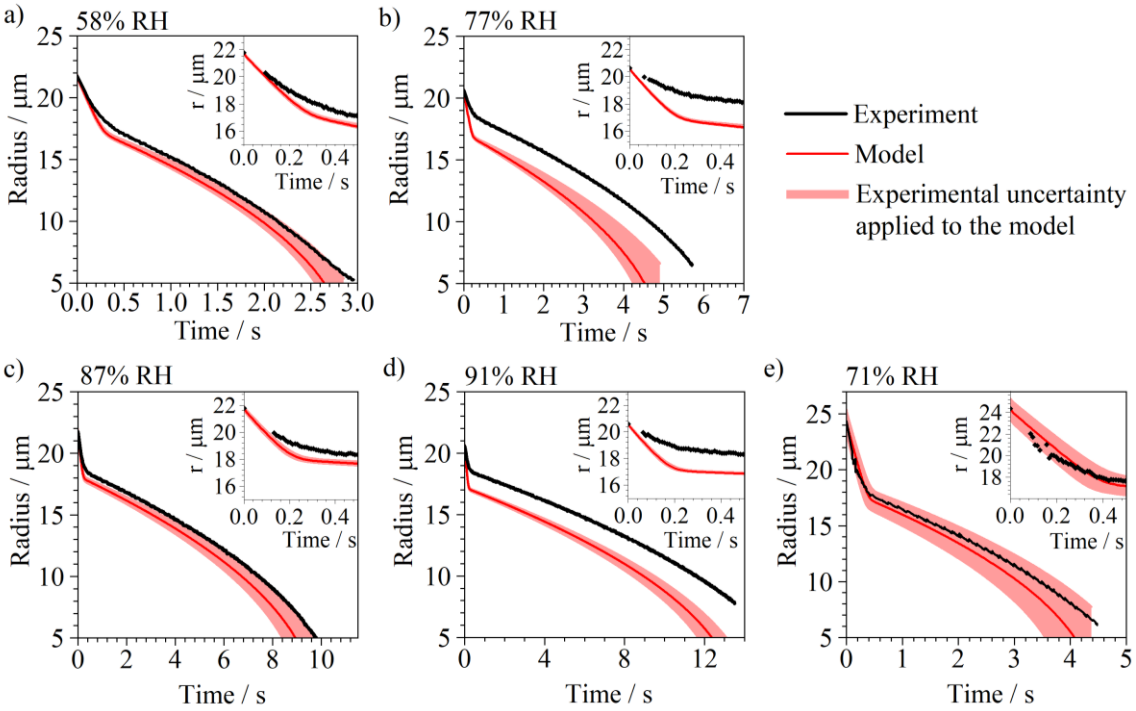

Figure 4-7: The evaporation of ethanol-water droplets (0.5 mass fraction each) in the EDB compared to the modified Maxwell model at 293 K with a gas-phase RH of a) 58%; b) 77%; c) 87% and d) 91 %. e) The evaporation of an ethanol-water droplet (0.7-0.3 mass fraction, respectively) at 293 K at a gas-phase RH of 71%. The shading refers to the effect on the model of the uncertainty in the experimental conditions, such as RH, temperature and initial droplet radius.

The model can provide insight into the time-dependent composition and the temperature of the evaporating ethanol-water droplets, and these results are compared for the varying RHs in Fig. 4-8 panels *a* and *b*, respectively.

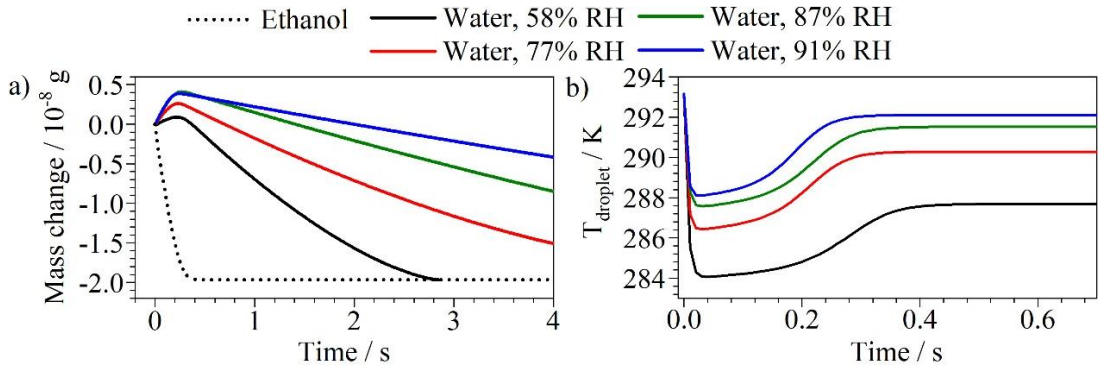

Figure 4-8: a) Model results of the time-dependent composition of mixed ethanol-water (0.5 mass fraction each) droplets shown in Figure 4-7. b) Model results of the droplet temperature within the first 0.7 s of evaporation.

The composition during the first 4 s of the droplet lifetime confirms the theory that, during the initial period of evaporation, ethanol evaporation occurs concurrently with water condensation onto the droplet from the gas phase. The data are reported in terms of an absolute mass change of the two components. Only one dataset for the ethanol mass loss is plotted for clarity (that for 58% RH dataset). However, all four datasets show the same trend of all the ethanol mass loss occurring within the first 0.3 s. The rapid loss of ethanol over this period causes a significant amount of evaporative cooling to drive water condensation from the gas phase vapour onto the droplet. Fig. 4-8a shows that an increase in RH leads to an increase in the mass of water that condenses onto the droplet. This suggests that the condensation step, like evaporation in these ambient conditions, is gas-diffusion limited rather than being limited by the rate of diffusion in the droplet bulk. The greater the RH surrounding the droplet, the greater the degree of water vapour supersaturation at the cooled droplet surface (estimated in Table 4-1).

Table 4-1: A comparison between the estimated degree of supersaturation of water in the gas phase at a cooled droplet surface during evaporation of an ethanol-water (0.5-0.5 initial mass fractions) in varying RHs. The partial pressure of water in the gas phase ($p_w(T_\infty)$) at 293 K is shown as well at the water vapour pressure at the droplet surface $p^0_{w,a}(T_\infty)$).

RH_∞ / %	$p_w(T_\infty)$ / kPa	T_a	$p^0_{w,a}(T_\infty)$ / kPa	Supersaturation
91	2.13	288.1	1.70	1.25
87	2.04	287.6	1.64	1.24
77	1.80	286.4	1.53	1.18
58	1.36	284.0	1.30	1.04

During evaporation of an ethanol-water mixed droplet, the time at which a reversal in the direction of the water mass flux is observed corresponds to the time at which all the ethanol has evaporated (~ 0.4 s in Fig. 4-8a). Indeed, in Fig. 4-8b, this time corresponds to the time at which the droplet temperature levels off at a wet-bulb temperature. The droplet temperature immediately decreases in the first ~ 0.03 s to a temperature minimum, followed by a steady increase over the next 0.3 s. The rise in temperature is a consequence of both the latent heat deposited into the droplet by the condensing water molecules and the thermal conduction from the gas phase to the droplet.

Table 4-2: The temperature (*T*) dependency on some thermodynamic parameters used in the Maxwell models performed in Fig. 4-2 and in Fig. 4-7.

Thermodynamic Parameter	Symbol	Equation to Calculate Parameter	Ref.
Diffusivity of water vapour through N_2 gas at temperature T / K	D_{water,N_2} / m s^{-1}	$= 2.190 \times 10^{-5} \times \left(\frac{T}{273.15}\right)^{1.81}$	241
Diffusivity of ethanol vapour through N_2 gas at temperature T / K	$D_{EtOH,\ N_2}$ / m s^{-1}	$= 1.180 \times 10^{-5} \times \left(\frac{T}{300.15}\right)^{1.75}$	242,243
Density of ethanol-water mixture for varying mole fractions of ethanol x_e or water x_w at varying T	$\rho_{m,T}$	$= x_w.\ln\rho_{w,T} + x_e.\ln\rho_{e,T} - 30.808\left(\frac{x_w.x_e}{T}\right) - 18.274\left(\frac{x_w.x_e.(x_w - x_e)}{T}\right) + 13.890\left(\frac{x_w.x_e.(x_w - x_e)^2}{T}\right)$	239
Thermal conductivity of dry N_2 / W K^{-1} m^{-1}	$K_{N_2,dry}$	$= 3.9827 \times 10^{-3} + 7.3167 \times 10^{-5}.T$	244
Thermal conductivity of water vapour / W K^{-1} m^{-1}	$K_{H_2O,g}$	$= 0.01695 - 5.1478 \times 10^{-5}.T + 1.89622 \times 10^{-7}.T^2$	245
Thermal conductivity of humidified N_2 for varying partial pressures p of N_2 and water vapour / W K^{-1} m^{-1}	K_{humid}	$= \frac{K_{H_2O}}{1 + 0.556\ \frac{p_{H_2O}}{p_{N_2}}} + \frac{K_{N_2}}{1 + 1.189\ \frac{p_{H_2O}}{p_{N_2}}}$	246

4.5. The Evaporation of Pure Ethanol Droplets in a Humid Atmosphere

The process of water condensation occurring concurrently with ethanol evaporation in humid vapour is even more prevalent in cases of pure ethanol droplets that contain no water initially. With pure ethanol, the activity coefficient is 1 meaning that the vapour pressure is larger than if water were present, so the initial evaporation rate is faster. The evaporation of a pure ethanol droplet in 91% RH at 293 K is compared to that in 0% RH in Fig. 4-9a. In humid N_2, the initial evaporation rate appears to be equivalent to that in dry N_2, but after ~ 0.4 s there is an inflexion point, similar to that observed in the mixed ethanol-water droplets, after which the evaporation rate slows significantly. The inflexion point is a result of the water condensation from the humid gas phase, arising from the evaporative cooling of

the droplet. Despite being initially an ethanol droplet, the ethanol evaporates and water condenses, so after ~ 0.4 s the composition is totally changed to pure water. Following this transformation, the water droplet begins to evaporate when the vapour pressure of the water inside the droplet becomes greater than the partial pressure in the surrounding atmosphere.

The observation of a complete transformation in droplet composition is supported by the modified Maxwell model that is also shown in Fig. 4-9a (red line). Again, there is a discrepancy between the absolute value of the radius at the point of inflexion. However, qualitatively this model confirms the experimental result; water condensation occurs in the initial period of ethanol evaporation. The model results of the mass flux of the droplet at 91% RH compared to the mass flux of the pure ethanol droplet in 0% RH is shown in Fig. 9b, with the inset showing the initial evaporation period in greater detail. The pure ethanol droplet in 0% RH sustains a large mass flux on the order of ~ 1×10^{-10} kg s^{-1} for the majority of the evaporation process and only reduces in magnitude in the very final ~ 0.05 s of the droplet lifetime. Conversely, in humid vapour, the pure ethanol droplet has a mass flux that decreases almost immediately due to the condensation of water onto the droplet. By the time the inflexion point occurs, the mass flux has reduced by two orders of magnitude to reach a relatively steady value at 2.2×10^{-10} kg s^{-1}.

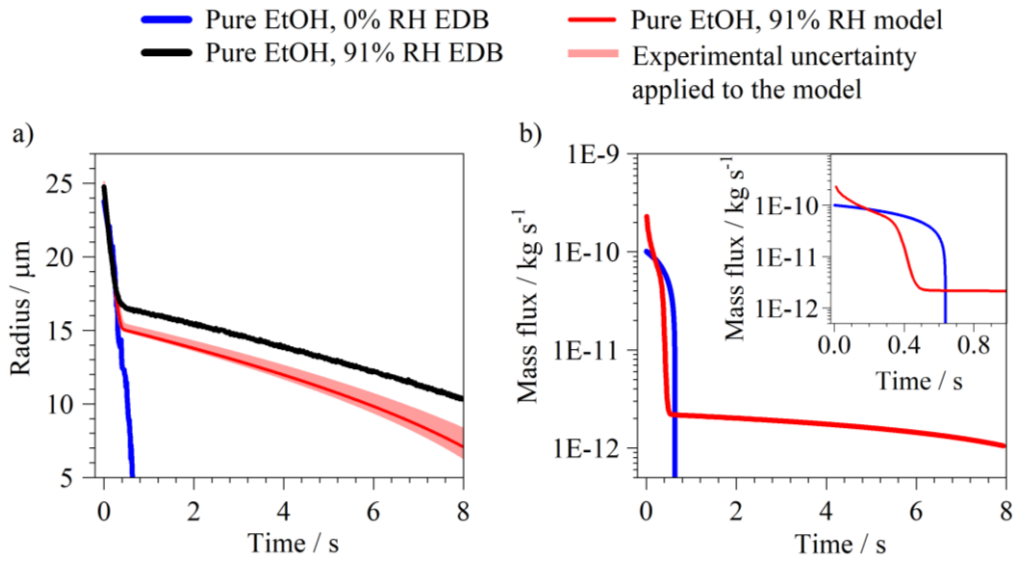

Figure 4-9: a) The evaporation of a pure ethanol droplet in 0% RH (blue) in the EDB compared to in 91% RH gas-phase (black), and model results of the 91% RH dataset (red). b) The simulated mass flux of a pure ethanol droplet as it evaporates in 0% RH (blue) or 91% RH (red) at 293 K.

The droplet temperature and time-dependent composition for the pure ethanol droplet evaporating in 91% RH, as predicted by the numerical model, are displayed in Fig. 4-10. Whilst ethanol initially evaporates, the droplet temperature is suppressed to several degrees below the ambient temperature, driving water condensation onto the droplet from the surrounding vapour. The minimum in temperature reached by the droplet is 287.8 K, which is 5.3 K lower the ambient conditions. The saturation vapour

pressure at such a temperature is 287.8 K is 1.67 kPa,[184] so the surrounding ambient atmosphere with 91% RH and a partial pressure of 2.13 kPa has a degree of supersaturation of 1.28 with respect to the droplet surface. This temperature suppression of 5.3 K is not as low as the wet-bulb temperature of pure ethanol evaporating at 293 K, which is ~ 18 K colder, due to the latent heat deposited back onto the droplet surface caused by the water condensation.

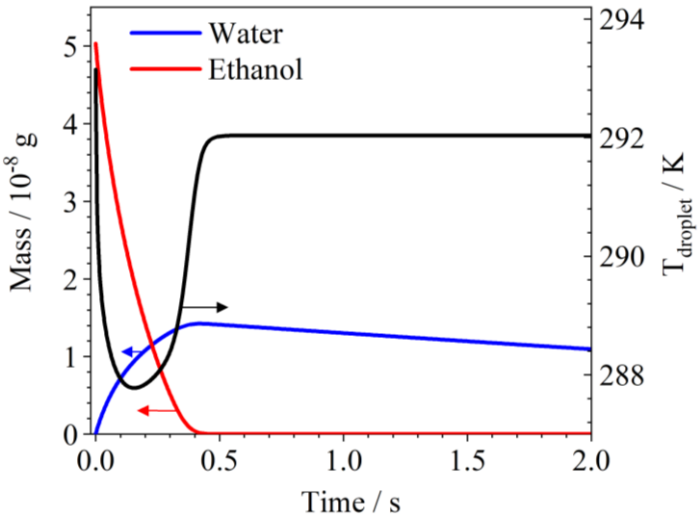

Figure 4-10: The mass of water (blue) and ethanol (red) in a pure ethanol droplet as it evaporates in 91% RH at 293 K, as predicted by the modified Maxwell model. The droplet temperature in the first 2 s is shown in black.

The minimum temperature reached for the pure ethanol droplet in 91% RH is very close to that reached for the mixed ethanol-water droplet (0.5 mass fraction each) when evaporating into the same RH in Fig. 4-8b. The two cases are compared in Fig. 4-11a and b, showing the minimum droplet temperature reached during drying and the mass of water uptake. The amount of water that can condense onto a droplet during evaporation is indeed dependent upon the minimum droplet temperature, but here we see that it also depends upon the initial droplet composition. Whilst the pure ethanol droplet and the mixed ethanol-water droplet reach the same temperature minima, the pure ethanol droplet takes up over three times as much mass of water (1.42×10^{-12} kg compared to 0.39×10^{-12} kg, respectively). The rate of evaporation of ethanol for both is similar, because there is zero partial pressure of ethanol in the gas phase. However, when the initial droplet is pure ethanol, the greater mass of ethanol to be lost from the droplet means that there is a longer timeframe at which the droplet temperature is cooled below the wet-bulb temperature. In addition, there is a value of zero water-activity inside the pure ethanol droplet, so the magnitude of the difference in $C_{a,w}$ and $C_{\infty,w}$ in the Maxwell equation (Eq. 4-1) is larger for the pure ethanol droplet case and thus gives a greater value of water mass flux. Combining this with the lengthened timescale of droplet temperature suppression means that more water condenses onto the pure ethanol droplet than the 0.5-0.5 mixture at the same RH.

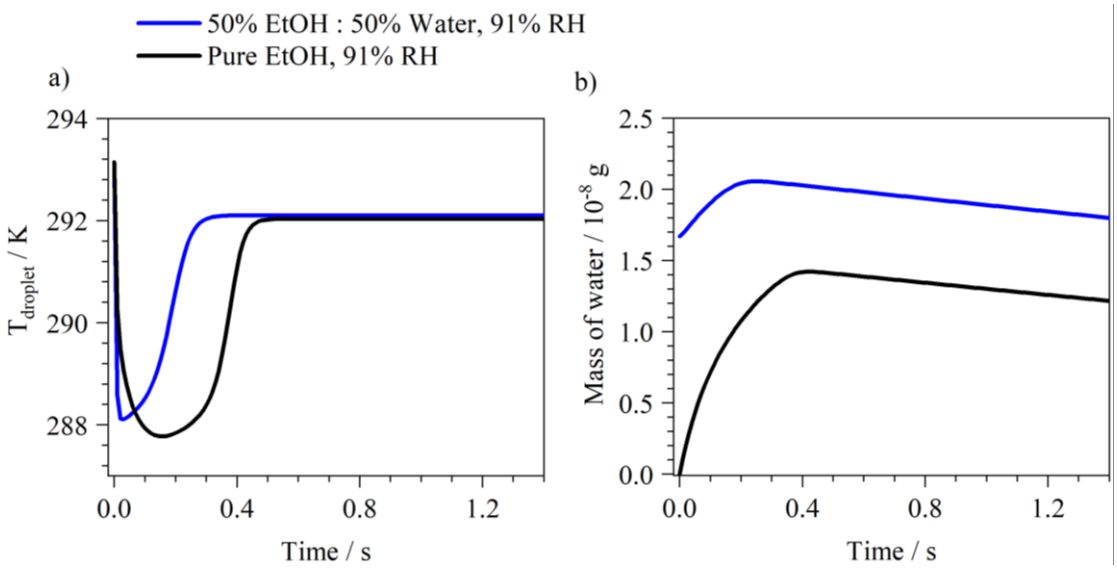

Figure 4-11: a) Comparison between the droplet temperature of a pure ethanol droplet and a mixed ethanol-water droplet (0.5 mass fraction each), both evaporating at 91% RH at 293 K, as predicted by the modified Maxwell model. b) The mass of water predicted to condense onto the droplets during ethanol evaporation.

4.5.1. Simulating the Evaporation of Ethanol-Water Droplets with the Kulmala Model

Kulmala et al. developed a model to describe the evaporation or condensation of droplets containing two volatile components.[182] The semi-analytical approach assumes quasi-steady-state coupling between the heat and mass flux between a droplet and the gas phase, assuming that the droplets are uniform across the radial coordinate in terms of both temperature and composition. As discussed in Chapter 2, the Kulmala model approximates the exponential form of the Clausius-Clapeyron equation for the temperature-dependent vapour pressure of a solvent at the droplet surface as the first term in a Taylor expansion. This allows the diffusive transport equation to become first-order with respect to mass flux and to be solved. The mass flux, I_m, from an evaporating droplet of radius r that contains two components (subscript *1* and *2*) is

$$I_m = \frac{-4\,\pi\,r}{R\,T_\infty} \times \frac{M_1 D_1 P_1^0(T_\infty)\left(S_{\infty,1} - S_{a,1}\right) + M_2 D_2 P_2^0(T_\infty)\left(S_{\infty,2} - S_{a,2}\right)}{1 + \left[\left(\frac{x_1 L_1 + x_2 L_2}{K\,R^2\,T_\infty{}^2}\right) \times \left(L_1 {M_1}^2 D_1\, P_1^0(T_\infty) S_{a,1} + L_2 {M_2}^2 D_2\, P_2^0(T_\infty)\, S_{a,2}\right)\right]} \qquad (4\text{-}7)$$

where M_i, L_i and D_i are the molar mass, specific latent heat of vaporisation and gas-phase diffusivity of species *i*, respectively. $P_i^0(T_\infty)$ is the temperature-dependent saturation vapour pressure of species *i* and *S* is the saturation ratio of species *i* in the gas phase at the droplet surface or far from the droplet (subscript *a* or ∞, respectively).

The exponential-Taylor series approximation used to formulate Eq. 4-7 only holds as long as the droplet temperature does not deviate significantly from the gas phase temperature, i.e. isothermal evaporation with a $|T_{droplet} - T_{gas}| < 3$ K. Using Eq. 4-7, the evaporation of a pure ethanol droplet in 91% RH at 293

K was simulated using Matlab, and the results are compared to the modified Maxwell simulation and the experimental data in Fig. 4-12a. The droplet temperature as predicted by both models is shown in Fig. 4-12b. Whilst the binary Kulmala model shows a reasonably close agreement to the experimental data in terms of the rate of initial ethanol evaporation, it has an inflexion point occurring too early and at too high a radius. The droplet temperature suppression is over predicted, showing that the Kulmala model cannot account for the high mass flux of ethanol. The very low temperature of the droplet leads the model to simulate too great a mass of water condensation onto the droplet surface. However, once water condensation has occurred, the droplet returns to a wet bulb temperature that is within 3 K of the gas phase, and hence, the model can accurately simulate the water mass flux from the droplet after t = 0.4 s.

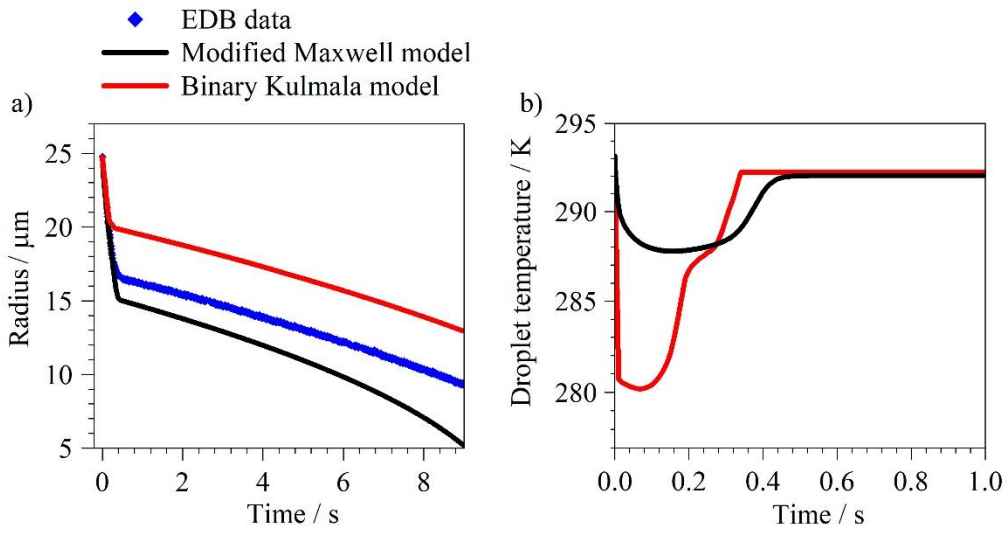

Figure 4-12: a) The blue datapoints show the evaporation of a pure ethanol droplet at 293 K and 91% RH, i.e. the data in Fig. 4-9a, compared to the numerical modified Maxwell model (black line) and a Kulmala model simulation (red line). b) The droplet temperature in the first 1.0 s of the droplet's lifetime as predicted by the modified Maxwell model and Kulmala model.

4.5.2. Comparison to Previous Literature Data on the Evaporation of Alcohols in a Humid Atmosphere

The concept of water vapour condensing onto a cooled droplet surface during the vaporisation of a different volatile liquid has been observed previously in large droplets, millimetres in size. Law et al.[226] suspended pure methanol or ethanol droplets from a filament and observed a significant deviation from a linear evaporation rate (dr^2/dt) when the drying occurred in humid air instead of in dry air. Their results are reproduced in Fig. 4-13. Similar to the work in this thesis in Fig. 4-9a, the deviation from the r^2-law is attributed to the condensation of water vapour from the surrounding gas phase onto the droplet surface. Although the evaporation of the alcohol droplet occurred over several minutes, the droplet

temperature, measured by a thermocouple attached to the droplet, dropped to a minimum of ~ 15 K below the gas temperature. The authors concluded that the water condensation in humid environments enhanced the alcohol evaporation rate above that in 0% RH; the 'condensation heat' that was released to the droplet by the water vapour warmed the droplet and thus raised the vapour pressure of methanol. We do not believe this to be a valid conclusion from the measurement. The increased gradient in the first minute of evaporation in 100% RH compared to 0% RH is very slight (Fig. 4-13). The droplets were suspended, so there would be significant uncertainty in the measurement of the droplet diameter due to a distortion from a spherical shape caused by the filament, and thus we do not believe that this increase is resolvable from the measurement uncertainty.

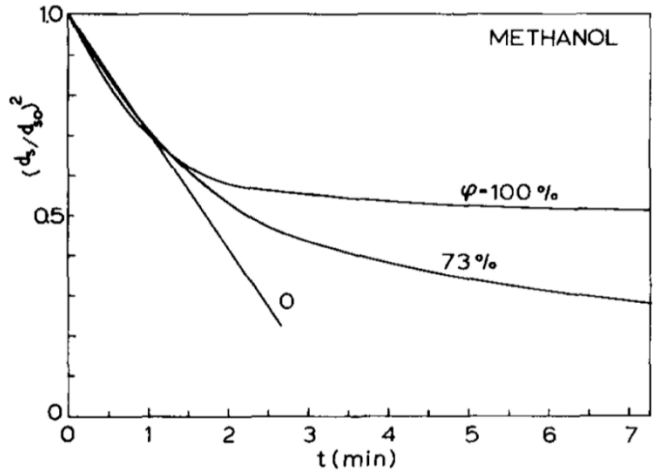

Figure 4-13: The evaporation of pure methanol droplets with initial volume of 1.6 mm at 293 K at varying relative humidities, as reported by Law et al. [226] **Reprinted (adapted) with permission from The Journal of Heat and Mass Transfer, 30 (7), 1435-1443. Copyright 1987, Elsevier.**

The large degree of water condensation onto ethanol droplets in high RH conditions has broad implications, particularly in the field of inhalable pharmaceutics. The formulations used in metered dose inhalers typically contain ethanol as well as highly volatile liquids for propellants. Such liquids have very large evaporation rates, enabling rapid aerosolization of droplets containing the drug. An example of a commonly used propellant is HFA-134a, which is a hydrofluorocarbon with the IUPAC name 1,1,1,2-Tetrafluoroethane that has boiling point at atmospheric pressure of -25.5 °C and so is stored as a liquid under elevated pressure.[247] HFA-134a has been prevalently used in the pharmaceutical industry, since the use of chlorfluorocarbons (CFCs) in metered-dose inhalers was phased-out from the 1990s due to environmental concerns.[248] The temperature-dependent vapour pressure of HFA-134a is compared to that of ethanol and water in. Fig. 4-14. At 293 K the vapour pressure is 598 kPa, more than 100 times larger than ethanol.

The latent heat of vaporisation of HFA-134a is 182 kJ kg^{-1} at 293 K, a fifth of the value of latent heat of ethanol at the same temperature (930 kJ kg^{-1}).[249] However, with such a large vapour pressure of HFA-

134a, metered-dose inhaler formulations would be expected to cause a very large degree of evaporative cooling. Given that the RH inside human lungs typically reaches values around 99.5% [250], such a cooled droplet entering the lung would certainly undergo water condensation from the lung water vapour onto the inhaler droplets. Hence, the composition of such a droplet could completely change in a matter of only a few hundred milliseconds.

A key property for the pharmacokinetics of drug delivery via the inhalation route is the dissolution rate, i.e. how rapidly an aerosolised drug will become dissolved in the aqueous lung fluid. Numerous studies investigate the drying rate of ethanol-drug droplets,[251–254] but the results presented in this chapter suggest that there is a very low chance of ethanol-drug droplets being present in the lung without water, as the rapid mass flux of propellant would cause mass condensation of water onto the droplet surface. In fact, the evaporation rates and pharmacokinetics of formulations containing water and the drug compounds are more relevant for the application. Many inhaled corticosteroids, such as beclometasone dipropionate (BDP) and budesonide (BUD) that are typically used to treat asthma or Chronic Obstructive Pulmonary Disease are highly insoluble in water.[255] Hence, the condensation of water onto such an inhaled droplet would probably not lead to dissolution of the drug. The droplet would be more likely to undergo phase-separation or solute precipitation following propellant-loss and water condensation.

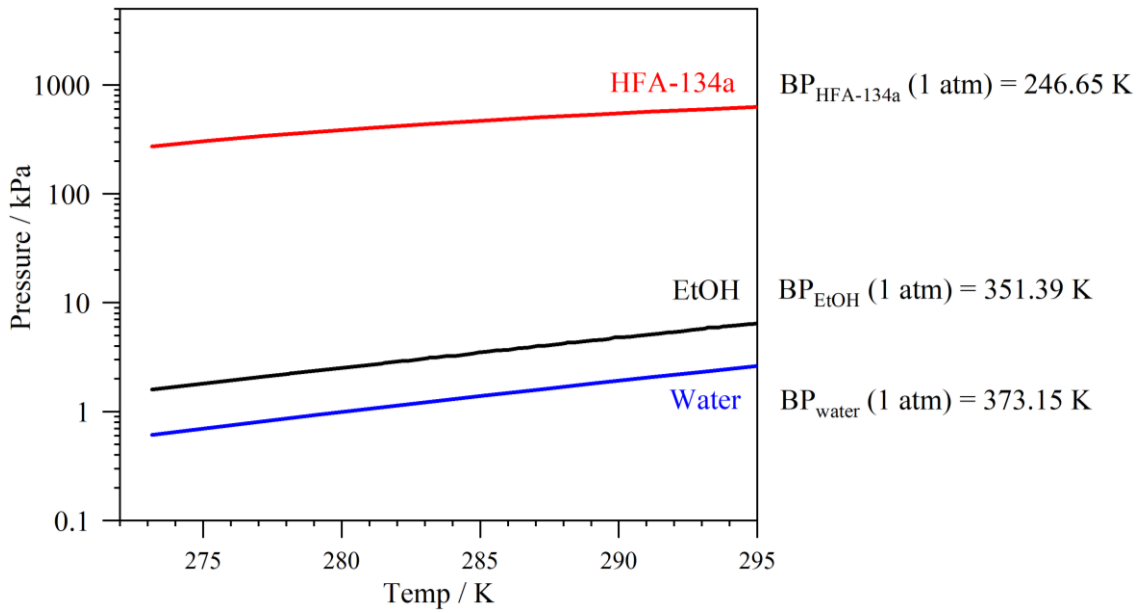

Figure 4-14: The temperature-dependent vapour pressure of HFA-134a (from Mason et al.[256]) is compared to that of ethanol (Mishchenko et al.[231]) and water (Wagner and Pruss [184]). In addition, the boiling point at atmospheric pressure is shown for HFA-134a [247], water and ethanol.[218]

4.6. The Evaporation of Ethanol Droplets Containing a Solute

The process of rapid ethanol evaporation when a solute is present is demonstrated in Fig. 4-15a, where a droplet containing an ethanol-glycerol droplet (0.9-0.1 mass fractions, respectively) was dried in the EDB at 293 K in dry N_2 (black data), and this is compared to the evaporation of a droplet with the same composition in humidified N_2 (60% RH). When the experiment was performed in 0% RH, the ethanol evaporated to leave a pure glycerol droplet remaining in the electrodynamic trap. There appears to have been a slight kinetic limitation to drying at the end of the ethanol evaporation, which can be attributed to the fact that glycerol is a viscous liquid. As a pure component, glycerol has a viscosity of 0.93 Pa.s at 298 K.[218] For an ethanol-rich droplet drying at 293 K the expected wet-bulb temperature is 275 K (Fig. 4-2a), at which temperature the viscosity of glycerol is 9.2 Pa.s.[257] This value of viscosity is sufficiently high to hinder the diffusional transport properties of remaining liquid ethanol in the droplet to the surface to evaporate, similar to that seen in water-evaporation experiments of viscous organic aerosol.[112] When the ethanol-glycerol droplet evaporated in 60% RH, not only was there an inflexion point with a reduced evaporation rate after that point, but there was also a higher final radius that when the droplet was dried in 0% RH. This serves as evidence that the rapid evaporation of ethanol at the start of the experiment led to evaporative cooling, and when there was water vapour in the gas phase in the 60% RH case, water condensation occurred. After the inflexion point, when presumably the droplet temperature had risen closer to the ambient temperature, the condensed water evaporated until a water-glycerol droplet remained in equilibrium with the partial pressure of water in the gas-phase.

To interpret the measurements of ethanol-glycerol evaporation, equilibrium hygroscopicity measurements of glycerol-water solutions were performed in the EDB, using the methods described in Chapter 3, and the results are shown in Fig. 4-15b and c in terms of the radial growth factor and density across the water activity range. By knowing the initial starting radius of the ethanol-glycerol droplet in the 60% RH droplet (blue data), and calculating the initial density of the ethanol-glycerol solution as 820 kg m^{-3} using ideal mixing,[258] the dry radius of pure glycerol in the droplet is calculated as 10.88 µm. The radial growth factor (GF_r) is defined as:

$$GF_r = \frac{r_{wet}}{r_{dry}} \qquad (4\text{-}8)$$

The GF_r at any time can be calculated using the radius (r_{wet}) to determine the water activity and the density from the equilibrium hygroscopicity data in Fig. 4-15b and c. We make an assumption that the point of inflexion occurs approximately when the ethanol has fully evaporated and the droplet is only water and glycerol. The radius at that point in Fig. 4-15a is 16.99 µm, which is a GF_r of 1.56 with a density of 1076 kg m^{-3} and a droplet mass of 2.21×10^{-11} kg. With the known dry-mass of pure glycerol present, we can hence determine that, in the first 0.4 s until the inflexion point, a total of 1.53×10^{-8} g of water condensed onto the droplet. This is within the same range as the mass of water condensation calculated in the previous section using the Maxwell model.

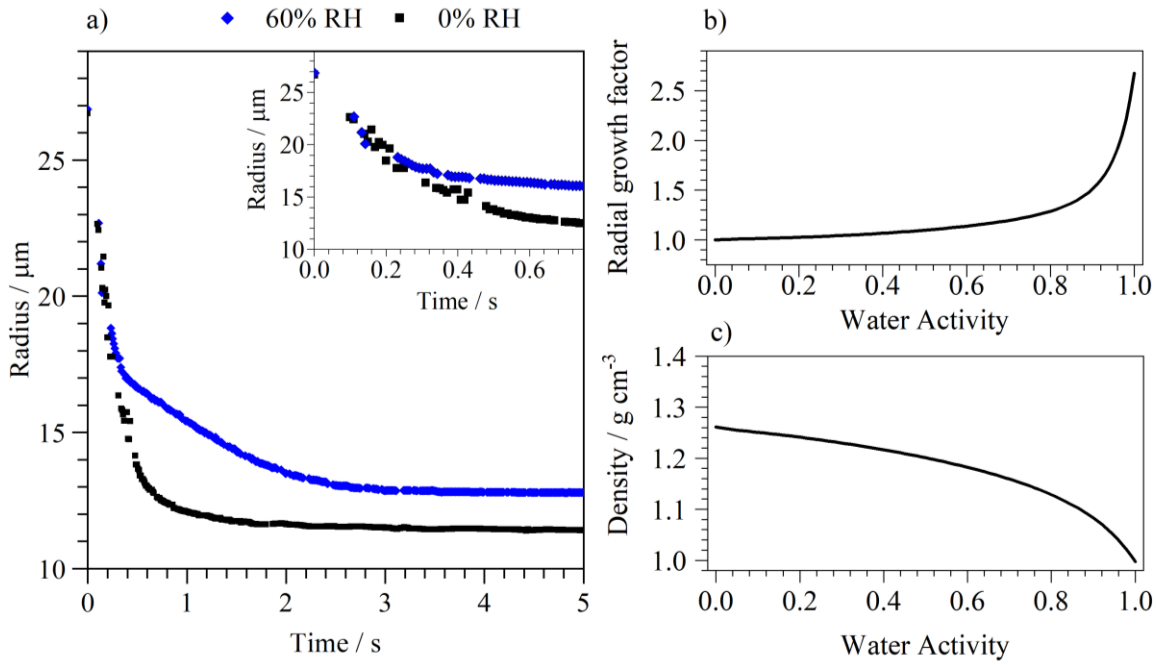

Figure 4-15: a) The evaporation of an ethanol-glycerol droplet (0.9-0.1 mass fraction, respectively) at 293 K at 0% RH and 60% RH. The inset figure shows the same data but with greater detail on the first 0.8 s of evaporation. b) The radial growth factor of a water-glycerol mixture determined through hygroscopicity measurements on the EDB b) the density as determined using a density meter.

4.7. Uncertainties in Experimental Evaporation Measurements and the Sensitivity of the Modified Maxwell Model

Uncertainty in the experimental parameters, such as temperature and RH, and assumptions about how they are interpreted, could result in inaccurate choices of parameters to implement into the modified Maxwell simulation. In addition, some assumptions made in the model may not necessarily hold under the conditions of these ethanol-water experiments. Whilst the model qualitatively confirms the experimental result of observing an inflexion point with a decrease in evaporation rate, with a change from water condensation to water evaporation, there is typically an underprediction in the model of the size of the droplet at the inflexion point. This implies that there is a discrepancy in the absolute mass of water condensing onto the droplet during the initial period of ethanol evaporation between the model and the experimental data. The next sections will review some possible reasons for this discrepancy.

4.7.1. Assumptions used when Implementing the Maxwell Model

The calculation of the absolute mass of water that condenses on to an evaporating ethanol–water droplet is highly dependent on the extent of the droplet surface temperature suppression. The latent heat is an

important parameter in the calculation of the droplet temperature. The model treats the latent heats of the binary ethanol-water system as follows. Temperature-dependent parameterisations for the pure component latent heats of ethanol [236] and water [235] are retrieved from the literature. Then, the contribution from each component to the latent heat is put into the energy balance equation in Eq. 4-6 in terms of a molar contribution. Whether the latent heat of each component scales with its concentration in an ideal manner at all temperatures is not known, and this could be a source of error in simulating the binary evaporation of ethanol-water mixtures.

In addition, the model assumes that the mixing inside the droplet is infinitely fast compared to the evaporation rate. Evaporation of ethanol and condensation of water from a humid gas phase are both processes that occur at the surface and, if the rate of the mass flux outweighs that of diffusional mixing, then the surface could become initially enriched with water. The binary diffusion coefficient of ethanol-water solutions has been measured as varying slightly with composition,[259] but remaining within the region of 1×10^{-9} m^2 s^{-1}. For the case of a pure ethanol droplet in humid N_2 in Fig. 4-9, the initial evaporation rate is ~ 1.5×10^{-9} m^2 s^{-1}. Thus, in terms of the Péclet number, the droplet is within the region wherein the evaporation rate and diffusional mixing rates are competitive ($Pe \sim 1$).

An enrichment of water at the surface would reduce the vapour pressure and evaporation rate of remaining ethanol, leading to a smaller degree of temperature suppression. Thus, less water would condense onto the droplet the radius at the inflexion in the model would be decreased. This is the opposite effect to that required to resolve the discrepancy between the model and the experimental data, so diffusional mixing can be assumed to not be the source of the inconsistency in the radii of the inflexion points.

4.7.2. Uncertainty in the Initial Droplet Composition

An aspect of the experiment that could affect how the mass of condensed water is interpreted is the uncertainty in the ratio of ethanol to water in the initial droplet. An error in the initial composition would causes errors in the density and in the calculation of the initial droplet mass. Such an error in the initial ratio between ethanol and water in the starting droplet could come about from the preferential evaporation of ethanol during solution storage prior to experiments, or from the droplet dispenser tip, as the vapour pressure of ethanol is higher than of water.

The sensitivity of the model to the initial droplet composition is shown in Fig. 4-16. The experimental data from Fig. 4-7a is plotted alongside the modified Maxwell simulation plots, with the same initial radius as the experimental measurement but with increasing values of the initial mass fraction of water in the droplet. Indeed, the model can be made to accurately reflect the experimental data if the mass fraction of water in the droplet is increased. This is a plausible correction as ethanol would be the species to most likely evaporate from the starting formulation during storage. However, the extent to which the

initial droplet composition must be changed for the model to match the data is large and inconsistent across all datasets. The closest match is an initial composition of 60% water for the 58% RH dataset, greater than 75% water for the 77% RH dataset, 65% water for the 87% dataset and 70% water for the 91% dataset. Such high values of water enrichment are not realistic for the evaporation of ethanol from the bulk solution, as the samples were only in storage for a matter of minutes prior to the experiment. The droplet dispenser uses an electric pulse to actuate a piezoelectric crystal, which produces a liquid jet that subsequently breaks up into a series of droplets; the front droplet in the stream enters the EDB instrument for the measurement. The solution at the dispenser tip is continuously flushed through using a constant pulse of 10 Hz to maintain a constant composition of solution in the dispenser. Such pulses have a lower voltage than that required for the droplets to enter the chamber, so that they do not interfere with the experiment.[137] This method has been validated to maintain a constant droplet concentration through the study of isothermal aqueous droplet evaporation.[116] However, the high volatility of ethanol may lead to a changing composition in this 0.1 s between each purge pulse. The modelled data in Fig. 4-8a shows that, in only 0.1 s, the absolute mass in a mixed ethanol-water droplet (0.5 mass fraction each) can drop from 1.97×10^{-11} kg to 1.11×10^{-11} kg, which is a 44% loss of ethanol mass. That is the evaporation rate in a ~25 µm spherical droplet so it is difficult to know whether the evaporation at the tip of the dispenser would be as rapid.

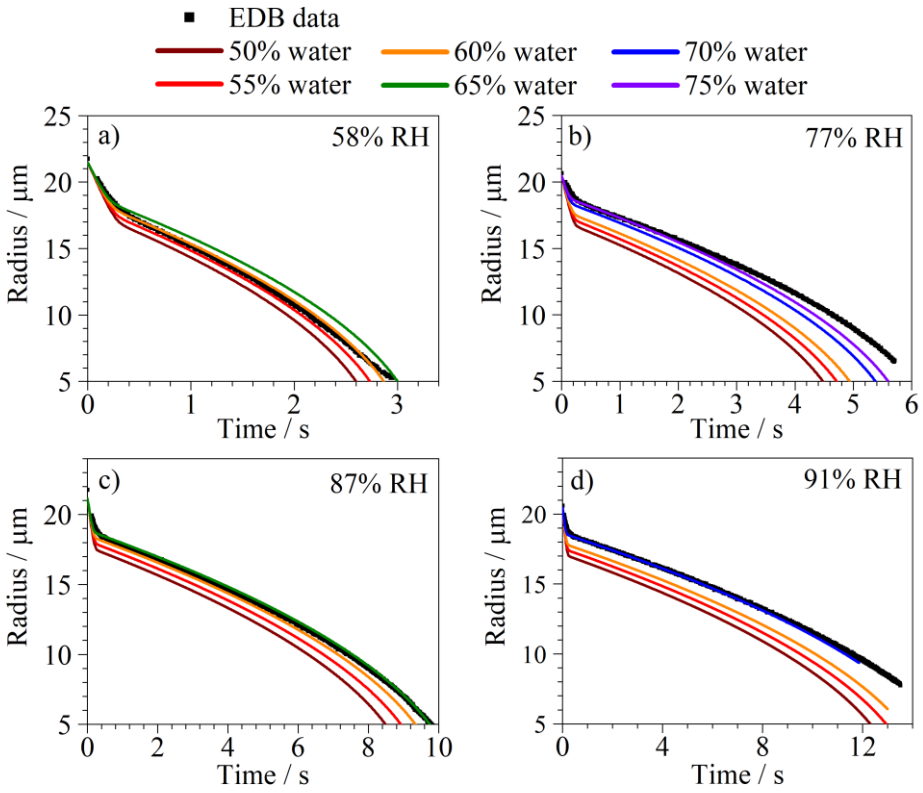

Figure 4-16: Mixed ethanol-water droplets (0.5 mass fraction each) evaporating into varying humidities at 293 K, compared to the modified Maxwell simulation when the initial starting composition of ethanol and water is varied to increasing levels of water content.

For the case of the pure ethanol droplet evaporating into humid N_2, the model underpredicts the radius at the point of inflexion compared to the measurement. In that dataset, there could be no error in the initial ethanol-water ratio as the solution in the dispenser was pure ethanol. Hence, uncertainty in the initial droplet composition cannot be the only aspect of uncertainty causing the discrepancy between the model and the measurements. However, this work shows that in some of the datasets it could be a contributing factor.

4.7.3. Uncertainty in the Initial Droplet Radius

An additional area of uncertainty that could affect the accuracy of the modified Maxwell model is the initial droplet radius. Droplets to be studied in the EDB are formed externally and fired into the instrument, so there is a flight-time of ~ 0.1 s before the droplet becomes trapped and during this time there is no way to record the droplet radius from the light scattering. As the absolute time of droplet generation is known from the time that the pulse was supplied to the dispenser, it is possible to estimate the initial droplet radius by extrapolating back to this time. For typical EDB measurements, the initial droplet size is back-extrapolated in the *radius*^{2}, due to the constant gradient of the *radius*^{2} vs. time in steady evaporation.[186] However, the initial evaporation of an ethanol droplet at 293 K is likely to be unsteady, with a varying rate.

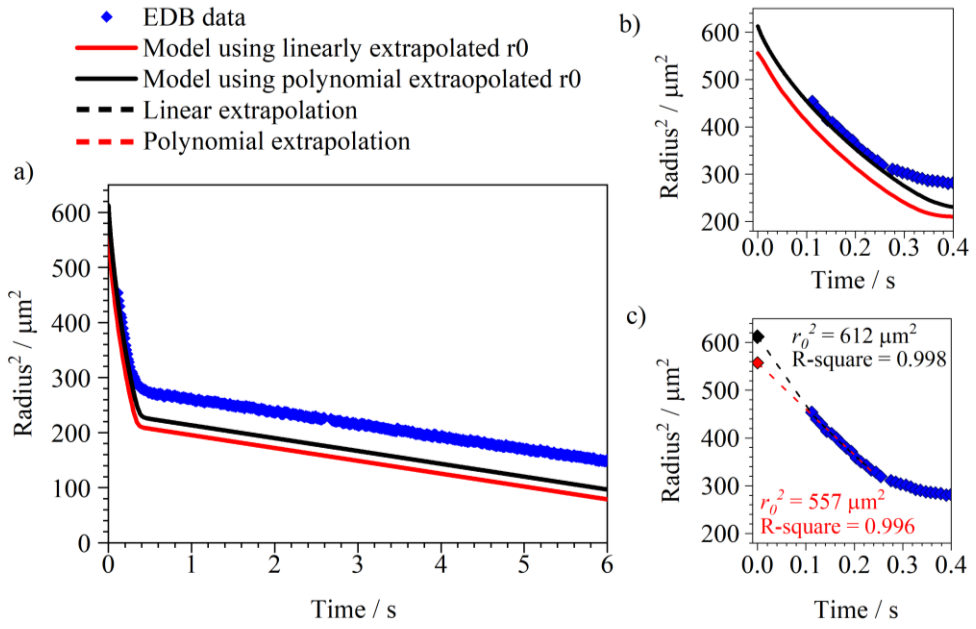

Figure 4-17: a) Blue datapoints show the evaporation of a pure ethanol droplet at 293 K and 91% RH, i.e. the data in Fig. 4-9a, compared to the numerical modified Maxwell model. The numerical model uses an r_0 that arises from a linear extrapolation of the first ~ 0.1 s of data (red line) or a polynomial extrapolation (black line). b) The same data as a) but focused on the first 0.4 s of evaporation in greater detail. c) The extrapolations of the data to retrieve the values for r_0.

A pure ethanol droplet evaporating in 91% RH at 293 K is compared to a Maxwell simulation which has an r_0 determined by a linear extrapolation of the first ten experimental data points, and that with a r_0 from a second-order polynomial extrapolation, and the results are shown in Fig. 4-17a. The same data but showing in greater detail the start of the evaporation process is shown in Fig. 4-17b, and the fit to the datapoints to determine the r_0 is in Fig. 4-17c. Throughout this chapter, the Maxwell model used to simulate the data used a linearly extrapolated r_0 as a parameter for the simulations. The evaporation of pure ethanol at room temperature is expected to be unsteady in the initial period so a second-order polynomial fit in the temporal-r^2 is more likely to represent the non-isothermal start of the drying process. Indeed, the polynomial fit provides a higher value of r_0 than a linear fit and gives a closer agreement between the model and the experimental data. There remains a lower radius at the inflexion point than the measurement data. Fig. 4-17 demonstrates that the fitting of the first few points to determine the initial radius could be a contributing factor to the discrepancy between model and measurements.

4.8. Chapter 4: Summary and Future Work

In this chapter, the evaporation of pure ethanol and mixed ethanol-water droplets has been studied in a range of RHs and temperatures using an EDB, with experimental data compared to various numerical models. The results have demonstrated the extent to which mass and heat flux can be coupled during the evaporation of mixed ethanol-water droplets. The rapid evaporation of ethanol has been shown to lead to significant evaporative droplet cooling. If droplets undergo rapid ethanol evaporation in humid environments, the evaporative cooling can lead to a supersaturation of water vapour in the gas phase compared to at the droplet surface, driving water condensation onto the droplet. Indeed, even for a pure ethanol droplet evaporating in a humid environment, these kinetic processes can lead to the droplet composition switching to being pure water within only 400 ms. A modified Maxwell numerical model showed reasonable agreement with the evaporation data of pure ethanol and mixed ethanol-water droplets, and the reasons behind the discrepancy in the absolute mass of water condensation occurring concurrently with ethanol evaporation have been discussed in detail. Such a discrepancy arises from some experimental uncertainties, such as the temperature, RH, initial droplet size determined from data extrapolation, and the initial droplet composition, as well as some assumptions made in the use of the Maxwell model.

Formulations containing multiple volatile liquids are highly prevalent in a wide range of droplet drying applications. In particular, many feed solutions for spray drying contain multiple solvents, with varying volatilities, and also metered-dose inhaler (MDI) products often contain mixtures of ethanol and HFA. For such applications, the results from this chapter are of importance. However, industrial formulations also contain non-volatile components, such as the active pharmaceutical ingredient (API) in an MDI,

or the solid content in spray drying formulations. The presence of a solute in mixed solvent systems has only been briefly discussed in Section 4.5.2, with ethanol-water-glycerol droplets. Glycerol is soluble in both water and ethanol, so the phase-state of the droplet was unaffected by the evaporation of ethanol and the condensation of water. For an API, the solubility in water is typically very low,[260] so water condensation occurring onto an MDI droplet may cause solute precipitation or phase-separation of the droplet. Hence, an important area of future work for this field is to study the implications of water condensation onto MDI droplets occurring in humid lung atmospheres on the pharmacokinetics of the deposited drug particles. The microphysical processes occurring in a drying droplet that have been studied in this chapter could be used to optimise the region of respiratory drug delivery and the dose.

The modified Maxwell model described in this chapter [43] showed a better performance than a simple isothermal Maxwell model and the binary-solvent Kulmala model [182] at simulating the evaporation of pure ethanol and mixed ethanol-water droplets compared to experimental data. However, the modified Maxwell model still has limitations. At the time of writing it does not incorporate the possibility of internal concentration gradients in an evaporating droplet and assumes a continuously homogeneous droplet. This assumption held for the droplet size studied in this chapter (~ 25 μm radius) but for larger droplets that are several hundred micrometres in radius the build-up of concentration gradients may become more relevant and would affect the evaporation rate. Spray dryer chambers and MDI mists are likely to have broad ranges of size distributions. Hence, it would be an important and interesting piece of work to incorporate diffusional mixing timescales into the Maxwell model and to study the evaporation of larger droplets in the EDB for comparison.

Chapter 5

Evaporation, Crystal Nucleation and Morphology Development of Aqueous Sodium Chloride Aerosol Droplets

Chapter 5 is based on a published paper in The Journal of Physical Chemistry B, entitled: *Drying Kinetics of Salt Solution Droplets: Water Evaporation Rates and Crystallization*. J. Phys. Chem. B, 2018, **123**, 266–276, for which I am the first author.[261] I collected, analysed and interpreted all experimental data presented in the manuscript. I discuss a model that was developed by Joshua Robinson, a Physics PhD candidate at the University of Bristol. The NaCl particles in Fig. 5-15 were collected by Dr. Jim Walker and imaged using the SEM by Dr. Justice Archer, but I collected the accompanying kinetic EDB data for that dataset.

The technique of studying evaporation rates and observed time of nucleation for evaporating droplets is using the Electrodynamic Balance (EDB). Dried particles were collected using a falling droplet column (FDC), and collected samples were imaged using a Scanning Electron Microscope (SEM). This chapter will discuss how using these approaches combined with models can provide a picture of how changing evaporation conditions such as the drying temperature, humidity and initial solute concentration can affect the evaporation rate, final particle size, morphology and crystal size.

5.1. Previous Studies on Rapidly Evaporating Salt Solution Droplets

Whilst the thermodynamic principles behind the underlying phase behaviour and equilibrium compositions of inorganic solution droplets have been well documented in the literature, there have been fewer studies on the kinetics of rapid droplet drying and efflorescence. There has been work on the concentration required to induce crystallisation in droplets suspended from filaments,[189,262] on surfaces (sessile droplets),[77,263,264] or on TEM grids.[187,265] Droplet levitation has been used to study the efflorescence process but such studies typically involve slow drying processes that proceed isothermally and approach the equilibrium composition at all times.[146,266,267] Far fewer studies have examined rapid drying kinetics and crystallization of free droplets or aerosols. Vehring et al. performed sophisticated studies on the formation of crystalline microparticles from free falling droplets in a vertical column, within which they were able to record the radius as well as the density throughout the evaporation process of inorganic solution droplets.[148,158] Combining density measurements along with optical sizing

gave insight into morphology development during droplet drying; they observed surface enrichment during rapid evaporation processes leading to crust formation.[268] The work presented in this thesis chapter aims to build on this concept of surface enrichment. Using NaCl as a model system, the surface concentration throughout drying and its link to final particle morphology will be investigated.

5.2. The Kinetic Basis of Evaporation of Droplets containing an Inorganic Solute

The rate of evaporation in a pure-water droplet in the continuum regime has a constant gradient when plotted as r^2 with respect to time, according to the Maxwell equation (Equation 2-21 in Chapter 2), scaling with the surface area from which water is available to vaporise. In the presence of a solute, such as NaCl, water will evaporate if the water activity at the droplet surface is higher than the RH in the surrounding gas phase. Fig. 5-1a shows the evaporation of a 0.02 MFS NaCl droplet evaporating into 0% RH. As this droplet is initially low in NaCl concentration, there is a large initial difference between the solution water activity and the gas phase RH (a_w – RH) of 98.7%. This difference remains high for most of the evaporation process, only reducing to 42% towards the end of drying when the droplet effloresces at t = 1.63 s (data points after efflorescence are not shown). The red line in the figure shows a linear fit tangential to the evaporation data at t = 0 s, and the evaporation data only deviates from this line approximately 0.2 s before the end of drying. Thus, the high value for (a_w – RH) throughout evaporation means that the drying behaviour is very similar to a pure water droplet. Conversely, the droplet in Fig. 5-1b has an initial mass fraction of 0.1 and evaporates into an RH of 89%, so a_w – RH is initially lower, at 4.6%. As the droplet evaporates, a_w – RH decreases by over two orders of magnitude. The reduction in a_w – RH causes the gradient in radius in Fig. 5-1b to continue to decrease, and the droplet deviates from the tangential fit relatively early into the evaporation process.

Simulated evaporation profiles using the Kulmala model are shown in Fig. 5-1 (black dotted line).[182] The Kulmala model fits the EDB data very closely in panel b), where the evaporation is slow and isothermal. However, in Fig. 5-1a, the Kulmala model underpredicts the rate of the evaporation of water, as the evaporation occurs rapidly leading to evaporative cooling at the droplet surface. Here, the Kulmala model cannot accurately calculate the value of the vapour pressure of water at the droplet surface, and hence the mass flux, under such conditions.

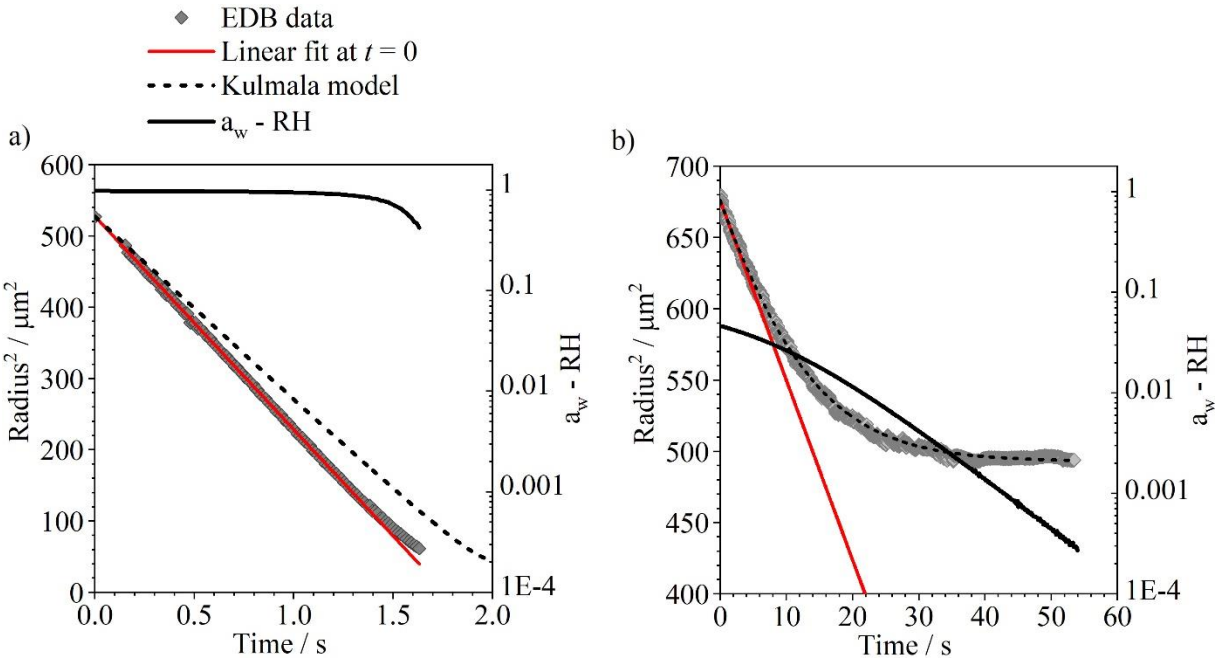

Figure 5-1: The evaporation of an aqueous NaCl droplet (grey datapoints) at 293 K with a) initial mass fraction of 0.02 and RH of 0% and b) initial mass fraction of 0.1 and RH of 89%. The data is compared to a line that is fit to be tangential to the evaporation data at t = 0 s (red line) and to an evaporation simulation using the Kulmala model (dotted line). The log plot of the time-dependent difference between the droplet water activity and the RH is plotted in black to be comparable in both panels.

5.3. Observing Efflorescence of NaCl in the EDB using the Phase Function (PF)

As outlined in Chapter 2, the elastic light scattering of the laser from a droplet can be used to infer the morphology at different times throughout drying. Fig. 5-2 shows the evaporation of an aqueous NaCl droplet with initial concentration of 0.1 MFS, evaporating in N_2 at 42% RH and 293 K. The datapoint colour corresponds to the morphology indicated by the elastic light scattering collected at that time: navy-blue denotes a homogeneous, spherical droplet; yellow indicates a droplet containing inclusions; light-blue indicates a core-shell morphology; and red indicates a crystalline morphology. The figure shows that the droplet is homogeneous and spherical for most of the evaporation process, until crystals are nucleated at 4.7 s into the droplet lifetime. After 4.7 s, the droplet displays a PF that indicates inclusions are present, suggesting that one or multiple crystal nuclei have formed and they disrupt the light scattering pattern from the droplet. As the droplet is spherical overall, there are still interference fringes that allow the radius to be inferred by the EDB software. The droplet then continues to reduce in radius and the elastic light scattering indicates that it is a crystalline particle after ~ 5.4 s. Fig. 5-2c shows the stacked PFs for every time-step throughout the evaporation process, with Fig. 5-2d showing

the data highlighted by the red region-of-interest in greater detail. The peaks in the PF (lighter regions) are regularly spaced until the abrupt change at 4.7 s, where inclusions are detected. The light scattering intensity generally becomes brighter once the droplet has become a completely crystallised particle.

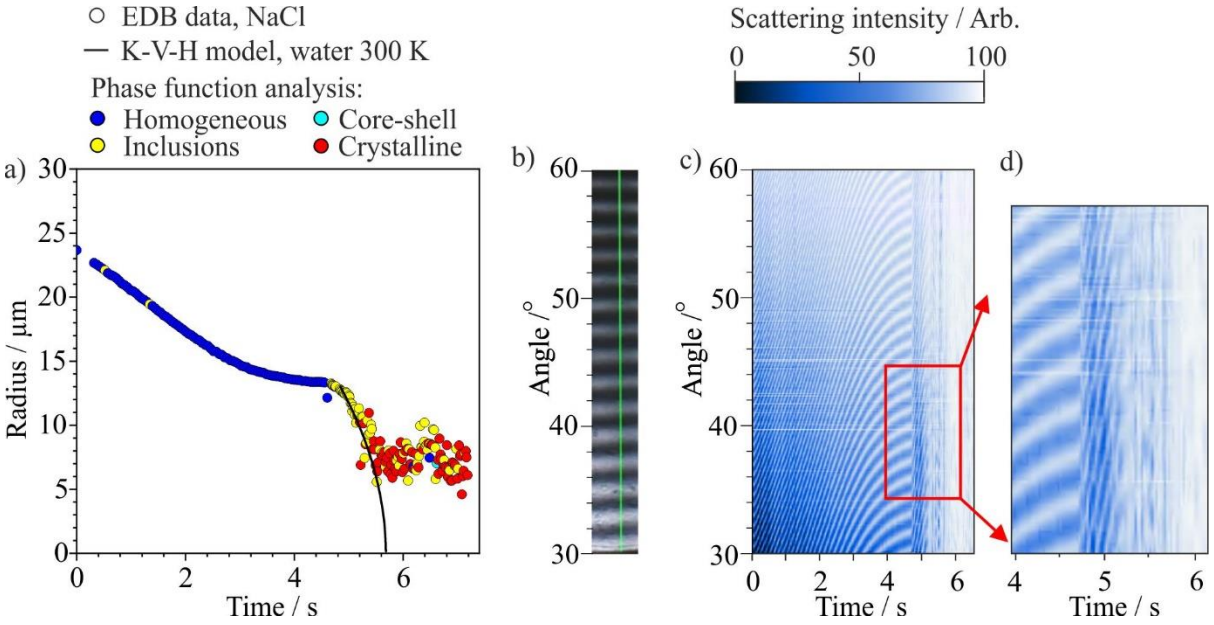

Figure 5-2: a) The radius of an aqueous NaCl droplet, with initial mass fraction of 0.1, evaporating at 293 K in 42% RH N_2 gas. The colour of the datapoints correspond to the assignment of the droplet morphology from the elastic light scattering. The black line shows a simulation of pure water droplet of radius 12.9 µm evaporating at 42% RH and 300 K, using the K-V-H model.[115] b) An example of the PF detected by the CCD at one time-point, with the intensity of light scattering recorded across the green line. c) A stacked set of the PFs recorded for every time-step throughout the drying process, with d) showing the red region of interest in greater detail.

In Fig. 5-2a, in the ~ 1 s before crystal nucleation occurs, the evaporation rate of the NaCl droplet slows down significantly and the radius almost equilibrates. However, after crystal nucleation occurs at 4.7 s the evaporation rate then increases leading to further shrinkage of the droplet until complete crystallisation occurs. This increase in evaporation rate, where the datapoints are showing inclusions, can be attributed to the fact that crystal nucleation is an exothermic process. The enthalpy of fusion of NaCl out of solution can be considered as the reverse of the enthalpy of dissolution, i.e. -3.88 kJ mol^{-1}, with heat given off during the formation of crystalline NaCl.[218] Such heat leads to a temperature rise at the droplet surface, increasing the vapour pressure of the remaining water in the droplet, inducing a subsequent increase in evaporation rate. To quantify this effect, the absolute mass of NaCl in the droplet in Fig. 5-2a is 5.98×10^{-12} kg, which is 1.02×10^{-10} moles. Assuming that all the NaCl crystallises, and that the droplet upon crystallisation has an isobaric specific heat equivalent to water, then the volume of 9.97 pL at t = 4.7 s would be predicted to undergo a temperature change of 6.78 K, which is significant enough to increase the evaporation rate of the remaining water. The gradient of the evaporation of the remaining water in the droplet at t = 4.7 s is compared to a simulation of pure water evaporating at a temperature of 300 K and 42% RH (black line), performed using the K-V-H model presented by Su et

al.[115] The simulated water droplet shows an evaporation rate that is similar to that of the water after nucleation of NaCl crystals, showing that this temperature change upon nucleation is resolvable in the evaporation kinetics that are recorded in the EDB.

5.4. Evaporation Kinetics of Aqueous NaCl Droplets under Different Environmental Conditions

The evaporation kinetics of 230 separate droplets containing an aqueous solution of NaCl (0.202 MFS), dried in a sequence in the EDB at 293 K and 0% RH, are compared in Fig. 5-3a. The figure demonstrates not only the ability of the droplet dispenser to produce droplets of the same initial radius with high reproducibility (23.79 ± 0.08 μm), but also the reproducibility in the evaporation rate. A very reproducible time of efflorescence is also observed: the droplets nucleate crystals after 0.95 ± 0.02 s into the drying process, seen in Fig. 5-3a as the point at which the datapoints become very noisy. This is because the elastic light scattering becomes disrupted from a phase function into a highly erratic pattern from which the EDB software can no longer calculate an accurate value of the radius. We can determine a volume-averaged concentration at the point of efflorescence, calculated using the initial droplet volume and the dry mass of NaCl known from the initial concentration. The aqueous NaCl droplets nucleate crystals at a volume-averaged concentration of 636 ± 7 g L^{-1}.

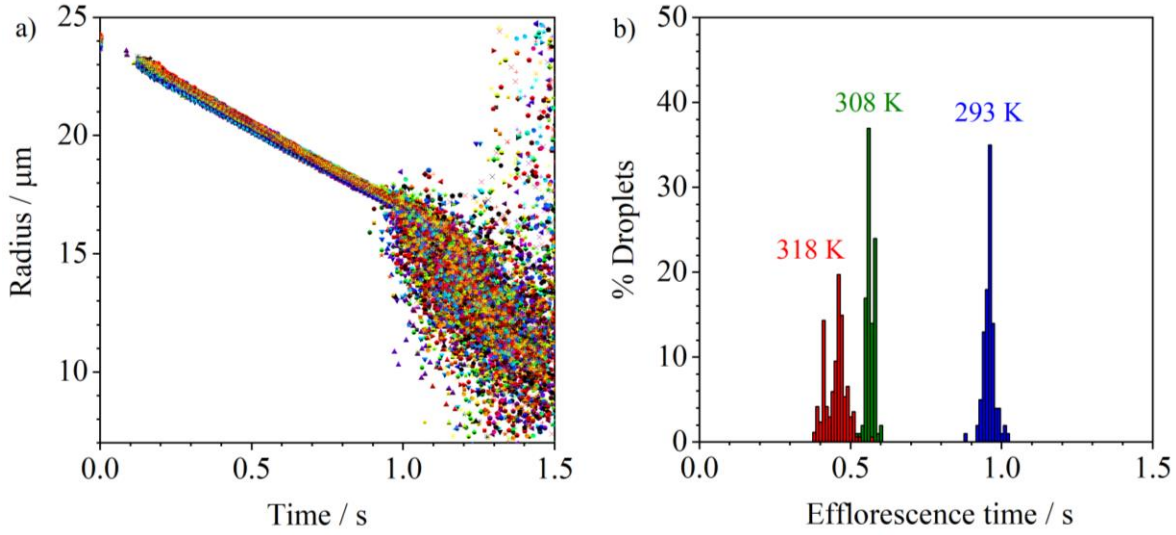

Figure 5-3: a) Overlaid radius profiles of 230 aqueous NaCl droplets with initial mass fraction of 0.2 as they evaporate into dry N_2 at 293 K. b) Distribution in the time that efflorescence is observed in evaporating aqueous NaCl droplets (initial mass fraction of 0.2) at different gas-phase temperatures for a large population of droplets (upwards of 200 for each temperature).

The time at which nucleation is observed for each individual droplet in the series is recorded and shown in a histogram of 0.01 s bins in Fig. 5-3b, alongside data from equivalent experiments at 308 K and 318 K. Over 200 droplets are included in each dataset. At each temperature, the distribution of efflorescence times in a drying droplet of aqueous NaCl is narrow. Previous work on homogeneous nucleation has indicated that it is a stochastic process, and reports have shown close fits between experimentally measured nucleation times at varying supersaturations with those predicted by Poisson statistics.[203] However, the distributions shown in Fig. 5-3b are not Poisson-shaped. This is because the efflorescence time recorded in this work is not an 'induction time' measured at one constant value of supersaturation, as in the work of Durán-Olivencia *et al*. [203] Instead, the aqueous NaCl droplets continually experience a rising degree of supersaturation during evaporation.

The time at which crystal nucleation is observed in a drying droplet decreases as the temperature is increased, from 0.95 ± 0.02 s at a temperature of 293 K to 0.56 ± 0.01 s at 308 K and 0.45 ± 0.03 s at 318 K. As the evaporation rate of water increases with an increasing gas phase temperature and the droplets all have the same initial concentration of salt, it takes less time to reach a high enough concentration for crystallisation if the temperature is higher. It would be expected that the reproducibility in the time that nucleation is observed across multiple droplets would be poorer for the experiments performed at higher temperatures. If a droplet evaporates rapidly it is more likely to move position slightly in the trap whilst it loses mass and hence the data are noisier for faster drying. This noise could give bias to the method of detecting crystal nucleation. However, the standard deviation for nucleation times as shown in Table 5-1 remains low, within ± 0.03 s for all drying experiments.

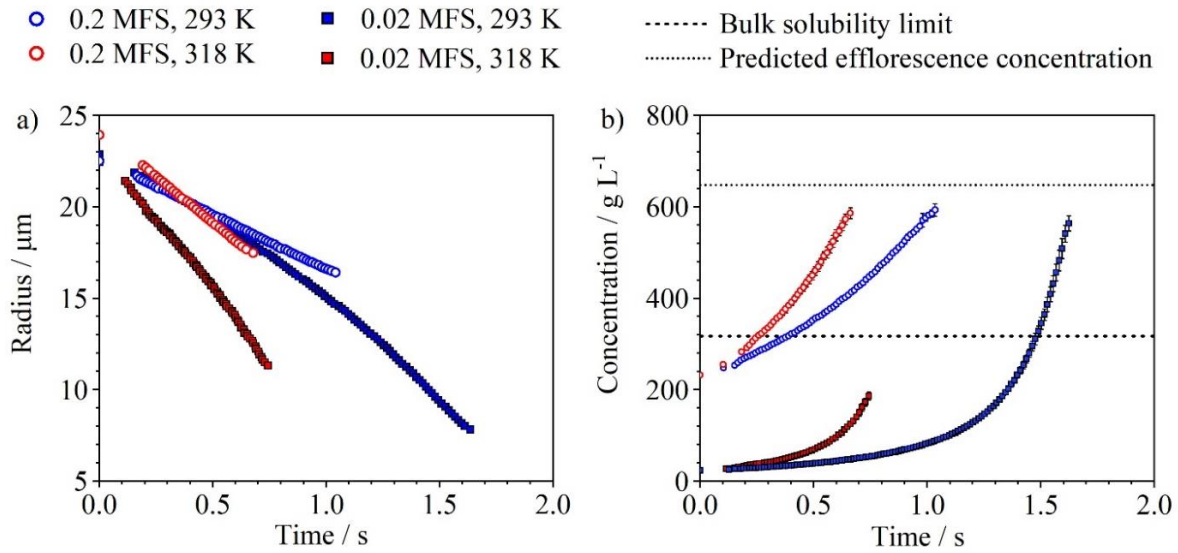

Figure 5-4: a) The radius of aqueous NaCl droplets with different initial solute concentrations as they evaporate in dry N_2 at different temperatures. The data is averaged over a minimum of 10 droplets. The error bars are smaller than the data points. b) The volume-averaged concentration of NaCl in the droplets during evaporation as inferred from the experimental measurements of radius in a). The bulk solubility limit and the predicted efflorescence concentration are shown by the dotted and dashed line, respectively.

We report the effect of decreasing the initial salt concentration for drying NaCl droplets at 293 K and 318 K in Fig 5-4a. The initial evaporation rate of water from the droplet, in terms of dr^2/dt, increases slightly in going from a starting concentration of 0.202 MFS to 0.023 MFS. For example, at 293 K the evaporation rate increases from $2.49 \pm 0.02 \times 10^{-10}$ m^2 s^{-1} with 0.2 MFS to $2.993 \pm 0.006 \times 10^{-10}$ m^2 s^{-1} to 0.02 MFS. This increase in evaporation rate is caused by an increase in the vapour pressure of water as the NaCl ionic activity is lower in a less concentrated droplet. In addition, with a lower starting concentration the droplet efflorescence time increases. With less salt in the droplet, there is more water to evaporate and it takes longer for the droplet to reach the critical supersaturation required for crystal nucleation.

5.4.1. Volume-Averaged Concentration of NaCl in Evaporating Droplets

For the four drying experiments shown in Fig. 5-4a, the volume-averaged concentration of salt in each droplet as a function of time is shown in Fig 5-4b. This volume-averaged concentration is calculated with two assumptions: first, that an evaporating droplet maintains a spherical shape throughout evaporation, which is likely to be valid due to capillary forces and because the droplet would evaporate from all directions equally. The second assumption is that the droplet maintains a homogeneous concentration throughout evaporation. This assumption may not be valid, as rapid evaporation from the droplet surface may lead to enrichment of NaCl in the outer regions of the droplet while the diffusion rate of component redistribution throughout the droplet to the centre may not be fast enough to maintain a uniform concentration. The evaporation rate, the recorded time for efflorescence and volume-averaged concentration at efflorescence for the different drying datasets in Fig. 5-4a are shown in Table 5-1.

The E-AIM model predicts efflorescence of aqueous NaCl in an equilibrated droplet occurs at a water activity of 0.45.[175] E-AIM is a well-established model that has been demonstrated to accurately predict the equilibrium concentration of a variety of inorganic solutes at a range of RHs.[116,269,270] The concentration at $a_w = 0.45$ is at a supersaturation of 2.04 at 293 K as determined by the E-AIM model in terms of molality, as shown in Fig. 5-5. A supersaturation of 2.04 corresponds to a concentration of 648 g L^{-1} at 293 K and 654 g L^{-1} at 318 K.

As shown in Table 5-1, for the dataset of 0.02 MFS NaCl droplets evaporating into 318 K in 0% RH, crystal nucleation is observed in droplets when they are at an average concentration of 200 ± 20 g L^{-1}.[261] This is far below the expected efflorescence concentration as predicted by the E-AIM model of 654 g L^{-1}.[175] In fact, this efflorescence concentration of 200 g L^{-1} is lower than the equilibrium bulk-solubility limit of NaCl at 318 K, which is 322 g L^{-1}.[218] This indicates that it is unlikely that the droplet is homogeneous in composition at this point in time, as the average concentration is not high enough to trigger crystal nucleation. We propose that the rapid evaporation in such droplets cause a high degree

of surface enrichment in NaCl and the concentration locally at the surface exceeds the solubility limit and reaches a sufficiently high value for crystal nucleation to occur. It must be noted that the efflorescence observation reported in Table 5-1 is a loss in uniformity in the scattering pattern, reproducible across all droplets, such that the EDB software can no longer use the fringes in the phase function to determine an accurate value of the droplet radius. We must not assume that this indicates complete crystallisation has occurred in the whole droplet at this moment in time: nucleation has occurred at the surface.

Table 5-1: The recorded evaporation rate, efflorescence time (t_{eff}), volume-averaged concentration at t_{eff} ($V_{vol,eff}$) and initial Péclet number for four datasets of the evaporation of aqueous NaCl solution droplets of different initial concentrations and gas temperatures (T_∞) , in dry N_2. Data is reported in order of increasing evaporation rate, as an average over a minimum of 15 droplets. Evaporation rate is reported as the negative gradient of the radius^2 vs. time.

Initial NaCl MFS	Initial NaCl conc. / g L^{-1}	T_∞ / K	Evaporation rate / m^2 s^{-1}	t_{eff} / s	$V_{vol,eff}$ / g L^{-1}	Pe_0
0.20202	232	293	$2.49 \times 10^{-10} \pm 0.02 \times 10^{-10}$	0.95 ± 0.02	636 ± 7	0.432
0.02333	24	293	$2.993 \times 10^{-10} \pm 0.006 \times 10^{-10}$	1.51 ± 0.02	630 ± 10	0.184
0.20202	232	318	$4.21 \times 10^{-10} \pm 0.03 \times 10^{-10}$	0.45 ± 0.03	640 ± 20	0.656
0.02333	24	318	$5.44 \times 10^{-10} \pm 0.07 \times 10^{-10}$	0.74 ± 0.03	200 ± 20	0.296

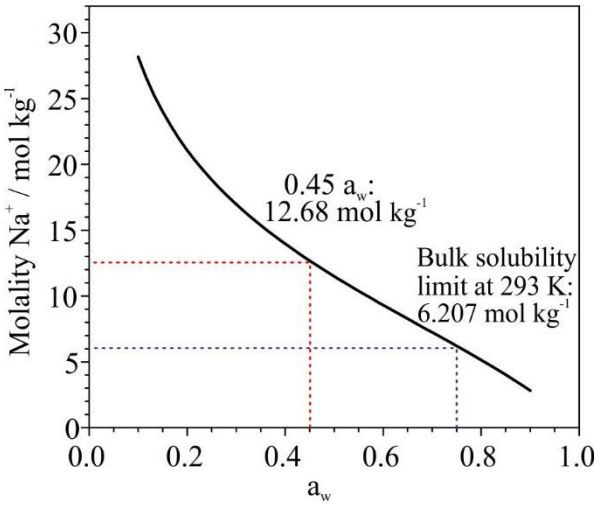

Figure 5-5: The molality of aqueous NaCl as a function of water activity, as calculated by the E-AIM model.[175] The dotted lines indicate how the value for the supersaturation of a 0.45 a_w NaCl droplet was obtained.

5.4.2. The Initial Péclet Number for the Different Drying Conditions

The Péclet number (*Pe*) is commonly used to describe the interplay between the rate of diffusional transport within a drying droplet and the rate of solvent evaporation:[3]

$$Pe = \frac{k}{D} \tag{5-1}$$

where k is the radial evaporation rate, dr^2/dt, and D is the binary diffusion coefficient in the droplet. A value of *Pe* lower than 1 typically indicates that a homogeneous composition will be maintained throughout drying, where diffusional mixing is fast enough to replenish the surface with solvent from the droplet centre. A *Pe* larger than 1 suggests an inhomogeneous droplet concentration, with a surface that is enriched with solute as the solvent evaporates faster than it can be replenished through internal diffusional transport.[271,272]

In increasing the gas phase temperature, and so also the droplet temperature, the evaporation rate of the NaCl droplets increases due to a rise in the vapour pressure of water at the surface (Fig. 5-4a). However, in addition to a rise in evaporation rate comes an increase in the binary diffusion coefficient of water through the droplet, which acts to maintain a homogeneous composition. This increase in diffusivity can be described by the Stokes-Einstein relation,

$$\frac{D_1}{D_2} = \frac{T_1}{T_2}\frac{\mu_2}{\mu_1}, \tag{5-2}$$

where D_T is the binary diffusion coefficient and T is the temperature (K) at two temperature points, subscript 1 and 2. μ_T is the solvent dynamic viscosity, which for water is assumed to remain constant between 293 and 318 K for an aqueous NaCl solution. An increase in the temperature leads to earlier efflorescence, and, for the 0.02 MFS case, at a much lower volume-averaged concentration. This suggests that the rise in evaporation rate on going from 293 K to 318 K is large enough to lead to a high level of supersaturation earlier in the drying process to compensate for the additional increase in the rate of diffusional mixing. From a quantitative perspective, increasing the temperature from 293 K to 318 K for the 0.02 MFS dataset increases the evaporation rate from 2.993×10^{-10} m s^{-1} to 5.44×10^{-10} m s^{-1}, which is an 88% increase. Conversely, the binary diffusion coefficient is 8.5% greater at the higher temperature. Given that the Péclet number is a ratio between the evaporation rate and the binary diffusion coefficient and is used to describe the extent of surface enrichment, observing efflorescence at a lower volume-averaged concentration and earlier time for this NaCl dataset is in accordance with the expected changes in the Péclet number.

The initial Péclet numbers for each of the NaCl droplet datasets are quoted in Table 5-1. All four droplet evaporation events have Péclet numbers at t=0 that are below 1, which according to Equation 5-1 suggest that the evaporation rate under such conditions is small compared to the binary diffusion constant. This suggests that the droplet should be maintaining a homogeneous concentration profile throughout evaporation leading to a final particle that is densely packed rather than hollow; this is inconsistent with the result in Fig. 5-4b that suggests the evaporating droplets become enriched in NaCl

at the surface. As a result of this discrepancy, we must examine the internal concentration profiles of aqueous NaCl at different radial points inside an evaporating droplet, as outlined in the next section.

5.5. Diffusive Transport Model to Study the Surface Enrichment of Droplets During Drying

We model the internal diffusional mixing inside an evaporating droplet alongside the experimentally derived evaporation rate to track the concentration of NaCl at different radial "shells" within the a droplet, to pay particular attention to the extent of surface enrichment as a droplet evaporates to form a crystalline particle.

The droplet is modelled as a sphere containing a series of radial shells, each ~ 20 nm in width. As indicated in Fig. 5-6, the solute concentration $c(r, t)$ as a function of time, t, at different distances from the centre of the droplet, r, is calculated assuming spherical symmetry using a numerical integration of the nonlinear diffusion equation.[261]

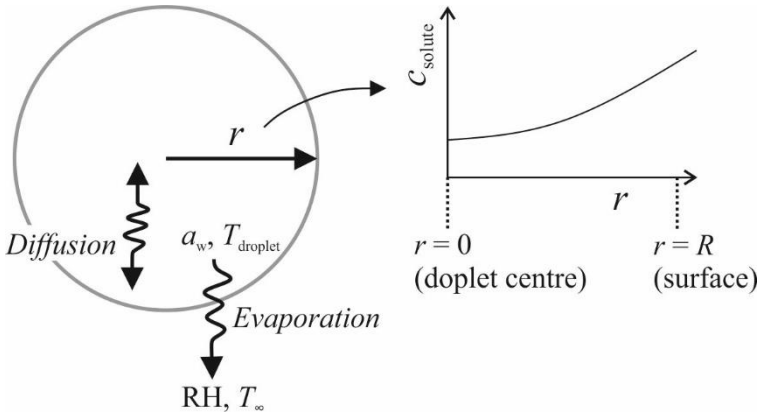

Figure 5-6: The basis behind the concentration droplet drying model used in this work. An aqueous droplet of radius *R* evaporates due to an imbalance in a_w and RH, leading to evaporative cooling. The competition between evaporative mass flux and internal diffusive transport of water between the droplet centre and surface is modelled to calculate the solute concentration across the radial profile of the droplet.

Previous work has reported the viscosity of aqueous NaCl solutions at 293 K up to high concentrations in the aerosol phase by performing aerosol coalescence experiments using aerosol optical tweezers,[273] as shown in Fig. 5-7a. The solution viscosity increases with an increase in concentration of NaCl, suggesting that the binary diffusion coefficient of the solution decreases as a droplet evaporates. To convert the viscosity measurements into a binary diffusion coefficient $D(T)$ we use the Stokes-Einstein relation:

$$D(T) = \frac{k_B T}{6 \pi r_s \eta} \qquad (5\text{-}3)$$

where k_B is the Boltzmann constant, T is the temperature, η is the solution viscosity and r_s is the Stokes radius, which is defined as the radius of a hard-sphere with a diffusion rate that is equivalent to that of the solute. We obtain $D(T)$ by converting the viscosity data using iterative variations on r_s, calibrating with aqueous NaCl diffusivity data from molecular dynamics simulations at lower concentrations from Lyubartsev et al.[274] to get a fit, as shown in Fig. 5-7b. The value of r_s that gives the closest fit is 0.163 nm, which is within the range of reported values of r_s for the sodium and chloride ions of 0.184 nm and 0.121 nm, respectively.[275] To determine values for the binary diffusion coefficient of the droplet solution at different temperatures, we assume an Einstein scaling to obtain the relationship:

$$D(T) = \frac{D(293\ K)}{293} \times T \qquad (5\text{-}4)$$

At the time of writing, this model does not take into account the fact that the rapid evaporation of salt solution droplets would lead to evaporative cooling of the droplet and would hence decrease $D(T)$. During evaporation of aqueous NaCl droplets, only water evaporates leaving NaCl behind in an increasing concentration with time.

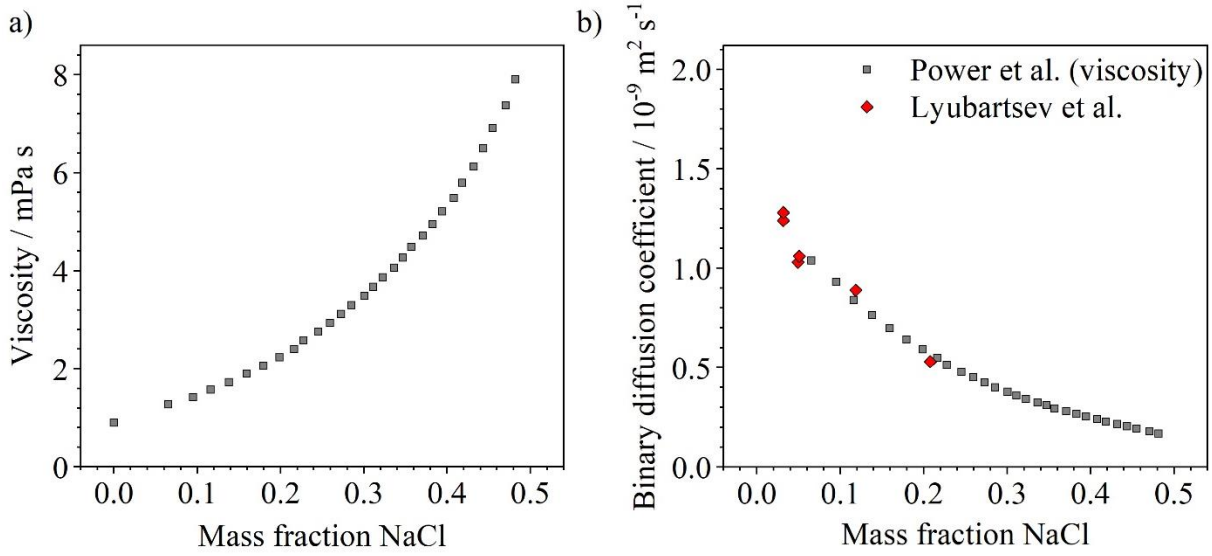

Figure 5-7: a) The viscosity of aqueous NaCl aerosol as measured using optical tweezers (Power et al.[273]), which are converted to a binary diffusion coefficient in b) using the Stokes-Einstein relation and a Stokes radius of 0.163 nm, compared to a molecular dynamics simulation by Lyubartsev et al.[274]

A supersaturation value of 2.04 was set as a limit to terminate the model if this concentration is reached at any location within the evaporating droplet. This value is the supersaturation of an equilibrated NaCl droplet at a water activity of 0.45 at 293 K, as shown in Fig. 5-5. A supersaturation of 2.04 corresponds to a concentration of 648 g L^{-1} at 293 K and 654 g L^{-1} at 318 K. A fuller description of the model implementation is provided in a recent publication.[261]

Alternative values for the critical supersaturation, S_c, for homogeneous nucleation of NaCl have been reported. Desarnaud et al. performed experiments in micro-capillaries with gradual increasing concentration of an aqueous NaCl solution, and they reported S_c to be 1.6.[198] We attribute that the value of S_c determined by Desarnaud is lower than that used in this study to the fact that the micro-capillary

study was performed with bulk NaCl in a confined environment with, possibly, the presence of container walls or dust to induce heterogeneous nucleation at a lower level of supersaturation than that could be reached in the aerosol phase. In addition, Utoft et al. and Tang et al. reported the value of S_c to be 1.9 and 1.87, respectively.[262,276]

5.5.1 Modelled Radial Concentration Profiles Droplets During Drying

The modelled concentration profiles for the four datasets in Fig. 5-4 are shown in Fig. 5-8. The data is presented in terms of concentration (g L^{-1}) as a function of distance from the centre of the droplet, assuming spherical symmetry about the centre, for every 0.02 s. Whilst initial concentrations of droplets in experiments are reported in terms of a mass fraction, the concentration of NaCl throughout drying is plotted in terms of a molarity (g L^{-1}) as this takes into account the fact that the solution density changes as the droplets become more concentrated.

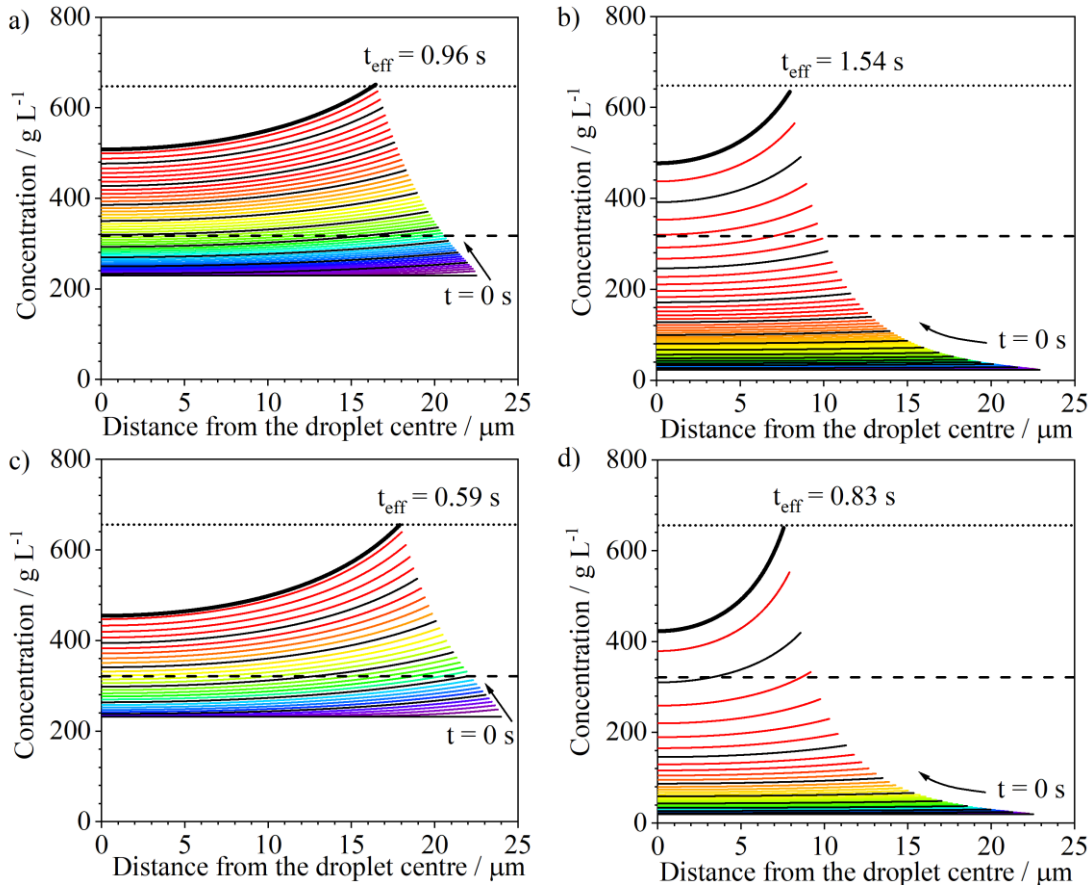

Figure 5-8: The modelled radial concentration inside an aqueous NaCl droplet during evaporation in 0% RH, at different gas phase temperatures and with varying starting concentrations. The initial mass fraction of NaCl and temperature for each dataset are: a) 0.2, 293 K, b) 0.02, 293 K, b) 0.2, 318 K and d) 0.02, 318 K. Lines are plotted every 0.02 s timestep, with black lines every 0.1 s for clarity. The final black line shows the concentration at the predicted nucleation time, i.e. at a supersaturation of 2.04 when the model was terminated. Dashed and dotted lines indicate the bulk solubility limit and a supersaturation of 2.04, respectively.

In all four datasets in Fig. 5-8, the model predicts that there is a degree of surface enrichment during evaporation leading to a higher concentration of NaCl at the surface than at the centre of the droplet. This suggests that nucleation of a NaCl crystal most likely occurs at the droplet surface where the concentration is highest. The concentration profiles across the droplet radius throughout evaporation vary when the initial starting concentration or gas phase temperature is changed. Comparing Fig. 5-8a with Fig 5-8b, i.e. the two experiments performed at 293 K, we observe that for the higher initial concentration droplet a slight concentration gradient (enriched surface) takes shape early in the evaporation process, which steadily increases while the droplet dries. The lines are quite evenly spaced throughout the drying process, and eventually the critical supersaturation is reached at the droplet surface and nucleation occurs. Conversely, the droplet with the 0.02 MFS starting concentration (Fig. 5-8b) maintains a homogeneous concentration profile for most of the evaporation process and only begins to show any surface enrichment at approximately 1.45 s when the surface concentration rises very steeply. An increase in temperature from 293 K to 318 K leads to an increase in the magnitude of the surface enrichment during evaporation for both initial starting concentrations, as shown in Fig. 5-8c and d. Whilst this increase in temperature leads to an increase in the diffusivity coefficient, acting to maintain a homogeneous composition, it also leads to an increase in the evaporation rate.

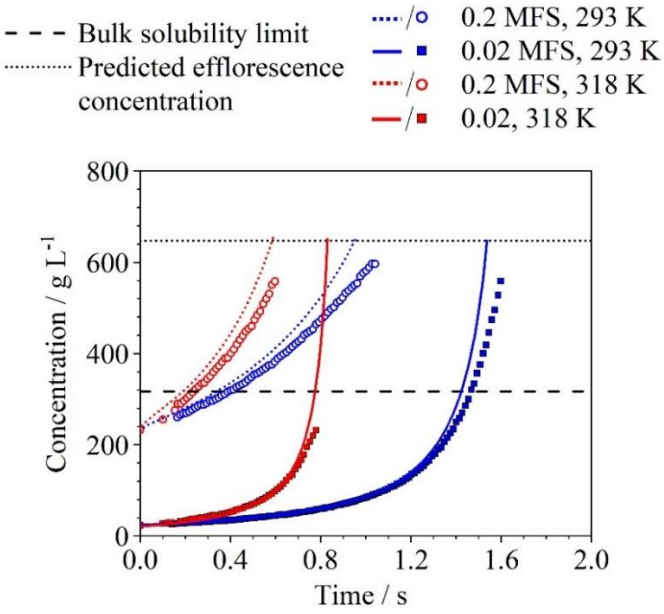

Figure 5-9: The surface concentration of NaCl during evaporation of an aqueous NaCl droplet in different gas phase temperatures and with differing initial mass fraction of solute, as calculated using the diffusive transport model (lines). The modelled surface concentration is compared to the volume-averaged concentration of the droplets calculated from the experimental radius (datapoints).

The effect on the surface concentration of the evaporating aqueous NaCl droplets from an increase in gas temperature is shown in Fig. 5-9, where the surface concentration as a function of time is plotted (lines). All four datasets show a surface concentration that exhibits a positive deviation from the volume-averaged concentration (datapoints), demonstrating that the surface is becoming enriched

during evaporation. For the two datasets with the higher initial concentration 0.2 MFS, this positive deviation occurs almost immediately into the evaporation process, demonstrating that the surface is becoming enriched in NaCl. However, for the droplets of 0.02 MFS at 293 K and 318 K, this positive deviation only really becomes evident towards the end of the drying process. For the case of the 0.02 MFS droplet evaporating into 318 K this deviation is seen after 0.6 s and results in a very steep rise in the surface concentration of the droplet. When the model predicts efflorescence in this droplet, the surface concentration is 233 g L^{-1} greater than at the centre of the droplet.

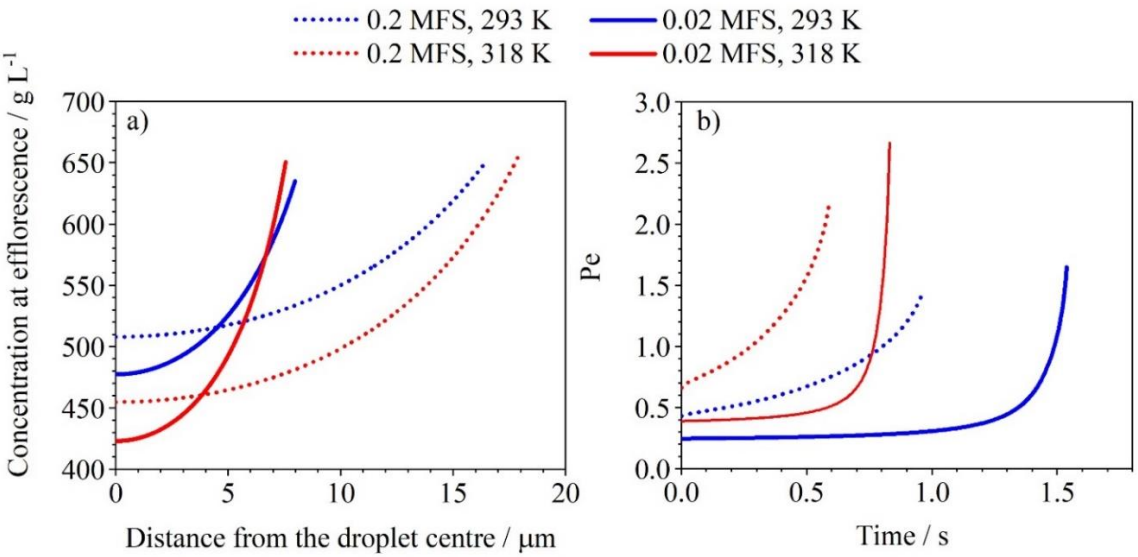

Figure 5-10: a) The concentration of NaCl across the radial co-ordinate of an evaporating aqueous NaCl droplet at the point of efflorescence, as predicted by the diffusive transport model. Droplets are drying into varying gas phase temperatures with different starting mass fractions of NaCl. b) The Péclet number for each droplet throughout the evaporation.

The initial Péclet numbers reported in Table 5-1 are calculated using the methods used by Vehring et al.[44] Typically, a Péclet number lower than 1 indicates that a droplet will maintain a homogeneous composition throughout evaporation. However, the modelled results in Fig. 5-8 show that the surface of the NaCl droplet becomes enriched leading to a non-homogeneous composition at the time of efflorescence even though the initial Péclet number is less than 1. This can be attributed to a decrease in the binary diffusion constant due to a rising viscosity as the droplet becomes more concentrated in drying. Hence, a time-dependent Péclet number, considering the diffusion constant at the surface, is more appropriate to visualise the development of morphology in a drying droplet, and this is shown in Fig. 5-10a. The concentration across the droplet radial profile at the time of efflorescence for each dataset is shown in Fig 5-10b, illustrating the level of surface enrichment at efflorescence. The figure shows that the order of the datasets in terms of the degree of surface enrichment is the same as the order of the Péclet number at efflorescence. This observation is consistent with the use of the Péclet number,

as outlined by Vehring et al.; a larger Péclet number leads to greater surface enrichment and, hence, a more hollow particle.[44]

5.5.2. Comparison Between Model-Predicted Efflorescence Times and Experimental Data

The experimentally determined efflorescence times are presented alongside the model-predicted efflorescence time using a supersaturation cut-off value of 2.04 ± 0.02 in Fig. 5-11a. The model identifies an efflorescence time in good quantitative agreement with the measurements, assuming a value of S_c = 2.04. For the two datasets at 293 K, the model-predicted efflorescence time is within the standard deviation of the experimental time. For the two experiments performed at 318 K, the experimentally determined efflorescence times are earlier in both cases than the model prediction. This can be attributed to the fact that the evaporation rate is large in these measurements, and hence, the droplet is likely to undergo significant evaporative cooling. As a result, the temperature-dependent binary diffusion constant of the solution in the droplets is possibly overpredicted by the model. A droplet that is cooler than the model anticipates would have a slower rate of diffusion than expected, leading to a greater Péclet number and higher degree of surface enrichment than expected from the model. Hence, droplets would reach the critical concentration for crystal nucleation at an earlier time than predicted. If the model took into account the fact that the droplet temperature could become suppressed during evaporation, the model may accurately predict the efflorescence time for the two datasets at 318 K.

The data provide justification for using the value of S_c = 2.04 ± 0.02 as the critical supersaturation with which to terminate the model. The deviation between the measured crystallization time, $t_{measured}$, and the modelled crystallization time, t_{model}, as a function of the value of S_c used to terminate the model is shown in Fig. 5-11b. Only the two experiments performed at 293 K are shown, as the critical supersaturation value is determined by the E-AIM model, which was based on experiments performed at room temperature. A value of S_c = 2.04 ± 0.02 yields consistency between the modelled and experimental crystallization times for the two salt solution concentrations reported here. For measurements performed at 318 K, a value of S_c = 2.04 is still used. However, the increase in the NaCl bulk solubility limit with temperature, from 317.6 to 321.7 g L^{-1}, is explicitly included in the model when calculating supersaturation.

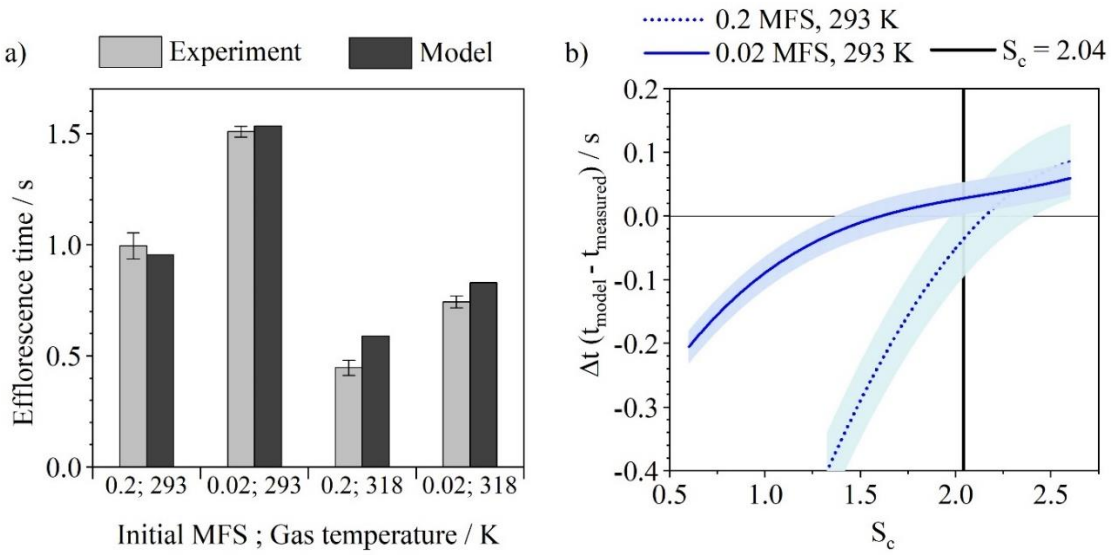

Figure 5-11: a) The experimentally determined efflorescence time of the droplets in the EDB compared to that predicted by the model, for the different gas-phase temperatures and initial starting concentrations. The error bars in the experimental data correspond to the standard deviation in efflorescence times averaged over more than 100 droplets. b) Validation for the use of S_c = 2.04 ± 0.02 to terminate the model. The deviation between experimentally determined efflorescence times of evaporating NaCl droplets under two conditions and the modelled crystallisation time is plotted for different S_c values used to cease the model. b) only shows data for 293 K, as the critical supersaturation value is determined by the E-AIM model, which was based on experiments performed at room temperature.

5.6. SEM Images of Dried NaCl Particles

The experiments of aqueous 0.02 MFS NaCl and 0.2 MFS NaCl solutions evaporating into 318 K have been repeated in the falling droplet column (FDC). Dried particles were collected from the falling droplet column with aqueous NaCl droplets evaporating under identical conditions to the EDB experiments performed at 318 K. The EDB evaporation data demonstrated that the droplets with both initial starting conditions at 318 K would nucleate crystals within ~ 0. 8 s, indicating that by the time the droplets in the FDC reached the glass slide at the bottom of the column, they should have undergone complete crystallisation and should be fully dry.

The SEM images of particles prepared from evaporating 0.02 MFS and 0.2 MFS NaCl aqueous solutions in 0% RH at 318 K, with initial droplet sizes of ~ 25 µm, are shown in Fig. 5-12. There are clear differences in the dried particle morphology between these two samples. Several SEM images are analysed using ImageJ to quantify the particle size and crystal size in the dried particle samples, and the results are shown in Fig. 5-13 and 5-14, which will be discussed in the next section.

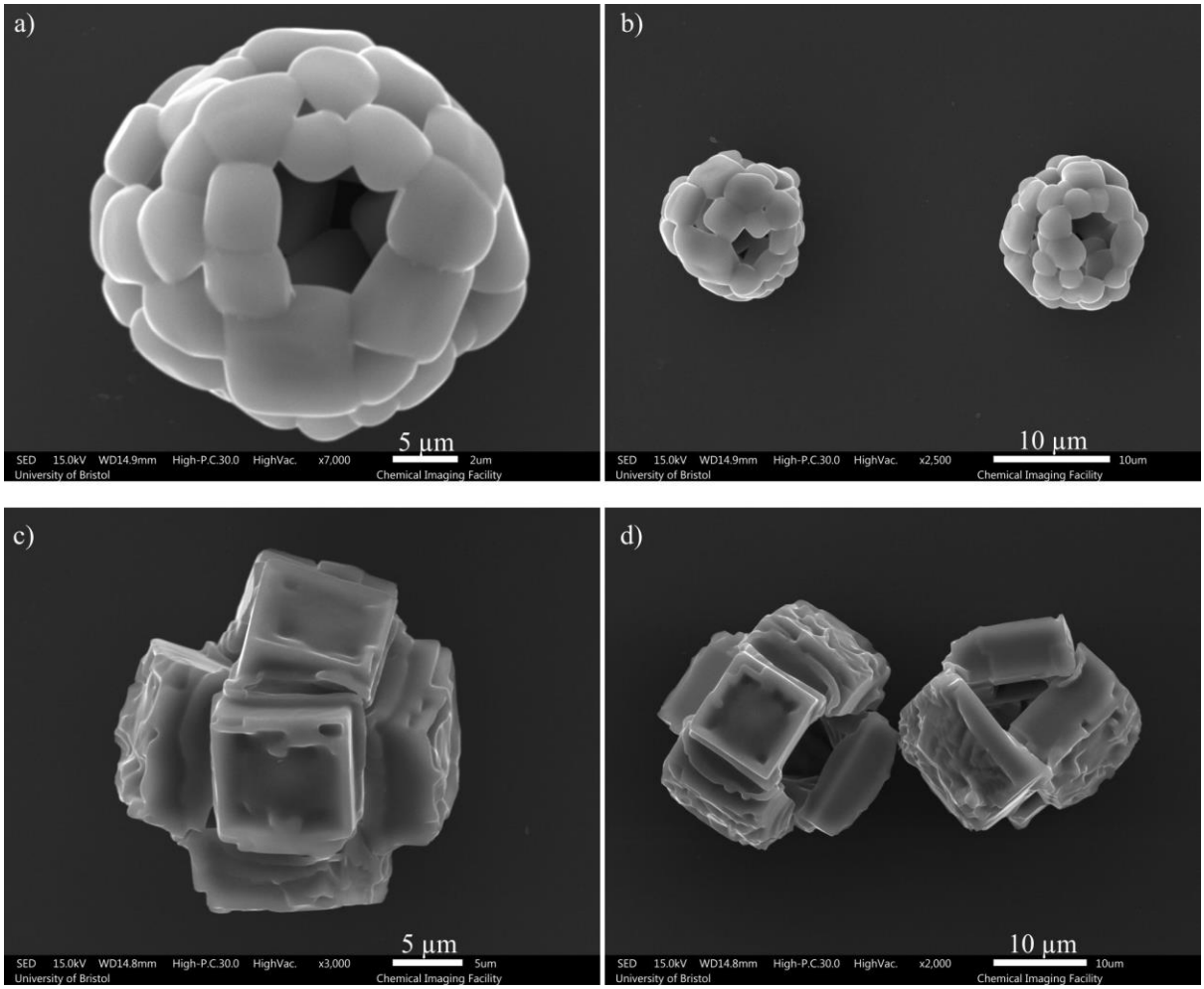

Figure 5-12: SEM images of dry NaCl particles, prepared by evaporating aqueous NaCl in a falling droplet column 318 K and 0% RH. Starting mass fraction of NaCl in the droplets is 0.02 for a) and b), and 0.2 for c) and d).

Both sets of dried particles are crystalline, made up of several large crystals that are joined to form a central hollow cavity. This indicates that crystal nucleation is initiated at the surface of the droplets, in several places, with the resulting different crystals growing across the surface of the drying droplet and eventually meeting when the droplet runs out of water. This observation is in agreement with the EDB data in the previous section of this chapter in which the model predicted a high degree of surface enrichment in the evaporating droplets; the surface is the place in the drying droplet with the highest degree of supersaturation and hence a larger driving force for crystal nucleation. While the droplets evaporate, the model predicts that the concentration of NaCl at every point in the droplet continues to rise, but in all datasets, it is the surface of the droplet that first passes the critical supersaturation required for crystal nucleation.

5.6.1. The Volume of Dried Particles formed through Evaporation of Aqueous NaCl Droplets

The droplets with the higher starting concentration of NaCl produced larger dried particles, due to the larger degree of non-volatile component present in the formulation. The volume of the dried particles from the images, averaged over 39 particle images for the 0.2 MFS dataset and over 20 particles images for the 0.02 MFS dataset are compared in Fig. 5-13.

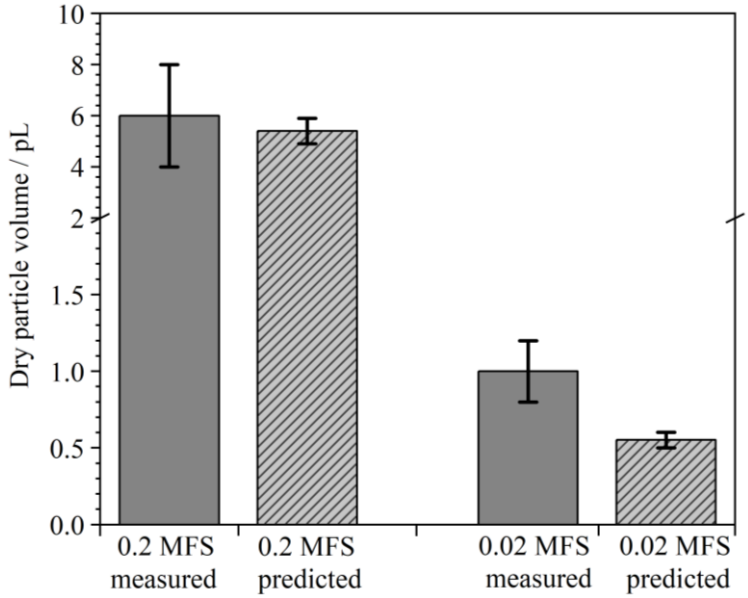

Figure 5-13: The volume of NaCl particles dried at 318 K with different initial concentration, as calculated from SEM images, compared to a predicted volume assuming that the mass in the NaCl droplet dries to form a single dense cube.

The dried NaCl particle volume is estimated from the SEM images including any empty space inside the dried particle by fitting a cube-shape to the dried particles from the 0.2 MFS dataset, as they resemble a cube-like structure. A spherical shape is fitted to the 0.02 MFS due to their spherical-like morphology. In addition, a 'predicted volume' of dried particle is shown, which is calculated as follows. Initial droplet radii for the falling droplet column experiment are assumed to be the same as the average from the EDB data, which is 22.9 ± 0.7 µm. From a parameterisation the density of 0.202 MFS and 0.0233 MFS NaCl solutions is determined to be 1149 kg m^{-3} and 1015 kg m^{-3}, respectively.[175] Given that NaCl typically forms cubic crystals,[277] with a density of 2165 kg m^{-3},[218] we can predict the size of the dried particle if it were to dry to form one single perfect cube. For the initial concentrations of NaCl of 0.202 MFS and 0.0233 MFS, the size of this solid homogeneous cube is 5.4 ± 0.5 pL and 0.55 ± 0.05 pL, respectively. The 0.2 MFS dataset has dried particles that are slightly larger, but within the experimental uncertainty, of the predicted solid cube size. However, the 0.02 MFS droplets evaporating in the falling column dried to form solid particles that are twice as large as the predicted particle volume. The discrepancy between the estimated particle volume from the SEM images and the predicted particle

volume from the starting concentration is a result of the dried particles being hollow, arising from the surface enrichment during drying.

5.6.2. Quantity, Size and Morphology of the Crystals in Dried NaCl Particles

Forming a crystal out of a supersaturated solution via homogeneous nucleation requires the formation of an initial surface between the new crystal and the liquid surrounding it. The surface tension associated with the interface between the two phases is unfavourable for the free energy of the system. Classical nucleation theory considers the Gibbs free energy change of crystallisation using the competition between the favourable free energy change of arranging contact ion pairs into an organised crystal nucleus, and the energetically unfavourable formation of the boundary between the liquid and the nucleus.[197,278,279] Enough contact ion pairs need to come together to form a cluster of a critical size that the free energy gain of forming a surface is outweighed by the free energy loss of all of the ion pairs forming a crystal. Once a crystal nucleus has been created, the boundary between crystal and solution has already been formed for other ions in the surrounding supersaturated solution, so it is more likely for them to arrange appropriately to join this crystal than to overcome the surface energy barrier in forming a new crystal nucleus. Hence, crystal growth occurs and spreads through the droplet. However, if the concentration rises very rapidly all over the droplet surface, there is an increased likelihood that another crystal nucleus forms at an identical time in another supersaturated area before the growth of the first crystal has reached that area. Thus, the number of crystals in a final particle could be indicative of how rapidly the surface concentration is rising: more crystals suggests that the surface concentration rises so rapidly that multiple nucleation sites form on the surface before the crystal growth of the first crystal reaches that part of the solution.

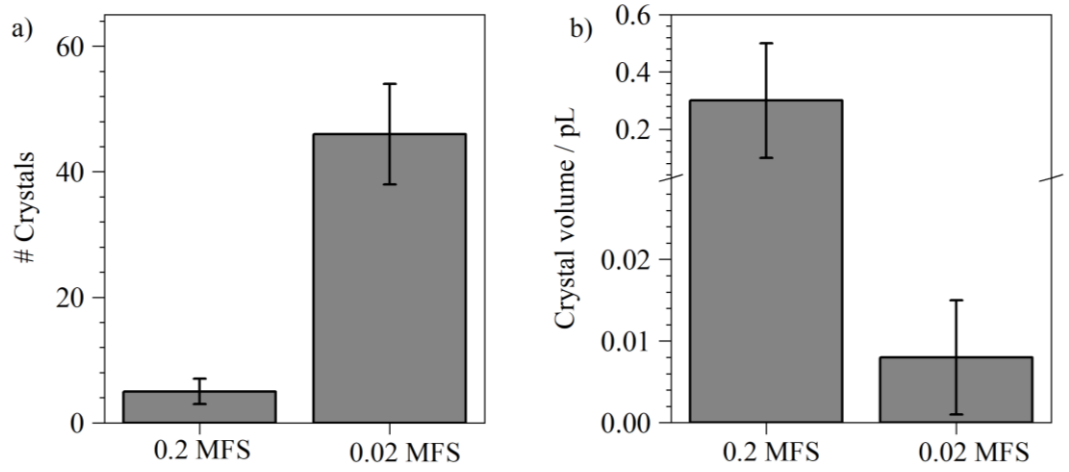

Figure 5-14: a) The average number and b) the average volume of NaCl crystals making up the particles dried at 318 K with different initial concentration, as calculated from SEM images.

From Fig. 5-12 it is evident that there are more crystals in the dried particles formed from drying the 0.02 MFS NaCl solution than from the 0.2 MFS NaCl solution. This suggests that in the lower concentration droplet, the surface concentration rises much more rapidly at the end of the drying process leading to more nucleation sites at the surface than the higher concentration solution. This observation confirms the model results in Fig. 5-9, that show a very steeply rising concentration gradient in the droplet of 0.02 MFS at this temperature of 318 K.

The crystals in the dried particles formed from the 0.02 MFS dataset are generally much smaller than those crystals in the dried droplets with the larger initial starting concentration (Fig. 5-14b). This is expected as, first, there are more crystals forming in the 0.02 MFS dataset, as well as there being one tenth of the mass of NaCl in the lower concentration dataset, so the smaller mass of NaCl spread across more crystals in the dried particles means each crystal is smaller in mass and volume than the crystals in the 0.2 MFS dataset.

The general 'spherical shape' of the dried particles appears to be controlled by the rate of crystal growth. It is expected that once a crystal nucleus is formed, it will grow into the supersaturated solution surrounding it, until either all of the droplet has crystallised or until that crystal meets another crystal that is also spreading across the surface. When the first crystal nucleus is formed, there is still plenty of water in the droplet with a continued drive for evaporation, so drying and droplet shrinkage may still occur during the crystal growth process. There is, hence, a competition between the rate of crystal growth and the rate of further evaporation. The images of the dried particles from the 0.02 MFS drying experiment show a near spherical morphology, the same shape as the liquid aerosol droplets. This indicates that the crystals formed quickly, while the droplet was still very round and that, possibly, the rate of crystal growth outweighed the rate of further droplet shrinkage. In contrast, the dried particles from the 0.2 MFS sample have lost the spherical shape of a droplet, and instead look like a network of connected cubes. After crystal nucleation, the rest of the droplet did not 'instantly' crystallise. Rather, the droplet continued to evaporate and there was movement of the remaining NaCl solution to join onto the crystals in a way that led to more ordered cubic crystals than in the 0.02 MFS particles.

5.6.3. Comparison of the Dried Particle Morphology formed through Rapid and Slow NaCl Droplet Drying

Aqueous droplets of 100 g L^{-1} NaCl (0.094 MFS) were dried in the falling droplet column in ambient conditions, and the collected dried particles are shown in Fig. 5-15. This experiment had no N_2 gas flow directing the droplets down the column, so the RH was ~ 40% and the temperature was ~ 293 K. An EDB experiment replicating these conditions is performed and the evaporation profile is shown in Fig. 5-16a, compared to the two 318 K evaporation experiments for the other SEM images in this chapter.

The aqueous NaCl droplet evaporating in ambient conditions shows a much slower evaporation rate, $1.343 \pm 0.005 \times 10^{-10}$ $\mu m^2 s^{-1}$, and would have a much lower Péclet number. Fig. 5-16b compares the modelled surface concentration of the two droplets dried at 318 K, i.e. the same data as shown previously in Fig. 5-9, to the drying of the 0.1 MFS NaCl droplet in ambient conditions. The much slower drying rate suggests that the solute concentration across the whole droplet can be assumed to be homogeneous throughout most of the drying, and it is not expected to show a deviation in the surface concentration from the volume-averaged concentration.

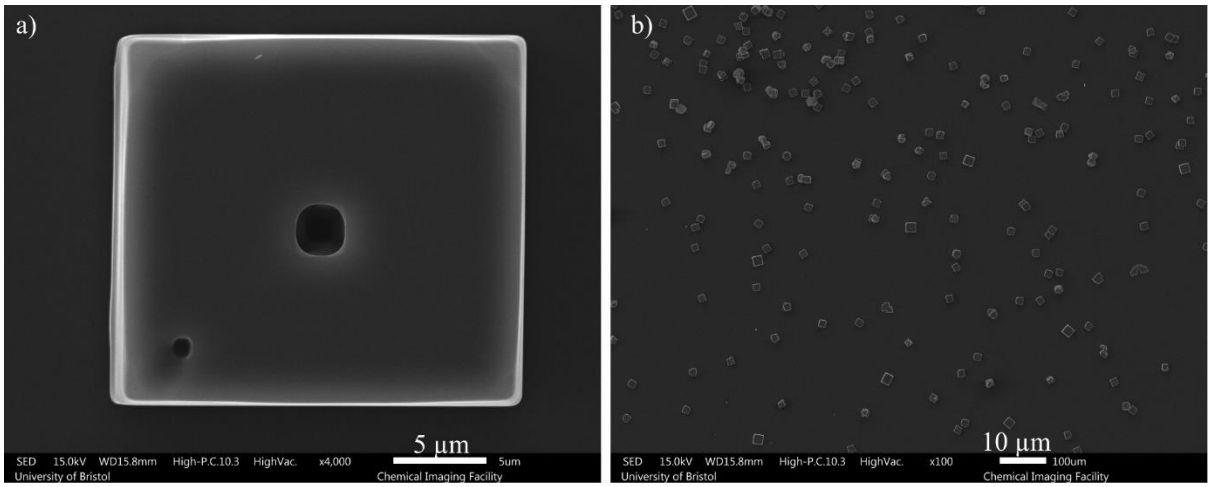

Figure 5-15: SEM images of dry NaCl particles, prepared by evaporating 0.1 MFS aqueous NaCl in a falling droplet column at 293 K and ~ 40% RH.

The SEM images confirm that the ambient NaCl drying experiment leads to dried particles that form a single crystal. The particles formed from the ambient drying process do not appear to be hollow and have only a very small hole that is face-centred in the cubic particle. This is stark contrast to the hollow spherical nature of the very rapid 0.02 MFS droplets dried at 318 K in Fig. 5-12.

This ambient dataset adds a third point to the trend shown in the change of NaCl particle morphology with drying conditions. As the drying rate becomes faster, there is a greater degree of surface enrichment during drying due to the higher Péclet number. With a greater drying rate, the particles become more hollow with a lower density. The rate at which the surface concentration of NaCl increases affects how many crystals are formed: in the ambient drying process the concentration is expected to be uniform across the whole droplet, and rises very steadily. Once one crystal nucleus is formed it causes crystal growth to spread throughout the entire droplet leaving one single crystal as the dried particle. As discussed previously, for the droplets drying rapidly at 318 K, the rising concentration at the surface leads to multiple nucleation sites forming with a final particle that is made up of many smaller crystals.

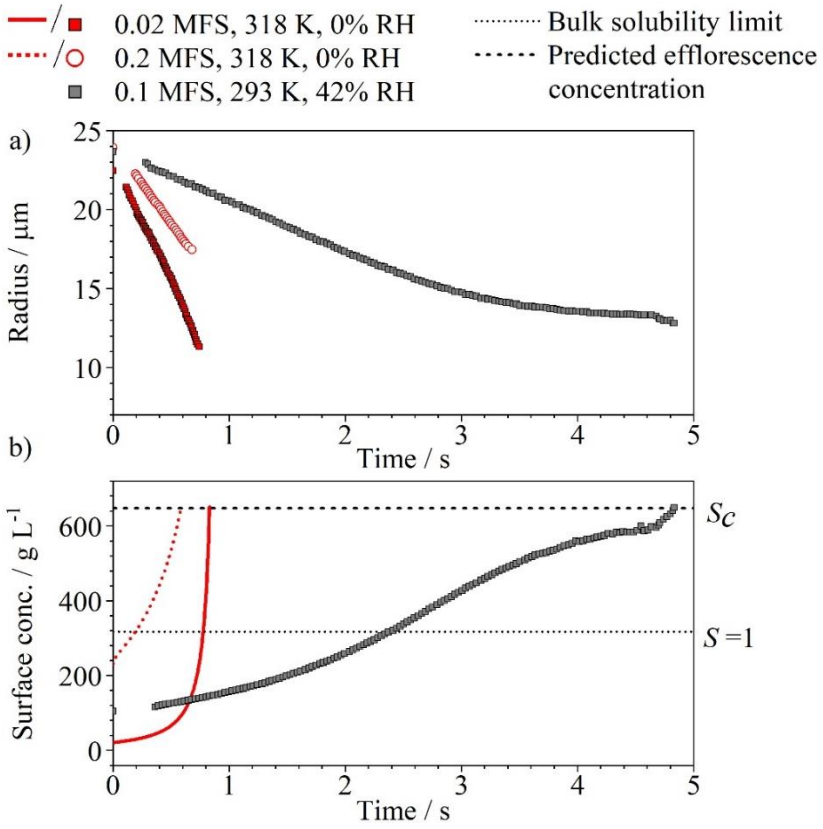

Figure 5-16: a) The radius throughout evaporation of an aqueous NaCl droplet drying in different RHs, gas phase temperatures and with different initial NaCl concentrations and b) the surface concentration throughout drying. The data at 318 K is predicted by the diffusive transport model, and the data at 293 K is the volume-averaged NaCl concentration calculated from the radius datapoints in a).

5.7. Chapter 5: Summary and Future Work

This chapter has explored the evaporation kinetics of aqueous NaCl solution droplets using the combination of the electrodynamic balance, SEM imaging and a concentration model. The EDB allows for direct measurements of the evaporation rates of rapidly evaporating droplets, as well as detection of the formation of a crystal nucleus from the instant that the phase function in the light scattering becomes disrupted. A micro-droplet dispenser can produce droplets with high reproducibility in the initial droplet radius, allowing for experiments with several hundred droplets in a series to be carried out. Thus, statistical data of when an evaporating NaCl droplet nucleates crystals have been retrieved, under varying environmental conditions. Not only does NaCl show a remarkable degree of reproducibility regarding the time at which identical droplets effloresce but also there is a clear dependence of the crystallization time on the temperature and evaporation rate. The internal concentration profiles at different radial points within the droplets are inferred using a Fickian integration model. The basis for identifying solute crystallization is that NaCl achieves a particular level of solute supersaturation at

which the nucleation rate of forming a crystal increases by orders of magnitude, such that nucleation becomes instantaneous.[175] When assuming this, a remarkable level of consistency is observed in interpreting the crystallization time across all drying environments investigated here, if crystallization is assumed to occur at a critical supersaturation of solute of 2.04 ± 0.02, a value that is always achieved first at the droplet surface. Particles collecting from drying events in the falling droplet column, with identical drying conditions to those studied in the EDB, were imaged using SEM. The particle morphology was shown to vary drastically from different drying conditions, with, in one instance NaCl drying into a dense cube and in another forming a hollow sphere. This demonstrates the sensitivity of the final particle shape, size and density to the evaporation conditions, which would strongly affect the resulting properties such as solubility and powder flowability. This work highlights the importance in understanding the drying kinetics of droplets in an industrial spray dryer for producing a powdered product with desirable properties.

Aqueous NaCl has been shown to serve as a useful model system to study the crystallization of drying droplets and the dependence of the time required to achieve crystallization on the evaporation rate, as governed by the initial solute concentration and gas-phase temperature. However, there is a period in the drying process that has been neglected in this study: the period between crust formation (the time at which the supersaturation is achieved) and termination of the drying process. If an aerosol droplet enters conditions drier than the ERH, it still may not necessarily precipitate and may not immediately reach a threshold saturation. There will be an interplay between the nucleation rate and drying rate. If a droplet is dried very quickly and the internal components have a very low crystal nucleation rate, the aerosol may lose water more rapidly than crystals can form and the droplet would become amorphous solid.

In extension to the work presented in this chapter, future work should focus on the drying and crystallisation kinetics of increasingly complex solutions, such as those containing multiple solutes, solvents or mixtures of inorganics and organics. In addition, a study that can observe the drying process following crust formation would be very useful for the field of spray drying. In the EDB, the light scattering that is used to size the aerosol droplets becomes disrupted upon formation of a crystal nucleus. Hence, the process of how crystal growth proceeds and whether such growth may be affected by a rising viscosity in the end-stages of drying is potentially an area of future interest.

Chapter 6

Evaporation and Nucleation of Aqueous Droplets of Sodium Nitrate and Other Nitrates: Crystalline vs. Amorphous Particle Formation

---

Chapter 6 is based on a paper that is currently under review in The Journal of Physical Chemistry B, entitled: *Drying and Crystallisation of Evaporating Sodium Nitrate Aerosol Droplets*, for which I am the first author, and a paper in The Journal of Chemical Physics, for which I am second author.[280] I collected, analysed and interpreted all experimental data presented in the manuscript. I discuss a model that was developed using my experimental data by Dr. Joshua Robinson, a post-doctoral researcher in the School of Physics at the University of Bristol. I present modelling results that were retrieved by Dr. Robinson that provide insight to the experimental data (Fig. 6-16 and Fig. 6-17).

In Chapter 5, I discussed the evaporation kinetics and nucleation behaviour of aqueous sodium chloride droplets. I demonstrated the high reproducibility in large populations of sodium chloride droplets to nucleate crystals at the same evaporation time and at the same degree of solute supersaturation. In this chapter I will present results from evaporation experiments of aqueous droplets containing sodium nitrate solutions, showing that the nucleation propensity is much more complicated than in NaCl, and can be strongly affected by the evaporation conditions, such as temperature, RH and initial solute concentration. I will compare sodium nitrate to the results from evaporation data of other nitrates with alkali metal cations ($LiNO_3$, KNO_3 and $RbNO_3$) to show how variations in properties such as ionic radius and hygroscopicity can affect the nucleation behaviour in evaporating aerosol droplets.

6.1. Previous Studies of $NaNO_3$ Crystallisation

The crystal nucleation behaviour of sodium nitrate has been studied previously as it is important in atmospheric chemistry, being a major component of aged sea salt aerosol.[281] Sodium chloride aerosol droplets are readily produced from sea spray, which can then react with nitrogen oxides such as NO_2, HNO_3 or N_2O_5 to form sodium nitrate aerosol.[282] Sodium nitrate is thus of particular interest in climate modelling, as it can undergo photolysis under UV radiation leading to free radicals which, in the presence of organics, can induce further reactions to form secondary organic aerosol.[283] Hence, an understanding of the crystallisation and the phase of sodium nitrate aerosol has importance for quantifying the photochemical lifetime of particulate nitrates.

Nucleation of crystals out of solution in an aerosol droplet is often described in terms of an absolute "efflorescence RH" (ERH). However, sodium nitrate does not exhibit a well-defined ERH, and efflorescence has been observed to occur over a range of RHs from 0.05% to 40%. Ghorai and Tavanski reported the RH at which $NaNO_3$ crystallised as 35%, measured using X-Ray Spectromicroscopy.[284] Tang and Munkelwitz levitated $NaNO_3$ droplets in an EDB and evaporated them in a range of RHs, and observed efflorescence in individual droplets between 0.05% and 30% RH.[285] Lee et al. [286] supported micron-sized $NaNO_3$ droplets on a TEM grid and studied their propensity to crystallise. They reported different types of droplets, each of which had different efflorescence and deliquescence RHs (between 18-45%, and 73-75% respectively), with some droplets not appearing to undergo either process. Likewise, in optical tweezers, $NaNO_3$ droplets have been evaporated slowly to as low as 10% RH without crystallisation occurring, showing that a liquid droplet at such high levels of solute supersaturation can still remain in equilibrium with the gas-phase RH.[158] We will demonstrate that the nucleation of $NaNO_3$ cannot be described by an ERH and by a thermodynamic critical supersaturation. By observing distributions of nucleation events across many different drying conditions, we show that the drying kinetics leads to different outcomes in the competition between crystalline and amorphous particle formation, which explains the inconsistency in the reported ERH in the above studies. A combination of EDB measurements, SEM imaging of dried particles and a numerical model are used.

6.2. Comparison Between $NaNO_3$ and NaCl Nucleation Behaviour

A series of 100+ droplets containing an aqueous solution of $NaNO_3$ (0.2 MFS, initially) was evaporated in the EDB at 293 K and in a dry N_2 atmosphere. The time at which the formation of a crystal nucleus was observed in a drying droplet, from the disruption in the light scattering, is shown in Fig. 6-1a. The data for $NaNO_3$ are plotted alongside data for the observed nucleation data of aqueous NaCl (also 0.2 MFS, initially).[261] First, the nucleation time for $NaNO_3$ is consistently later than that for the same starting concentration of NaCl droplets, which highlights the higher bulk solubility limit of $NaNO_3$ compared to NaCl (0.465 MFS compared to 0.265 MFS,[218] respectively). Second, the distribution in time over which different droplets in the series nucleated crystals is very different between NaCl and $NaNO_3$. Where all of the NaCl droplets nucleated crystals reproducibly after 1 s into the evaporation process with very little variation in that time, the $NaNO_3$ droplets nucleated crystals over a broader time distribution, with most droplets nucleating between 1.6 s and 2.4 s into the drying process, but with some nucleation events occurring later. Also, 2.5% of the droplets did not show any nucleation event in the time at which the droplet remained trapped for an experimental window of 10 s, so are not plotted on this figure. Throughout the time that such a droplet remained trapped it continued to show regularly spaced fringes in its scattering pattern, implying that the droplet continued to be homogeneous and spherical.

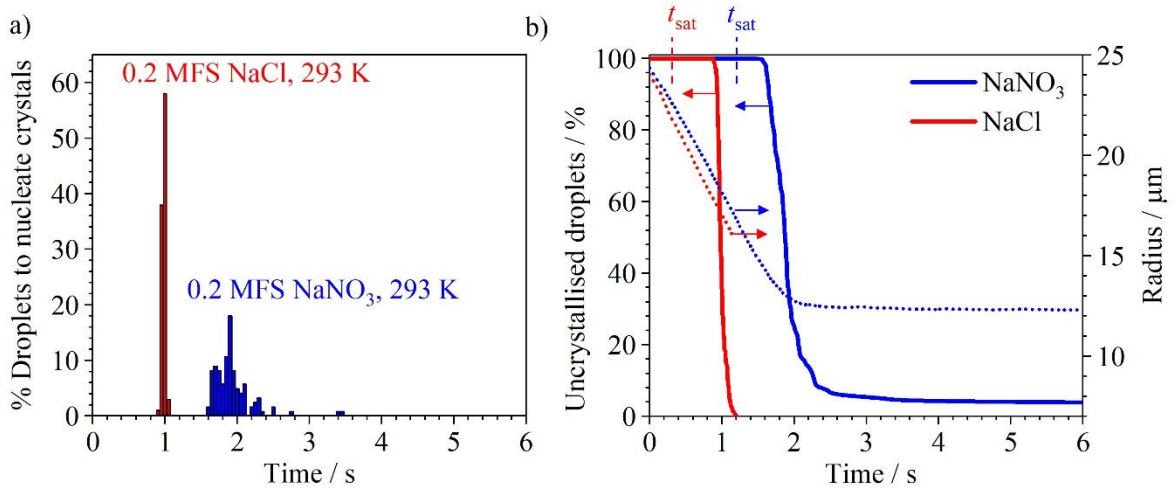

Figure 6-1: The time at which nucleation was observed for a population of 100+ $NaNO_3$ droplets (0.2 MFS, starting radius ~ 24 µm) as they evaporated in the EDB in 0% RH and 293 K, compared to a population 0.2 MFS NaCl droplets evaporating under the same conditions. b) The data in a) plotted as a percent of droplets that have not yet nucleated crystals as a function of time. The dotted lines show the radius evolution of the longest surviving $NaNO_3$ droplet and NaCl droplet in the datasets. The time of solute saturation i.e. when the droplet passed the bulk solubility limit, is indicated as t_{sat}.

Fig. 6-1b shows the same data as in panel *a* but plotted in terms of a temporal loss of uncrystallised droplets, i.e. the line drops down from 100% whenever a nucleation event was observed in a droplet at that period into the evaporation process. The NaCl data decline immediately from 100% to 0%, demonstrating the reproducibility in the crystal nucleation process under these conditions. However, the $NaNO_3$ data shows a decay of uncrystallised droplets that does not reach 0% after the end of the experimental window.

The decay function of the $NaNO_3$ data in Fig. 6-1b is similar to that for radioactivity. Like radioactive decay of a sample, homogeneous nucleation is a stochastic (i.e. random) process.[195,203] Considering one droplet in a long series of subsequent droplet experiments, the chance of such a droplet crystallising is independent of when the other droplets crystallised. This is similar to observing the radioactive radiation collected from a collection of atomic nuclei; it is not possible to predict when one single atom will exhibit radioactive decay but by considering the population of atoms, one observes a half-life of the population and can hence calculate the decay rate. However, the aqueous $NaNO_3$ droplets in Fig-6-1b were exposed to increasing levels of supersaturation as they dried, maintaining a constant supersaturation only after ~ t = 2 s. Thus, an exponential function does not fit the $NaNO_3$ data in the figure and would only describe the decay after t = 2 s.

The droplets evaporating in the EDB have a very small initial volume (~ 60 pL) and the $NaNO_3$ and water used to make the solutions is of very high purity, so the chance of dust or contaminants being present and inducing heterogeneous nucleation is low. Hence we assume all nucleation events herein to be homogeneous. The veracity of this assumption is discussed later in Section 6.11.

6.2.1. Viscosity and Binary Diffusion Coefficients in $NaNO_3$ and NaCl Aerosol Droplets

The model results in Chapter 5 identified a critical solute supersaturation in aqueous NaCl solutions of 2.04, and if such a concentration is reached in a droplet then nucleation is observed.[261] For $NaNO_3$, Fig. 6-1 shows that there is clearly no 'critical solute supersaturation', as the droplets nucleate crystals at different times. Rather, upon reaching the bulk solubility limit the $NaNO_3$ droplets enter a 'crystallisation window',[268] within which there is a chance that nucleation may occur but there is still a degree of droplet-to-droplet variability in terms of the nucleation time. A possible reason behind this difference between the two solutions is the value of the viscosity that is reached in the aerosol droplets upon drying. Both NaCl and $NaNO_3$ solutions increase in the viscosity as the concentration rises. In Chapter 5, we showed that this increase in viscosity infers that the binary diffusion coefficient decreases, defined through a Stokes-Einstein relation. This decrease in the binary diffusion coefficient, coupled with a receding droplet surface caused by the evaporative flux, can lead to a build-up of the solute at the surface of the droplet during rapid evaporation, if the internal diffusional mixing cannot replenish the surface with water at the same rate that it evaporates. The viscosity of aqueous $NaNO_3$ solutions is compared to that of NaCl solutions in Fig. 6-2. The viscosity in aerosol droplets can be measured using coalescence experiments to very high concentrations, higher than that achievable typically in a bulk solution.[204] The data plotted in Fig. 6-2 were recorded using coalescence measurements with aerosol optical tweezers, and the data is from Baldelli et al.[158] for $NaNO_3$ and from Power et al.[273] for NaCl. The dashed lines indicate the bulk solubility limit for the solutes at 293 K.[218] A solution of $NaNO_3$ is, in general, higher in viscosity than the equivalent concentration of NaCl, but also $NaNO_3$ has a higher bulk solubility limit than NaCl so typically higher concentrations and greater viscosities of $NaNO_3$ can be reached before the chemical potential of the liquid state begins to present a significant driving force for crystal nucleation. By that point, the viscosity of $NaNO_3$ is much higher and this may present a barrier to nucleation through physically impeding the formation of contact ion pairs.

The binary diffusion coefficients in aqueous NaCl and $NaNO_3$ solutions are plotted in Fig. 6-2b. These values are calculated from a Stokes-Einstein relationship, as outlined in Chapter 5. The Stokes-Einstein equation relies on a value for the Stokes radius, a, to convert viscosity data into a binary diffusion coefficient. a was retrieved by calibrating a Stokes-Einstein relation of the viscosity in Fig. 6-2a against direct measurements of diffusion from bulk experiments for $NaNO_3$ [287] and molecular dynamics simulations for NaCl.[274] This led to the retrieval of a = 1.67 Å for $NaNO_3$ and 1.69 Å for NaCl, with a being the average Stokes radius of the ions in water. The resulting values in Fig. 6-2b show that for a $NaNO_3$ solution the binary diffusion coefficient can increase by orders of magnitude during evaporation, and this reduction in ionic mobility inside the droplet could be the reason for the apparent reduction in nucleation rate of $NaNO_3$ crystals at high concentration.

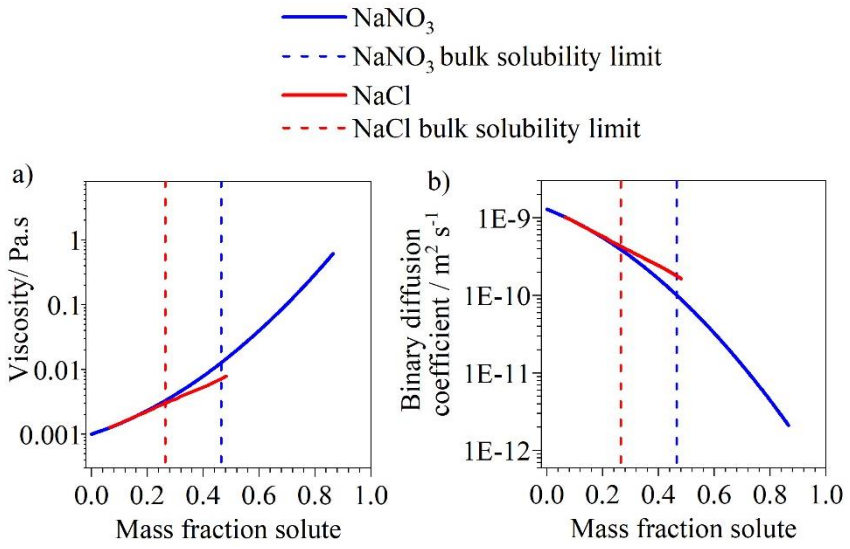

Figure 6-2: a) The viscosity of aqueous solutions of $NaNO_3$ and NaCl at 293 K as a function of mass fraction, measured using coalescence experiments with aerosol optical tweezers. The figure is plotted using data from Baldelli et al.[158] for $NaNO_3$ and Power et al.[273] for NaCl. b) The binary diffusion coefficient for $NaNO_3$ and NaCl, calculated using a Stokes-Einstein relationship, calibrated alongside experimental measurements of the diffusion coefficient for NaCl[274] and molecular dynamics simulations for $NaNO_3$.[287]

The evaporation data of the longest-surviving single droplet of aqueous $NaNO_3$ and aqueous NaCl are also plotted in Fig. 6-1b (dotted lines). For $NaNO_3$, in the first ~ 1 s of the droplets' lifetimes, water is continuously lost through evaporation but no nucleation occurs until after the bulk solubility limit (indicated by t_{sat}) is passed, and the droplets enter the crystallisation window. After this point, droplets in the series begin to nucleate crystals on a regular, if not predictable, basis, whilst the concentration continues to rise. However, if a droplet has not yet nucleated crystals before the time that the droplet has almost lost all water, after ~ 2 s, the viscosity then apparently becomes so high that the number of droplets nucleating crystals after this point reduces significantly. Essentially, the crystallisation window has now closed. This could be a reason behind why the number of remaining uncrystallised $NaNO_3$ droplets flattens-out after ~ 2 s, and why the 'corner' in the plot of the ratio of uncrystallised droplets is at a similar time to the apparent equilibration in the radius vs. time profile: it corresponds with when the water is lost from the droplet and the diffusion coefficient becomes very low. For NaCl, the viscosity never reaches higher values that 0.01 Pa s, so the diffusion coefficient is always high enough to allow sufficient ion mobility for nucleation.

The $NaNO_3$ data in Fig. 6-1b is, hence, an example of a situation wherein the crystallisation window is too short for the nucleation rate of crystals, and an amorphous particle is formed. It is known that viscosity can impede nucleation of crystals.[288] For example, sucrose and lactose rarely crystallise in a spray-dryer, as the evaporation of water from the aqueous solutions is very high at typical spray-drying temperatures, and droplets containing sucrose rapidly rise in viscosity over orders of magnitude, becoming glassy before crystal nuclei can form.[205,289] Indeed, previous thermodynamic studies have

shown that the viscosity of $NaNO_3$ solutions is important in determining the phase state. Ji et al.[290] studied the efflorescence RH of $NaNO_3$ droplets that contained increasing amounts of additional sucrose as a co-solute. The presence of sucrose delayed the ERH, i.e. it led to the droplets generally reaching higher levels of supersaturation (lower RHs) before $NaNO_3$ crystallisation was observed, as shown in Fig. 6-3. The work by Ji et al. discusses the variation nucleation behaviour across a droplet population, i.e. that at a specific RH, a certain number of aerosol droplets in a population will have nucleated $NaNO_3$ crystals and others not, consistent with our observation of stochastic behaviour in $NaNO_3$ nucleation. In some droplets, the presence of sucrose inhibited the nucleation of $NaNO_3$ crystals, and this is attributed to the slow diffusion of Na^+ and NO_3^- ions with a kinetic barrier to the arrangement of crystal nuclei. However, this work by Ji is a thermodynamic study, observing a proportion of droplets that nucleate $NaNO_3$ crystals at specific RHs and sucrose concentrations, and does not investigate the rate of crystal formation or the distribution of time over which different droplets in a population exhibit crystallisation during rapid drying.[290]

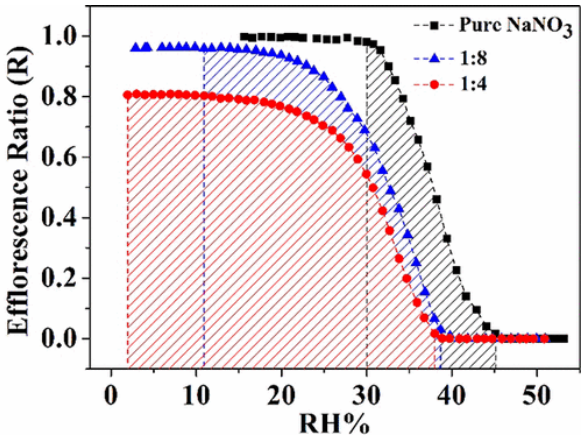

Figure 6-3: The ratio of aqueous $NaNO_3$ droplets or mixed $NaNO_3$/sucrose droplets with varying organic-to-inorganic ratios in a population to effloresce at different RHs in a dehydration experiment. From Ji et al.[290] reprinted with permission from The Journal of Physical Chemistry A, 121 (41), 7968-7975. Copyright 2017, American Chemical Society.

The work presented in this chapter builds on this study from Ji et al.[290] by studying the variation in time at which different droplets of $NaNO_3$ in a series nucleate crystals to hence gain insight into the nucleation kinetics, and demonstrate that the viscosity of aqueous $NaNO_3$, even without the presence of sucrose, can be sufficiently high during rapid droplet drying that it can present a barrier to nucleation.

6.3. Phase Functions of $NaNO_3$ Droplets During Evaporation

If an evaporating droplet nucleates crystals, the particle could show two different types of PF. It could show a crystalline morphology, where there are no regularly spaced fringes from which the EDB software can calculate the radius from and typically the data after this point is noisy. Such a PF generally suggests that the particle is non-homogeneous or non-spherical. Alternatively, the PF could show inclusions, wherein the particle is still relatively spherical in shape but there are regions of inhomogeneity inside that disrupt the light scattering. There are still interference fringes, but the variation in scattered intensity with angle no longer smoothly decreases with increasing angle, and instead shows a rapidly fluctuating intensity profile.[210]

Fig. 6-4 shows the evaporation profiles of three droplets of aqueous $NaNO_3$ (0.2 MFS), drying in 293 K and 0% RH, i.e. the same conditions as in Fig. 6-1. The three droplets, whilst all exposed to identical drying conditions, nucleated crystals at different times in the process: 2 s, 3.2 s and 49 s for panels *a*, *b* and *c*, respectively. The light scattering at each data point was analysed by the phase-function algorithm [210] and the inferred morphology is labelled using the colour of the datapoints. In addition, examples of the phase function at certain points in the evaporation is shown in the figures that are inset. In Fig. 6-4a the droplet nucleated crystals early in the evaporation process, prior to ~ 2 s, and the phase function before and after nucleation showed that of a homogeneous droplet and crystalline particle, respectively. After crystal nucleation the datapoints in Fig. 6-4a showed a large degree of noise due to the crystalline PF.

On the other hand, in panels *b* and *c*, the droplet nucleated crystals after the 'corner' in the temporal radius, and the PF showed that of inclusions after the nucleation event. The reason behind why aqueous $NaNO_3$ droplets that nucleated at times later than ~ 2 s into evaporation exhibited a different PF to those that nucleated crystals earlier in the process is thought to be a viscosity-driven effect. If ion-pair formation and nucleation occurred quite soon after solute saturation was reached, there may still have been sufficient water present to act as a plasticiser and ensure a level of ion mobility that could support subsequent crystallisation throughout the rest of the droplet. The droplet thus displayed a PF representative of a completely crystallised particle. However, a droplet that nucleated after 2 s did not retain sufficient water to act as a plasticiser, suppressing internal diffusion within the particle. This could lead to crystal nucleation at multiple unconnected sites within the particle, giving rise to phase functions indicative of the presence of inclusions within the final particle. The morphology of the droplets in Fig. 6-4b and c is hence assumed to have one or some crystal nuclei separated by regions of amorphous $NaNO_3$.

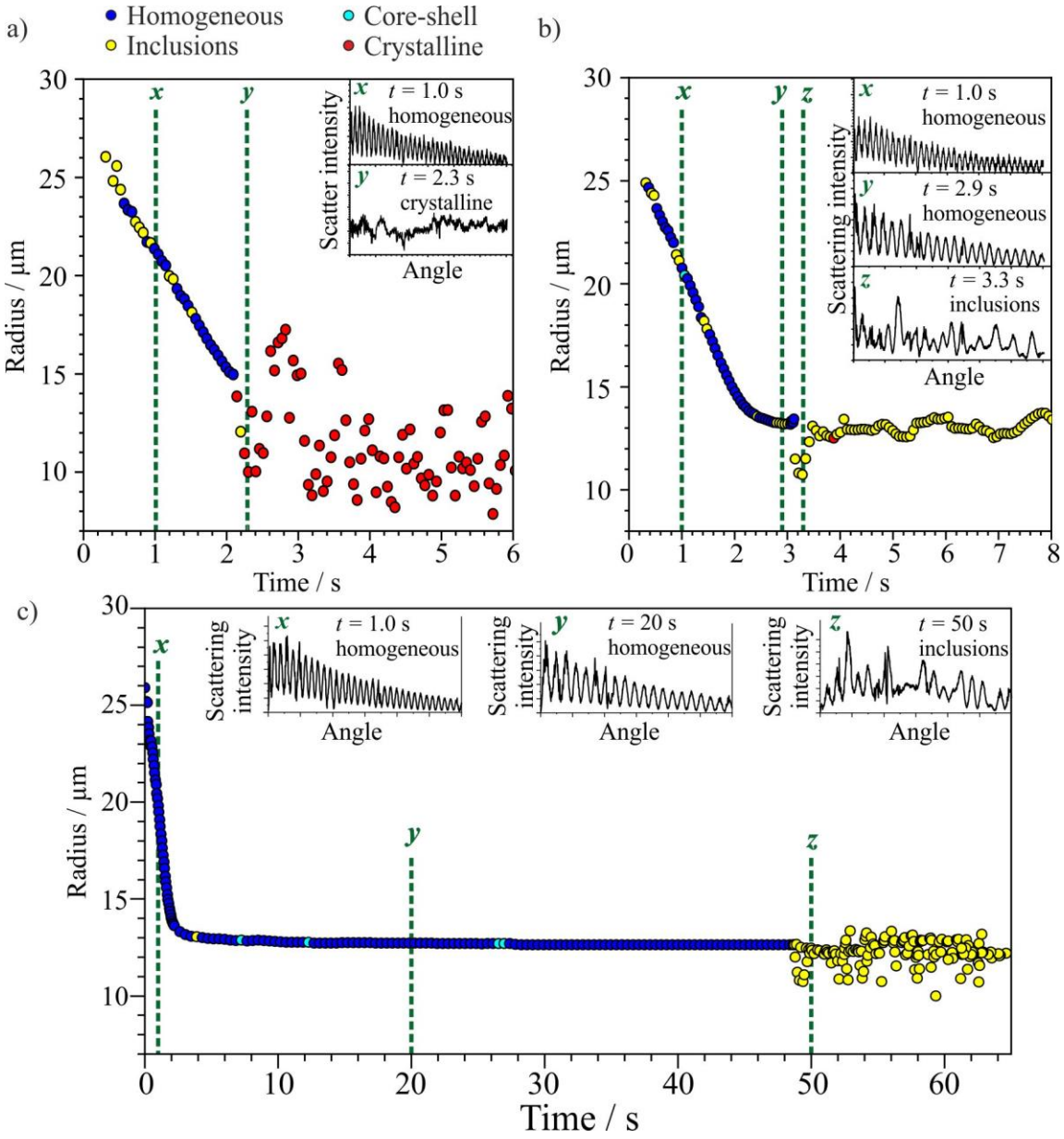

Figure 6-4: The evaporation of three aqueous droplets of $NaNO_3$ (0.2 MFS) evaporating in 0% RH at 293 K. The colour of the datapoints in the figure show the time-dependent phase identified by the light scattering, for a droplet that a) nucleated crystals "early" in the process at ~ 2 s and then had a largely crystalline PF. b) and c) show droplets that nucleated crystals "late" in the process at ~ 3 s and ~ 49 s, respectively, and such droplets had a PF showing inclusions after nucleation. The figures inset show examples of the phase-function exhibited in the light scattering at different times in the experiment, as indicated by the green dashed lines.

6.4. SEM-Images of Dried $NaNO_3$ Droplet Morphologies

Droplets of $NaNO_3$ dried under the same conditions (0% RH, 293 K) as the data shown in Fig. 6-1 were collected on a glass slide and imaged with scanning electron microscopy, as shown in Fig. 6-5a, with a zoomed-in image shown in Fig. 6-5b. All dried particles were close to a sphere in shape, with wrinkles,

cracks and dimples in the surface of the particles. This can be attributed to small damages caused by the SEM imaging step. The SEM is under vacuum, so if dried particles contain even very small amounts of water or amorphous content that may not be mechanically stable, then the observation of such samples under the electron beam could lead to collapse, shrinkage and distortion.[291] In Chapter 5 with studies of dried NaCl particles, there was no such damage on any of the dried NaCl particles, indicating that they were fully crystalline and stable under the electron beam. The difference here with $NaNO_3$ is attributed to the high viscosity reached during drying; perhaps some small amounts of water content remained in all droplets due to the kinetic limitation on water evaporation in the late stages of the droplet lifetime. In the EDB data, the vast majority of evaporating $NaNO_3$ droplets under these conditions underwent crystal nucleation, yet in the SEM images all of the dried particles still looked spherical. At the point of nucleation of $NaNO_3$ crystals the spherical droplet was not plasticised enough to form a full regular crystal shape across the whole particle.

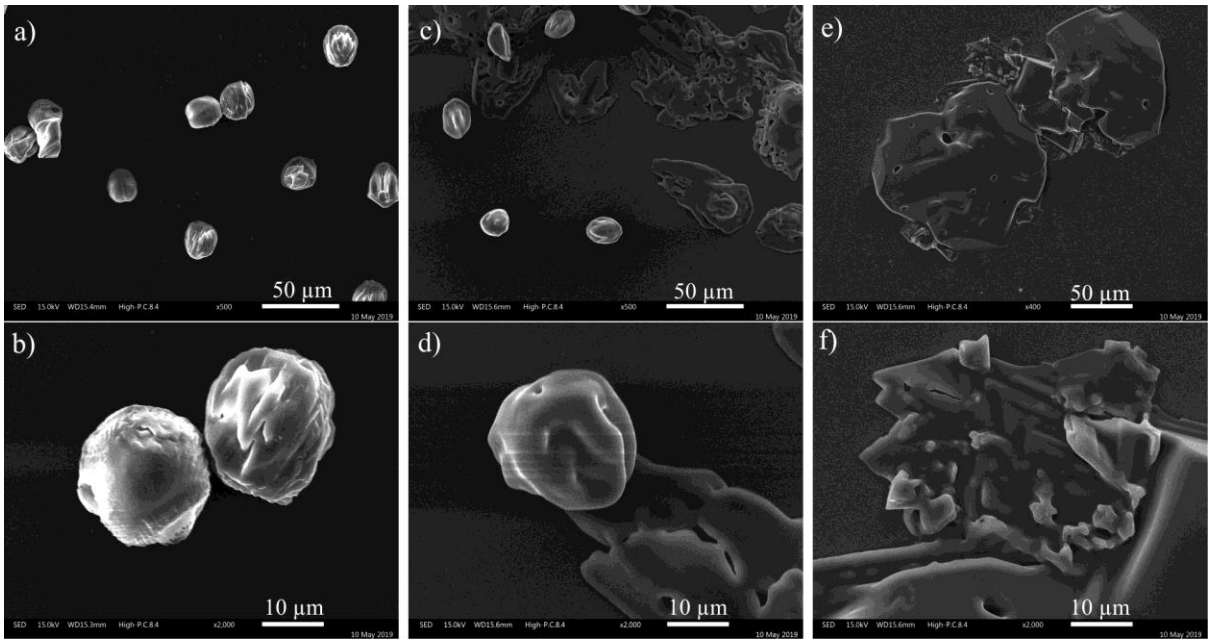

Figure 6-5: SEM images of $NaNO_3$ particles collected on a glass side, which were produced by evaporating aqueous 0.2 MFS $NaNO_3$ droplets in 0% RH at 293 K in a falling droplet column. Storage conditions from the point of collection until the SEM imaging step were a) and b) in a 0% RH desicator for 24 hours (Sample 1); c) and d) stored for a 7-hour period at 60% RH before being stored in a 0% RH desicator for the remaining 17 hours (Sample 2); e) and f) a 2 hour period stored at 90% RH before being stored in a 0% desicator for the remaining 22 hours (Sample 3).

6.5. Further Insight into the Phase of Dried $NaNO_3$ Particles Through Control of the Storage RH

Two additional samples were collected from the same drying event as the dried particles in the SEM image Fig. 6-5a (here called 'Sample 1') but stored at different RHs prior to SEM imaging to explore the phase (crystalline or amorphous) and morphology of dried $NaNO_3$ particles. Where the sample in Fig. 6-5a was stored in a 0% RH desiccator following the initial drying but before SEM imaging, the sample in Fig. 6-5c and d (Sample 2) was stored for 7 hours in a sealed container at 60 ± 2% RH, before being returned to a desiccator prior to the SEM imaging step. In addition, the sample in Fig. 6-5e and f (Sample 3) was stored for 2 hours at 90 ± 5% RH before being returned to a desiccator prior to imaging. A schematic showing the different conditions for each sample is shown in Fig. 6-6.

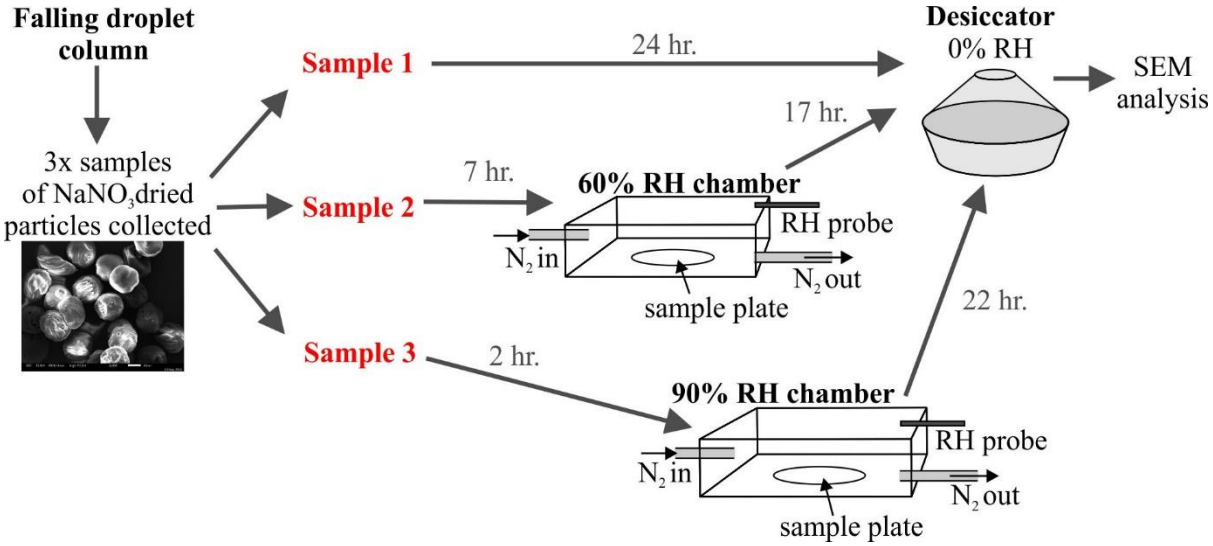

Figure 6-6: Schematic showing the different conditions of storage of the three samples of dried particles of $NaNO_3$, prior to the SEM imaging in Fig. 6-5.

The SEM images of the dried particles of Sample 2 show two different types of particles in the same images. First, some dried particles remained individually placed and spherical, for example those in the bottom left hand corner of Fig. 6-5c. These particles look similar to those in Sample 1, which remained in a 0% environment prior to the imaging process. Hence, these particles did not dissolve in period that they were stored at 60% RH. It can be inferred from such an experiment that, since 60% RH is lower than the deliquescence RH (DRH) of $NaNO_3$ of 75%, such particles were crystalline after the initial drying step, and could not deliquesce when introduced to the 60% RH storage step. Other particles in Fig. 6-5c of Sample 2 have clearly dissolved in the higher storage RH and spread on the glass slide, possibly even coalescing with other condensed droplets to form "puddles", which have then dried out

in the subsequent 17-hour period in the desiccator. The particles that are seen to have dissolved and spread are those that did *not* nucleate during the initial drying step, and hence formed amorphous particles. In the absence of crystallinity, these particles could absorb water from the 60% RH atmosphere. Some dried particles that did not absorb water from the 60% RH vapour were even touching the "puddles" from droplets that absorbed water, but the contact between the two different types of particles did not lead to coalescence. Such an experiment confirms the observations of evaporating $NaNO_3$ droplets in the EDB; crystal nucleation in $NaNO_3$ can be highly variable with some droplets not appearing to nucleate crystals at all.

Finally, the SEM images in Fig. 6-5e and f, of Sample 3, show that all of the dried $NaNO_3$ absorbed water during the storage step and spread on the glass slide. No individual crystalline particles remained. The storage RH for this sample was 90%, higher than the DRH of $NaNO_3$. Thus, all particles in Sample 3 deliquesced and absorbed water, whether they had nucleated crystals or not. The morphology of Sample 3 looks the same as the particles in Sample 2 that had absorbed water in the 60% RH storage step.

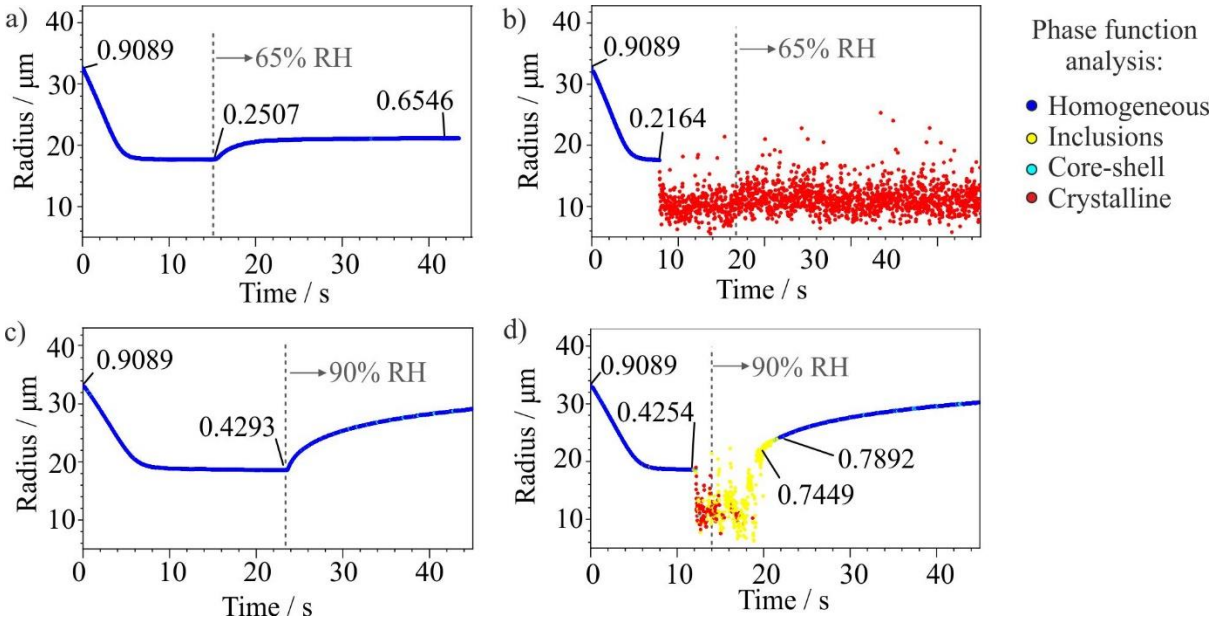

Figure 6-7: The radius evolution of 0.2 MFS aqueous $NaNO_3$ droplets dried into RHs lower than the ERH, followed by a rapid switch to a higher RH. EDB experiments performed at 293 K. In a) and c) the droplets equilibrated with the low RH prior to the RH switch and in b) and d) the droplets nucleated crystals prior to the switch. The RH was switched at the grey line, to 65% in a) and b) and to 90% in c) and d). The colour scheme of datapoints represents the phase-state of the aerosol as indicated by the key.

The storage-experiment of the dried $NaNO_3$ particles serves as evidence that the rapid drying of $NaNO_3$ can lead to both crystalline and amorphous (or uncrystallised) particles. This experiment can be repeated in the EDB, because the RH of the N_2 gas passing over a trapped particle can be rapidly changed (over

a timescale of ~ 0.1 s) by switching between two separate gas-flows of different humidity, i.e. the 'upper' and 'lower' flow. Fig. 6-7 shows the radius of droplets of aqueous $NaNO_3$ (0.2 MFS) that evaporated into RHs lower than the ERH (~ 25% RH for panels *a* and *b*, ~ 42% RH for panels *c* and *d*). The droplets in Fig. 6-7a and Fig. 6-7c did not nucleate crystals in the low RH conditions and remained as an uncrystallised liquid with a high chemical potential. The droplets in Fig. 6-7b and 6-7d nucleated crystals whilst drying in the low RH, at t = 8 s and 12 s, respectively. The dominant gas flow passing over the droplet was switched, to induce a rapid RH increase at the time defined by the grey line, to 65% RH in panels *a* and *b*, and to 90% RH in panels *c* and *d*. The figure shows that when the RH was stepped up to 65% RH, which is lower than the DRH of 75%, only the droplet that had not nucleated crystals was able to condense water and grow in radius. This is consistent with the results in the SEM image of Sample 2 in Fig. 6-5c. The nucleated particle in Fig. 6-7b, assumed to be crystalline from its phase function, did not deliquesce. By contrast, in Fig. 6-7c and d the RH was stepped up to be greater than the DRH and hence both particles re-absorbed water, whether a crystal had nucleated in the drying step or not. This is consistent with the SEM image of Sample 3.

The colour scheme of the datapoints in Fig. 6-7 is shown in the figure legend, with blue indicating a homogeneous and spherical droplet and red and yellow indicating nucleation, either complete crystallisation or in the form of smaller nuclei inclusions, respectively. The data labels indicate the water activity of the droplet at certain time-points, calculated using the radial growth factor and the known hygroscopicity of $NaNO_3$ aerosol.[175] The nucleated particle in Fig. 6-7d only became a homogeneous liquid droplet above a water activity of 0.75, which is the DRH.

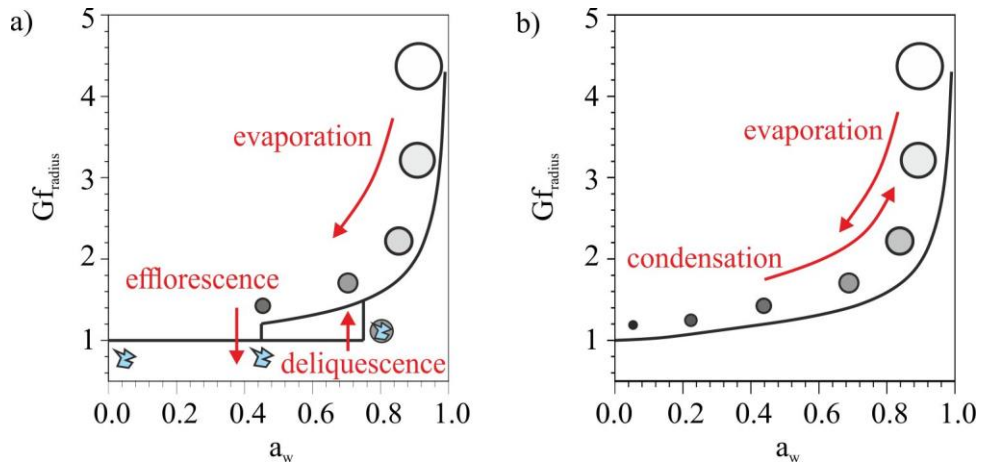

Figure 6-8: The aerosol phase behaviour diagram (radial growth factor) to demonstrate the dehydration-rehydration steps for aqueous $NaNO_3$ droplets that crystallise (a) and those that dry to form amorphous particles (b).

The hygroscopic curve of $NaNO_3$ in terms of the radial growth factor is depicted in Fig. 6-8a, which is a measure of how much water is taken up by the droplet at a certain a_w (RH). According to the extended aerosol-inorganic (E-AIM) model, droplets evaporating from high a_w can crystallise at a_w < 0.45 to

form a solid crystal, and an increase in humidity only leads to deliquescence if the RH is greater than 75%.[175] This is the path that the droplets in Fig. 6-7b and d followed. The dehydration and rehydration trajectory of an aqueous $NaNO_3$ droplet that does not nucleate crystals is shown in Fig. 6-8b. This trajectory is followed by the particles in panels *a* and *c* of Fig. 6-7. Such droplets simply lose water through evaporation and then grow again when the RH is increased.

6.6. Observing the Stochastic Nature of Crystal Nucleation across a Population of Evaporating $NaNO_3$ Droplets

To highlight the stochasticity of crystal nucleation, the time that different droplets in a series of aqueous $NaNO_3$ droplets (0.2 MFS) nucleated crystals as they evaporated at 293 K and 0% RH is shown in Fig. 6-9a. Those indicated by an asterisk did not nucleate crystals in the experimental window.

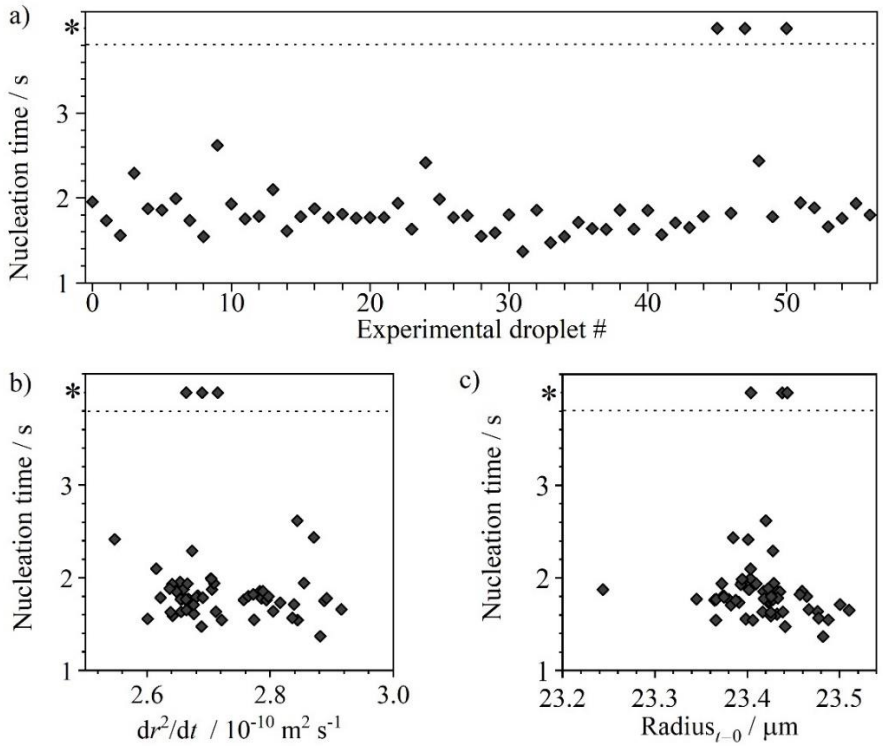

Figure 6-9: a) The time that different 0.2 MFS aqueous $NaNO_3$ droplets in a series nucleate crystals as they evaporate at 293 K and 0% RH, where those indicated by an asterisk do not nucleate crystals in the experimental window. b) The correlation between the nucleation time and the evaporation rate of each droplet. c) The correlation between the nucleation time and the initial radius of each droplet.

The time that the droplets exhibited crystal nucleation does not show any correlation with the order of the droplet in the series. This removes the possibility for environmental drift in the experiment causing the nucleation variation, such as a steady change in RH, temperature or time that the solution was held

in the dispenser prior to droplet formation. The initial evaporation rate of the water from the $NaNO_3$ droplets varies across a small range from 2.55 to 2.92 × 10^{-10} μm^2 s^{-1}, but Fig. 6-9b shows that there is no correlation between the nucleation time and the evaporation rate. In fact, the three droplets that did not nucleate crystals had evaporation rates that were close to the mean rate. The initial starting radius of a droplet affects how much $NaNO_3$ solid mass is in the final particle, however, this also did not seem to affect the nucleation time in the droplets (Fig. 6-9c). Again, the three droplets that did not nucleate crystals had starting radii that were very close to the average of 23.4 ± 0.04 μm for this experiment. The nucleation time for each droplet in the series appeared to be a random, stochastic process. This is confirmed further in the next section where the variable nucleation behaviour observed in one single droplet of $NaNO_3$ is discussed.

6.7. Observing Variable Nucleation Behaviour in a Single Droplet

Crystal nucleation can be induced in supersaturated droplets by the presence of an external surface, such as dust or impurities.[87,196] In order to confirm that the time distribution for nucleation in a population of $NaNO_3$ droplets is not due to a varying presence of impurities in each droplet, a single droplet was processed through repeated evaporation and condensation cycles. The time at which crystals nucleated during multiple drying events was determined. One droplet was kept in the EDB trap for the duration of the experiment, and the RH was repeatedly switched using the EDB dual gas flows between 18% RH and 90% RH to induce evaporation or condensation in the droplet, respectively. The RHs set on the lower and upper gas flows were lower than the ERH and higher the DRH, respectively. Initially, a droplet evaporated in 18% RH and was held trapped for 30 s to see if crystals nucleated. Following nucleation, or at the end of a 30 s time period, the RH was rapidly switched to an RH of 90%. Once the droplet had re-equilibrated with its initial starting size, the gas flow was returned to 18% RH and the droplet was dried again. A total of 42 drying events was investigated.

An example of a part of the evaporation-condensation cycle is shown in Fig. 6-10a, with the resulting radius vs. time profile shown in black and the RH cycle shown in red. On some occasions the droplet did not effloresce in the 30 s time window allocated for the RH switch, for example the drying event at 300 s, whilst in others it nucleated in only 2 s. The nucleation events were characterised by the moment that the PF became disrupted leading to noise in the radius data. The time-dependent decay (over all the evaporation-condensation cycles) for the liquid droplet as a function of time is shown in Fig. 6-10b. It can be assumed that, if there were impurities or dust in the droplet in Fig. 6-10a, this would be constant for the entire RH-cycling experiment. Droplet-to-droplet variations remained in the time that nucleation was observed, with some drying events leading to no crystal nucleation, across multiple drying events

with the exactly same mass of $NaNO_3$ and the same potential for impurities. This highlights the stochastic nature of homogeneous nucleation of $NaNO_3$ crystals.

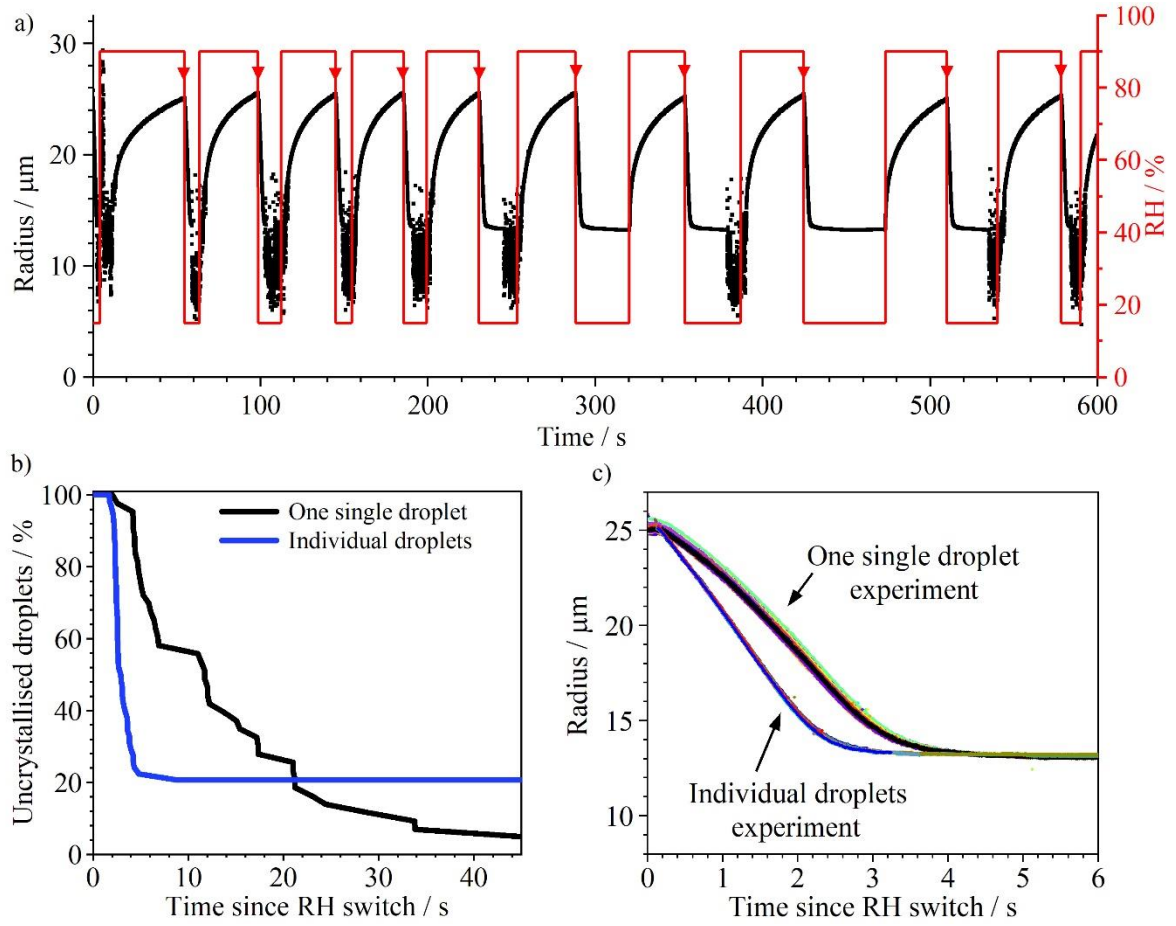

Figure 6-10: The radius evolution of a single aqueous $NaNO_3$ droplet (0.2 MFS) as the RH was continuously stepped up to 90% or down to 18% in 11 examples of a series of 42 drying events all with the same droplet. b) The distribution of time taken for the droplet to nucleate crystals in each drying event, compared to the distribution for a series of 56 individual droplets to nucleate crystals when evaporated under the same conditions. c) The comparison of the evaporation rates in the RH-cycling experiment compared to the individual droplets experiment.

The same 18% RH conditions were repeated for a population of 56 *individual* droplets, to compare the distribution observed in the RH-cycling experiment. The time-dependent distribution is also shown in Fig. 6-10b. The distribution of nucleation events looks different, even though this experiment was performed on the same day directly after the RH-cycling experiment, with the same temperature, RH and solute mass fraction. The evaporation profiles of all drying events in the RH-switching experiment and all droplets in the individual droplets experiment are shown in Fig. 6-10c. Whilst the evaporation rate for the single-droplet RH-switching drying events was highly reproducible, it was slower than in the many-droplets experiment. The difference in the drying kinetics suggests that, in this experiment, the EDB did not fully equilibrate at the upper end when the RH was switched. The evaporation rate of an aqueous $NaNO_3$ droplet does appear to affect the time that a droplet nucleates crystals, and hence, this is explored in more detail in the next section.

6.8. The Variation in Nucleation Propensity for $NaNO_3$ at Different Relative Humidities

The droplet-to-droplet variation in nucleation time observed in $NaNO_3$ droplets can be observed across a range of experimental conditions. The evaporation profiles of aqueous $NaNO_3$ droplets (initial MFS of 0.125, 293 K) in different RHs is shown in Fig. 6-11a, with a reducing evaporation rate for a higher RH. It must be noted that the 20% and 25% RH datasets had a lower initial droplet size; the data is normalised with respect to the initial starting radius to better compare the evaporation rates in the inset figure. The time-dependence on the nucleation of crystals in a large population of droplets (70+ droplets for each RH) is shown in Fig. 6-11b. As droplets evaporated in lower RHs, the percentage of droplets that nucleated in a 10 s experimental window increased, and the nucleation events were observed at earlier times.

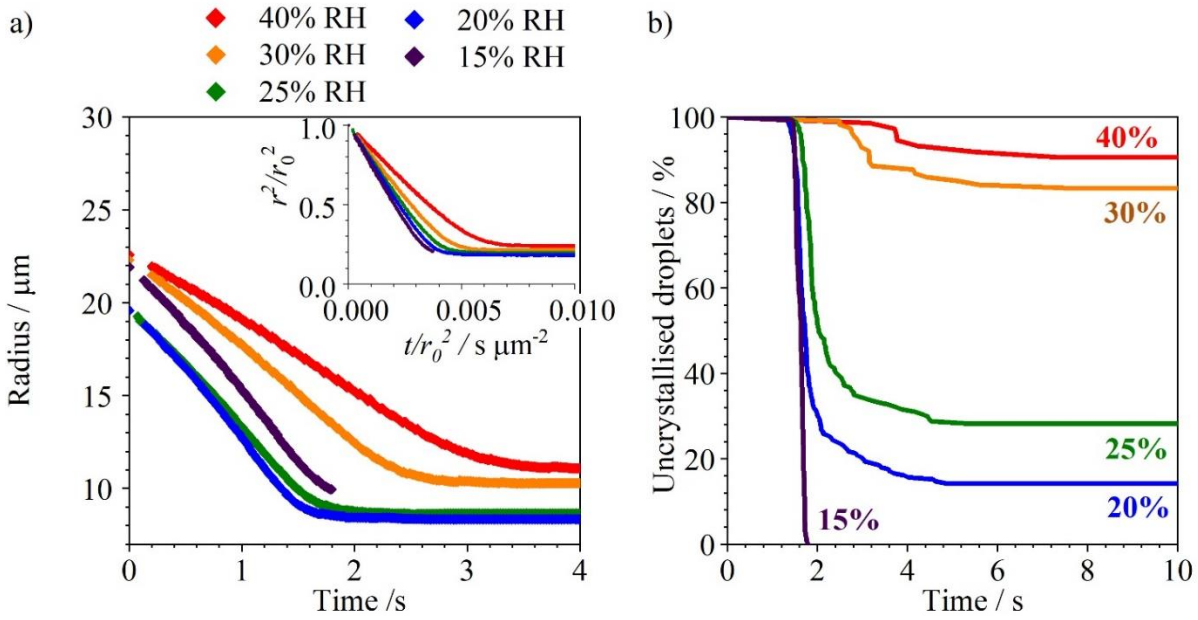

Figure 6-11: a) The evolution of droplet radius for $NaNO_3$ droplets (0.125 MFS) evaporating in the EDB at 293 K at varying RHs. Inset: the data in a) normalised with respect to the initial radius, r_0. b) The distribution of nucleation events with time for the different RHs.

To investigate the relationship between the evaporation rate and the changing propensity to nucleate crystals, we model the concentration profiles within the evaporating droplet (Fig. 6-12). The $NaNO_3$ concentration at the surface is predicted to increase quicker at the lower RHs (Fig. 6-12f). The general trend of the concentration profiles showed a steep rise in surface solute concentration with time, which peaked at a maximum value; the maximum was higher for evaporation in lower RHs. All droplets at 15% RH nucleated crystals by the time that this maximum in supersaturation was reached and it is likely that the nucleation occurred at the surface, where there was a very steep concentration gradient. For the

RHs 20% and greater, some droplets did not nucleate crystals when the peak in solute concentration was reached. For these droplets, the concentration gradient became more uniform across the droplet as bulk diffusional flux started to outweigh the evaporative flux of water leaving the surface.

At long timescales, the droplets that had not nucleated crystals eventually reached a radially uniform solute concentration, with an equilibrated solute supersaturation that is greater for a lower RH. The degree of supersaturation for an uncrystallised, equilibrated droplet in terms of the molarity calculated using the E-AIM model, can be as high at 3.48 for the droplets at 15%, as shown in Table 6-1.[175] The $NaNO_3$ concentration at the surface and at the centre of a droplet evaporating into 15% and 40% RH are compared in Fig. 6-12f. A large degree of surface enrichment is predicted at 15% RH (large disparity between the centre and the surface). The model predicts that a droplet evaporating at 40% RH would have an enriched surface, but not to the same extent as at 15% RH, and as the evaporation rate reduces the droplet becomes homogeneous in composition after 10 s.

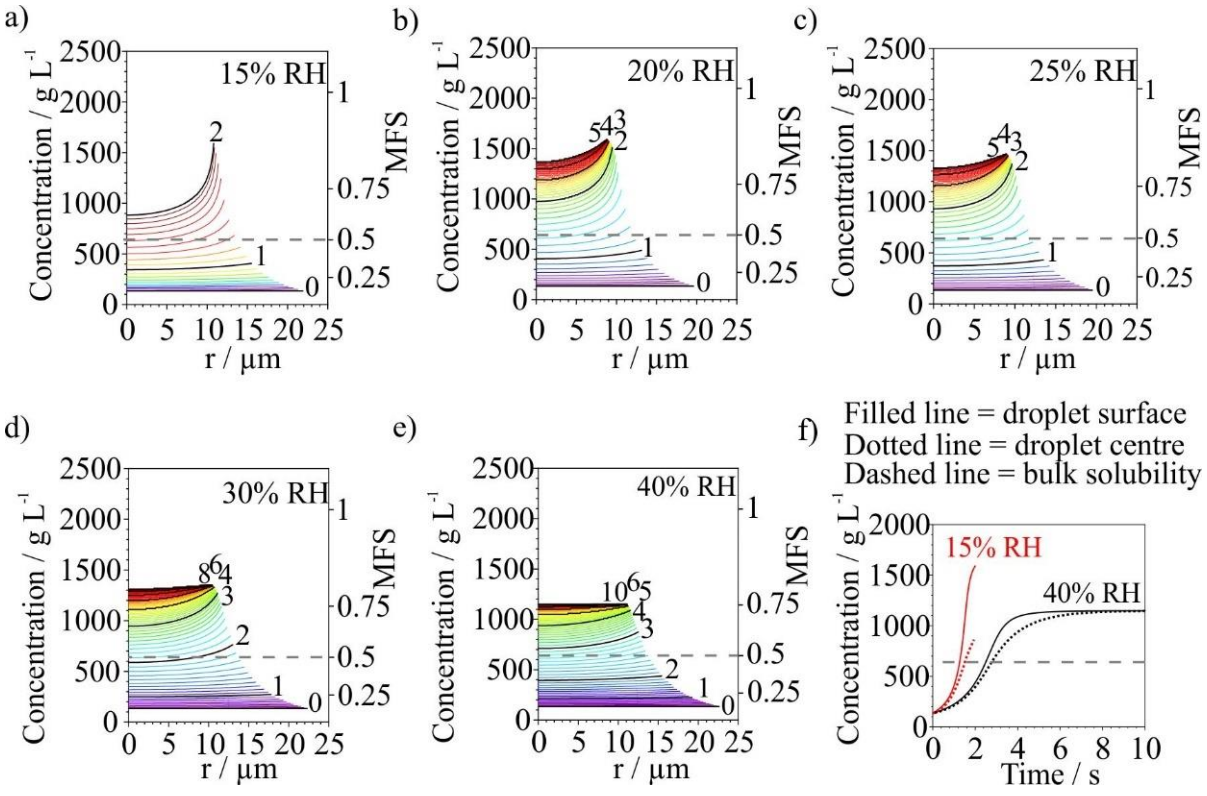

Figure 6-12: a - e): Modelling results of the internal solute concentration profiles along the cross-section of an $NaNO_3$ droplet in Fig. 6-6a as it evaporates into varying RHs, where r = the distance from the droplet centre. The data is plotted as a molarity concentration as well as a mass fraction of solution (MFS). The black dotted line shows the $NaNO_3$ bulk solubility limit at 293 K. f) The comparison between the time-dependent concentration of $NaNO_3$ at the droplet surface (filled) and the droplet centre (dotted) for a $NaNO_3$ droplet drying at 15% and 40% RH.

Table 6-1: The solute concentration and degree of supersaturation for a $NaNO_3$ droplet that has equilibrated to a range of RHs and not yet nucleated crystals, calculated in terms of molarity.

RH / %	Concentration / g L^{-1}	Supersaturation at 293 K
40	1480	2.60
30	1650	2.89
25	1740	3.05
20	1840	3.23
15	1940	3.40

Concentration at solubility limit (0.465 MFS) = 570 g L^{-1}

6.9. The Variation in Nucleation Propensity at Different Temperatures

The temperature is an important factor in classical nucleation theory, appearing in the exponent in the equation for nucleation rate (Eq. 6-1), acting to increase the nucleation rate with an increasing temperature.[196] As discussed in Chapter 2, the nucleation rate, *J*, according to classical nucleation theory can be described by an Arrhenius equation:

$$J = A \exp\left[\frac{-\Delta G^*}{k_B T}\right] \qquad (6\text{-}1)$$

where *A* is a pre-exponential factor, ΔG^* is the Gibbs free energy barrier to crystal nucleation, k_B is the Boltzmann constant and *T* is the equilibrium temperature.

The increase in temperature leads to more thermal motion of the ions, causing a greater chance of the necessary collisions that lead to nucleation. The radius evolution of aqueous $NaNO_3$ droplets (0.2 MFS) evaporating into 0% RH and varying temperatures is shown in Fig. 6-13a. Indeed, with an increasing gas phase temperature, the chance of forming a crystal nucleus in an evaporating $NaNO_3$ droplet increases (Fig. 6-13b). The proportion of droplets remaining uncrystallised decreases from 100% to 0% within only a few hundred milliseconds at 306 K, whereas the distribution of crystal nucleation events spreads over several seconds at 278 K, with the majority of droplets not displaying nucleation within the experimental window. At colder temperatures, the droplet evaporation rate decreases, leading to a greater time available for nucleation. However, the data suggest that the nucleation rate is lower at 278 K. Even with the slower evaporation rate, the measurements suggest that the droplet loses all water through evaporation before the contact-ion pairs have time to arrange into a crystal nucleus.

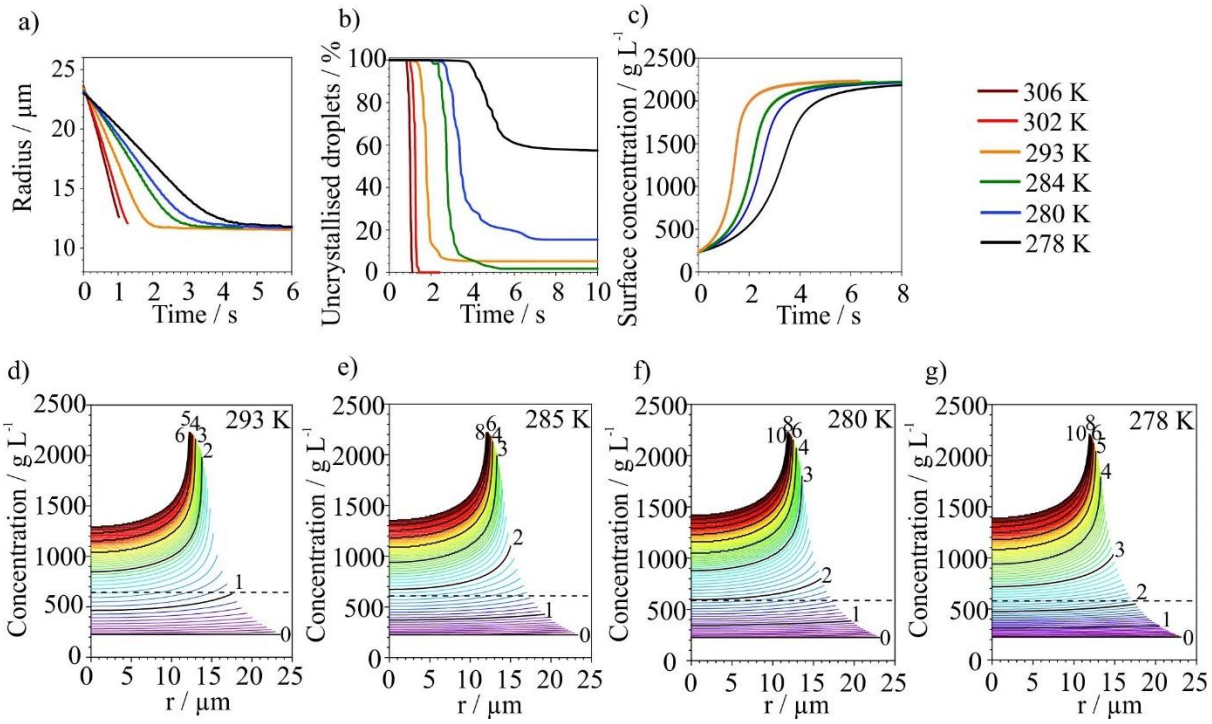

Figure 6-13: a) The radius evolution of 0.2 MFS $NaNO_3$ droplets evaporating into 0% RH at varying gas-phase temperatures in the EDB. b) The time-dependent distribution of nucleation events across the series of droplets. c) The surface concentration throughout drying as determined by the model, d-g) The modelled concentration profiles across a droplet cross section for the drying events 278 K – 293 K in a), where r = the distance from the droplet centre. The dashed line indicates the bulk solubility limit.

Understanding the interplay between time available for nucleation and nucleation rate is pertinent in spray drying. Typically in spray drying of droplets containing organic solutes, one sees a higher propensity to crystallise when the evaporation rate is lower, because then the nucleation rate has a chance of outcompeting with the drying rate.[47] The crystallisation window, i.e. the timescale within which crystallisation could occur, is narrower for a faster evaporation rate, as the droplet runs out of water (ending the drying period) before the crystals have had a chance to form.

The modelled surface concentration for evaporating aqueous $NaNO_3$ droplets (initial MFS of 0.2) in 0% RH at 293 K, 285 K, 280 K and 278 K are compared in Fig. 6-13c, with the time-dependent concentration profiles across the entire droplet breadth shown in panels *d-g*. The figures show that the maximum solute concentrations reached at the surface of the droplets was similar in all cases because the droplets were all evaporating in 0% RH and reaching roughly the same equilibrated radius. This demonstrates that the $NaNO_3$ nucleation rate must be strongly temperature-dependent, not just related to the degree of supersaturation reached in a droplet.

The distribution of when nucleation is observed in a series of evaporating droplets can be described in terms of a half-life, τ, of remaining liquid droplets. The value for τ in Fig. 6-13b for the dataset at each temperature is defined as the time at which half of the droplets that nucleated crystals within the experimental dataset were observed to nucleate. For example, τ was 1.01 ± 0.08 s for T = 306 K to get

to 50% of the droplets, but for 278 K, at the end of the experimental window of 10 s, 44% of droplets nucleated crystals, so τ to get to a loss of 22% of the droplets was 4.76 ± 0.08 s. The uncertainty in τ is determined as the standard deviation in the τ retrieved from distributions of nucleation events in multiple populations of $NaNO_3$ droplets (60+ in each case) as shown in Fig. 6-14b.

τ is related to the inverse of the nucleation rate, J. According to Eq. 6-1, plotting $\ln(\tau)$ against $1/T$ should yield a straight line with gradient $-\Delta G^*/k_B$. This is shown in Fig. 6-14a, wherein a straight-line can be fit through the datapoints. This shows that the data are consistent with the exponential form of the nucleation rate from the Arrhenius equation (Eq. 6-1). The gradient of the line is 4300 ± 300 K, which determines the Gibbs free energy barrier to nucleation of $NaNO_3$ crystals at this degree of supersaturation being 36 ± 3 kJ mol^{-1}. It should be noted that the temperature in this figure represents the gas phase temperature, rather than the droplet temperature, which was likely suppressed during drying. In addition, the droplets were not maintaining a constant supersaturation for the duration of the experiment in Fig. 6-13b; rather, in the first few seconds the droplets rapidly increased in concentration due to the evaporation process. These two aspects could both contribute to an error in the calculation of the barrier ΔG^*.

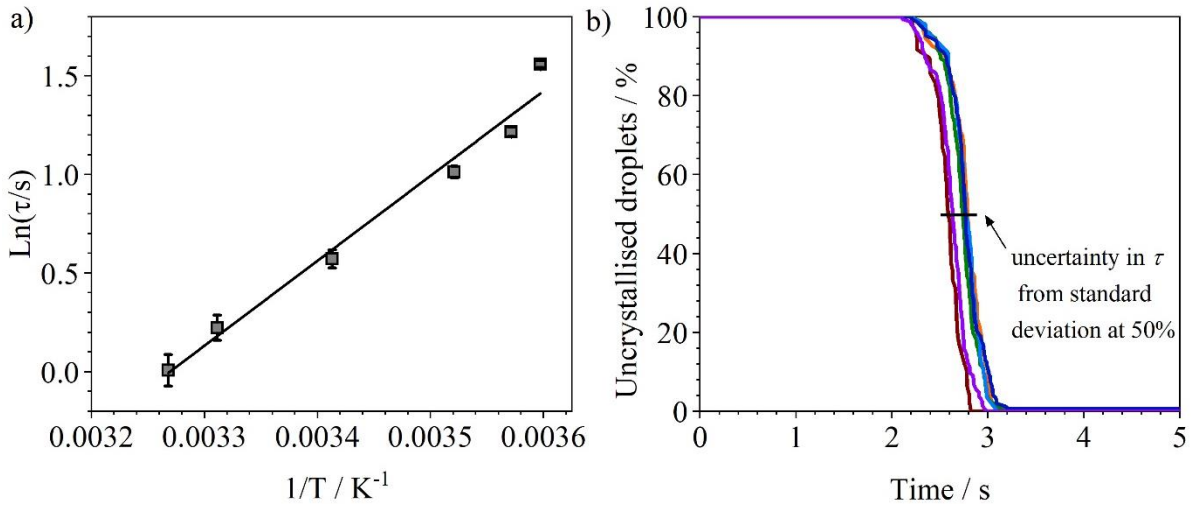

Figure 6-14: The plot of ln(τ) with respect to the inverse of the gas phase temperature, for the datasets of aqueous $NaNO_3$ droplet-drying at varying temperatures in Fig. 6-12b. τ is the time taken for half of the droplets that nucleate within the experimental window of 10 s to exhibit nucleation. b) The time-dependent distribution of nucleation events across 6 populations of droplets (60+ in each case), to retrieve a standard deviation in the average τ, which is the uncertainty in τ for panel (a). Evaporation conditions for the experiment in panel (b) are initial MFS of $NaNO_3$ of 0.2, initial radius of 27 µm, 293 K and 0% RH.

6.10. The Variation in Nucleation Propensity for Different Starting Concentrations

The concentration dependence upon the nucleation propensity of aqueous $NaNO_3$ is demonstrated in Fig. 6-15, where the initial concentration was varied for different populations of droplets evaporating at 285 K and 0% RH. The chance of forming a crystal nucleus varied as a function of time in each case. The evaporation rate of the lower solute concentration droplets was marginally faster, as shown in Fig. 6-15a; the water had a greater vapour pressure due to the lower $NaNO_3$ ionic activity. Hence, the evaporating droplets would be exposed to a greater degree of evaporative cooling when starting at lower concentrations. Liquid droplets of ~ 25 μm in radius evaporating into dry air have been shown to drop several tens of degrees lower in temperature than the surrounding gas temperature.[225] The Kulmala model estimates that the mass flux for the evaporating aqueous $NaNO_3$ droplet with MFS of 0.011 (Fig. 6-15a) would have an initial temperature suppression of 11 K, compared to a 5 K temperature suppression if the initial MFS were 0.35. Thus, the trend in nucleation propensity is a result of the interplay between nucleation rate at the droplet temperature and the time available for crystals to form. Fig. 6-15 panels *d-g* show the modelled concentration profiles of the droplets evaporating with different initial starting concentration; Fig. 6-15d reports that for the lowest initial concentration droplet. There was very little time available for crystallisation because the whole droplet was far below the bulk solubility limit until quite late into evaporation. However, when it did pass the solubility limit the solute concentration at the droplet surface was very high due to the large degree of enrichment from the rapid evaporation, and thus, nucleation occurred readily. Conversely, a slightly higher initial concentration of 0.052 MFS or 0.2 MFS led to a more gradual degree of surface enrichment during evaporation, and some droplets nucleated crystals before the surface of the droplet became too viscous.

The droplet with an initial concentration of 0.35 MFS was already quite close to the $NaNO_3$ bulk solubility limit and evaporated the slowest. Thus, on passing the solubility limit it had the longest crystallisation window out of all droplets in Fig. 6-15. This argument does not explain why the lowest concentration, with 0.011 MFS, nucleated very rapidly and reproducibly for many droplets, as those droplets had the smallest amount of time available for crystal nucleation. The nucleation behaviour of this type of droplet may be related to how rapidly the surface concentration rose at the end of evaporation.

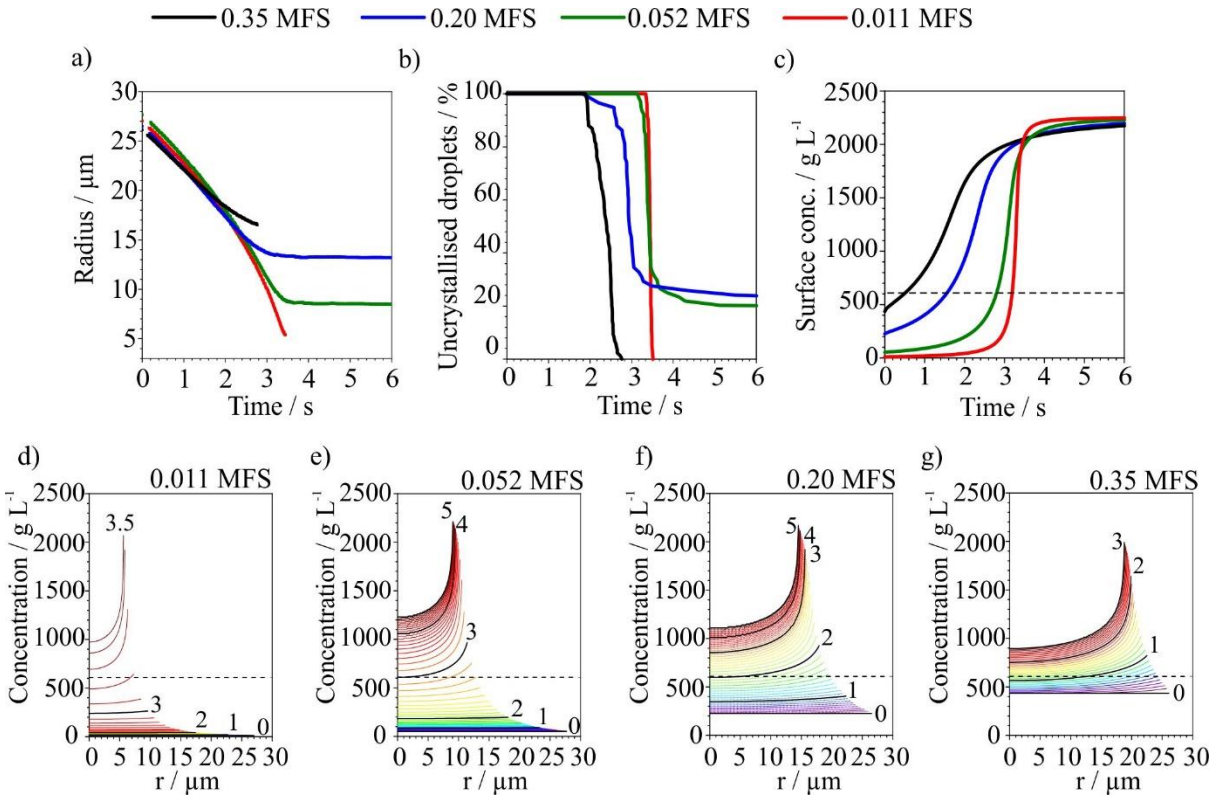

Figure 6-15: a) The radius evolution of $NaNO_3$ droplets evaporating into 0% RH at 284.5 K with varying starting mass fraction of solute (MFS). b) The time-dependent distribution of nucleation events across the series of droplets. c) Model results of the time-dependent surface concentration. d-f) The modelled concentration profiles across a droplet cross section for the drying events in a), where r = the distance from the droplet centre. The dashed line indicates the bulk solubility limit.

Overall, Fig. 6-15 demonstrates how variable the nucleation behaviour for evaporating $NaNO_3$ droplets can be, and how it is dependent upon the initial conditions. By only varying the starting concentration, we show that the ratio between crystalline and amorphous particles formed during drying can be tuned. These data can be used to infer the absolute values of the temperature-dependent and concentration-dependent nucleation rate for aqueous $NaNO_3$, which is discussed in more detail in a later next section.[280] The ability to model the interplay between the crystal nucleation rate and the time available for crystallisation would be very valuable for spray-drying models of viscous droplet evaporation.

6.11. Is the Nucleation Observed in $NaNO_3$ Homogeneous or Heterogeneous?

Nucleation mechanisms can either be homogeneous or heterogeneous. The former occurs in pure substances as a result of random fluctuations in the positions of ions until a cluster is formed. The cluster size must be large enough that the free energy loss through the ionic interactions can outweigh the

unfavourable formation of a boundary between crystal and liquid. As a result, homogeneous nucleation in inorganic salt solutions is considered a rare event and only occurs over long timescales or under very high solute supersaturation.[196]

On the other hand, heterogeneous nucleation occurs in the presence of a surface, such as a container wall dust or impurities. To form an ionic cluster, the free energy gain caused by the formation of a boundary between solid and liquid is insignificant because there is already a pre-existing surface, with an associated interfacial tension. Thus, heterogeneous nucleation does not require as large a critical cluster size and it can occur at lower degrees of solute supersaturation. For bulk studies on crystal nucleation, the surface of the container holding the solution can act as the surface that induces nucleation, so crystallisation almost always proceeds via heterogeneous nucleation in the bulk.[196]

In previous work aerosol droplets have been shown to serve as a contactless container of liquid, in which experiments can probe fundamental liquid properties at high concentrations, such as viscosity,[62] surface tension [63,292] and binary diffusion coefficients.[293] It has been suggested that aerosol droplets can be a route to studying homogeneous nucleation.[140] An aerosol droplet on the order of micrometres in radius is absent of any solid interface, and there is a low probability of dust or impurity being present in such a small volume. As a consequence, very high degrees of solute supersaturation can typically be reached. Inorganic aerosol droplets regularly exceed concentrations greater than the bulk solubility limit.[172,175,200]

However, it may be possible that the vapour-liquid interface at the boundary of an aerosol droplet could still act as a surface to induce nucleation. Whilst this surface is not a boundary to a solid, it could still reduce the free-energy gain of forming a new solid-liquid boundary during crystal nucleation, or arrange ions a certain to induce nucleation which would, by definition, make this a heterogeneous nucleation process. Being a different 'type' of surface, perhaps there is a different heterogeneous nucleation rate when occurring at a vapour-liquid boundary compared to a solid-liquid boundary. The SEM images of crystallised sodium chloride in Chapter 5 show hollow particles that had nucleation occurring most likely at the surface. However, the model also showed that the surface was the most concentrated region in the droplet. So, we cannot distinguish between the interface inducing *heterogeneous* nucleation, and *homogeneous* nucleation occurring at the surface where the solute is most concentrated. The distinction between these two processes comes down to semantics. In the aerosol literature, nucleation of crystals occurring when droplets undergo efflorescence is described as homogeneous nucleation, if it occurs in the absence of solid colloidal particles inside the droplet.[87,140]

Whichever mechanism is occurring in these droplets, be it homogeneous or heterogeneous due to the liquid-air interface, the nucleation rate clearly varies with solute concentration and with droplet temperature. The next section explores how this nucleation rate can be inferred from the experimental data, and how these results compare with classical nucleation theory.

6.12. The Crystal Nucleation Rate of Evaporating Aqueous $NaNO_3$ Droplets

6.12.1. Classical Nucleation Theory

Classical nucleation theory (CNT) is commonly used to interpret the nucleation kinetics and crystallisation of solutions. The basis of the theory is the competition between the free energy loss of forming an ordered solute crystal out of solution and the free energy penalty of forming a phase boundary between the new crystalline phase and the existing solution.[197,278,279] The nucleation rate of crystals out of solution as derived through CNT takes the form of an Arrhenius equation (see Eq. 6-1) and relates to parameters such as the interfacial tension between liquid and crystalline phases and the mean ionic activity coefficient of the solution. The homogeneous nucleation rates of crystals from aqueous NaCl and $NaNO_3$ solutions were simulated using Eq. 6-1 in a recently published paper (Fig. 6-16).[280] To estimate the nucleation rate, ΔG^* was estimated using classical nucleation theory as outlined in Chapter 2:

$$\Delta G^* = \frac{16}{3} \frac{\pi \alpha^3}{n_c^2 \, |\Delta\mu|^2} \tag{6-2}$$

where α is the interfacial energy of the crystal in the solution, n_c is the crystal number density and $\Delta\mu$ is the chemical potential change between crystal and solution, expressed using:

$$\Delta\mu = 2 \, k_B \, T \ln\left(\frac{\gamma}{\gamma_0}\frac{m_s}{m_{s,0}}\right) \tag{6-3}$$

where γ and γ_0 are the mean activity coefficients of the solute in the solution and at the value of saturation (subscript 0), respectively. m_s and $m_{s,0}$ are the solute molality in solution and at saturation.[198] The mean ionic activity coefficients of Na^+ and NO_3^- ions are provided by the E-AIM model.[175] A literature value of α = 0.08 N m^{-1} was implemented for NaCl;[198] no such value was found for $NaNO_3$ so α was varied through reasonable values of 0.06 – 0.08 N m^{-1} to model the nucleation rate (Fig. 6-16).

For NaCl, the CNT-predicted nucleation rates could be described by a step-function; at a particular value of solute supersaturation and temperature the nucleation rate increased by four orders of magnitude.[280] This is consistent with the EDB results presented in Chapter 5 of the nucleation of NaCl appearing to be instantaneous at a supersaturation of 2.04.

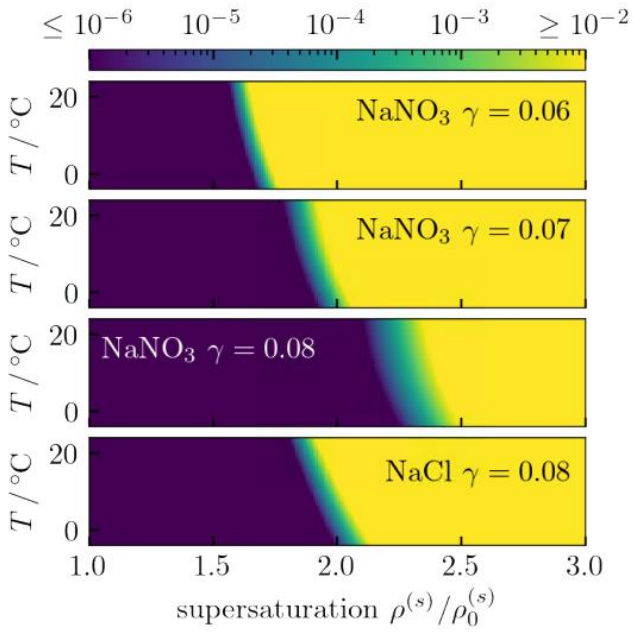

Figure 6-16: The crystal nucleation rate at the surface of a $NaNO_3$ or NaCl droplet (in μm^{-2} s^{-1}) predicted by classical nucleation theory as a function of temperature and degree of solution supersaturation, for varying values of the interfacial energy between liquid and solid phases. Reprinted with permission from the Journal of Chemical Physics.[280]

Classical-nucleation theory predicted that even for varying the interfacial tension between the liquid and crystalline phases between reasonable values for $NaNO_3$, CNT predicted a step function of nucleation rate that monotonically increases with solute supersaturation and temperature. Due to this large step function, CNT could not fully describe the nucleation behaviour of aqueous $NaNO_3$ in this thesis. The nucleation rates reported in Fig. 6-16 predict that all aqueous $NaNO_3$ droplets in the evaporation conditions in this thesis would exhibit nucleation, and all at similar times in the experiment. As shown throughout this chapter, some evaporating droplets nucleated $NaNO_3$ crystals and others did not, indicating that the nucleation rate may display a more complicated function that the step function in Fig. 6-16.

6.12.2. Inferring the Crystal Nucleation Rate of $NaNO_3$ from Experimental Data

By observing the stochastic nucleation behaviour of aqueous $NaNO_3$ droplets over the whole population of droplets, the survival probability of uncrystallised liquid phase, p_{liq}, can be retrieved. The rate of droplet nucleation, W, can be determined by differentiation of this survival probability:

$$\frac{\mathrm{d}p_{\mathrm{liq}}}{\mathrm{d}t} = -Wp_{\mathrm{liq}} \qquad (6\text{-}4)$$

Based on the assumption that crystal nucleation occurs at the surface of the liquid aerosol droplets of radius r, the nucleation rate per unit time and per unit area across the surface becomes:

$$J = -\frac{1}{4\,\pi\,r^2\,p_{\mathrm{liq}}} \times \frac{\mathrm{d}p_{\mathrm{liq}}}{\mathrm{d}t} \qquad (6\text{-}5)$$

By fitting the experimental data for p_{liq} with a Fermi-Dirac form,[280] the crystal nucleation rates of $NaNO_3$ out of an aqueous solution was determined, and the results are shown in Fig. 6-17. The nucleation rates are plotted in terms of droplet temperature, rather than the air temperature, by explicitly considering the effect of evaporative cooling undergone by the droplets in each experiment.

The analysis confirms that the nucleation rate of $NaNO_3$, denoted by the colours of the datapoints, is non-monotonic with increasing temperature and supersaturation, passing through a maximum at certain points in the temperature-concentration space but then decreasing to essentially zero (Fig. 6-17). Plotting $\ln(\tau)$ against $1/T$ in Fig. 6-14 showed that an exponential (Arrhenius) function in the nucleation rate holds well for $NaNO_3$ at varying temperatures across one supersaturation. However, the results in Fig. 6-17 show that CNT cannot consistently describe the Gibbs free energy barrier to nucleation, and thus the nucleation rate, at varying degrees of supersaturation. The nucleation kinetics of aqueous $NaNO_3$ are more complicated than the simple homogeneous process described by CNT.

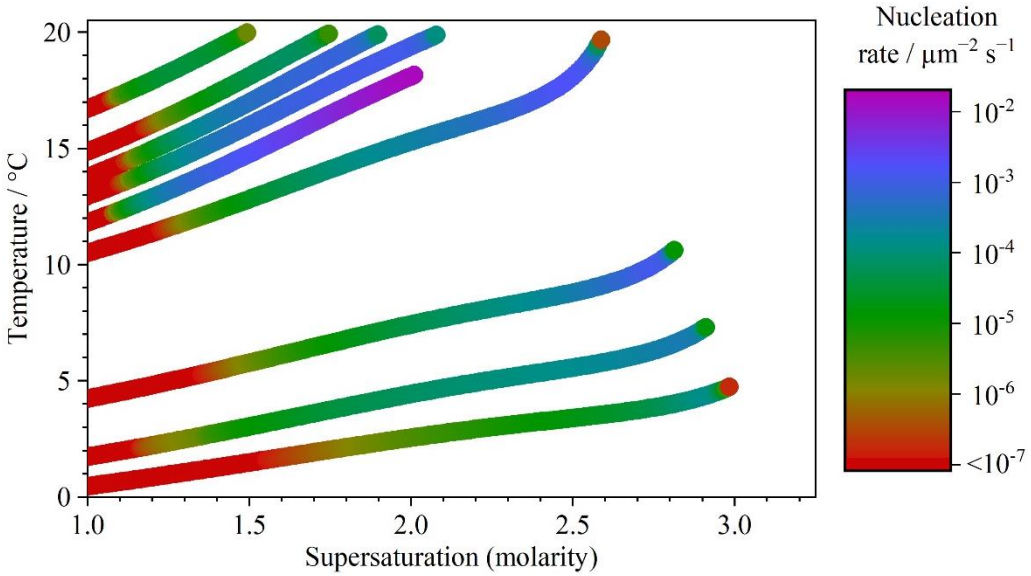

Figure 6-17: The crystal nucleation rate of aqueous $NaNO_3$ as a function of droplet temperature and degree of solute supersaturation, as inferred by the experimental data of the survival probability of uncrystallised $NaNO_3$ droplets in this thesis chapter. Nucleation is assumed to occur at the droplet surface.

A difference between nucleation out of aqueous NaCl solutions, which shows behaviour consistent with a 'step-function' of monotonic nucleation rate, and aqueous $NaNO_3$ solutions, is that the viscosity of $NaNO_3$ can increase several orders of magnitude throughout drying. The increase in viscosity suggests

a dramatic decrease in the rate of the binary diffusion constant, potentially impeding the transport of Na^+ and NO_3^- ions that necessarily must come together to form a crystalline cluster. The appearance of the crystallised $NaNO_3$ particles in the SEM images indicate that the viscosity rise prevented a fully crystalline shape in the final stage of drying. However, given that the diffusion coefficient only comes into the CNT nucleation rate as part of the pre-exponential factor rather than within the exponent, any rise in viscosity during drying makes little difference to the nucleation rate as predicted by CNT. It is possible that the crystal nucleation of $NaNO_3$ proceeds via a more exotic process than CNT, such as a multiple-step process.[193] For example, the ions may first need to come into proximity, as in CNT, but then rearrange into a specific core geometry. Pan et al.[294] also observed a maximum in the rate of homogeneous nucleation of lysozyme crystals as a function of temperature, and qualitatively justified this by considering that nucleation proceeds with initial formation of a high-density protein cluster, followed by subsequent rearrangement. The second step, in which the metastable cluster orientates into an ordered nucleus, can become rate-limited by a rising viscosity. In addition, Lee et al. electrostatically levitated droplets of increasingly supersaturated solutions of potassium dihydrogen phosphate (KH_2PO_4) and observed multiple pathways to crystal nucleation.[295] Through analysing the raman spectra of $P(OH)_2$ and PO_2 bands in the droplets during evaporation, they observed the solution went through different local structural reconfigurations with increasing supersaturation, leading to multiple peaks in the nucleation rate with increasing concentration.

CNT was developed to study the condensation of liquid droplets from a supersaturated gas. This means it does not consider the ion orientation and cannot distinguish between the formation of an organised structure and of a cluster of randomly positioned ions whose structure does not resemble that of a crystal. Density is assumed to be the only property that varies between the two phases.[296] An additional assumption of CNT is that the crystal nucleus has identical macroscopic properties to the equilibrium crystalline phase, such as interfacial free energy, density and crystal structure. The interface between a crystal nucleus and the surrounding phase is also considered as a sharp, spherical boundary, which may not be the case for the nucleating cluster.

6.13. Comparison of Nucleation Behaviour Down the Alkali Nitrates Series

In this section, the nucleation behaviour of aqueous solutions of $LiNO_3$, $NaNO_3$, KNO_3 and $RbNO_3$ will be compared. The efflorescence of potassium nitrate aerosol has been studied previously, as well as bulk crystallisation studies,[297] due to its particular importance to atmospheric chemistry. Potassium salts can be prevalent in the plumes from biomass burning [298,299] and potassium nitrate, as well as other

nitrates, are often associated with atmospheric aerosol weathering of masonry and buildings.[297] Freney et al.[298] studied the efflorescence and deliquescence behaviour of KNO_3 particles on a TEM grid and reported seeing no obvious phase change occurring upon dehydration of aqueous KNO_3, i.e. no ERH was reported. They implied that the solution droplets dried into an amorphous solid. However, work by Baldelli et al. showed that aqueous KNO_3 aerosol droplets in the micrometre size-range had a strong tendency to crystallise.[268] There is no reported ERH in the literature for rubidium nitrate or lithium nitrate, although $LiNO_3$ is known for being a deliquescent salt and can exist as a trihydrate at room temperature.[300]

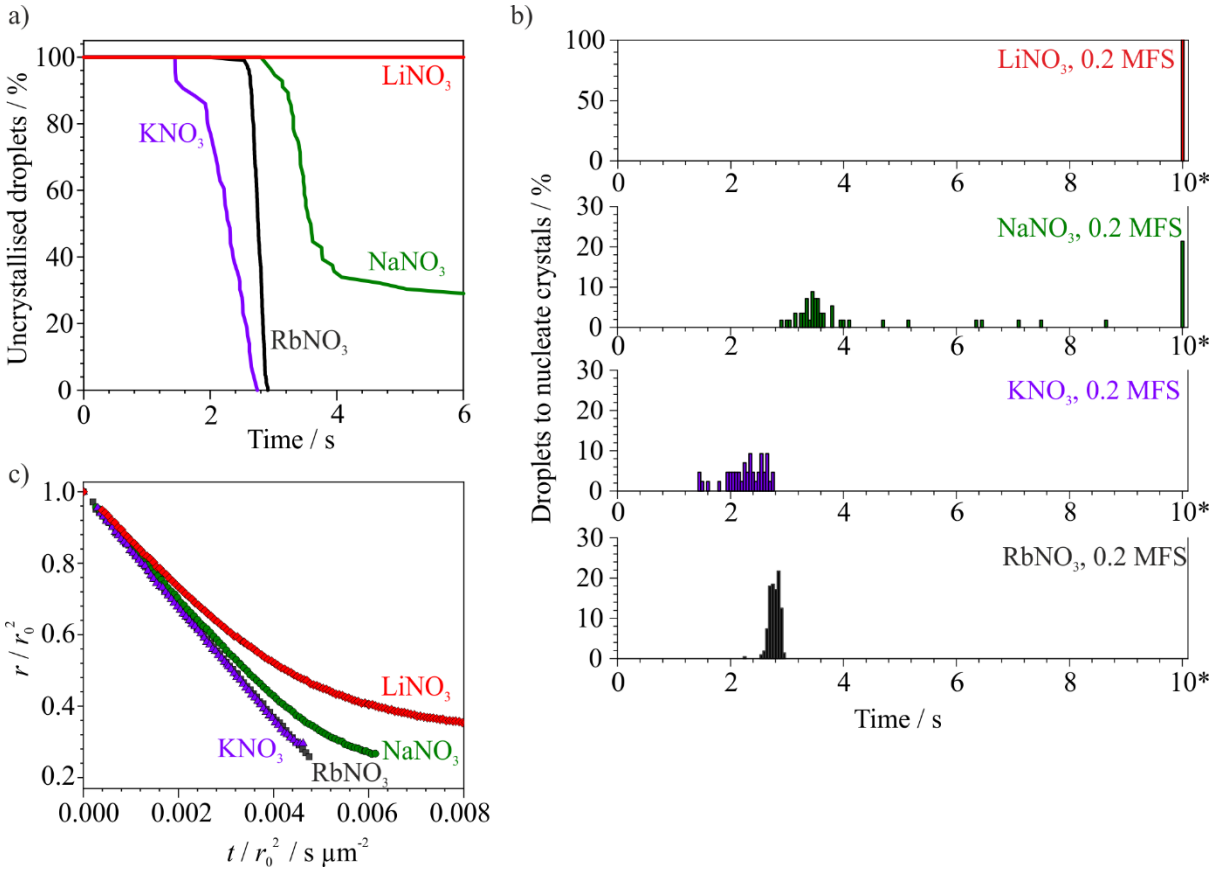

Figure 6-18: a) The time-dependent distribution of nucleation events observed across a series of 40+ aqueous droplets for $LiNO_3$, $NaNO_3$, KNO_3 and $RbNO_3$, all with initial mass fraction of 0.2, evaporating at 0% RH at 276 K. b) The distribution of nucleation events in a) plotted in terms of a histogram, * the values at 10 s indicate droplets that did not nucleate within the 10 s experimental window. c) The evaporation rates of example droplets from each dataset, normalised with respect to the initial radius.

As discussed in the previous section, under some drying conditions, particularly those performed at colder temperatures, aqueous $NaNO_3$ droplets in a series can show a large variation in the time that they exhibit nucleation, with some droplets not nucleating crystals even when all of the water had evaporated. This is shown in Fig. 6-18a (green line) where the nucleation events of droplets (initial $r \sim 25$ µm, initial concentration of 0.2 MFS) evaporating at 276 K and 0% RH spanned over several seconds, with 21% of the droplets remaining uncrystallised after the 10 s experimental window. When the experiment was

repeated for aqueous KNO_3 aerosol, also with initial MFS of 0.2, every droplet in the series nucleated crystals in a narrower time distribution spread over 1 s (purple line). This contradicts the work by Freney which concluded that aqueous KNO_3 aerosol does not effloresce.[298] Like the KNO_3 experiment, every droplet in a large population of 0.2 MFS aqueous $RbNO_3$ droplets nucleated crystals, this time in a very narrow time distribution. This shows the nucleation of $RbNO_3$ crystals out of aqueous solution to be highly reproducible, as shown in Fig. 6-18b (black line). Finally, for a series of aqueous 0.2 MFS $LiNO_3$ droplets, no droplets nucleated crystals, and all continued to produce a light scattering pattern consistent with liquid or amorphous particles for the entire experimental window, even when all water had apparently evaporated. Given that $LiNO_3$ can exist at room temperature in a hydrated form as lithium nitrate trihydrate, it could be possible that, upon evaporation of aqueous $LiNO_3$ in 0% RH, some water was retained in the droplet associated with the ions. However, if any water was retained then the particle did not form an ordered hydrate crystal because the elastic light scattering did not show a pattern consist with the formation of crystalline material.

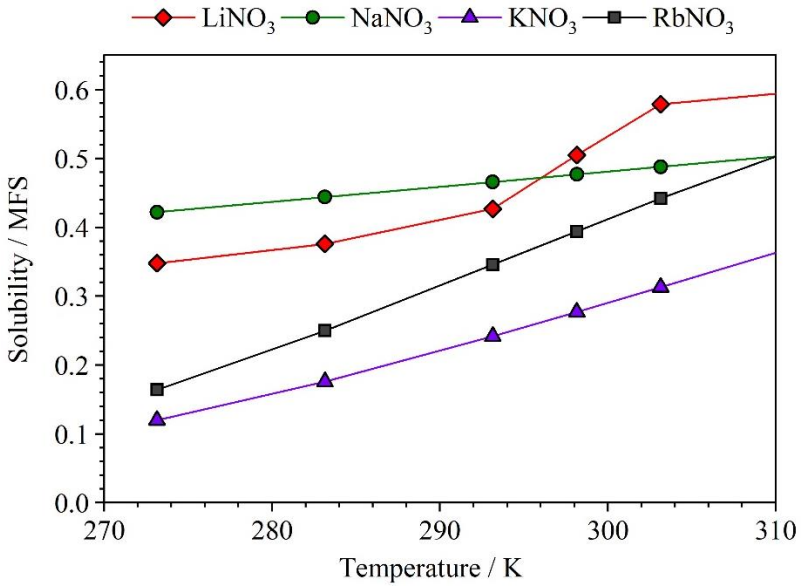

Figure 6-19: The bulk solubility of XNO_3 where X = Li, Na, K and Rb, in terms of mass fraction of solute, at varying temperatures, as reported by the CRC Handbook of Chemistry and Physics.[218]

The distribution of nucleation events that were observed became narrower and more reproducible as the cation in the aqueous alkali nitrate solution became higher in molecular weight (i.e. $LiNO_3$ → $RbNO_3$) (Fig. 6-18a). The widths of the distributions are shown more clearly when depicted in terms of a histogram (Fig. 6-18b). This order of propensity to crystallise upon dehydration is similar to the trend of bulk solubility for each nitrate (Fig. 6-19). All $LiNO_3$ droplets and some $NaNO_3$ droplets did not nucleate any crystals in the drying event in Fig. 6-18a, and both have a much greater solubility at 276 K, so a greater degree of water affinity, than KNO_3 and $RbNO_3$. KNO_3, with the lowest solubility of all four alkali nitrates, is the first species to begin to nucleate crystals during evaporation in Fig. 6-18a, i.e.

the first line to drop from 100%. This indicates that the hygroscopicity of the solute may influence the nucleation kinetics, so this will be discussed in the next section.

6.13.1. The Hygroscopicity of the Alkali Nitrates Series

Equilibrium hygroscopicity measurements were performed on droplets of aqueous XNO_3, where X = Li, Na, K and Rb, and the results are shown in Fig. 6-20 in terms of the MFS, radial growth factor (GF) and solute moles as a function of water activity (a_w). It should be noted that hygroscopicity data for KNO_3 and $RbNO_3$ was only retrieved for the high a_w region of the curve because the aerosol effloresced at RH ~ 0.88 and 0.85, respectively. The figure shows that aqueous $LiNO_3$ is the most hygroscopic solute, with decreasing hygroscopicity in a clear trend down the alkali nitrate series. This trend is related to the charge density of the cation decreasing going down the group, as all cations in the alkali nitrates typically carry a single positive charge but the cation increases in ionic radius with more electron shielding effects from Li^+ down to Rb^+, as shown in Table 6-2.

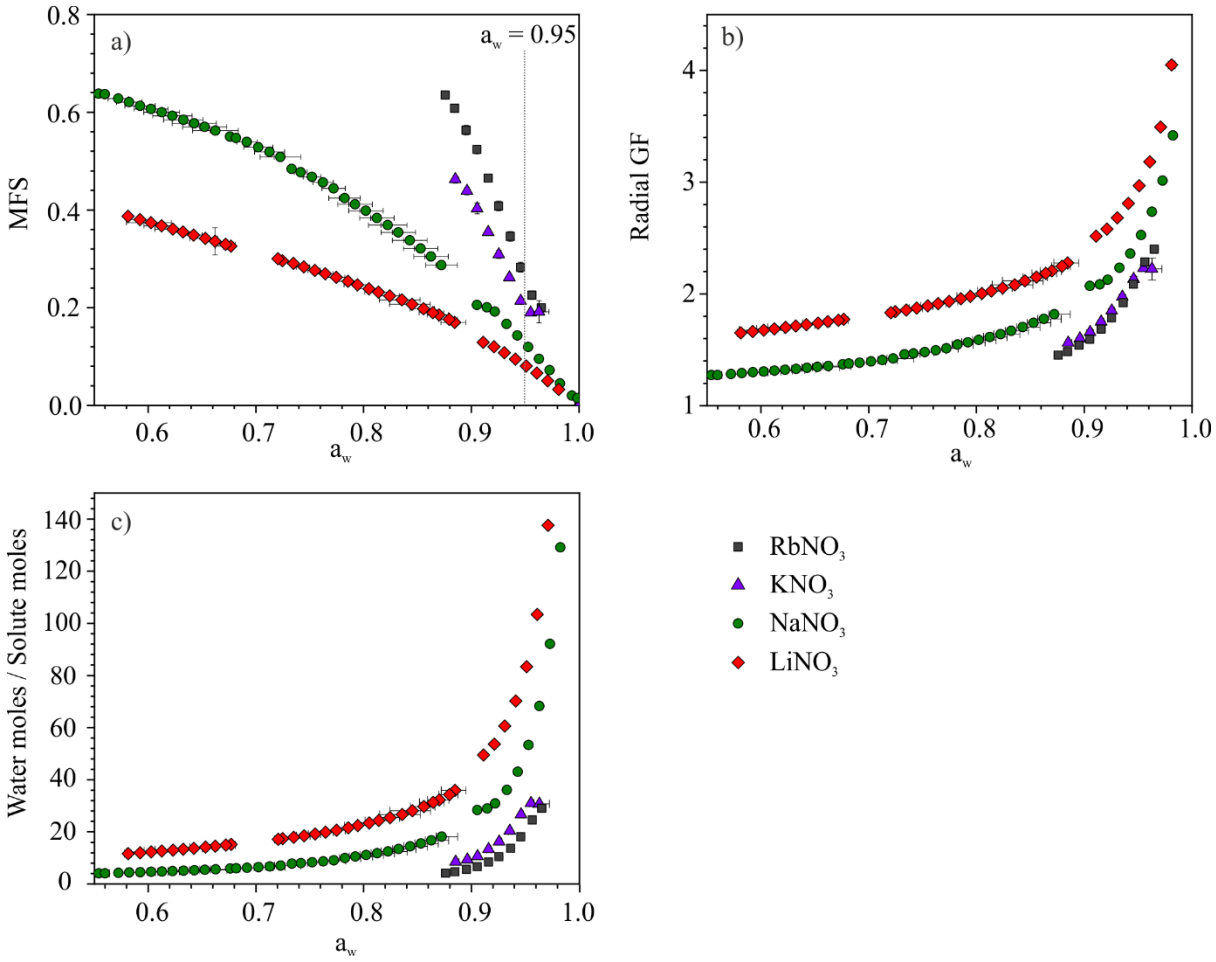

Figure 6-20: The hygroscopicity of aqueous XNO_3 aerosol, where X = Li, Na, K and Rb, represented in terms of a) the mass fraction of solute, b) the radial growth factor and c) the ratio of water moles to solute moles, with respect to the water activity.

$LiNO_3$ is the most hygroscopic nitrate of the four as the solute has a lower MFS during evaporation, demonstrating a greater retention of water by $LiNO_3$ as the RH is decreased than the other alkali nitrates (Fig. 6-20a). This greater water retention of $LiNO_3$ during drying is shown in terms of a larger radial GF (wet radius divided by the dry radius) in panel *b*, and also in panel *c* in terms of a larger ratio between moles of water and solute in the droplet. These figures show that in order to reach a high concentration to drive crystal nucleation, the water activity of the $LiNO_3$ droplet must be decreased to a much greater extent than the other nitrates. Literature data of the viscosity of aqueous $LiNO_3$ solutions show a rising viscosity with increasing mass fraction of $LiNO_3$,[301] as for $NaNO_3$, however the data only reaches concentrations up to 1.54 mol kg^{-1} (mass fraction of 0.022), so it is not known whether the viscosity would rise up to the Pa.s range at higher concentration. If $LiNO_3$ were to show similar values of viscosity at high mass fractions as $NaNO_3$, then it could be expected that the viscosity is a significant factor in impeding nucleation of $LiNO_3$ crystals.

Table 6-2: Standard thermodynamic parameters that are useful for comparison of alkali nitrate crystal nucleation behaviour.

Alkali nitrate	Cation ionic radius* / pm [302]	Bulk solubility at 293 K / MFS (ref. [218])	Crystal structure at 293 K	$\Delta H_{lattice}$ / kJ mol^{-1}
$LiNO_3$	90	0.427	Calcite [303]	848
$NaNO_3$	113	0.466	Rhombohedral [304]	755
KNO_3	151	0.242	Orthorhombic [304]	685
$RbNO_3$	166	0.346	Trigonal [305]	662

*** The values cited for the ionic radius of the cation are for four-coordinate ions for Na^+ and K^+, but six-coordinate ions for Rb^+ and Li^+.**

6.13.2. The Propensity to Form Contact Ion Pairs in Alkali Nitrates Solutions

Work by Gao et al.[306] investigated the thermodynamics of the alkali nitrates $LiNO_3$, $NaNO_3$ and KNO_3, particularly focusing on the likelihood of forming contact ion pairs between the cation and nitrate anion. Ion pairs or clusters can form in electrolyte solutions when the electrostatic attraction between cations and anions is sufficiently greater than the thermal energy of the ions in solution, or the hydration energy of the ions.[307] The electrostatic forces between solute molecules can be considered in terms of an activity coefficient, which represents the deviation from ideality (Raoult's Law). The activity coefficients (γ) of KNO_3, $NaNO_3$ and $LiNO_3$ are shown in Fig. 6-21.[306] KNO_3, of the three nitrates described in their work, shows the biggest negative deviation from Raoult's law, with $\gamma << 1$. $NaNO_3$ also has a negative deviation, suggesting that for both of these nitrates the intermolecular forces between ions are attractive and the formation of contact ion pairs is likely. For $LiNO_3$, at low concentrations of solute, attractive interactions between the ions dominate but the activity coefficient begins to increase at molality greater

than 0.5 and then shows positive deviation from ideality, implying that the interactions between the ions becomes repulsive at higher concentrations and perhaps the ions are more likely to exist in hydrated states rather than in ion pairs.[306]

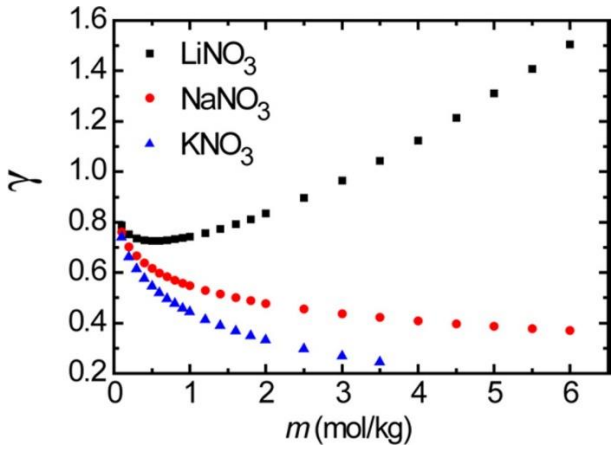

Figure 6-21: Activity coefficients of $LiNO_3$, $NaNO_3$ and KNO_3 in aqueous solutions at varying concentration. From Gao et al.,[306] reprinted with permission from the Journal of Physical Chemistry B, 120 (9) 2343–2351. Copyright 2016, American Chemical Society.

The activity coefficients shown in Fig. 6-21 are consistent with the 'Law of Matching Water Affinities', which states that oppositely charged ions with a similar size and charge density tend to have a similar degree of hydration free energy, and are thus more likely to form contact ion pairs.[308] The ionic radii of the cations Li^+, Na^+, K^+ and Rb^+ are provided in Table 6-2, showing an increasing radius of cation going down the group, resulting in the cation becoming less polarising and more 'soft'. The NO_3^- ion, with an ionic radius of 165 pm, is closer in size, and thus polarizability, to Rb^+ of the four alkali cations discussed. In conclusion, the tendency to form contact ion pairs in the alkali nitrates appears to be increase down the group, with Li^+ and NO_3^- the least likely contact pair to form and with Rb^+ and NO_3^- the greatest. It is possible that this likelihood to exist in contact ion pairs in solution is a contributing factor to the trend in propensity to nucleate crystals at high concentrations in the alkali nitrates. The relative ionic radii of cation and anion could also influence the packing efficiency in a nucleation cluster; such a packing efficiency has been shown to correlate with the glass-forming ability of metallic glass alloys.[309] Molecular dynamics simulations showed that varying the size ratio and concentration ratio of particles in the alloys led to large differences in packing efficiency and in the ability to form glass. It is possible that size ratios between cations and anions in the highly concentrated solutions reached in the aerosol droplets is an important factor in their ability to nucleate crystals.

6.13.3. The Effect of Drying Rate on the Nucleation Propensity of the Alkali Nitrates

A factor that could cause the variation in crystal nucleation time distribution in Fig. 6-18a is the varying drying rates for the four alkali nitrates. As $LiNO_3$ is more hygroscopic, the water activity for a 0.2 MFS solution is 0.853 according to Fig. 6-20a, which is much lower than the 0.915, 0.951 and 0.964 water activity for a 0.2 MFS droplet of $NaNO_3$, KNO_3 and $RbNO_3$, respectively. Hence, the water in the $LiNO_3$ droplet in Fig. 6-18a has a lower vapour pressure than in the other alkali nitrates, which explains the reduced evaporation rate.

Using the hygroscopic curves in Fig. 6-20a, aqueous solutions were made of the four alkali nitrates to all have an equal value of initial water activity (a_w = 0.95), to compare the crystal nucleation kinetics in droplets that have equal evaporation rates. The results of 0.95 a_w droplets evaporating at 276 K and 0% RH are shown in Fig. 6-22, with the time distribution over which nucleation events were observed shown in panel *a* and the evaporation profiles in panel *b*, normalised with respect to the initial radius.

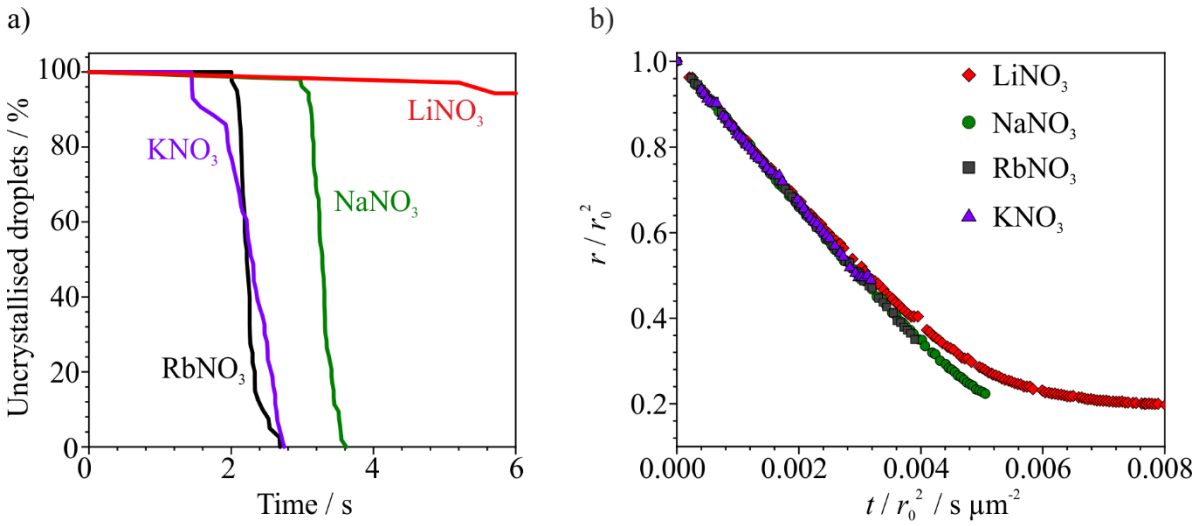

Figure 6-22: a) The time-dependent distribution of nucleation events observed across a series of 40+ aqueous droplets for $LiNO_3$, $NaNO_3$, KNO_3 and $RbNO_3$, all with initial water activity of 0.95, initial MFS of 0.089, 0.12, 0.20 and 0.25, respectively. Evaporation conditions are 0% RH and 276 K. b) The evaporation rates of example droplets from each dataset, normalised with respect to the initial radius.

The results show that the $RbNO_3$ distribution of nucleation events (black line) broadened slightly with respect to in Fig. 6-18, due to the initial mass fraction of $RbNO_3$ being higher (0.25 MFS), possibly leading to an increased viscosity of the solution during drying. The $NaNO_3$ evaporation rate increased due to lower initial mass fraction (0.12) than in Fig. 6-18, which appears to have narrowed the time distribution over which $NaNO_3$ crystals are nucleated. This reflects the data shown in previous sections that show the width of the crystal nucleation time distribution to be highly sensitive to the build-up of concentration gradients within the droplet, and here the faster drying of $NaNO_3$ droplets have made

crystallisation more reproducible. The much smaller initial mass fraction of aqueous $LiNO_3$ in this dataset led to 5.7% of the droplets nucleating crystals within the experimental time window of 10 s. Thus, comparing the experiments performed in Fig. 6-18 and Fig. 6-22, the compounds whose initial mass fraction decreased, i.e. $LiNO_3$ and $NaNO_3$, had an increased propensity to crystallise, and $RbNO_3$ had a decreased propensity to crystallise, with a broader time distribution of nucleation events. The same KNO_3 data in Fig. 6-18 and Fig. 6-22 was used as it already had an a_w of 0.95.

6.14. Chapter 6: Summary and Future Work

Although there have been multiple studies on the hygroscopicity of $NaNO_3$ aerosol particles, there remains an absence of agreement on the value of the ERH, and there has been limited work on the kinetics of the nucleation rate. In this chapter, the times that nucleation of $NaNO_3$ crystals occurred during the evaporation of populations of aqueous droplets was shown to be highly variable, droplet-to-droplet, forming broad distributions of nucleation time that reflected the stochastic nature of homogeneous nucleation. Such a distribution of nucleation events varied according to changes in the drying conditions, such as temperature, RH and initial solute concentration. One possible reason behind this interesting nucleation behaviour is that $NaNO_3$ solutions can increase in orders of magnitude in viscosity as the solute concentration rises, which in turn reduces the nucleation rate at very high supersaturations. There is a competition between nucleation rate and the time available for crystallisation (the drying time), and this interplay controls the ratio of amorphous or crystallised dry particles. The nucleation behaviour of aqueous $NaNO_3$ droplets could not be fully predicted using classical nucleation theory (CNT), but the nucleation rate could be inferred from the experimental data. It showed non-monotonic behaviour in the nucleation rate as a function of concentration, showing that the nucleation in evaporating aqueous $NaNO_3$ must occur through qualitatively different kinetics to CNT. In addition, the nucleation propensity of $NaNO_3$ was compared to that for other alkali nitrates: $LiNO_3$, KNO_3 and $RbNO_3$. The results showed an increasing propensity for crystal nucleation during evaporation going down the alkali nitrate group, with $RbNO_3$ showing the highest propensity to crystallise. This reflected observed trends in the group of hygroscopicity, ionic activity and ionic radii.

This work shows an important step in relating the nucleation rate of evaporating droplets to the drying rate and the evolving internal microstructure, which is very important for the application of spray-drying. However, the environmental conditions studied here do not reflect those experience by droplets in a spray-dryer. The temperatures in a spray-dryer can rise to several hundreds of degrees, with very dry gas flows. In addition, spray-drying formulations typically do not involve just one solute with one solvent. Whilst aqueous $NaNO_3$ represent a good model system for studying the competition between evaporative flux and internal diffusive transport in a drying droplet that becomes increasingly viscous,

studies such as this should develop to involve more complex formulations with mixtures of solvents and solutes. Therefore, to build upon the work presented in this chapter, future work should study increasingly dry and hot conditions, with more complex mixtures of starting formulation. Such environmental conditions make *in situ* study of evaporating droplets very difficult. The data in this thesis could be used to help with the development of droplet-drying models, which consider both mass and heat transfer between droplets and the gas-phase. Such models could then be used to simulate drying at temperatures that may not be accessible in experiments but are prevalent in spray-dryers.

Chapter 7

The Evaporation Kinetics and Nucleation Behaviour of Mixed Solution Droplets

In the previous chapters, the complexities around the crystal nucleation process in evaporating droplets of simple one-component systems has been discussed. NaCl solutions demonstrate high reproducibility in the time that identical droplets in a series pass the solubility limit and reach a critical supersaturation, leading to crystallisation, typically at the surface. However, the evaporation conditions can affect how rapidly this critical supersaturation is reached, and the interplay between the nucleation rate and the evaporation rate leads to varying crystal morphologies in the dried particle. For droplets containing aqueous sodium nitrate, the nucleation rate appears to show non-monotonic behaviour with the solute concentration. The nucleation rate is predicted to rise with increasing concentration but pass through a maximum and reduce at high concentrations. Whilst complex, the nucleation rate, and thus the chance of $NaNO_3$ crystallisation, could be predicted under certain conditions based on the experimental data presented in Chapter 6, provided that the concentration and droplet temperature is known.

In this chapter, experimental data of the evaporation kinetics and nucleation behaviour of more complex mixtures and solutions in aerosol droplets will be presented. First, the influence of non-crystallising additives such as organic components or colloidal nanoparticles on the evaporation kinetics and nucleation behaviour of inorganic aqueous solution droplets will be studied. This work aims to investigate whether the crystallisation process can be controlled, through delaying, preventing or inducing the onset of crystal nucleation. Secondly, the evaporation and crystal nucleation kinetics of mixtures of inorganic components will be studied, to explore how the nucleation of one component may affect the other, and ultimately, the morphology of the resulting particle.

The results presented in this chapter are currently being prepared for publication. I collected, analysed and interpreted all data presented in this chapter, except for Fig. 7-1 and Fig. 7-17 that are reprinted from manuscripts with the relevant copyright permissions.

7.1. Delaying Nucleation in Evaporating Inorganic Solution Droplets with a Surface-Active Fatty-Alcohol

The ability to control the proportion of crystalline to amorphous particles produced in a spray dryer would be highly valuable. An evaporating droplet in a spray dryer experiences a competition between the rate of water evaporation and the rate of crystal nucleation. A droplet enters a crystallisation window when it passes the bulk solubility limit at the surface, and to lengthen the crystallisation window in an evaporating droplet would allow more time for the nucleation process to take place.[158] An option to increase the time available for nucleation would be to decrease the evaporation rate after the point of saturation, exposing the droplet to high levels of supersaturation for a longer period of time. The evaporation rate could be reduced by decreasing the vapour pressure of water, such as a lower temperature, higher concentration of solute or higher RH. These three aspects have been explored in Chapter 6 with $NaNO_3$ and the propensity for a droplet to nucleate crystals was shown to be affected in all cases through minor changes in the drying kinetics.

The evaporation coefficient, or the equivalent mass accommodation coefficient, is a fraction describing the proportion of molecules hitting the droplet surface that are incorporated into the gas phase (for the evaporation coefficient) or the condensed phase (accommodation coefficient). Reducing the evaporation coefficient of a droplet thus reduces the evaporation rate.[310] Organic solutes are typically more surface active than inorganic salts in aqueous solutions owing to their generally reduced solubility in the bulk phase.[311] We would expect surface active organic molecules to reduce the evaporation coefficient of a droplet. Indeed, early work such as that by Fox showed a reduction in the evaporation rate of water from a flat surface when long-chain fatty-alcohols were present.[312] In such bulk systems of water with a very flat interface, the Knudsen number is very low, and Davies et al. demonstrated that the effective reduction in mass flux caused by the presence of long-chain alcohols is greatly magnified in going to systems of aerosol droplets with higher Knudsen numbers, i.e. typically those with smaller droplet sizes (Fig. 7-1).[313]

Davies calculated the mass flux from a water droplet at 293 K, 100 kPa, with variations across several orders of magnitude in the Knudsen number and in the evaporation coefficient, γ (Fig. 7-1a). The effect on the evaporation profile of droplets containing a 1:1 mixture (by volume) of ethanol and water and increasing amounts of additional hexadecanol is shown in panel *b*. The evaporation proceeds by the initial loss of ethanol, followed by water evaporation that becomes significantly slower once a complete monolayer of the hexadecanol has formed at the surface of the droplet. The surface area occupied by each molecule at the point of reduction in the evaporation rate was found to be 20 – 22 $Å^2$ for each dataset, which is consistent with the theory that a complete monolayer film has been formed at that point.[313] The thickness of the monolayer film could be varied by adjusting the length of the carbon chain

in the fatty-alcohol. Davies et al. identified that an increased carbon chain length, hence a thicker monolayer film, led to a more significant reduction in the evaporation rate after film formation.[313]

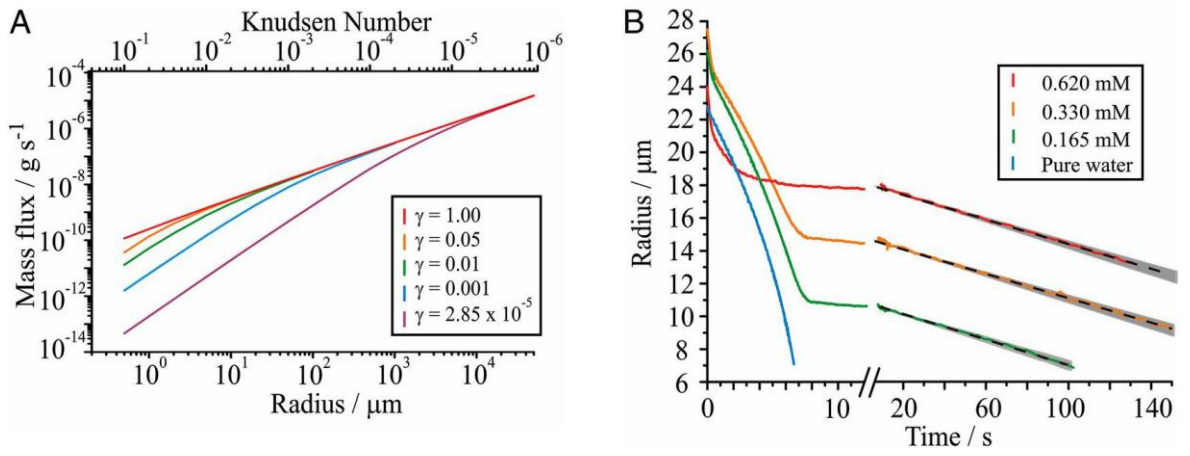

Figure 7-1: a) Calculations of the mass flux for varying droplet radii and Knudsen number, at a pressure and temperature of 100 kPa and 293 K, respectively. The evaporation coefficient, γ, is varied in the calculations. b) Evaporation profiles of droplets containing 1:1 by volume water-ethanol solutions with varying concentrations of added hexadecanol. Figure is reprinted from Davies et al.[313] with permission from the authors, who retain the copyright.

In this work, the inclusion of fatty-alcohol monolayers to evaporating droplets will be investigated, to increase the time available for crystal nucleation to occur.

7.1.1. The Effect of a Surface-Active Fatty-Alcohol on the Nucleation of Aqueous NaCl Solution Droplets

In Chapter 5, sequential evaporating droplets of aqueous NaCl in a large population showed reproducible crystal nucleation in a narrow time-distribution, when the droplet surface reaches a critical supersaturation level of 2.04. To investigate the effect of a fatty-alcohol monolayer on the evaporation and nucleation of aqueous NaCl droplets, tetradecanol is used as a co-component. A mixture of ethanol and water is used as the solvent, because like most fatty-alcohols, tetradecanol has very low solubility in pure water.

The evaporation of a droplet in the EDB containing ethanol, water and NaCl (initial mass fractions of 0.475, 0.475 and 0.05, respectively) is compared in Fig. 7-2a with droplets of the same composition but with additional tetradecanol in concentration of 0.29 mM (mass fraction 7.2×10^{-5}) and 0.60 mM (mass fraction 1.4×10^{-4}). The droplets were evaporated in the EDB at 293 K and 0% RH. The inset figure focuses on the first few seconds of evaporation in closer detail. In the droplet that does not contain tetradecanol, rapid evaporation of the solvents led to NaCl crystallisation. The evaporation rate of the droplets containing the fatty-alcohol decreased after a short period of time, and this time interval was

shorter for a larger initial concentration of tetradecanol. This is also evident in the work by Davies with hexadecanol; with a greater initial concentration of fatty-alcohol, the timescale for diffusional transport of the fatty-alcohol to populate the interface is reduced because there is already a large concentration in close proximity.[313]

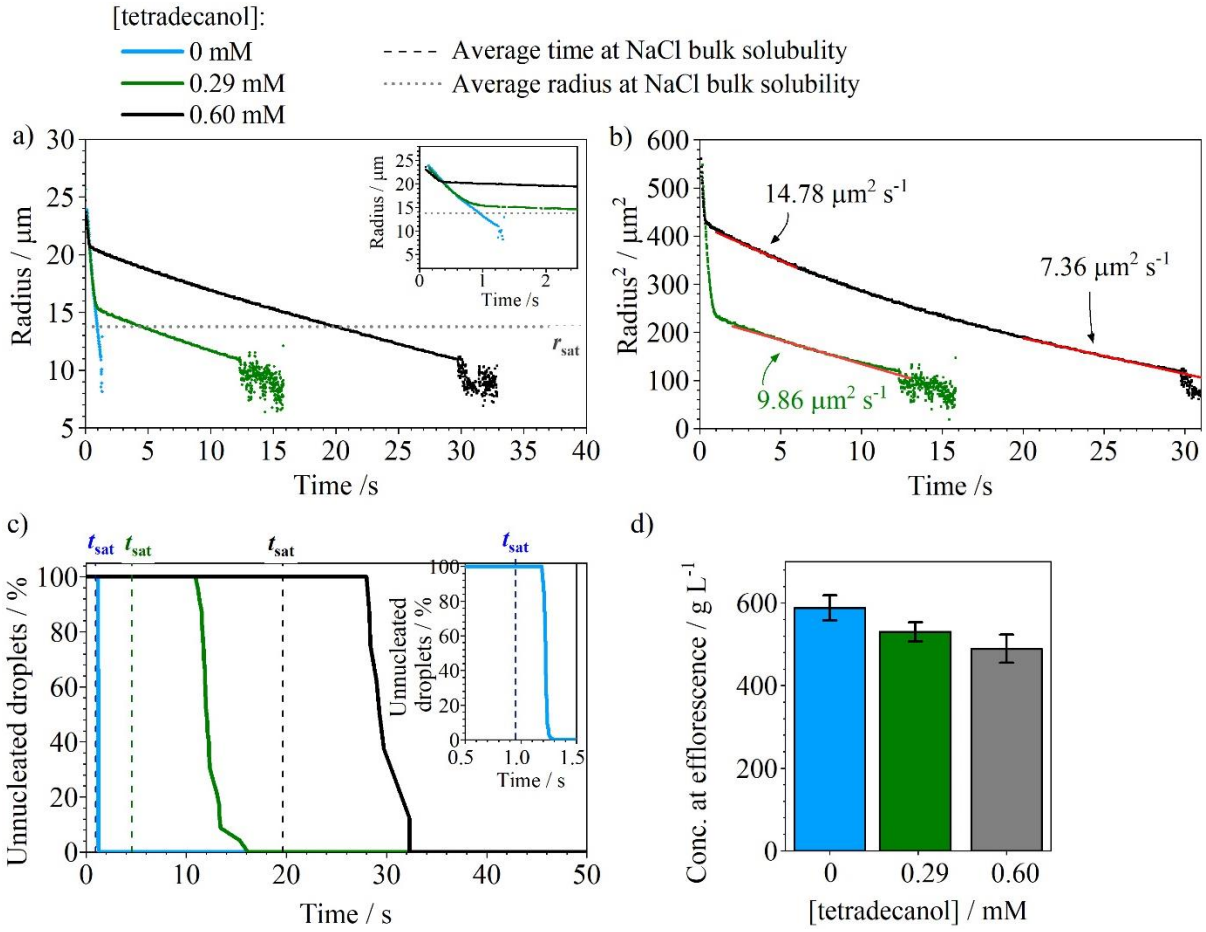

Figure 7-2: a) The evaporation and crystal nucleation process of a droplet containing ethanol, water and NaCl (initial mass fractions of 0.475, 0.475 and 0.050, respectively) in the EDB, with additional tetradecanol in concentrations as indicated in the figure legend. EDB conditions are 293 K and 0% RH. b) The radius^2 as a function of time for the aqueous NaCl droplets containing tetradecanol, with linear fits indicated to show the evaporation rate at certain times. c) The time-dependent distribution of crystal nucleation events observed in populations of droplets for each dataset, d) the average calculated concentration of NaCl at the time of observed crystal nucleation.

For a higher initial concentration of tetradecanol, evaporation down to a critical radius for NaCl crystal nucleation took longer, because the abrupt decrease in evaporation rate occurred at a larger droplet radius (Fig. 7-2a). The grey dotted line shows the droplet radius, averaged over all droplets in the figure, when the bulk solubility limit of NaCl was reached; this was the point at which the droplets entered the crystallisation window. The droplet containing no tetradecanol (blue) had a very short crystallisation window before efflorescence occurred, which was at a radius of ~ 11 µm. When tetradecanol was present in the formulation at 0.29 mM, the crystallisation window was lengthened from 0.27 ± 0.02 s to 7 ± 1 s due to the decrease in evaporation rate (green). The evaporation rate after the formation of a

complete monolayer of tetradecanol would be expected to be the same in 0.60 mM droplet as the 0.29 nM droplet, as evaporation should limited by the kinetics of water transport through the fatty alcohol film. However, the 0.6 mM droplet has a decreasing evaporation rate throughout the drying process (Fig. 7-2b), with a final evaporation rate that is slower than that in the 0.29 mM droplet. Hence, the crystallisation window was also lengthened going from the 0.29 mM initial tetradecanol concentration to 0.60 mM, 7 ± 1 s to 10 ± 1 s. The change in evaporation rate after the formation of the tetradecanol monolayer film in the 0.60 mM case (Fig. 7-2b) could be caused by a restructuring of the fatty alcohol film. Miles et al. observed a similar effect in in the evaporation of aqueous droplet containing mixtures of tridecanol and pentadecanol.[310] As in Fig. 7-2b, film formation occurred early into the evaporation process, causing an evaporation rate reduction, and as the radius continued to decrease a second reduction in evaporation rate occurred. This was attributed restructure of the mixed film (tridecanol and pentadecanol); a change in composition decreased the evaporation coefficient and thus, the evaporation rate. It is possible that the tetradecanol used in Fig. 7-2 was not pure and that a different long-chain fatty alcohol was present, leading to a similar evaporation profile to the droplets in Miles et al.[310]

The time-dependent distribution of nucleation events in each dataset is shown in panel *c*. The abrupt decrease in uncrystallised droplets from 100% to 0% for the droplets containing no tetradecanol reflects the reproducibility in NaCl to nucleate crystals when it reaches a critical supersaturation. The droplets containing tetradecanol passed the bulk solubility limit at t_{sat} and then there were still a few seconds of water evaporation until the crystal nucleation was observed. For the two datasets of droplets containing tetradecanol, crystal nucleation was observed in all droplets but there was a broader distribution in the nucleation time across the droplet population. Hence, it can be deduced that tetradecanol does not prevent crystal nucleation in NaCl but delays the time at which nucleation occurs.

The average concentration of NaCl at which crystal nucleation occurred for each dataset is compared in Fig. 7-2d. It must be noted that the concentration, in g L^{-1}, is highly sensitive to the calculated mass of NaCl in each droplet. As these droplets initially contained a large volume of ethanol, the initial evaporation is expected to be unsteady. Thus, there is a large uncertainty associated with the back extrapolation in the radius^2 to determine the initial radius and mass of the droplet. There appears to be a weak trend of NaCl crystal nucleation occurring at lower levels of solute supersaturation for greater initial concentrations of tetradecanol. However, for a higher initial concentration of tetradecanol, fewer points were used for the back-extrapolation to determine the initial droplet radius; it is possible this led to an under-estimation of the initial radius and the initial mass of the droplet, leading to a lower calculated NaCl concentration at efflorescence.

An additional point to note from Fig. 7-2d is the standard deviation in different values of the efflorescence concentration, which do not appear to vary much for the three datasets. Although the nucleation times showed a much broader distribution when tetradecanol was present, in Fig. 7-2d the

concentration of NaCl at nucleation did not show a broader distribution. This can be attributed to the fact that the concentration in the red dataset in panel *c* was rising sharply due to the steepest dr^2/dt at the point of nucleation; even millisecond variations in the time that nucleation was observed, droplet-to-droplet, led to a large standard deviation in the calculated NaCl concentration. The green and black data show a slower increase in NaCl concentration due to a reduced evaporation rate; hence, the distribution for the NaCl concentration that triggered nucleation in a droplet stayed narrow.

The crystallisation window for NaCl nucleation has been shown to be lengthened by adding increasing amounts of tetradecanol. To nucleate crystals, an evaporating droplet must overcome the competition between the evaporation rate and the nucleation rate. Typically, it can be challenging to get sugar molecules with a slow nucleation rate, such as lactose, to crystallise during spray-drying.[289] This NaCl-tetradecanol data shows that if the NaCl were substituted for a compound with a slow nucleation rate, it could be possible to use this technique to increase the quantity of droplets that can crystallise during evaporation.

7.1.2. The Effect of a Surface-Active Fatty-Alcohol on the Nucleation of Aqueous $NaNO_3$ Solution Droplets

Following on from the work presented in Section 7.1.1, similar experiments were performed with $NaNO_3$ instead of NaCl, to study the effect of added tetradecanol on the nucleation rate of $NaNO_3$ crystals. The time distribution of when crystal nucleation was observed during the evaporation of populations of droplets containing ethanol, water and $NaNO_3$, (initial mass fractions of 0.425, 0.425, and 0.15, respectively) is shown in Fig. 7-3a (red). The data is compared to droplets with the same composition but with additional tetradecanol in concentrations of 0.32 mM (green, mass fraction of 7.13×10^{-5}), 0.48 mM (blue, mass fraction of 1.07×10^{-4}) and 0.64 mM (black, mass fraction of 1.41×10^{-4}). The experiments were all performed at 293 K and 0% RH. Examples of a droplet evaporating from each dataset are compared in Fig. 7-3b.

As discussed in Chapter 5, aqueous $NaNO_3$ droplets containing no tetradecanol show a broader time distribution of nucleation events than for NaCl crystal nucleation. One aqueous $NaNO_3$ droplet nucleated crystals after 37 s and one droplet did not nucleate crystals in the experimental window, which for this experiment was 50 s. When tetradecanol was added in increasing concentrations, the time that nucleation was observed was delayed due to the abrupt decrease in evaporation rate once the tetradecanol has adsorbed to the droplet surface. Interestingly, the distribution over which droplet nucleation were observed did not appear to be dependent upon the concentration of tetradecanol; going from 0.32 mM to 0.48 mM and 0.64 mM of tetradecanol led to a similar gradient in the decay of the uncrystallised droplets (Fig. 7-3a). The percentage of droplets that had still not nucleated crystals at the

end of the experimental window did not show dependence on the concentration of added tetradecanol. For 0 mM, 0.32 mM, 0.48 mM and 0.64 mM tetradecanol, the proportion of droplets to not nucleate crystals within the experimental window was 1%, 0%, 2% and 4% respectively. Such a weak dependence is surprising; one would have expected that a longer crystallisation window would lead to more chance of nucleation to occur as the droplet is exposed to a high supersaturation for a greater time. It is possible that an increase over several orders of magnitude in the length of the crystallisation window would be required to cause a significant increase in the number of droplets to crystallise. However, the conclusions to this experiment are similar to those with NaCl; the addition of tetradecanol to the solution delayed the onset of $NaNO_3$ crystal nucleation.

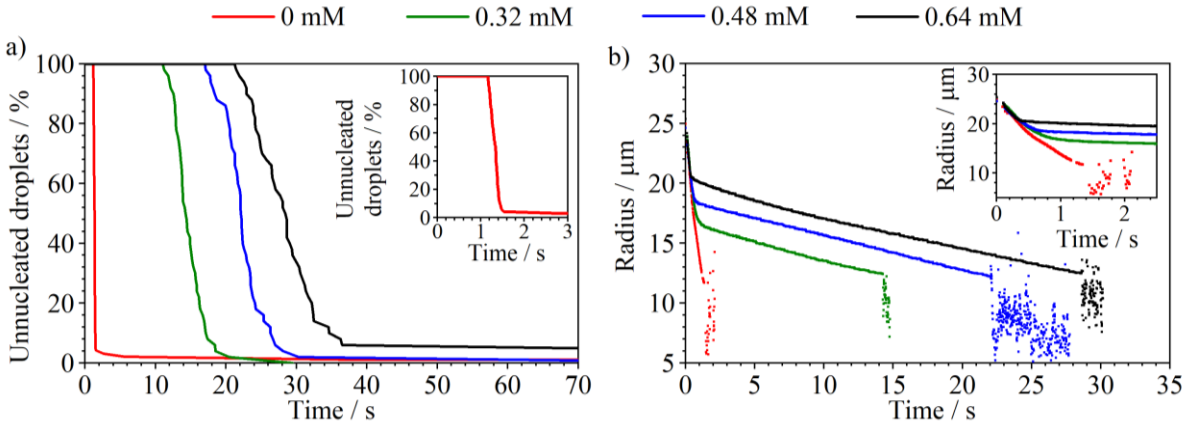

Figure 7-3: a) The time-dependent distribution of crystal nucleation events observed in populations of droplets containing 0.425 mass fraction EtOH, 0.425 mass fraction water and 0.15 mass fraction $NaNO_3$, with additional tetradecanol in concentrations as indicated by the legend. The inset figure shows the red dataset in greater detail. Droplets evaporate in 293 K at 0% RH. b) The evaporation and crystal nucleation process for example droplets from panel a, with the inset showing the early experimental times in greater detail.

7.2. Impeding Crystal Nucleation in $NaNO_3$ Droplets with Glycerol

In this section, the crystal nucleation behaviour of droplets containing both an inorganic and organic solute will be explored, to observe if the presence of the organic component affects the nucleation process of the inorganic solute. Glycerol was used as an organic solute and $NaNO_3$ as the inorganic solute. Previous work has shown that glycerol can prevent certain phase transitions on dehydration for lipid cubic phase samples [314] and bilayers.[315] Yu et al. studied the hygroscopicity of mixed droplets of $NaNO_3$ and glycerol, for different molar ratios, in droplets deposited on a PTFE film.[316] Whilst not an aerosol study, the PTFE surface was hydrophobic with a high contact angle to minimise the contact point between the substrate and droplet. The efflorescence process was observed by looking at morphological changes with a microscope. In addition, a micro-Raman technique studied the stretching band of NO_3^- in $NaNO_3$ and the stretching band of CH_2 in glycerol to study the conformational changes

during the efflorescence. Some interesting findings from this work were that $NaNO_3$ changed the conformation of glycerol by electrostatic interactions and hydrogen-bonding, which is detectable using Raman-spectroscopy. This in turn suppressed the formation of contact ions for $NaNO_3$ and inhibited crystal nucleation. This study by Yu et al. was a thermodynamic study and reported the suppression of nucleation in terms of a reduction in the observed efflorescence RH (ERH), rather than discussing the kinetics of crystal formation. The work in this thesis aims to investigate if this suppression of crystal nucleation is observable in the timescale of a rapidly evaporating $NaNO_3$ droplet and hence whether glycerol can affect the phase of the final product.

Evaporation experiments of populations of droplets containing aqueous $NaNO_3$-glycerol, of two different initial ratios, are compared to that for aqueous-$NaNO_3$ solution in shown in Fig. 7-4. The initial composition of each solution was chosen to maintain a constant initial ratio of $NaNO_3$ to water (20% $NaNO_3$: 80% water, by mass), as in Chapter 5 the initial $NaNO_3$ concentration in aqueous droplets was shown to affect the nucleation behaviour. Additional glycerol was added to observe the effect on the propensity for $NaNO_3$ crystals to nucleate in 0% RH and 293 K, so the initial solutions were $NaNO_3$-glycerol-water in mass fractions of 0.176, 0.118, 0.706 (blue) and 0.184, 0.095, 0.721 (green), respectively. In the work by Yu et al. they report the concentrations in terms of an organic to inorganic ratio (OIR) of glycerol to $NaNO_3$. The OIR for these solutions was 0.62 and 0.48, respectively. It should be noted that a solution of only glycerol and water would not nucleate crystals; they are miscible liquids at ambient pressure and temperature. Glycerol has a very low volatility < 0.01 kPa at 293 K.[218]

The time distribution of observed crystal nucleation became broader through increases in the initial concentration of glycerol, and the chance of crystal nucleation within the experimental window reduced. After 20 s, the proportion of droplets that had not yet nucleated crystals went from 1.6% with pure aqueous $NaNO_3$, to 41.4% and 74.7% when the glycerol mass fraction was 0.095 and 0.12, respectively.

The evaporation rates of an example droplet from each dataset are compared in Fig. 7-4b, with the examples shown being droplets that did not nucleate within the experimental window. The final equilibrated radius increased with added glycerol content as that led to more mass of solute in the final particle. The equilibrated radii of each droplet are compared to a linear fit to the droplet radius at t=20 s in Fig. 7-4c. After the initial period of water evaporation (t ~ 3 s), the radii of all three droplets continued to reduce in radius. This shows evidence of a droplet-bulk kinetic limitation to evaporation, which is typically observed in droplets of viscous liquids (greater than ~ 1 Pa s in viscosity)[317] such that the rate of water transport through the droplet to the surface becomes the limiting rate in evaporation. The extent of a kinetic limitation on the later stage of water evaporation appears to have increased slightly with increased glycerol content, but it was very similar across all three droplets, even when no glycerol was present. Thus, the mechanism through which glycerol reduces the propensity for crystal nucleation in aqueous $NaNO_3$ droplets appears to not be wholly caused by an increase in viscosity. This

supports the theory from Yu et al. about the conformational structure of the components; that hydrogen bonding between glycerol and $NaNO_3$ impeded the formation of Na^+ and NO_3^- ion pairs for crystal nucleation.

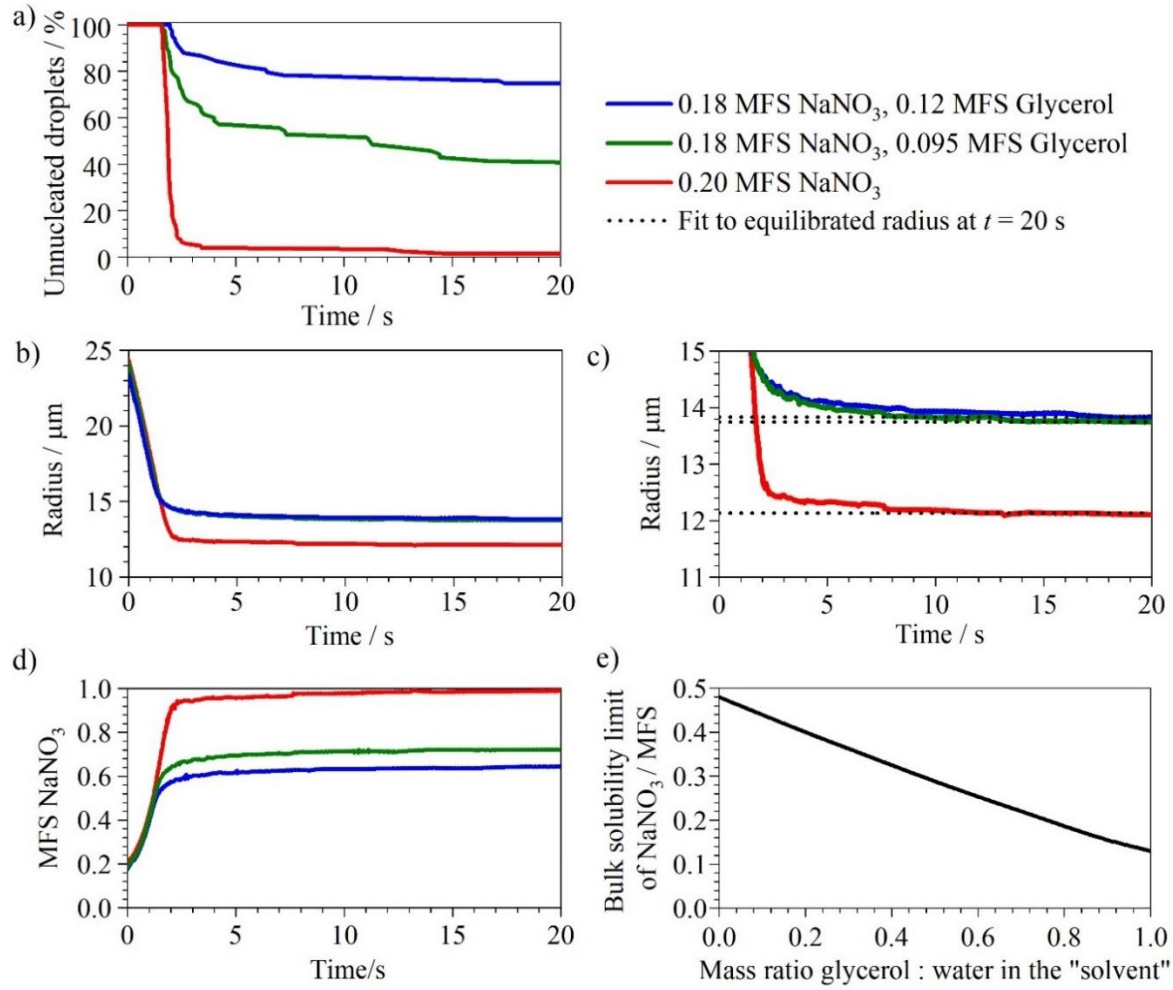

Figure 7-4: a) The time-dependent distribution of nucleation events observed in a population of aqueous droplets containing varying amounts of $NaNO_3$ and glycerol, with initial mass fractions indicated by the figure legend. Droplets evaporate in 0% RH at 293 K. b) The evaporation profile of an example droplet from each dataset in panel a) that does not nucleate crystals in the experimental time window of 20 s. c) The radii of 'equilibration' of each droplet in panel b) in closer detail, compared to a linear fit to the radius at t = 20 s to demonstrate the continued evaporation after the radius appears to have levelled off. d) The mass fraction of $NaNO_3$ in each droplet throughout the evaporation of water. e) The bulk solubility of $NaNO_3$ in terms of mass fraction in a solvent that comprises varying ratios of glycerol and water, at 298 K. Data is plotted from Zhang et al.[318]

The mass fraction of $NaNO_3$ in the mixed aqueous $NaNO_3$-glycerol droplets throughout evaporation of the water is shown in Fig. 7-4d. Without glycerol present in the droplet, the $NaNO_3$ mass fraction approaches 1 at t = 20 s. For the droplets that contain glycerol (with initial mass fractions of glycerol of 0.095 and 0.12), the mass fraction of $NaNO_3$ is ~ 0.72 and 0.64 once the water has evaporated, respectively. The bulk solubility limit of $NaNO_3$ in a solvent of varying ratios of glycerol:water decreases as the water content decreases (Fig. 7-4e). In the absence of water, the bulk solubility limit

of $NaNO_3$ in glycerol is 0.13 (mass fraction).[318] This value is significantly below the mass fraction of $NaNO_3$ reached upon evaporation of the $NaNO_3$-glycerol-water droplets. From the relative bulk solubility limits of $NaNO_3$ in water and in glycerol we can infer that the thermodynamic drive for crystal nucleation of $NaNO_3$ is greater in the droplets containing glycerol than in the $NaNO_3$-water droplets. This thermodynamic drive for crystallisation of $NaNO_3$ is overcome by a kinetic barrier to crystal nucleation imposed upon $NaNO_3$ by the increasing glycerol content.

It should be noted that glycerol is volatile, however its volatility is very low, < 0.01 kPa at 293 K,[218] so within the 20 s timeframe of the droplet evaporation data presented in Fig. 7-4 it is not expected that any notable radius reduction would be caused by the evaporation of glycerol from the droplet.

7.3. The Evaporation and Nucleation Kinetics of Aqueous Inorganic Droplets Containing a Colloidal Silica Suspension

Due to the high air temperatures and typically short residence times in a spray dryer, spray-dried products are often amorphous.[289] Amorphous products can often be sticky, which is undesirable as wall-deposition of sticky powders in the dryer can cause reduction in product yield, challenges to product handling and fire hazards.[206] Allowing droplets to crystallise in a spray dryer can reduce the stickiness, and thus the product output,[47] and one method to do so is to induce heterogeneous nucleation.

In heterogeneous nucleation, as outlined by classical nucleation theory, the presence of a surface reduces the free energy barrier to nucleation by negating the need for the initial unfavourable formation of an interface between crystal and solution. Thus, heterogeneous nucleation is expected to occur at lower values of supersaturation.[197] However, there have been reports of different "types" of surface leading to different outcomes in heterogeneous nucleation. Espinosa et al. reported simulation results of wall-induced nucleation for colloidal fluids of hard-spheres, and showed that the structure of the wall (roughness) affected the degree of supersaturation required to induce crystal nucleation.[288] Surfaces with certain morphologies could more readily position ions into a particular cluster arrangements, affecting the supersaturation required to induce nucleation, or even the particular polymorph of crystal. For example, Halliwell et al. identified that the crystalline polymorph IV of Carbamazepine can only be accessed if a polymer is present to template the solution into that particular morphology.[319]

Typically, in bulk experiments, heterogeneous nucleation dominates over homogeneous nucleation as the mechanism of crystal formation because the surface of the container can act as the templating site. In the work discussed in this thesis, the droplet volume is very small (~ 60 pL) and the inorganic salts and water used in such experiments are very high in purity, so the likelihood for there being dust or

contaminants entering the droplets on generation is very small. Aerosol droplets can typically access much higher degrees of supersaturation than in the bulk phase.[6] The reasons for this are assumed to be because crystal nucleation in the aerosol phase must proceed homogeneously. Alternatively, the droplet's air-liquid interface could act as a heterogeneous nucleation site, but one that only induces crystal nucleation at much higher degrees of supersaturation.

Here we investigate if a small amount of colloidal particle inside the droplet can affect the nucleation kinetics of aerosol droplets. Such particles introduce solid-liquid boundaries into the droplets and this section will investigate whether this influences the supersaturation at which nucleation in aerosol droplets is observed, being a 'different type' of surface to the air-liquid interface. Previous work has investigated the presence of colloidal fumed silica nanoparticles in evaporating sessile droplets of volumes on the microlitre[320] and picolitre scale.[72,321] These studies utilise colloidal silica microspheres or polystyrene nanoparticles to track the internal flows, to study the dried pattern formed from printing droplets onto a flat substrate.

The evaporation kinetics and nucleation behaviour of droplets containing inorganic salts and colloidal silica nanoparticles will be studied. First, it is important to investigate the evaporation kinetics of droplets containing only a suspension of silica nanoparticles, which will be described in the following section.

7.3.1. The Evaporation of Water Droplets Containing a Colloidal Silica Suspension

Colloidal suspensions of hydrophilic silica nanoparticles (HDK® Fumed Silica, N20, Wacker) were prepared by gradually adding the silica to pure water under magnetic stirring. After 30 minutes of stirring, the suspension was sonicated for 30 minutes, followed by stirring for a further 30 minutes. Once a visually homogeneous solution had formed, the solution was injected into the MicroFab dispensers for evaporation experiments in the EDB as normal. A concentration of 0.1% silica (by volume) in water was used, which is 0.002 mass fraction of silica. Typically, a solution of such a concentration visibly aggregates after approximately 1 day of storage.

HDK N20 consist of so-called primary particles of ~ 12 nm in diameter which are firmly sintered together to form branched aggregates of ~ 180 nm in diameter.[322] For a well-dispersed colloidal suspension with 0.1% by volume of silica nanoaggregates, a droplet of initial radius 25 μm would contain on average 21,400 silica aggregates. Naturally, there would be a distribution of the number of silica particles in each droplet, but this quantity is sufficiently high that one can expect every droplet to contain silica particles (*particles* here meaning the 180 nm aggregates).

Aqueous droplets containing silica nanoparticles undergo water evaporation leaving a solid silica particle remaining.[323] The evaporation rate of a water droplet containing 0.1% volume SiO_2 nanoparticles at 293 K and 0% RH is compared to a pure water droplet under the same conditions in Fig. 7-5. The evaporation rates of the two droplets are identical (Fig. 7-5b), demonstrating that the presence of the SiO_2 has no effect on the vapour pressure of water. For the droplet containing silica, the light scattering becomes disrupted upon aggregation of the silica nanoparticles to form a solid particle at t = 2.4 s. As the silica does not nucleate crystals, but rather, aggregates upon the loss of water, this is not described as a 'nucleation time' but as a 'lock point', when the radius can no longer be resolved by the light scattering.

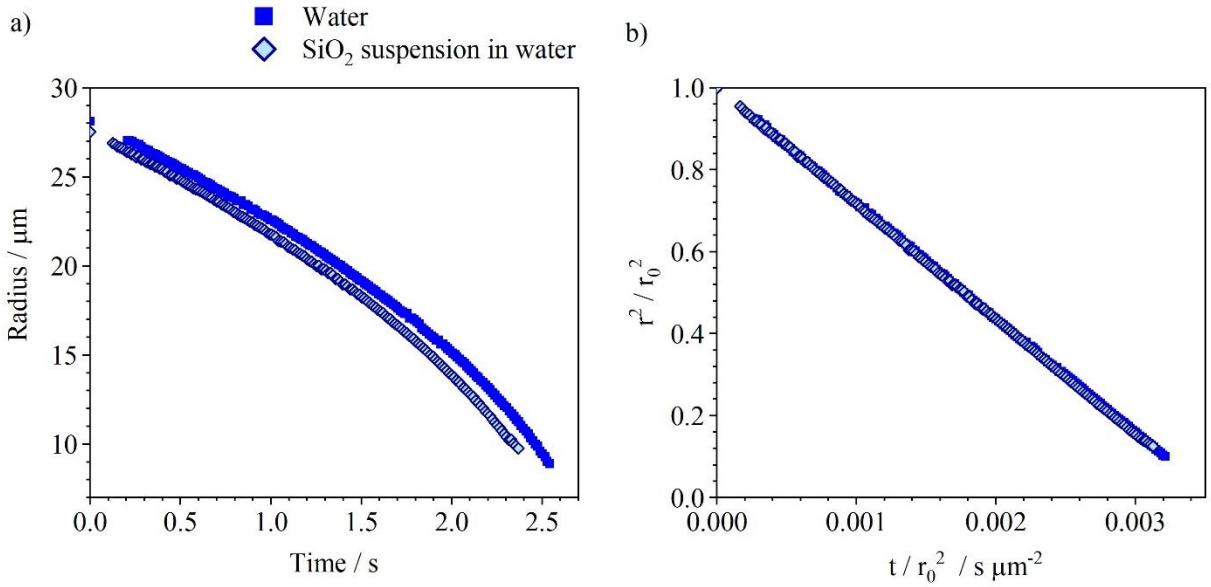

Figure 7-5: a) The evaporation of a pure water droplet compared to that of a water droplet containing a colloidal suspension of SiO_2 nanoparticles, at 293 K and 0% RH. The final datapoint shown for the droplet containing SiO_2 shows the time at which the SiO_2 aggregated, i.e. the 'lock point'. b) The evaporation data in panel a) normalised with respect to the initial radius, to compare the evaporation rates.

In the next sections, different inorganic salts will be included in the solution containing silica nanoparticles, to observe the nucleation behaviour and infer whether the silica is able to induce heterogeneous nucleation in the salts. The inorganic salts discussed are $LiNO_3$, $NaNO_3$ and NaCl, to compare the effect of silica nanoparticles on salts that range from those that rarely nucleate during evaporation ($LiNO_3$) to those that reproducibly nucleate crystals (NaCl).

7.3.2. The Evaporation of Aqueous $LiNO_3$ Droplets Containing Colloidal Silica

The studies of the nucleation behaviour of four alkali nitrates in Chapter 6 suggest that $LiNO_3$ has a much lower crystal nucleation rate than $NaNO_3$, KNO_3 and $RbNO_3$. The majority of a population of aqueous $LiNO_3$ droplets evaporating into dry conditions did not nucleate any crystals and dried to form an amorphous particle. An experiment was performed with aqueous $LiNO_3$ to investigate whether the solid surface of SiO_2 nanoparticles could induce nucleation in the evaporating droplets.

First, the high reproducibility in the radius during evaporation of a series of 30 droplets in the EDB, for an aqueous solution of $LiNO_3$, of initial mass fraction 0.1, is shown in Fig. 7-6a. The evaporation conditions were 0% RH and 293 K. No droplets in this experiment displayed any evidence of crystal nucleation within the experimental window of 20 s. Aqueous suspensions of hydrophilic silica nanoparticles (0.1% volume, 0.0022 MFS) were prepared using the same procedure as described in the previous section, but with $LiNO_3$ added under magnetic stirring afterwards (to make a concentration of $LiNO_3$ 0.1 MFS). The $LiNO_3$-SiO_2 droplets also showed no evidence of crystal nucleation during evaporation under the same conditions (Fig. 7-6b). The initial radii of the droplets in this experiment differed over a spread of ± 1 μm, so the same data is plotted in panel *c* normalised with respect to the initial droplet radius. This figure serves to demonstrate that, although the starting radii varied, the evaporation profile for the droplets showed very high reproducibility and the evaporation process appeared unaffected by the presence of SiO_2.

Aggregation of the SiO_2 particles was not detected in the aqueous $LiNO_3$, unlike in Fig. 7-5. One droplet from the dataset containing colloidal SiO_2, with the phase function (PF) mapping software identifying the phase with time (in 5-datapoint bins) is shown in Fig. 7-6d. The morphology for this droplet was indicated by the PF using the algorithm outlined in detail in Chapter 3. The morphology of the droplet was indicated to be homogeneous during the initial period of evaporation, and when the radius reached a steady value, a mixture of homogeneous, inclusions and core-shell morphologies were identified. The PF did not identify one distinct morphology, and the droplet radius was easily retrieved by the EDB software for the duration of the experiment indicating the presence of clear fringes in the PF. The PF sometimes infers the particle has an inclusions morphology, and sometimes a core-shell morphology. Perhaps the high viscosity of the amorphous $LiNO_3$ particle prevented SiO_2 aggregation. To conclude, SiO_2 nanoparticles did not induce heterogeneous nucleation in the evaporating aqueous $LiNO_3$ droplets and the droplets dried to form amorphous spherical particles.

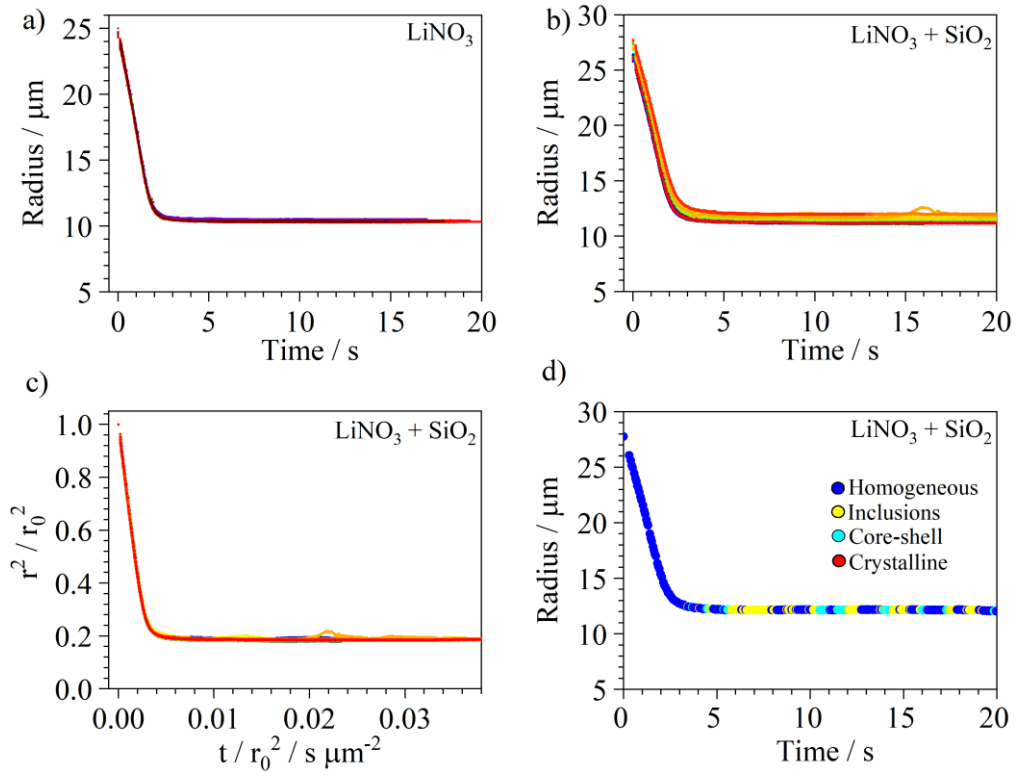

Figure 7-6: a) The evaporation profiles of a population of 30 droplets overlaid, containing an aqueous solution of 0.1 MFS $LiNO_3$, evaporating in 0% RH at 293 K. b) The evaporation profiles of 20 aqueous $LiNO_3$ droplets of 0.1 MFS, containing an additional 0.1% by volume (0.002 mass fraction) SiO_2 nanoparticles. c) The data in panel b) but normalised with respect to the initial droplet radius, to better show the reproducibility in the evaporation rates. d) The evaporation profile of one example droplet from the dataset in panel b) with the colour of the datapoints indicating the morphology at each point as inferred from the phase function.

7.3.3. The Evaporation of Aqueous $NaNO_3$ Droplets Containing Colloidal Silica

In Chapter 6 it was shown that aqueous $NaNO_3$ droplets showed a faster crystal nucleation rate during droplet evaporation than $LiNO_3$ droplets, but the $NaNO_3$ nucleation time was not reproducible across a large population of droplets. The distribution in crystal nucleation times for populations of aqueous $NaNO_3$ droplets (initial mass fraction 0.2) is compared to that for aqueous $NaNO_3$-SiO_2 droplets (mass fraction of 0.2 and 0.0022, respectively) in Fig 7-7a. Droplets are evaporated in the EDB at 0% RH and 293 K or 275 K.

When SiO_2 nanoparticles were present, the nucleation behaviour of the $NaNO_3$ solutions appeared to become more reproducible. This is more apparent with the experiment performed at the lower temperature. In Chapter 6, droplets of aqueous $NaNO_3$ (initial mass fraction of 0.2) were shown to be less likely to crystallise when dried at lower temperatures, with the majority of a $NaNO_3$ droplet

population drying to from amorphous particles. When SiO_2 was added to the formulation all droplets crystallised at 275 K, and in a narrow distribution of times.

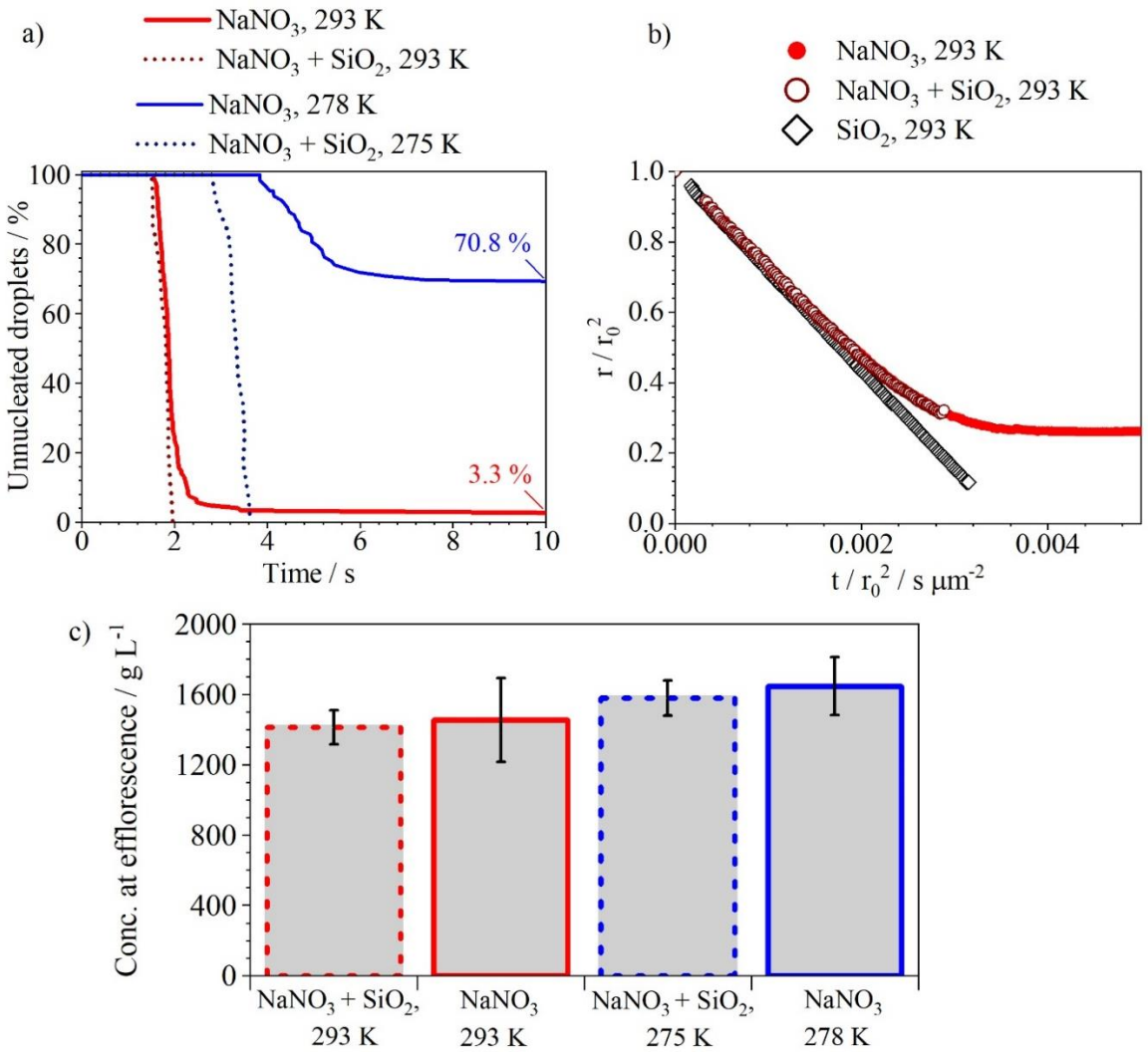

Figure 7-7: a) Time dependent distribution of nucleation events of aqueous droplets of 0.2 MFS $NaNO_3$ evaporating in 0% RH, at 293 K (red data) and 278 K (blue data). Droplets containing 0.1% by volume SiO_2 nanoparticles (0.002 mass fraction) evaporating under the same conditions are indicated by the dotted line. b) The evaporation rate of an aqueous droplet containing 0.2 MFS $NaNO_3$, or 0.002 MFS SiO_2 nanoparticles, or both components, at 293 K and 0% RH, normalised with respect to the initial radius. c) The average calculated concentration of $NaNO_3$ at the time of observed crystal nucleation, for the droplets that did nucleate crystals within the 10 s experimental time window.

The figure conceals the fact that the droplets containing SiO_2 that were dried at 275 K had a smaller initial radius than those without SiO_2. In this experiment, whilst both datasets performed at 293 K, and the pure aqueous $NaNO_3$ dataset at 278 K had droplets of initial radius 24 – 25.5 µm, the dataset of $NaNO_3$ with added SiO_2 at 275 K had droplets of initial radius 22 µm. Due to the smaller initial radius, these droplets evaporated in a shorter timeframe and hence reached a critical supersaturation for crystallisation at an earlier time. To overcome this discrepancy, the concentration of $NaNO_3$ at the point of crystal nucleation is shown in Fig. 7-7c. It must be noted that these data are an average of the droplets

that *did* nucleate crystals; droplets that did not nucleate crystals within the experimental timescale are omitted from the average. The $NaNO_3$ concentration at efflorescence is calculated in g L^{-1}. With SiO_2 present in the droplets, the concentration at efflorescence was, on average, marginally lower than that when no SiO_2 was present, however the standard deviation was smaller, reflected in the size of the respective error bars. The presence of colloidal SiO_2 particles in the $NaNO_3$ solution led to every droplet at both temperatures nucleating crystals, with a narrower time distribution of nucleation events.

We assume that the observed disruption in the light scattering in evaporating aqueous $NaNO_3$-SiO_2 droplets is a result of $NaNO_3$ crystal nucleation, rather than SiO_2 aggregation. We assume this because no SiO_2 aggregation was detected in the aqueous $LiNO_3$-SiO_2 droplets, and also because SiO_2 aggregation in SiO_2-water droplets with the same volume fraction occurred at a lower radius of (~ 9.1 µm) than the light scattering became disrupted in the $NaNO_3$-SiO_2 droplets (~13 µm), shown in Fig. 7-7b. However, being unable to resolve a difference in SiO_2 aggregation and $NaNO_3$ nucleation from the light scattering is a caveat of this study. Further work could involve performing X-Ray diffraction analysis on the dried particles of $NaNO_3$ dried with and without SiO_2 nanoparticles, to compare the extent of crystalline content. Such work would conclusively determine whether the $NaNO_3$ crystallisation is induced through heterogeneous nucleation by SiO_2.

7.3.4. The Evaporation of Aqueous NaCl Droplets Containing Colloidal Silica

Finally, the evaporation kinetics of aqueous NaCl droplets are compared to those containing additional colloidal silica nanoparticles, with the aim to observe if silica affects the nucleation kinetics of solutions that reproducibly crystallise during evaporation.

Previous work has highlighted that NaCl can increase the rate of aggregation in colloidal silica suspensions.[324] Thus, for this study, a low concentration of NaCl was used in this experiment (0.0234 MFS). When a higher concentration of NaCl was used, the solution visibly aggregated before the MicroFab dispensers could be filled. This was not a problem in the previous experiments with $LiNO_3$ and $NaNO_3$.

Solutions of a low concentration of NaCl (0.0234 MFS) dried at 293 K and 0% RH evaporated in a highly reproducible way, and crystals nucleated ~ 1.9 seconds into the drying process (Fig. 7-8). An example droplet with a crystal nucleation time that is closest to the average of the 10 droplets in this dataset is shown in panel *a* (grey datapoints). The noisy datapoints after crystal nucleation have been removed. The dataset is compared to the evaporation of an aqueous NaCl-SiO_2 droplet (red datapoints, mass fractions 0.0234 and 0.0022, respectively). The data are normalised with respect to the initial

radius in panel *b* showing that, although the initial droplet size for the droplets in the silica-containing droplets was larger than without silica, the evaporation rates appeared to be identical. The calculated concentration of NaCl at the point of crystal nucleation for the two datasets is compared in Fig. 7-8c. The error bars for this plot are large, which can be expected as this experiment was performed in 0% RH with a low concentration of NaCl: such rapid drying events can lead to the concentration rising very sharply at the end of the evaporation process.[261] Nevertheless, within the error bars, the concentration at the time of nucleation in NaCl droplets with and without colloidal silica appears to have been the same.

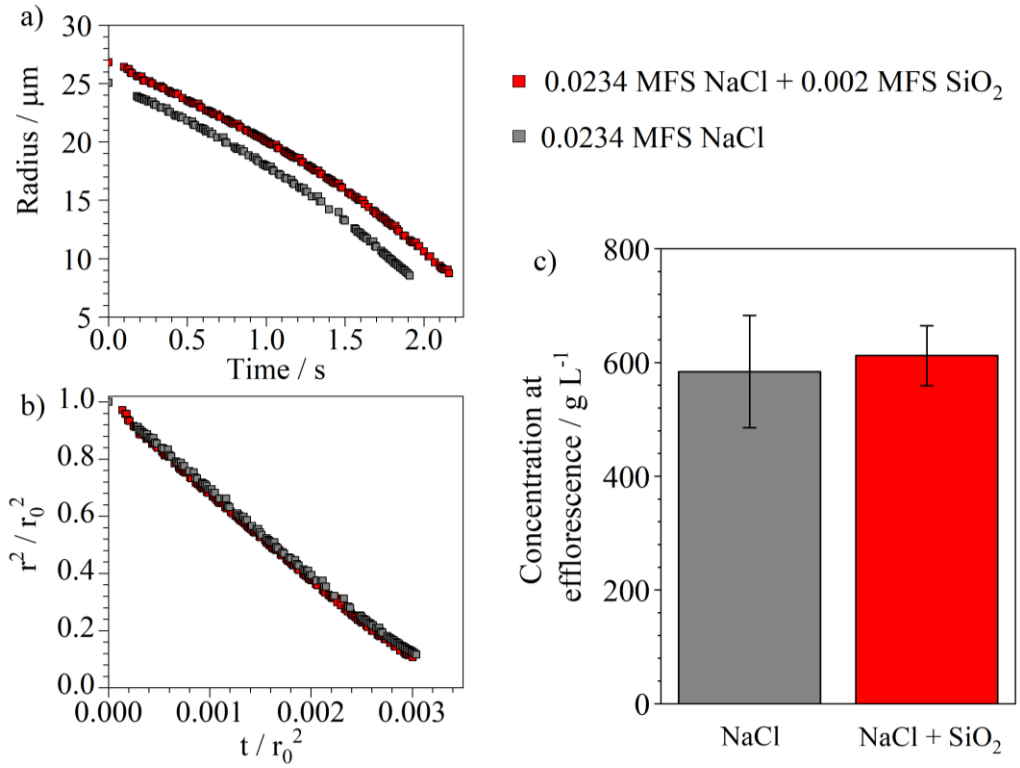

Figure 7-8: a) The evaporation of two droplets of aqueous solutions of 0.0234 MFS NaCl evaporating in 0% RH, at 293 K, one of which also contains 0.1% volume (0.002 mass fraction) SiO_2 nanoparticles. b) The evaporation data in panel a) normalised with respect to the initial radius, to compare the evaporation rates. c) The average calculated concentration of NaCl at the time of observed crystal nucleation for a population of droplets evaporating under the same conditions.

Aqueous NaCl droplets evaporating into dry air effloresce with no viscosity-inhibition to crystal nucleation, unlike in aqueous $NaNO_3$ and $LiNO_3$ droplets. The lower viscosity in NaCl solutions may be the reason behind why SiO_2 does not appear to affect NaCl nucleation behaviour; the nucleation rate of NaCl is high and at high supersaturations of NaCl there is no barrier to nucleation so the silica surface is not needed to drive the system to nucleate crystals.

7.3.5. Inducing Heterogeneous Crystal Nucleation in NaCl Droplets Above the Efflorescence RH using Colloidal Silica

An additional experiment was performed to study the effect of colloidal silica on the nucleation behaviour of aqueous NaCl aerosol in a gas-phase RH of ~ 52%, rather than in dry conditions. Pure aqueous NaCl aerosol droplets do not crystallise at 52% RH: multiple experimental observations and thermodynamic models report the efflorescence RH (ERH) of NaCl to be 45%.[266,325] Even though still above the bulk solubility limit of NaCl, and hence supersaturated, equilibrated aqueous droplets of NaCl at 52% RH are kinetically stabilised. Tolbert et al. observed efflorescence of aqueous NaCl aerosol droplets at RHs above 45% if they were made to come into contact with external solid crystalline particles of NaCl or other inorganic compounds.[87] They did not report kinetic rates of such heterogeneous nucleation processes but rather concluded that the thermodynamic ERH of NaCl is raised when in the presence of a solid surface.

In the previous section it was shown that the crystal nucleation behaviour of aqueous NaCl appeared unchanged in rapidly evaporating droplets in the presence of colloidal silica. However, when colloidal silica was present in NaCl droplets evaporating at 52% RH, crystal nucleation was observed in some droplets. The distribution at which nucleation occurred in these droplets was spread over lengthy timescales (Fig. 7-9a); one of the droplets was held in the EDB for 3000 s and no crystal nucleation was observed. In all cases, the crystal nucleation occurred after the droplet had equilibrated with the gas phase RH and had reached a stable radius.

All nucleation events in Fig. 7-9a took place after the droplet radius had equilibrated; hence, all droplets were at a constant degree of supersaturation. Thus, it is possible to estimate the heterogeneous crystal nucleation rate at that supersaturation.[201] Assuming that heterogeneous nucleation of NaCl is stochastic, it can be described with Poisson statistics. The probability P_m of forming m number of crystal nuclei in a certain time, t, is:

$$P_m = \frac{N^m}{m!} \exp\left(-N(\mathrm{t})\right) \tag{7-1}$$

where $N(\mathrm{t}) = J\,V\,t$ is the number of crystals nucleating in the set time in a set volume V, with nucleation rate J, at constant supersaturation.[195] Crystal nuclei are only detected after a certain time delay, t_g, which takes into account the time required to get the droplets to the required degree of supersaturation and also any growth time for crystals to become large enough in size to become detectable. The probability of detecting crystals as a function of time becomes:

$$P(\mathrm{t}) = 1 - \exp\left(-J\,V\left(t - t_g\right)\right) \tag{7-2}$$

The time-dependent distribution of nucleation events in Fig. 7-9 is converted into a probability of observing nucleation, *P*(t), (panel *b*). The degree of supersaturation of NaCl in droplets equilibrated at 52 ± 2% RH is 1.75 ± 0.07, according to the molality of a droplet as outlined by the E-AIM model.[175,325] *P*(t) was fit to an exponential Poisson function, $y = 1 - \exp(-A\,(x - B))$, estimating the constant $A = J\,V$ to be 0.020 ± 0.002. The average volume of the droplets once equilibrated in the ~52% RH atmosphere was $3.3 \times 10^{-15} \pm 0.7 \times 10^{-15}$ m^3. Thus, the nucleation rate, *J*, of NaCl at a supersaturation of 1.75 ± 0.07 was estimated from Fig. 7-9 as $6.1 \times 10^{-6} \pm 0.6 \times 10^{-6}$ μm^{-3} s^{-1}. This is within the same order of magnitude as the nucleation rate of NaCl at such a supersaturation as predicted by classical nucleation theory by Robinson et al. (1×10^{-6} μm^{-2} s^{-1}), which is reproduced in Fig. 6-16.[280]

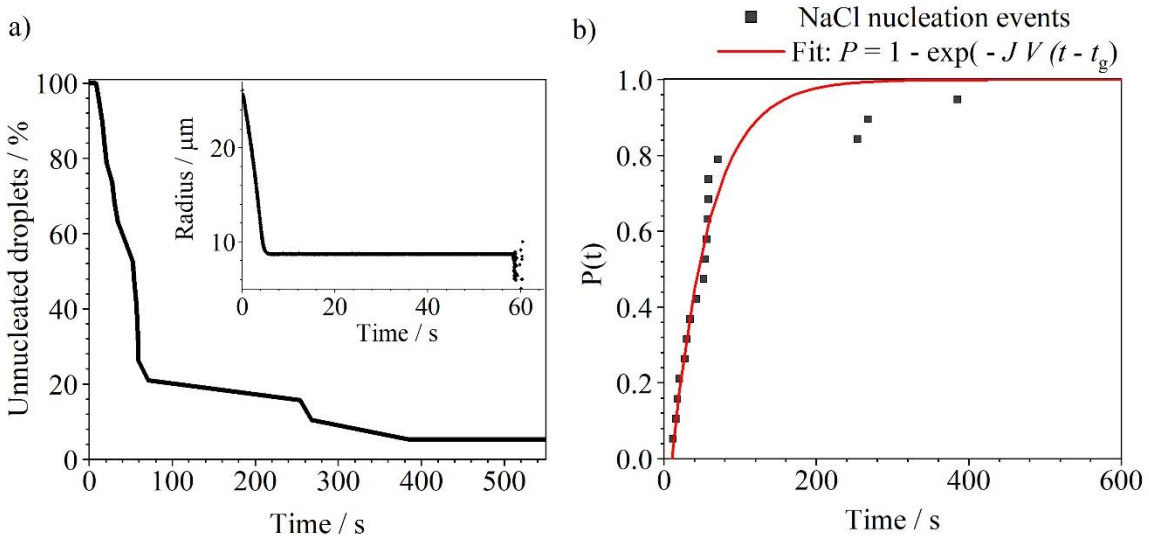

Figure 7-9: a) The time-dependent distribution of nucleation events observed in a population of aqueous droplets of 0.02 MFS NaCl droplets that contain additional 0.001 MFS SiO_2, evaporating in 52 ± 2% RH at 293 K. Inset figure shows the evaporation profile of one example droplet from the dataset, that nucleates crystals at 58.3 s. b) The probability, P(t) of observing a crystal nucleus in the aqueous NaCl droplets

As before, a caveat of this experiment is that the disruption in the light scattering, used to indicate that NaCl nucleation has taken place, could be caused by the aggregation of silica nanoparticles, as high concentrations of NaCl can increase the rate of aggregation of SiO_2. The fit to the nucleation data in Fig. 7-9 could, in fact, provide an estimate to the rate of SiO_2 aggregation at that particular NaCl concentration. However, given that the volume fraction of SiO_2 in the initial aqueous NaCl droplet was 4.6×10^{-4}, even after the droplet has evaporated to a reduced radius the volume fraction of SiO_2 at the point of equilibration remained low, at 0.012. Given that in the equilibrated aqueous NaCl droplet the volume fraction of SiO_2 nanoparticles was still very low, it is unlikely that the disruption in the light scattering was caused by SiO_2 aggregation and so we assume that it was caused by NaCl crystal nucleation.

It is not known whether the heterogeneous nucleation of NaCl crystals induced by the SiO_2 nanoparticles occurs at the droplet surface, or whether it leads to a different morphology of crystalline

NaCl particle than if SiO_2 were not present. Further work on this topic would involve comparing the dried particle morphology of NaCl crystals when evaporated just below the ERH, and with those dried from droplets containing SiO_2 nanoparticles at an RH just above the ERH.

7.4. Evaporation Kinetics and Nucleation Behaviour of Evaporating Droplets Containing Aqueous Alkali Nitrate Mixtures

The feed solutions for spray dryers or liquid formulations in metered dose inhalers will typically contain more complex solutions than single-solute formulations, so it is important to understand the evaporation behaviour of droplets containing more than one solute. If there are two (or more) inorganic components in an evaporating droplet that could crystallise, e.g. solute A and B, an important question is whether they will both crystallise during the drying process; whether A will nucleate crystals before B, and whether the nucleation of component A will induce heterogeneous nucleation in component B, or vice versa. Also, an understanding of the spatial arrangement of the resulting crystals is important, as often it is the surface properties that can dictate the overall particle properties such as solubility, rate of agglomeration and flowability.[268] For two crystallising components it is important to know whether the solutes will form segregated areas of separate crystals or whether the final particle consists of co-crystals of both components in a mixed matrix.

The hygroscopicity of mixed solutes have been studied in detail by various groups, particularly with atmospherically relevant mixed aerosol droplets and to study how the phase behaviour varies with temperature and RH for climate models.[219,326–328] This work tends to be equilibrium studies, with well mixed components. Nucleation kinetics have been discussed with reference to aqueous mixtures of ammonium sulphate and citric acid aerosol,[329] where they discuss a 'half-life' of droplets remaining uncrystallised at various RHs, with a variable ERH for different droplets. Baldelli et al. studied the kinetics of crystallisation of two nitrates: sodium nitrate mixed with potassium nitrate in varying ratios. They discuss the onset of nucleation in terms of the 'crystallisation window' of each species, which starts when that solute passes the equilibrium saturation concentration on the surface.[148] They observed that in a mixed droplet, the first component to pass this saturation concentration, and to hence have the longest crystallisation window, would be the component that is more abundant on the surface of the dried particles.[268]

This section will study the evaporation of mixed nitrates in aqueous aerosol droplets in the EDB. First, the mixture of $LiNO_3$ and $RbNO_3$ will be studied, followed by the mixture of $NaNO_3$ and KNO_3 in evaporating droplets.

7.4.1. The Evaporation and Crystal Nucleation of Mixed $RbNO_3$ and $LiNO_3$ Droplets

$RbNO_3$, as discussed in Chapter 6, has a rapid crystal nucleation rate during evaporation of aqueous droplets, showing high reproducibility in the time that one evaporating droplet in a large population will nucleate crystals. On the other hand, $LiNO_3$ appears to have a low nucleation rate, with most droplets drying in 293 K at 0% RH to form amorphous particles. $LiNO_3$ did not nucleate crystals even when heterogeneous nucleation sites were added into the droplets in the form of colloidal SiO_2 nanoparticles. Evaporation experiments were performed with mixtures of $LiNO_3$ and $RbNO_3$, to study if the presence of $RbNO_3$ could induce nucleation in $LiNO_3$.

The results of evaporation experiments of mixed $LiNO_3$-$RbNO_3$ droplets are shown in Fig. 7-10. The initial mass fraction of total solute was 0.1 MFS, with a varying ratio between $LiNO_3$ and $RbNO_3$ (mass ratio). Panel *a* shows the radius during evaporation of a droplet from each dataset that did not have crystals nucleate, with the exception of the 10% $LiNO_3$-90% $RbNO_3$ case (red line) which had every droplet nucleate crystals and, hence, an example droplet is shown up until the point of crystallisation. The molar ratio between $LiNO_3$ and $RbNO_3$ in the mixtures (going from top to bottom in the Fig. 7-10 legend, respectively) is 95%-5%, 68%:32%, 59%:41%, 35%:65% and 19%:81%.

The radius of the dried particle increased with increasing mass fraction of $LiNO_3$ (Fig. 7-10a). This is in part related to the fact that $LiNO_3$ is more hygroscopic than $RbNO_3$. In addition, the dry-density of pure $LiNO_3$, 2.210 g cm^{-3}, as calculated using the ideal mixing rules outlined in Chapter 3, is lower than for pure $RbNO_3$, 3.202 g cm^{-3}, so a particle with the same dry-mass of solute would be larger in volume if it is richer in $LiNO_3$ than $RbNO_3$.

The crystal nucleation time-distributions for the $LiNO_3$-$RbNO_3$ mixtures are compared in Fig. 7-10b. with panel *c* showing the red and blue datasets in greater detail. At the two extremes in composition, with majority $LiNO_3$ or majority $RbNO_3$, there was either no crystal nucleation or every droplet nucleated crystals, respectively. The dataset of $LiNO_3$-$RbNO_3$ in ratio 20%-80%, had 70% of the droplets showing signs of nucleation occurring, with the other 30% remaining amorphous for the entire experimental window of 20 s. This result suggests that the $LiNO_3$ can inhibit crystal nucleation of $RbNO_3$, which could be a viscosity-driven mechanism of preventing the contact ions of Rb^+ and NO_3^- coming together to form an initial crystal nucleus. The gradient in the loss of unnucleated droplets was very similar between the blue and red line (Fig. 7-10c). However, for the case with 20% $LiNO_3$ (blue line) if the liquid droplets survived past ~ 2 s, i.e. once the water had evaporated, they could not nucleate crystals after that point. This suggests that the droplets reached a limiting viscosity and the mobility of ions was arrested enough to prevent any arrangement into crystal nuclei.

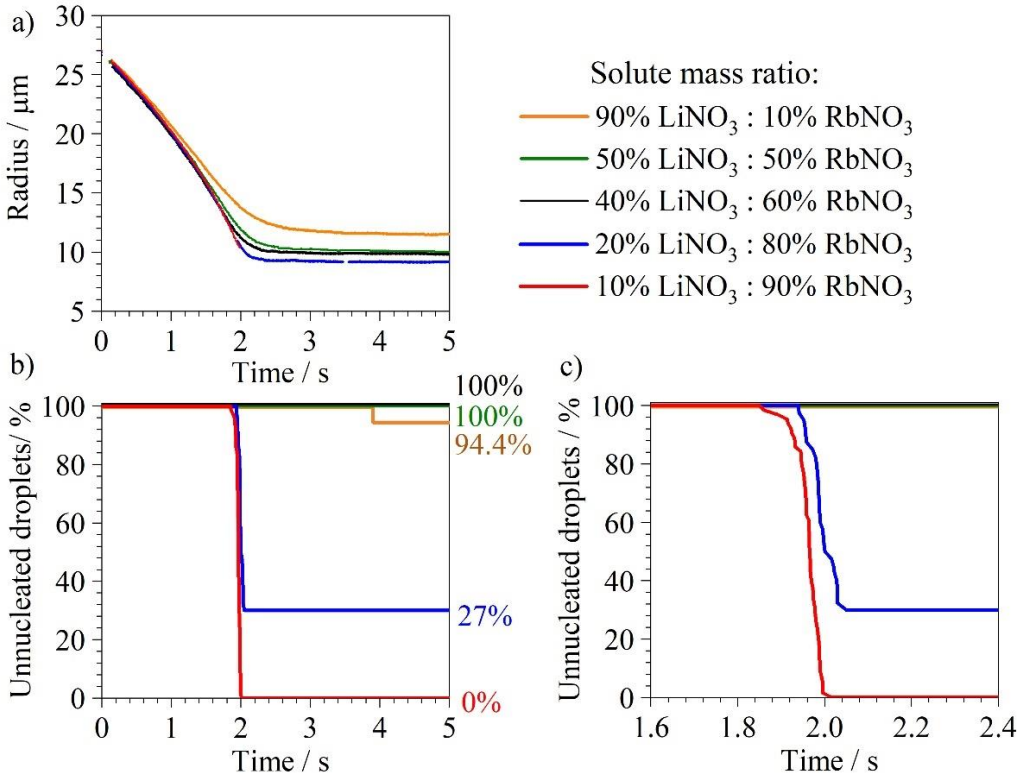

Figure 7-10: a) The evaporation profiles of example droplets from a dataset of aqueous droplets evaporating in 0% RH and 293 K, containing 0.1 mass fraction of solute in a mixture of varying ratios of $LiNO_3$ to $RbNO_3$, as defined in the legend by mass ratio. b) The time-dependent distribution of nucleation events observed in a 10 s experimental time-window for a population (upwards of 20 droplets in each case) for the datasets shown in panel a). c) The data shown in panel b) in greater detail focused on the nucleation times of the red and blue datasets.

The PFs of the evaporating droplets in the $LiNO_3$-$RbNO_3$ mixtures throughout the drying process were studied, with three examples of droplets shown in Fig. 7-11, with the colour of the datapoints indicating the morphology. Panels *a* and *b* are two separate examples from the dataset 20% $LiNO_3$-80% $RbNO_3$. Both droplets began the evaporation process as homogeneous mixtures but the droplet in Fig. 7-11a nucleated crystals after t = 2 s, whereas in panel *b*, the droplet remained in a homogeneous liquid-state (amorphous), even though all water had evaporated. In panel *a*, the morphology after crystal nucleation remained as an "inclusions" droplet, and it was possible to continue to resolve a radius from the phase-function, suggesting that the dried particle remained spherical. This implies that the droplet did nucleate small crystals but did not undergo complete crystallisation. A theory for this is that the droplet nucleated $RbNO_3$ crystals after 2 s into the drying process but did not nucleate $LiNO_3$ crystals. The particle remained with areas of Li^+ ions and a corresponding concentration of NO_3^- ions dissociated in an amorphous structure. This fits with the conclusions from the evaporation of mixed $LiNO_3$-SiO_2 droplets, that there was not $LiNO_3$ crystal nucleation even when all water had evaporated and a solid surface was present inside the droplet. The $RbNO_3$ crystal nuclei in Fig. 7-11a were still not able to act as a surface that could induce heterogeneous nucleation in $LiNO_3$. By contrast, Fig. 7-11c shows an example of a droplet from the 10% $LiNO_3$-90% $RbNO_3$ dataset, for which every droplet in the series nucleated

crystals at ~ t = 2 s. The PF suggests that the dried particle in panel *c* was more like a completely crystalline particle, as the radius could not be resolved from the peaks in the irregular light scattering. This suggests that the large proportion of $RbNO_3$ in the particle was able to induce heterogeneous nucleation in the remaining 10% $LiNO_3$, which may explain the transition from inclusion-like to crystalline-like phase-function at around t = 4 s. Alternatively, the particle may still not have undergone $LiNO_3$ crystal nucleation, even after 4 s, but as there was only 10% $LiNO_3$ present in that formulation there was not enough volume of remaining dissociated Li^+ and NO_3^- ions to make the phase function show an inclusions morphology.

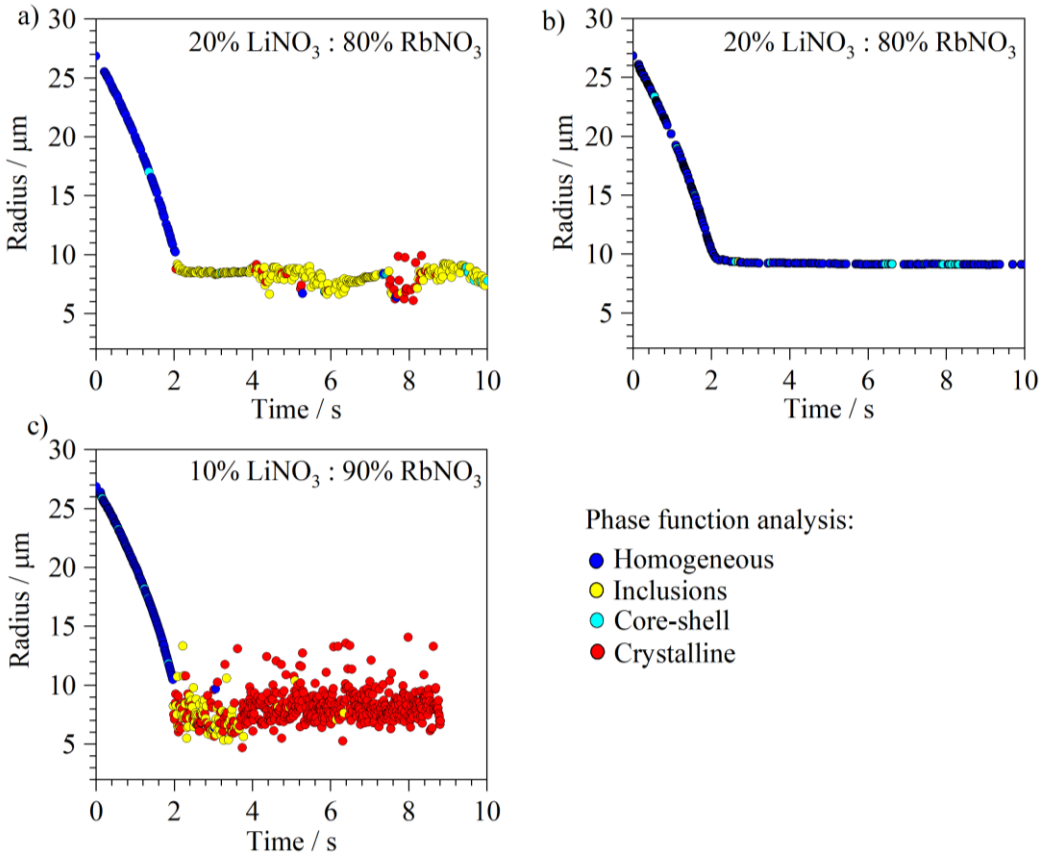

Figure 7-11: a) and b) The evaporation profiles of two example droplets from the dataset in Fig. 7-11 (blue) containing an aqueous solution with 0.1 mass fraction of solute, initially. The solute is a $LiNO_3$-$RbNO_3$ mixture (20%-80% by mass) evaporating at 0% RH and 293 K. The colour of the datapoints indicating the particle morphology as inferred from the PF. a) is a droplet that nucleated crystals at t ~ 2 s and b) did not nucleate crystals within the experiment. c) The evaporation profile of a droplet from the dataset in Fig. 7-11 (red) with the mass ratio of $LiNO_3$-$RbNO_3$ being 10%-90%.

In conclusion, the presence of $LiNO_3$ in quantities greater than 40% in a mixed $LiNO_3$-$RbNO_3$ solution prevented crystal nucleation for the Rb^+ and NO_3^- ions. They were able to form crystal nuclei in higher concentrations of $RbNO_3$ but this did not readily induce heterogeneous nucleation in the remaining $LiNO_3$. We will now study the crystal nucleation behaviour of mixtures of KNO_3 and $NaNO_3$.

7.4.2. The Evaporation and Crystal Nucleation of Mixed $NaNO_3$ and KNO_3 Droplets

7.4.2.1. The Evaporation of $NaNO_3$-KNO_3 mixtures that are rich in $NaNO_3$

In Chapter 6 the crystal nucleation of KNO_3 was shown to be more reproducible than for $NaNO_3$, in that all KNO_3 droplets in a series nucleated crystals during evaporation, within a narrow time distribution. To study the nucleation propensity of mixtures of $NaNO_3$ and KNO_3, aqueous solutions were made with a total with a total MFS of 0.2, with combinations of nitrates from 10% KNO_3-90% $NaNO_3$ down to 2.5% KNO_3-97.5% $NaNO_3$.

The time distrubution of crystal nucleation events in the droplets as they evaporated at 25% RH at 293 K are compared in Fig. 7-12a. In this dataset, when the alkali nitrate content in the droplet was only $NaNO_3$, a large proportion of the droplets (48%) did not nucleate crystals in the timescale of the experiment (20 s); this proportion reduced to 9% for when the solute content was 97.5% $NaNO_3$ and 2.5% KNO_3. When the nitrate content was 95% $NaNO_3$ and 5% KNO_3 only 1.7% of droplets did not nucleate crystals within 20 s. Once the KNO_3 content surpassed 10% of the solute mass, all of the droplets nucleated in a reproducible and narrow distribution, similar to if the droplets were only aqueous KNO_3. This data shows that droplets have a greater propensity to nucleate crystals with KNO_3 is included as a co-solute with $NaNO_3$.

The experimental radii throughout evaporation for an example of each dataset are compared in Fig. 7-12b. As the initial radii for the droplets in each dataset varied over a range of ± 0.5 μm, the data is normalised with respect to the starting radius to better compare the evaporation rates (Fig. 7-12c). The dashed and dotted lines show the radii at the point that each droplet passed bulk solubility limit for $NaNO_3$ and KNO_3, respectively, i.e. the beginning of that component's crystallisation window. The saturation radius, r_s of species *i* is calculated by:

$$r_{s,i} = \left[\frac{3}{4\,\pi}\left(\frac{m_i}{sol._i}\right)\right]^{\frac{1}{3}} \tag{7-3}$$

where m_i is the mass of species *i* in the droplet, which can be calculated using the known initial concentration of each species and the starting radius of the droplet. $sol._i$ is the bulk solubility concentration of species *i* in terms of a molarity, e.g. g L^{-1}.

KNO_3 has a lower solubility limit than $NaNO_3$, 279 g L^{-1} compared to 642 g L^{-1} at 293 K, respectively. However, the lower concentration of KNO_3 in these droplets means that the saturation radius of KNO_3 in all cases was below that of $NaNO_3$ and hence $NaNO_3$ entered the crystallisation window first. The solubility radii of the two components became more similar as the ratio between $NaNO_3$ and KNO_3 in

the formulation was made closer. An interesting feature of Fig. 7-12c is that the saturation radius of KNO_3 in all cases was far below the radius of the droplet, even when the droplet equilibrated with the gas-phase RH and reached a steady radius. When crystal nucleation occurred in a droplet, only $NaNO_3$ was above its saturation concentration, suggesting that the first crystal nuclei to form were $NaNO_3$ rather than KNO_3. It is curious to see that KNO_3 could increase the propensity of $NaNO_3$ to nucleate crystals even when it was in such a low concentration.

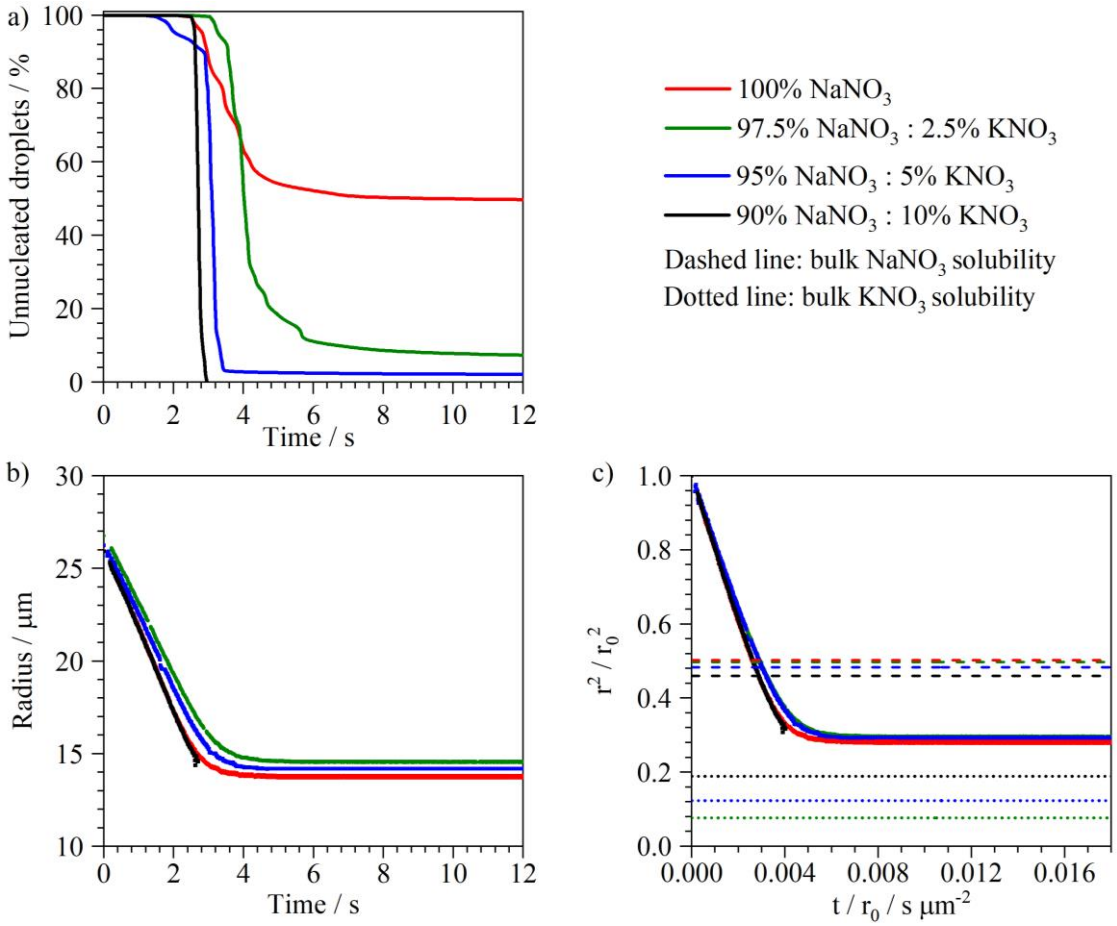

Figure 7-12: a) The time-dependent distribution of nucleation events during evaporation of droplets containing mixtures of $NaNO_3$ and KNO_3 in varying ratios (listed in the legend, by mass ratio). Initial mass fraction of solute is 0.2. The droplets evaporate at 293 K and 25% RH. b) The evaporation profiles of example droplets from the datasets in panel a). c) The data in panel a) normalised with respect to the initial droplet radius to compare the evaporation rates and the radii at which each droplet would pass the bulk solubility limit for $NaNO_3$ (dashed line) and for KNO_3 (dotted line).

To investigate the morphology of the evaporating mixed nitrate droplets, the PFs of a droplet that nucleated crystals in each of the datasets were studied (Fig. 7-13). Panels *a*, *b* and *c* show a droplet from the datasets 97.5% $NaNO_3$-2.5% KNO_3, 95% $NaNO_3$-5% KNO_3 and 90% $NaNO_3$-10% KNO_3. The colour of the datapoints indicate the morphology according to the PF. In all cases, a crystal nucleated long before the droplet was saturated in KNO_3. When the initial nucleation step occurred, the droplet appeared to have an inclusions morphology, followed by an increase in gradient (faster evaporation)

that led to the droplet radius passing the KNO_3 solubility limit and complete crystallisation occurred in the droplet. The gradient of the evaporation rate after the moment of crystal nucleation appears to have increased with increasing content of $NaNO_3$ in the formulation. This could be attributed to the fact that more $NaNO_3$ crystallising led to a greater degree of enthalpy of crystallisation, leading to greater heating of the droplet.

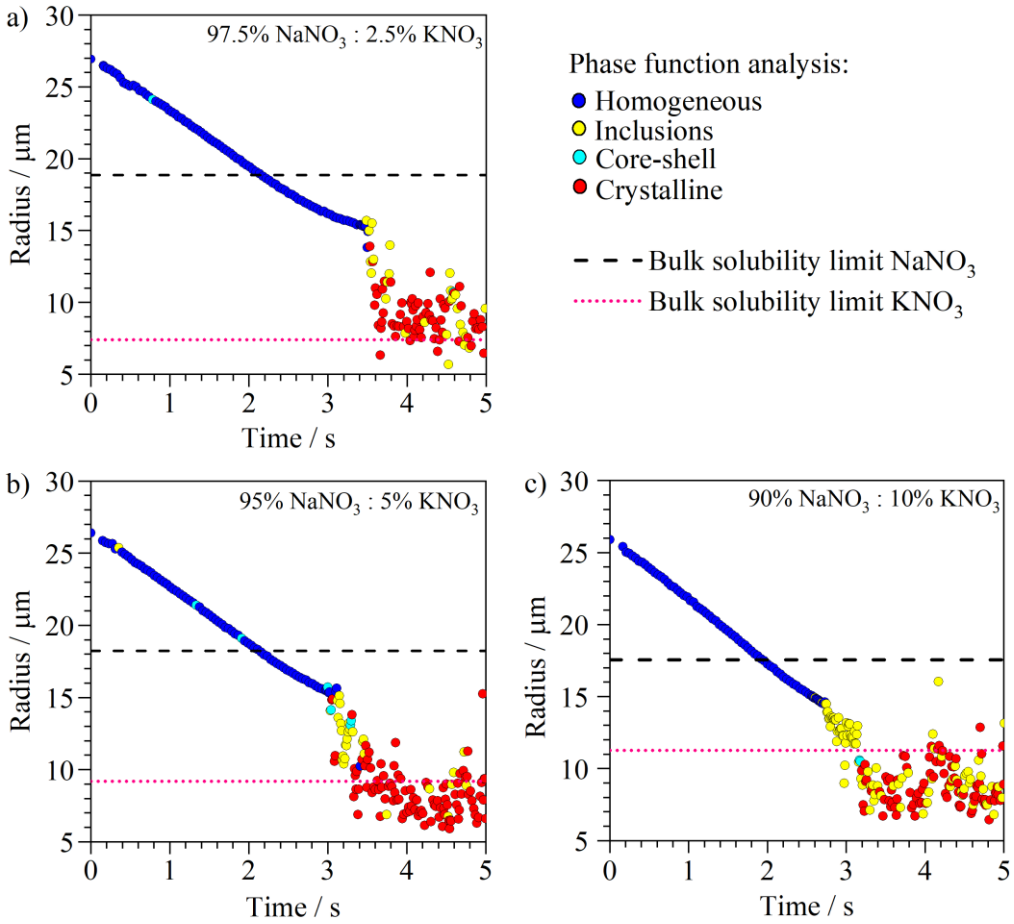

Figure 7-13: a) b) and c) The evaporation profiles of an example droplet from each of the green, blue and black datasets in Fig. 7-12, respectively. Droplets contain aqueous 0.1 MFS mixtures of $NaNO_3$ and KNO_3 in varying ratios (mass ratio) as indicated. Droplets evaporate at 293 K and 25% RH. The colour of the datapoints indicates the particle morphology as inferred from the PF. The dashed and dotted lines indicate the radius at which the droplet passes the bulk solubility limit of $NaNO_3$ and KNO_3, respectively.

7.4.2.2. The Evaporation of $NaNO_3$-KNO_3 mixtures that are rich in KNO_3

In the experiments presented so far of the evaporation of aqueous mixtures of $NaNO_3$-KNO_3 solutions, all mixtures were rich in $NaNO_3$, and had a longer crystallisation window for $NaNO_3$ than for KNO_3, i.e. they became saturated in $NaNO_3$ first. An additional experiment was performed to investigate the nucleation behaviour in a droplet for which KNO_3 became saturated earlier than $NaNO_3$, so a droplet with a longer crystallisation window for KNO_3.

The results of the evaporation experiments of aqueous droplets containing an initial solute mass fraction of 0.2, of a $NaNO_3$-KNO_3 mixture (25%-75% by mass, respectively), are shown in Fig. 7-14. The nucleation behaviour could not be plotted as before with a percentage of remaining uncrystallised droplets, because the droplets displayed different efflorescence behaviour to the other $NaNO_3$-KNO_3 mixtures. In all droplets, crystal nucleation was initially observed at ~ 2 s into evaporation. For some of the droplets, the EDB software was unable to resolve the particle radius immediately after that point, implying complete crystallisation had occurred. However, in other droplets, after crystal nucleation at t = 2 s the fringes in the elastic scattering remained regular and the radius continued to decrease in a period of inclusions for up to 1 s in time before complete crystallisation was observed. The period of time between the initial nucleation event and the complete crystallisation (Δt) for the 53 droplets in this dataset is shown in Fig. 7-14a. 21% of these droplets underwent complete crystallisation as soon as nucleation was observed, i.e. Δt = 0. For the other 79% there was a period of time between t_1, wherein an initial nucleation event was observed, and t_2, which was complete crystallisation.

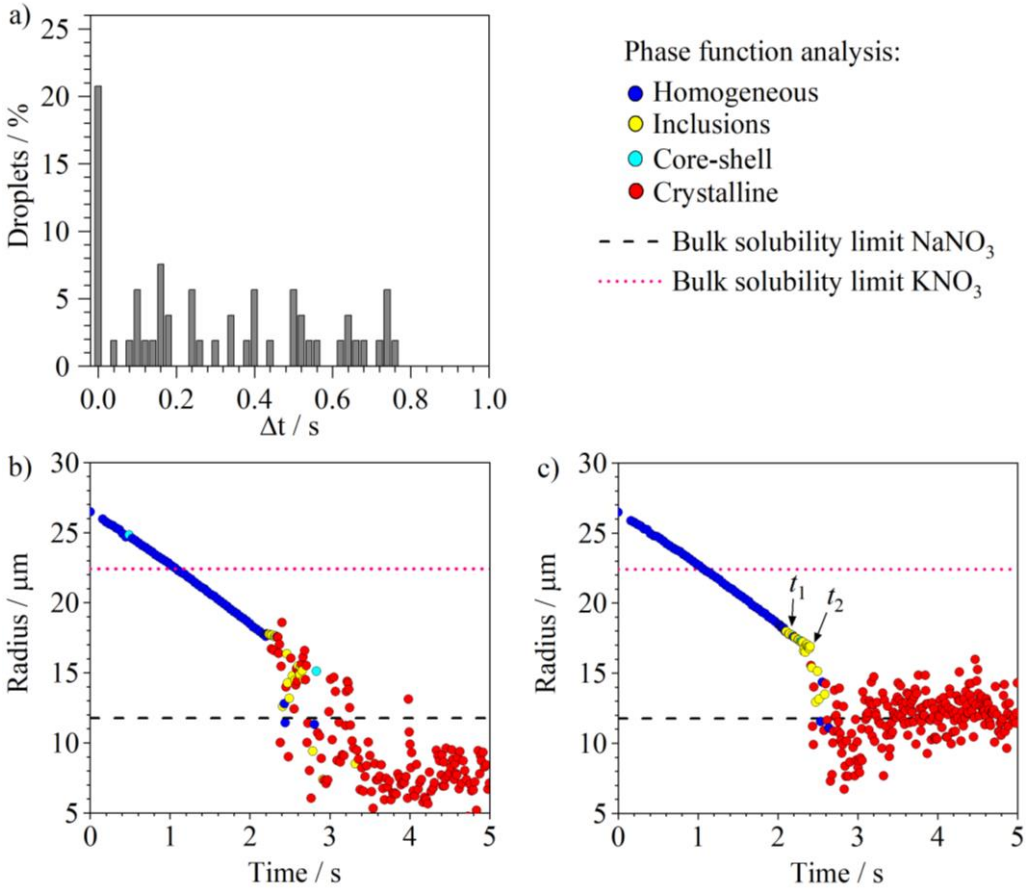

Figure 7-14: In a dataset of evaporating aqueous droplets of 0.2 MFS, ratio of $NaNO_3$-KNO_3 is 75%-25%, at 25% RH and 293 K, a) shows the difference in time between the first nucleation event that is observed in an evaporating droplet, t_1, and the time that the PF does not have defined fringes enough to resolve a radius, t_2. In some droplets, the PF becomes totally erratic as soon as nucleation is observed, so Δt = 0. b) and c) show examples of the evaporation profiles of droplet with a short Δt and one that has Δt = ~ 0.5 s, respectively.

To understand the different mechanisms of nucleation in the KNO_3-rich mixture, the PFs of two examples of droplets from this dataset are compared in Fig. 7-14. One droplet had very short Δt (panel *b*) and one had a long Δt (panel *c*). The PF identied the droplet morphology according to the colour of the datapoints. The time period between t_1 and t_2 showed an inclusions morphology (Fig. 7-14c). Given that the KNO_3 was the only species that was saturated at the point of t_1, it presumably was a KNO_3 crystal nucleus forming at that point. At t_2 the droplet radius was still above the saturation radius of $NaNO_3$, so the nucleation event at t_2 could have been $NaNO_3$ undergoing heterogeneous nucleation. Alternatively, not all of the KNO_3 may have crystallised at t_1, and the event at t_2 was crystallisation of the rest of the KNO_3. Either way, there were two distinct crystal nucleation behaviours in these KNO_3-rich droplets. Dried particles from this drying experiment were collected and imaged using SEM, which is discussed in the next section.

7.4.2.3. SEM Images of Dried Particles Containing Mixtures of $NaNO_3$ and KNO_3

To better understand the nucleation behaviour in mixed $NaNO_3$-KNO_3 droplets, we study the dried particle morphologies. Droplets were evaporated in the falling droplet column, and the dried particles collected for SEM imaging (Fig. 7-15).

First, to establish the morphology of a dried particle of a pure component, panel *a* in Fig. 7-15 shows we study the dried particles collected from evaporating 0.2 MFS of pure $NaNO_3$ (Fig. 7-15*a*) and 0.2 MFS or pure KNO_3 (panels *b* and *c*). As discussed in Chapter 6, the SEM images of dried $NaNO_3$ show the particles to be almost spherical in shape, with a rough surface that is cracked and buckled. The KNO_3 dried particles in the SEM images show more variable particle shapes, but all have smooth surfaces and look to be fully crystalline, with some corners and straight edges, similar to those observed for NaCl (Chapter 5).

The collection and SEM imaging of particles produced from drying the 0.2 MFS mixed droplets (25% $NaNO_3$-75% KNO_3) was performed twice, to allow for a repeat of the measurements. The results from the first round is shown in Fig. 7-15 panels *d-f* and the repeat measurement is shown in panels *g-i*. In both sets of images, there are clearly two different types of particles. There are spherical particles with slightly roughened surfaces, such as that shown in panel *g* or in the left hand side of panel *d*. There are also particles with a generally larger particle size, that have high variable shapes and appear to have clusters forming in regions on the surface. Examples of this second type of particle are shown in panels

h, i and the left hand side of panel f. The ratio between these two types of particles obseved in the SEM image is close to 50:50, as shown in panel e of Fig. 7-15.

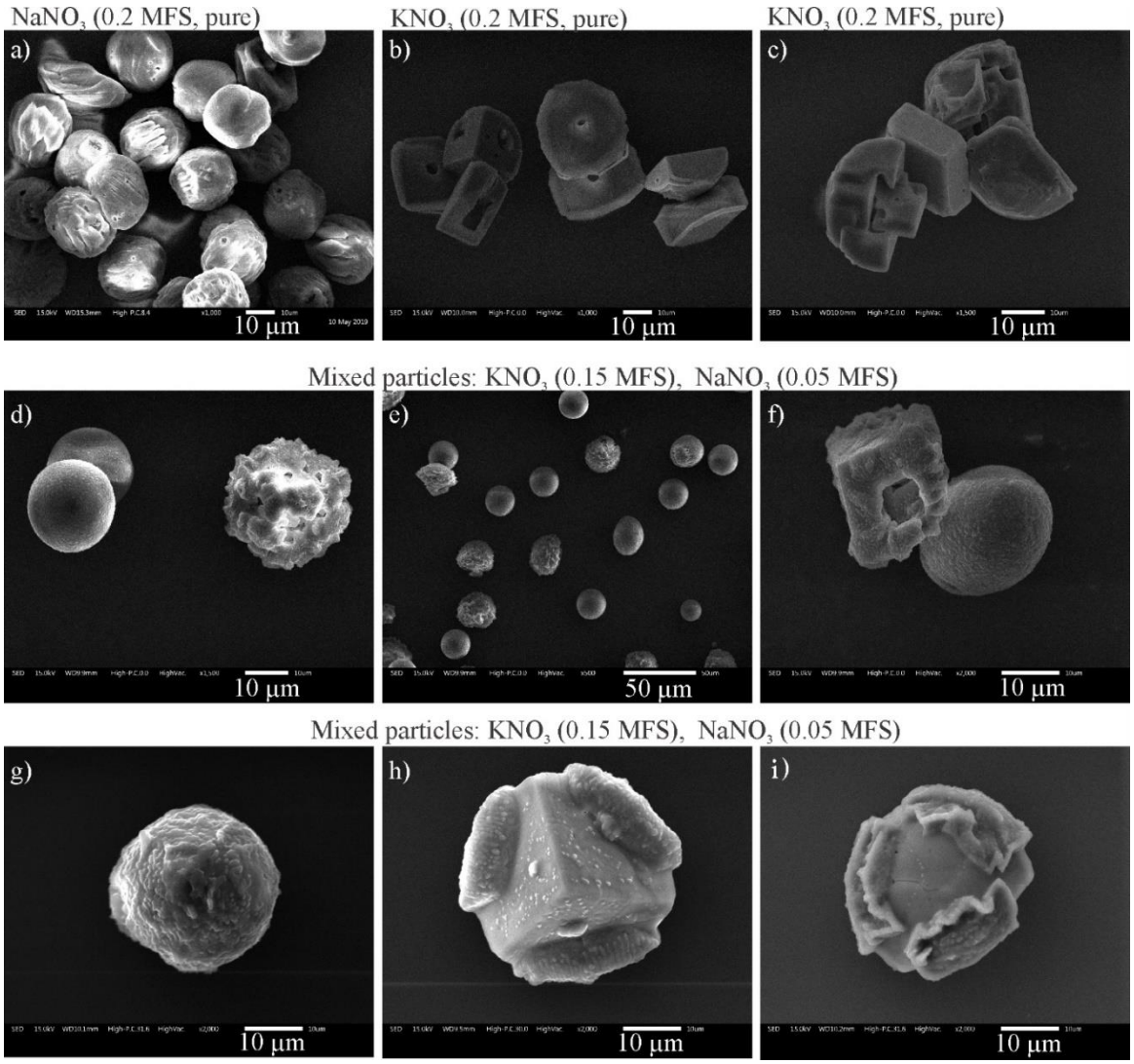

Figure 7-15: SEM images of dried nitrate particles, collected from evaporating aqueous droplets in the falling droplet column at 0% RH and 293 K, containing solutions of a) 0.2 MFS $NaNO_3$, b) and c) 0.2 MFS KNO_3, d-i) 0.2 mass fraction of solute of 25% $NaNO_3$-75% KNO_3 (i.e. 0.05 MFS $NaNO_3$ and 0.15 MFS KNO_3).

It is possible that these two "types" of particles in the SEM images correspond to the two types of nucleation behaviour observed in the EDB evaporation data (Fig. 7-14). The droplets that look spherical in the SEM images could represent those that had a large Δt; after the initial observation of KNO_3 crystal nucleation, the droplet remained spherical and still showed defined fringes in its PF, allowing the radius of the spherical particle to be retrieved for a longer time. The droplets that showed irregularlity in the PF as soon as the first nucleation event was observed are those that show the non-spherical shapes in the SEM images.

For more information about the different types of particles in the SEM images, Energy Dispersive X-Ray Spectroscopy (EDS) was performed on the mixed nitrate images in Fig. 7-15 panels *g-i*. EDS is an

analytical method of spacially characterising the components in a dried sample. The principle behind the technique is that every chemical element has a unique set of electronic structure of the atom. When X-Rays are focused onto a sample, the incident beam may excite an electron in the atom, ejecting the electron away and leaving an electron hole. The atom will then relax, a process that can be described in simplistic terms as an electron in an outer, higher energy shell dropping down to fill the electron hole. The difference in energy between the two electronic states will be released in the form of an X-Ray, which can then be detected by the spectrometer.[330] The most common type of X-Ray to be detected is the K-alpha, which arises from an electron filling an electron hole in the K-electron shell. The energy of X-Rays detected from a sample can be compared against a library of X-Rays emitted from different elements, to thus deduce the elemental composition in a region of interest. EDS is typically only sensitive to the upper region of a sample, over a depth of a few tens of nanometres.[331]

The mixed nitrate dried particles (Fig. 7-15 panels *g-i*) underwent EDS analysis, screening for the elements K and Na. It should be noted that the K-alpha X-Ray of potassium is three times higher in energy than that for sodium,[332] and hence the technique is more sensitive to potassium than sodium. The EDS maps are shown in Fig. 7-16. The bumpy regions clustered on the outer surface of the particle in panels *d-i* show elemental analysis consistent with sodium content; hence, these regions can be deduced as primarily $NaNO_3$ material. The structure of the central region of the particle is mainly KNO_3 material. As the EDS technique is more sensitive to potassium than for sodium, thin regions of $NaNO_3$ may appear slightly transparent to KNO_3 material underneath. However, from the figure, it can be assumed that KNO_3 and $NaNO_3$ crystallise in segreated regions of a mixed particle. The spherical particle, shown with EDS analysis in Fig. 7-16 panels *a-c*, shows the fingerprint of potassium and sodium across the whole particle. Given that in the corresponding SEM image (Fig. 7-15g) the surface of the sphere is rough and lumpy similar to the surface of the pure $NaNO_3$ particles, it could be assumed that in this droplet the $NaNO_3$ precipitate is covering the whole surface in a thin layer, rather than in segrated regions. The core of the particle is KNO_3, but the potassium K-alpha X-Ray is of high enough energy to transmit through the thin $NaNO_3$ surface layer.

To conclude this section, the SEM images and EDS analysis of the dried particles formed from evaporating 25%-75% $NaNO_3$-KNO_3 aqueous solution droplets show that the two solutes precipitate in segregated areas, rather than crystallise together in a mixed matrix. KNO_3 is the first solute to pass its bulk solubility limit and appears to form a central crystal, with $NaNO_3$ precipitating on the surface. In some droplets the KNO_3 crystallises in a smaller, and presumably denser particle, allowing the $NaNO_3$ to completely cover the central particle and the dried particle looks like a sphere. In such spherical particles, the EDS analysis shows a thin layer of $NaNO_3$ on the surface (Fig. 7-16 panels *a-c*). In other droplets, presumably in those that the KNO_3 nucleates crystals early in the evaporation process, the SEM images show a larger, less dense central particle consisting of KNO_3, with regions of $NaNO_3$ precipitated on the surface.

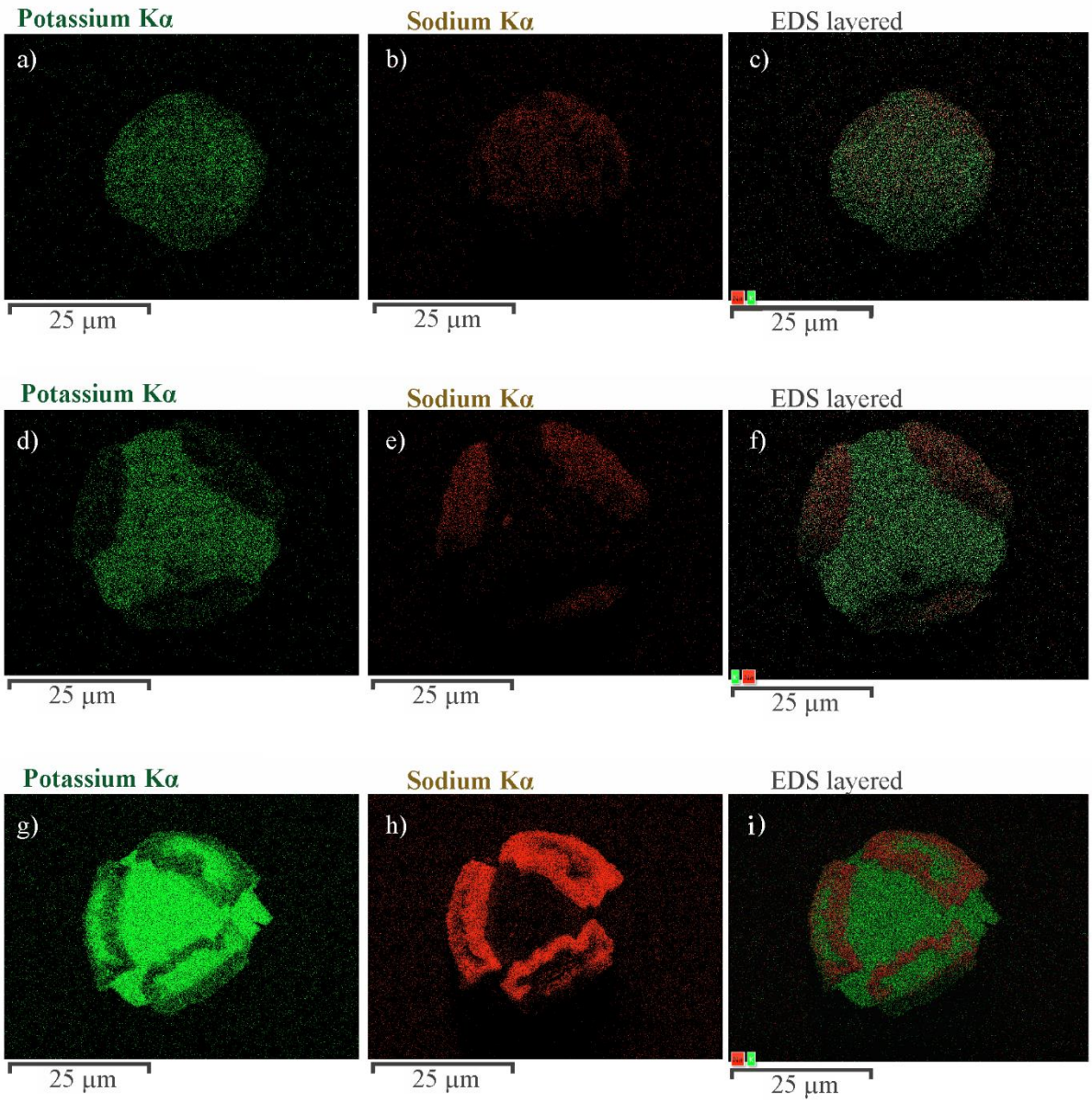

Figure 7-16: EDS analysis on the dried particles in Fig. 7-15 panels g-i, to spatially identify regions of potassium material (green colour) and sodium material (red colour). Both colours are overlaid in the EDS layered images in panels c), f) and i). All three rows of images correspond to the same evaporation conditions of 293 K, 0% RH, 0.2 mass fraction of solute in mass ratio 25% $NaNO_3$-75% KNO_3 (i.e. 0.05 MFS $NaNO_3$ and 0.15 MFS KNO_3).

These results can be directly compared to the evaporation study on mixed $NaNO_3$ and KNO_3 droplets performed by Baldelli et al.,[268] (reproduced in Fig. 7-17). The authors collected particles that had been dried in a monodisperse droplet chain, with an initial solute concentration of 0.01 MFS, and the mass ratio of $NaNO_3$-KNO_3 varying from 26.5%-73.5%, 45.7-54.3% and 70-30 (panels *a*, *b* and *c*, respectively). It should be noted that in Fig. 7-17 the colour scheme is the same as that in the work presented in this manuscript; regions of sodium are depicted with red colour and potassium with green colour. Baldelli's particle in panel *a* is the same $NaNO_3$-KNO_3 ratio as in the data presented in this section of the thesis (Fig. 7-16). The authors reported that KNO_3 was the first solute to enter its

cystallisation window, which is consistent with the work in this thesis, but Baldelli observed the dried particles to contain only potassium on the surface of the droplet, the opposite of what is seen in this work. This discrepancy could be a result of the different initial solute concentration; Baldelli worked with 0.01 MFS droplets where the work in this thesis used 0.2 MFS. It is possible that the higher solute concentration in this work led to a higher viscosity during drying, making the $NaNO_3$ not able to diffuse into the centre of the droplet and causing it to precipitate on top of the crystallising KNO_3.

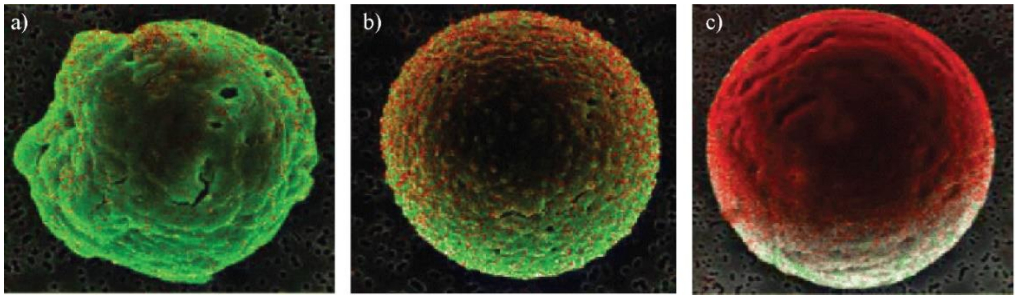

Figure 7-17: EDS analysis of SEM images of dried $NaNO_3$: KNO_3 particles, with initial solute concentration 0.1 MFS, in solute ratio $NaNO_3$: KNO_3 of a) 26.5 : 73.5, b) 45.7 : 54.3, c) 70 : 30. Regions identified as containing sodium are depicted in red colour, regions of potassium are depicted in green colour. From Baldelli et al.[268] Reprinted (adapted) with permission from Aerosol Science and Technology, 50 (10), 1130-1142. Copyright 2016, Taylor & Francis Group.

7.5. Chapter 7: Summary and Future Work

This chapter has built upon previous chapters in this thesis by discussing the evaporation and crystal nucleation kinetics of mixed aqueous solution droplets, rather than simple single-solute systems. Methods were investigated to delay, prevent or induce crystal nucleation in a drying droplet with additives.

When an organic fatty-alcohol is included in the formulation for an evaporating salt solution droplet, the fatty-alcohol diffuses to the surface of the droplet; the time for such a process is shown to depend upon the concentration of fatty-alcohol in the droplet. This adsorption process reduces the evaporation coefficient of the drying droplet, leading to delays in the time that the solute becomes supersaturated, and hence delaying the onset of crystal nucleation. Going forward, this technique of decreasing the evaporation rate could be studied in systems that typically have slow nucleation rates, that ordinarily would be challenging to crystallise in a spray dryer, such as lactose or sucrose.[289] It is possible that, by increasing the length of crystallisation window, a spray-dried product could be tuned to increasing degrees of crystallinity. For the opposite effect, droplets of aqueous $NaNO_3$ solutions were shown to dry with more amorphous content than crystalline, by adding increasing amounts of glycerol to the formulation. It is thought that this effect is brought about by a higher viscosity of solution, as well as

the observation from Yu et al. that in mixtures of glycerol and $NaNO_3$ there are conformational changes in both sets of molecules that may impede the arrangement of ions into crystal nuclei.

Work by Tolbert et al. showed that the external contact between solid crystalline species and supersaturated aerosol droplets could induce heterogeneous nucleation. In this study, we have investigated the drying and nucleation kinetics of when this contact occurs *within* the droplet, i.e. if the colloidal inclusions can induce heterogeneous nucleation in an inorganic component. The presence of colloidal silica nanoparticles in evaporating NaCl droplets appeared to induce heterogeneous nucleation at an RH above the efflorescence RH (ERH), and the time-dependent distribution over when nucleation was observed in different droplets enabled an estimation of the heterogeneous nucleation rate. Repeating this nucleation rate calculation at varying RHs and for a range of different mixtures could be very valuable for spray drying; it would be useful to predict what additives would induce nucleation in evaporating droplets, and how soon into the drying process that occurs.

In terms of mixtures of aqueous nitrate solutions, for $LiNO_3$ and $RbNO_3$, the presence of $LiNO_3$ reduced the propensity for crystal nucleation in $RbNO_3$. Any nucleation of $RbNO_3$ crystals did not appear to induce heterogeneous nucleation of $LiNO_3$. Mixtures of KNO_3 and $NaNO_3$ showed that one crystallising component did appear to induce heterogeneous nucleation in the other component, and even tiny mass fractions of KNO_3 in a $NaNO_3$-rich aqueous droplet made the nucleation of $NaNO_3$ more reproducible and predictable.

Whilst this work shows some interesting early trends of inorganic solutes affecting the nucleation behaviour of other components within a drying droplet, this study has limitations. This work was performed using only the PF of the elastic light scattering in the EDB to suggest whether partial nucleation (inclusions) or complete crystallisation had occurred. It can be difficult to distinguish between the PFs of these two morphologies in small volumes. These experiments could be repeated using X-Ray diffraction to analyse the resulting particles, then a ratio of crystalline to amorphous content in a sample could be retrieved, which would improve the mechanistic understanding of the particle formation process.

Chapter 8

Significant Conclusions and Future Work

The aims of this thesis were to study the drying kinetics of rapidly evaporating liquid aerosol solution droplets, the propensity of the inorganic solute to nucleate crystals during evaporation of the solvent, and how these two processes govern the final particle morphology. These aims were achieved in the results chapters 4-7, and the significant conclusions from each chapter are summarised as follows.

A detailed study of the evaporation rates of droplets containing ethanol and ethanol-water mixtures was presented in Chapter 4. The evaporation kinetics of such droplets under different conditions in the EDB were compared to a range of numerical models, such as a binary Kulmala model [182] and a numerical Maxwell model.[43] The results demonstrated the large degree of coupling between mass and heat flux during the evaporation of mixed ethanol-water droplets. The rapid evaporation of ethanol leads to significant evaporative cooling of the droplet. In humid environments, rapid ethanol evaporation was shown to lead to a supersaturation of water vapour in the gas phase with respect to the cooled droplet surface, driving water condensation onto the droplet. A striking implication of these kinetic processes is that the evaporation of a pure ethanol droplet in a humid environment was shown to lead to a droplet composition of entirely water within only 400 ms. This phenomenon is important in the field of respiratory drug delivery, where droplets generated by metered dose inhalers typically contain ethanol and highly volatile propellants. Hence, upon inhalation, such droplets would undergo significant evaporative cooling due to the rapid solvent evaporation, leading to water condensation in the highly humid lung atmosphere. This condensation step could strongly affect the pharmacokinetics of the inhaled drug, and the work presented in Chapter 4 represents a significant step-forward in the understanding of such kinetic processes.

In Chapters 5, 6 and 7, experimental measurements from the evaporation of droplets containing inorganic solutions were presented. The complexity of the solutions being probed was progressively increased. First, in Chapter 5, single droplet experiments using the EDB were performed using simple aqueous NaCl solutions. Many droplets in a series of multiple drying experiments were compared, demonstrating the high reproducibility of the evaporation rates and times that NaCl solution droplets nucleated crystals. A Fickian diffusive transport model was used to infer the development in solute concentration gradients during drying. By replicating the evaporation conditions in the EDB with that in a falling droplet column (FDC) instrument, dried particles from evaporating streams of falling droplets were collected. Thus, images of the dried particles were collected using a Scanning Electron Microscope (SEM). The morphology of the dried particles was shown to become more hollow and more

spherical, with more crystals, when the magnitude of rise in surface concentration (as predicted using the model) was greatest. This work demonstrates the importance in understanding the drying kinetics of droplets in an industrial spray dryer for producing a powdered product with desirable properties.

The experimental techniques involved in observing crystal nucleation during the evaporation of liquid solution droplets was developed in Chapter 6 with aqueous $NaNO_3$ solutions. Aqueous $NaNO_3$ droplets evaporating in a long series were shown to display a broad distribution of nucleation times, demonstrating the stochastic nature of homogeneous nucleation. Solutions of $NaNO_3$ were shown to rise by up to four orders of magnitude in viscosity during drying, which leads to a competition between the crystal nucleation rate and the time available for crystallisation (the drying time). We combined experimental measurements with the diffusive transport model to monitor the radial concentration profiles, which led to a quantitative prediction of the homogeneous nucleation rate of $NaNO_3$ crystals out of solution. This is a step forward in building an understanding of crystal nucleation in the presence of a viscosity-barrier, which is a key problem in the spray drying industry.

Finally, in Chapter 7, the complexity of the inorganic solution droplets was increased to include mixtures. Methods were investigated to delay, prevent or induce crystal nucleation of an inorganic solute in a drying droplet with additives. The addition of colloidal silica nanoparticles appeared to induce crystal nucleation in aqueous $NaNO_3$ droplets, but made no difference to the nucleation propensity of aqueous $LiNO_3$ droplets, which have a very low nucleation rate. The addition of very small amounts of a fatty alcohol to an aqueous inorganic solution droplet delayed the onset of crystal nucleation by decreasing the evaporation coefficient, and hence, the evaporation rate. Thus, the crystallisation window was lengthened. In addition, experimental results of the evaporation of droplets containing mixed alkali nitrate solutions (XNO_3, where X = Li, Na, K or Rb) were presented. A significant conclusion is that small volumes of KNO_3 appeared to influence the crystallisation propensity of $NaNO_3$, and vice versa. However, upon studying the dried particles with electron dispersive X-Ray spectroscopy (EDS) the dried particles showed segregation of the two species, with separate regions of dried KNO_3 and $NaNO_3$.

8.1. Future Work

This work has demonstrated that the electrodynamic balance is a useful instrument for measuring the evaporation rates of rapidly evaporating aerosol droplets. However, the measurement of droplet radius in the EDB as implemented in this work relied on defined fringes in the elastic light scattered from the laser beam by the droplet. Thus, kinetic evaporation measurements were limited to the period within which a levitated droplet was relatively optically homogeneous. Much of this thesis has focused on the onset of crystal nucleation in aerosol solution droplets. Whilst identifying the nucleation time is highly

important for industrial applications such as spray drying, there may be continued drying after a crust has formed at the droplet and this drying period can influence the final particle properties such as density or stickiness. Continued evaporation following crust-formation is a process that cannot currently be studied using optical techniques because the elastically scattered fringes become highly erratic. An important future study would combine the optical measurements for radius retrieval in the EDB with a separate measurement to record the mass of a levitated droplet.

The EDB instrumentation and methodology would require minor adjustments to perform mass measurements during droplet evaporation. An alternative CCD to that used for sizing is already focused on the trapping region, and the image of the droplet appears as a bright spot (Fig. 3-1). This second CCD was used in these experiments only for ease of aligning the droplet dispenser, as the position of a dispensed droplet could be clearly tracked as it entered the trapping region. However, this CCD could be used to track the position of a levitated droplet throughout the drying process. The voltage of the DC applied to the lower electrodes to offset the gravitational force acting upon the droplets in this study was kept at a constant value throughout drying. However, this DC could be exploited to record the mass of the droplet, because a software feedback loop (e.g. using LabVIEW) could adjust the voltage to account for a change in the vertical position of the droplet during drying. Where evaporation leads to a slight decrease in mass, the droplet would move up slightly in the trapping region, so the DC could be made to automatically reduce in voltage to account for the mass loss, to maintain a constant vertical position. From a record of the DC voltage throughout the experiment, the mass could be extracted through a calculation of the balance between the gravitational and drag forces.

Measurements of both the radius and the relative mass loss of aerosol droplets undergoing slow isothermal evaporation have been performed using an EDB previously by Flagan et al.[146] Future measurements of recording mass loss alongside the radius measurements for rapidly evaporating aerosol droplets would allow the time-dependent density, and hence the developing morphology, of a drying droplet to be predicted. This would be important for the spray drying community, where the ability to predict and control particle size and density would be highly valuable.

If a system for mass measurement during evaporation were implemented on the EDB in BARC, the evaporation of droplets containing liquids that are not optically transparent could be studied as there would be no reliance on elastically scattered fringes. Hence, this study could be extended to more complex liquids such as milk or paints. The work presented in this thesis has largely focused on the evaporation of model systems of water, ethanol and inorganic solutions, but an important future direction could be to study commercial products using these methods. Building an understanding of the Péclet number and morphology development in rapidly evaporating milk droplets could solve common problems associated with excessive stickiness and wall deposition in spray drying in the dairy industry.

In addition, the ability to predict and control specific dried particle morphologies from spray dried drug particles could revolutionise the field of inhalable pharmaceuticals.

References

1 C. G. J. Baker, Energy efficient dryer operation - An update on developments, *Dry. Technol.*, 2005, **23**, 2071–2087.

2 I. C. Kemp, in *Modern Drying Technology*, eds. E. Tsotsas and A. S. Mujumdar, Wiley-VCH, Weinheim, Germany, 1st edn., 2011, vol. 4, pp. 1–45.

3 R. Vehring, W. R. Foss and D. Lechuga-Ballesteros, Particle formation in spray drying, *J. Aerosol Sci.*, 2007, **38**, 728–746.

4 A. E. Bayly, *Structure development during drying - a review of the state of the art*, *IFPRI Report*, 2014.

5 *The Global Asthma Network*, *The Global Asthma Report*, Auckland, New Zealand, 2018.

6 U. K. Krieger, C. Marcolli and J. P. Reid, Exploring the complexity of aerosol particle properties and processes using single particle techniques, *Chem. Soc. Rev.*, 2012, **41**, 6631–6662.

7 N. Alexander, S. Allen, T. F. Stocker, D. Qin, G.-K. Plattner, M. M. B. Trignor, J. Boschung, Y. Xia, V. Bex. and P. M. Midgley, *IPCC Climate Change 2013: The Physical Science Basis. Contribution of Working Group I to the Fifth Assessment Report of the Intergovernmental Panel on Climate Change*, Cambridge University Press, Cambridge, United Kingdom and New York, NY, USA, 2013.

8 G. Myhre, D. Shindell, F.-M. Bréon, W. Collins, J. Fuglestvedt, J. Huang, D. Koch, J.-F. Lamarque, D. Lee, B. Mendoza, T. Nakajima, A. Robock, G. Stephens, T. Takemura and H. Zhang, *Anthropogenic and Natural Radiative Forcing. Climate Change 2013: The Physical Science Basis. Contribution of Working Group I to the Fifth Assessment Report of the Intergovernmental Panel on Climate Change*, Cambridge University Press, Cambridge, United Kingdom and New York, NY, USA, 2013.

9 C. Sadek, P. Schuck, Y. Fallourd, N. Pradeau, C. Le Floch-Fouéré and R. Jeantet, Drying of a single droplet to investigate process–structure–function relationships: a review, *Dairy Sci. Technol.*, 2015, **95**, 771–794.

10 A. Sosnik and K. P. Seremeta, Advantages and challenges of the spray-drying technology for the production of pure drug particles and drug-loaded polymeric carriers, *Adv. Colloid Interface Sci.*, 2015, **223**, 40–54.

11 N. Fu, M. W. Woo and X. D. Chen, Single Droplet Drying Technique to Study Drying Kinetics Measurement and Particle Functionality: A Review, *Dry. Technol.*, 2012, **30**, 1771–1785.

12 I. Zbicinski, Modeling and scaling up of industrial spray dryers: A review, *J. Chem. Eng. Japan*, 2017, **50**, 757–767.

13 M. I. Ré, Formulating drug delivery systems by spray drying, *Dry. Technol.*, 2006, **24**, 433–446.
14 Z. Berk, *Food Process Engineering and Technology*, Elsevier, 3rd edn., 2018.
15 R. Wisniewski, in *45th International Conference on Environmental Systems*, 2015, p. ICES-2015-094.
16 M. Jain, G. Lohare, M. Bari, R. Chavan, S. Barhate and C. Shah, Spray Drying in Pharmaceutical Industry: A Review, *Res. J. Pharm. Dos. Forms Technol.*, 2012, **4**, 74–79.
17 GEA Process Engineering, *GEA pharmaceutical spray drying*, 2020.
18 M. Ali, T. Mahmud, P. John, M. Ghadiri, D. Djurdjevic, H. Ahmadian, L. Martin, D. Juan, C. Amador, A. Bayly, W. Road, N. Upon and T. Ne, A one-dimensional plug-flow model of a counter-current spray drying tower, *Chem. Eng. Res. Des.*, 2013, **92**, 826–841.
19 A. Salem, M. Ahmadlouiedarab and K. Ghasemzadeh, CFD approach for the moisture prediction in spray chamber for drying of salt solution, *J. Ind. Eng. Chem.*, 2011, **17**, 527–532.
20 P. Schuck, R. Jeantet, B. Bhandari, X. D. Chen, Í. T. Perrone, A. F. de Carvalho, M. Fenelon and P. Kelly, Recent advances in spray drying relevant to the dairy industry: A comprehensive critical review, *Dry. Technol.*, 2016, **34**, 1773–1790.
21 Fortune Business Insight, *Infant Formula Market Size to Reach USD 103.75 Billion by 2026 | Fortune Business Insights*, Pune, India, 2019.
22 G. A. Reineccius and S. T. Coulter, Flavor Retention During Drying, *J. Dairy Sci.*, 1969, **52**, 1219–1223.
23 I. Tontul and A. Topuz, Spray-drying of fruit and vegetable juices: Effect of drying conditions on the product yield and physical properties, *Trends Food Sci. Technol.*, 2017, **63**, 91–102.
24 B. Adhikari, T. Howes, B. R. Bhandari and V. Truong, Experimental studies and kinetics of single drop drying and their relevance in drying of sugar-rich foods: A review, *Int. J. Food Prop.*, 2000, **3**, 323–351.
25 I. C. Kemp, Application of mechanistic drying models in pharmaceuticals and other industries, *Dry. Technol.*, 2019, **37**, 600–611.
26 Y. A. Pérez, C. M. Urista, J. I. Martínez, M. D. C. D. Nava and F. A. R. Rodríguez, Functionalized polymers for enhance oral bioavailability of sensitive molecules, *Polymers (Basel).*, 2016, **8**, 214.
27 R. G. Ricarte, N. J. Van Zee, Z. Li, L. M. Johnson, T. P. Lodge and M. A. Hillmyer, Recent Advances in Understanding the Micro- and Nanoscale Phenomena of Amorphous Solid Dispersions, *Mol. Pharm.*, 2019, **16**, 4089–4103.
28 K. Ohnishi, H. Tope and J. Zhang, *Assessment Report, Montreal Protocol on Substances that Deplete the Ozone Layer*, 2018.
29 H. Steckel and H. G. Brandes, A novel spray-drying technique to produce low density particles for pulmonary delivery, *Int. J. Pharm.*, 2004, **278**, 187–195.
30 M. T. Vidgrén, P. A. Vidgrén and T. P. Paronen, Comparison of physical and inhalation

properties of spray-dried and mechanically micronized disodium cromoglycate, *Int. J. Pharm.*, 1987, **35**, 139–144.

31 A. E. Haddrell, D. Lewis, T. Church, R. Vehring, D. Murnane and J. P. Reid, Pulmonary aerosol delivery and the importance of growth dynamics, *Ther. Deliv.*, 2017, **8**, 1051–1061.

32 M. Ali, T. Mahmud, P. J. Heggs, M. Ghadiri, A. Bayly, H. Ahmadian and L. Martin de Juan, CFD modeling of a pilot-scale countercurrent spray drying tower for the manufacture of detergent powder, *Dry. Technol.*, 2017, **35**, 281–299.

33 A. Farshchi, A. Hassanpour and A. E. Bayly, The structure of spray-dried detergent powders, *Powder Technol.*, 2019, **355**, 738–754.

34 V. Francia, L. Martín, A. E. Bayly and M. J. H. Simmons, Agglomeration in counter-current spray drying towers. Part B: Interaction between multiple spraying levels, *Powder Technol.*, 2016, **301**, 1344–1358.

35 F. Iskandar, L. Gradon and K. Okuyama, Control of the morphology of nanostructured particles prepared by the spray drying of a nanoparticle sol, *J. Colloid Interface Sci.*, 2003, **265**, 296–303.

36 A. B. D. Nandiyanto and K. Okuyama, Progress in developing spray-drying methods for the production of controlled morphology particles: From the nanometer to submicrometer size ranges, *Adv. Powder Technol.*, 2011, **22**, 1–19.

37 G. T. Vladisavljević, Structured microparticles with tailored properties produced by membrane emulsification, *Adv. Colloid Interface Sci.*, 2015, **225**, 53–87.

38 A. Lähde, J. Raula, E. I. Kauppinen, W. Watanabe, P. P. Ahonen and D. P. Brown, Aerosol Synthesis of Inhalation Particles via a Droplet-to-Particle Method, *Part. Sci. Technol.*, 2006, **24**, 71–84.

39 A. R. Najafabadi, K. Gilani, M. Barghi and M. Rafiee-Tehrani, The effect of vehicle on physical properties and aerosolisation behaviour of disodium cromoglycate microparticles spray dried alone or with L-leucine, *Int. J. Pharm.*, 2004, **285**, 97–108.

40 R. Jog and D. J. Burgess, Comprehensive quality by design approach for stable nanocrystalline drug products, *Int. J. Pharm.*, 2019, **564**, 426–460.

41 P. Gupta and A. K. Bansal, Spray drying for generation of a ternary amorphous system of celecoxib, PVP, and meglumine, *Pharm. Dev. Technol.*, 2005, **10**, 273–281.

42 M. Maury, K. Murphy, S. Kumar, A. Mauerer and G. Lee, Spray-drying of proteins: Effects of sorbitol and trehalose on aggregation and FT-IR amide I spectrum of an immunoglobulin G, *Eur. J. Pharm. Biopharm.*, 2005, **59**, 251–261.

43 M. Ordoubadi, F. K. A. Gregson, O. Melhem, D. Barona, R. E. H. Miles, D. D. Sa, S. Gracin, D. Lechuga-ballesteros, W. H. Finlay and R. Vehring, Multi-Solvent Microdroplet Evaporation : Modeling and Measurement of Spray-Drying Kinetics with Inhalable Pharmaceutics, *Pharm. Res.*, 2019, **36**, 100.

44 R. Vehring, Pharmaceutical Particle Engineering via Spray Drying, *Pharm. Res.*, 2008, **25**, 999–

1022.

45 C. Arpagaus, Pharmaceutical Particle Engineering via Nano Spray Drying - Process Parameters and Application Examples on the Laboratory-Scale, *Int. J. Med. Nano Res.*, 2018, **5**, 026.

46 M. A. I. Schutyser, E. M. Both, I. Siemons, E. M. J. Vaessen and L. Zhang, Gaining insight on spray drying behavior of foods via single droplet drying analyses, *Dry. Technol.*, 2019, **37**, 525–534.

47 D. Chiou, T. A. G. Langrish and R. Braham, Partial Crystallization Behavior during Spray Drying : Simulations and Experiments, *Dry. Technol.*, 2008, **26**, 27–38.

48 T. A. G. Langrish and D. F. Fletcher, Prospects for the modelling and design of spray dryers in the 21st century, *Dry. Technol.*, 2003, **21**, 197–215.

49 E. Rondet, G. Baylac and B. Bataille, Psychrometry as a methodological tool for optimizing the spray drying process, *Drug Dev. Ind. Pharm.*, 2008, **34**, 235–247.

50 J. S. Patton and P. R. Byron, Inhaling medicines: Delivering drugs to the body through the lungs, *Nat. Rev. Drug Discov.*, 2007, **6**, 67–74.

51 L. Heinemann, R. Baughman, A. Boss and M. Hompesch, Pharmacokinetic and Pharmacodynamic Properties of a Novel Inhaled Insulin, *J. Diabetes Sci. Technol.*, 2017, **11**, 148–156.

52 J. S. Patton, J. G. Bukar and M. A. Eldone, Clinical pharmacokinetics and pharmacodynamics of inhaled insulin, *Clin. Pharmacokinet.*, 2004, **43**, 781–801.

53 N. R. Labiris and M. B. Dolovich, Pulmonary drug delivery. Part I: Physiological factors affecting therapeutic effectiveness of aerosolized medications, *Br. J. Clin. Pharmacol.*, 2003, **56**, 588–599.

54 S. H. Van Rijt, T. Bein and S. Meiners, Medical nanoparticles for next generation drug delivery to the lungs, *Eur. Respir. J.*, 2014, **44**, 765–774.

55 A. H. L. Chow, H. H. Y. Tong, P. Chattopadhyay and B. Y. Shekunov, Particle engineering for pulmonary drug delivery, *Pharm. Res.*, 2007, **24**, 411–437.

56 Z. Zhang, C. Kleinstreuer and C. S. Kim, Water vapor transport and its effects on the deposition of hygroscopic droplets in a human upper airway model, *Aerosol Sci. Technol.*, 2006, **40**, 1–16.

57 J. Löndahl, A. Massling, J. Pagels, E. Swietlicki, E. Vaclavik and S. Loft, Size-resolved respiratory-tract deposition of fine and ultrafine hydrophobic and hygroscopic aerosol particles during rest and exercise, *Inhal. Toxicol.*, 2007, **19**, 109–116.

58 G. J. Dorr, S. Wang, L. C. Mayo, S. W. McCue, W. A. Forster, J. Hanan and X. He, Impaction of spray droplets on leaves: influence of formulation and leaf character on shatter, bounce and adhesion, *Exp. Fluids*, 2015, **56**, 1–17.

59 K. Qin, H. Tank, S. A. Wilson, B. Downer and L. Liu, Controlling Droplet-Size Distribution using Oil Emulsions in Agricultural Sprays, *At. Sprays*, 2010, **20**, 227–239.

60 G. Wang, Y. Lan, H. Qi, P. Chen, A. Hewitt and Y. Han, Field evaluation of an unmanned aerial

vehicle (UAV) sprayer: effect of spray volume on deposition and the control of pests and disease in wheat, *Pest Manag. Sci.*, 2019, **75**, 1546–1555.

61 F. Wang, Z. Hu, C. Abarca, M. Fefer, J. Liu, M. A. Brook and R. Pelton, Factors influencing agricultural spray deposit structures on hydrophobic surfaces, *Colloids Surfaces A Physicochem. Eng. Asp.*, 2018, **553**, 288–294.

62 Y. C. Song, A. E. Haddrell, B. R. Bzdek, J. P. Reid, T. Bannan, D. O. Topping, C. Percival and C. Cai, Measurements and Predictions of Binary Component Aerosol Particle Viscosity, *J. Phys. Chem. A*, 2016, **120**, 8123–8137.

63 B. R. Bzdek, R. M. Power, S. H. Simpson, P. Reid and C. P. Royall, Precise , contactless measurements of the surface tension of picolitre aerosol droplets, *Chem. Sci.*, 2015, **7**, 274–285.

64 L. Nayak, S. Mohanty, S. K. Nayak and A. Ramadoss, A Review on Inkjet Printing of Nanoparticle Inks for Flexible Electronics, *J. Mater. Chem. C*, 2019, **7**, 8771–8795.

65 M. Layani, A. Kamyshny and S. Magdassi, Transparent conductors composed of nanomaterials, *Nanoscale*, 2014, **6**, 5581–5591.

66 L. Lan, J. Zou, C. Jiang, B. Liu, L. Wang and J. Peng, Inkjet printing for electroluminescent devices: emissive materials, film formation, and display prototypes, *Front. Optoelectron.*, 2017, **10**, 329–352.

67 J. F. Dijksman, P. C. Duineveld, M. J. J. Hack, A. Pierik, J. Rensen, J. E. Rubingh, I. Schram and M. M. Vernhout, Precision ink jet printing of polymer light emitting displays, *J. Mater. Chem.*, 2007, **17**, 511–522.

68 F. C. Krebs, Fabrication and processing of polymer solar cells: A review of printing and coating techniques, *Sol. Energy Mater. Sol. Cells*, 2009, **93**, 394–412.

69 J. Jang, J. Ha and J. Cho, Fabrication of water-dispersible polyaniline-poly(4-styrenesulfonate) nanoparticles for inkjet-printed chemical-sensor applications, *Adv. Mater.*, 2007, **19**, 1772–1775.

70 F. Ramazani, W. Chen, C. F. Van Nostrum, G. Storm, F. Kiessling, T. Lammers, W. E. Hennink and R. J. Kok, Strategies for encapsulation of small hydrophilic and amphiphilic drugs in PLGA microspheres: State-of-the-art and challenges, *Int. J. Pharm.*, 2016, **499**, 358–367.

71 R. Deng, Y. Wang, L. Yang and C. D. Bain, In-Situ Fabrication of Polymeric Microcapsules by Ink-Jet Printing of Emulsions, *ACS Appl. Mater. Interfaces*, 2019, **11**, 40652–40661.

72 J. Shi, L. Yang and C. D. Bain, Drying of Ethanol/Water Droplets Containing Silica Nanoparticles, *ACS Appl. Mater. Interfaces*, 2019, **11**, 14275–14285.

73 W. E. Ranz and W. R. Marshall Jr., Evaporation from drops, *Chem. Eng. Prog.*, 1952, **48**, 141–146.

74 D. H. Charlesworth and W. R. Marshall, Evaporation from drops containing dissolved solids, *AIChE J.*, 1960, **6**, 9–23.

75 G. L. Goh, N. Saengchairat, S. Agarwala, W. Y. Yeong and T. Tran, Sessile droplets containing

carbon nanotubes: A study of evaporation dynamics and CNT alignment for printed electronics, *Nanoscale*, 2019, **11**, 10603–10614.

76 R. G. Larson, Transport and deposition patterns in drying sessile droplets, *AIChE J.*, 2014, **60**, 1538–1571.

77 R. D. Deegan, O. Bakajin, T. F. Dupont, G. Huber, S. R. Nagel and T. A. Witten, Capillary flow as the cause of ring strins from dried liquid drops, *Nature*, 1997, **389**, 827–829.

78 J. Perdana, M. B. Fox, M. A. I. Schutyser and R. M. Boom, Single-droplet experimentation on spray drying: Evaporation of a sessile droplet, *Chem. Eng. Technol.*, 2011, **34**, 1151–1158.

79 W. Xu and C. H. Choi, Effects of surface topography and colloid particles on the evaporation kinetics of sessile droplets on superhydrophobic surfaces, *J. Heat Transfer*, 2012, **134**, 1–7.

80 P. Sun, L. Zhong, C. Luo, W. Niu and X. Lu, Visual measurement of the evaporation process of a sessile droplet by dual-channel simultaneous phase-shifting interferometry, *Sci. Rep.*, 2015, **5**, 1–10.

81 H. Sadafi, S. Dehaeck, A. Rednikov and P. Colinet, Vapor-Mediated versus Substrate-Mediated Interactions between Volatile Droplets, *Langmuir*, 2019, **35**, 7060−7065.

82 Y. Tsoumpas, S. Dehaeck, A. Rednikov and P. Colinet, Effect of Marangoni Flows on the Shape of Thin Sessile Droplets Evaporating into Air, *Langmuir*, 2015, **31**, 13334–13340.

83 S. Manukyan, H. M. Sauer, I. V. Roisman, K. A. Baldwin, D. J. Fairhurst, H. Liang, J. Venzmer and C. Tropea, Imaging internal flows in a drying sessile polymer dispersion drop using Spectral Radar Optical Coherence Tomography (SR-OCT), *J. Colloid Interface Sci.*, 2013, **395**, 287–293.

84 V. Y. Borodulin, V. N. Letushko, M. I. Nizovtsev and A. N. Sterlyagov, The surface temperature of free evaporating drops, *J. Phys. Conf. Ser.*, 2016, **754**, 032018.

85 M. H. Sadafi, I. Jahn, A. B. Stilgoe and K. Hooman, A theoretical model with experimental verification for heat and mass transfer of saline water droplets, *Int. J. Heat Mass Transf.*, 2015, **81**, 1–9.

86 B. Ali Al Zaitone and C. Tropea, Evaporation of pure liquid droplets: Comparison of droplet evaporation in an acoustic field versus glass-filament, *Chem. Eng. Sci.*, 2011, **66**, 3914–3921.

87 R. D. Davis, S. Lance, J. A. Gordon, S. B. Ushijima and M. A. Tolbert, Contact efflorescence as a pathway for crystallization of atmospherically relevant particles, *PNAS*, 2015, **112**, 1–6.

88 C. Sadek, P. Schuck, Y. Fallourd, N. Pradeau, R. Jeantet and C. Le Floch-Fouéré, Buckling and collapse during drying of a single aqueous dispersion of casein micelle droplet, *Food Hydrocoll.*, 2016, **52**, 161–166.

89 L. Lanotte, F. Boissel, P. Schuck, R. Jeantet and C. Le Floch-Fouéré, Drying-induced mechanisms of skin formation in mixtures of high protein dairy powders, *Colloids Surfaces A Physicochem. Eng. Asp.*, 2018, **553**, 20–27.

90 E. H. Brandt, Levitation in Physics, *Science (80-.).*, 1989, **243**, 349–355.

91 F. Babin, J.-M. Gagne, P.-F. Paradis, J.-P. Coutures and J.-C. Rifflet, High temperature containerless laser processing of dielectric samples in microgravity - study of aerodynamic trapping, *Microgravity Sci. Technol.*, 1995, **7**, 283–289.

92 L. Hennet, V. Cristiglio, J. Kozaily, I. Pozdnyakova, H. E. Fischer, A. Bytchkov, J. W. E. Drewitt, M. Leydier, D. Thiaudière, S. Gruner, S. Brassamin, D. Zanghi, G. J. Cuello, M. Koza, S. Magazù, G. N. Greaves and D. L. Price, Aerodynamic levitation and laser heating: Applications at synchrotron and neutron sources, *Eur. Phys. J. Spec. Top.*, 2011, **196**, 151–165.

93 H. Schiffter and G. Lee, Single-Droplet Evaporation Kinetics and Particle Formation in an Acoustic Levitator. Part 2: Drying Kinetics and Particle Formation From Microdroplets of Aqueous Mannitol, Trehalose, or Catalase, *J. Pharm. Sci.*, 2007, **96**, 2284–2295.

94 A. Marzo and B. W. Drinkwater, Holographic acoustic tweezers, *Proc. Natl. Acad. Sci. U. S. A.*, 2019, **116**, 84–89.

95 F. Delißen, J. Leiterer, R. Bienert, F. Emmerling and A. F. Thünemann, Agglomeration of proteins in acoustically levitated droplets, *Anal. Bioanal. Chem.*, 2008, **392**, 161–165.

96 A. M. Seddon, S. J. Richardson, K. Rastogi, T. S. Plivelic, A. M. Squires and C. Pfrang, Control of Nanomaterial Self-Assembly in Ultrasonically Levitated Droplets, *J. Phys. Chem. Lett.*, 2016, **7**, 1341–1345.

97 A. Riaud, M. Baudoin, O. Bou Matar, L. Becerra and J. L. Thomas, Selective Manipulation of Microscopic Particles with Precursor Swirling Rayleigh Waves, *Phys. Rev. Appl.*, 2017, **7**, 1–8.

98 H. Schiffter and G. Lee, Single-Droplet Evaporation Kinetics and Particle Formation in an Acoustic Levitator. Part 1: Evaporation of Water Microdroplets Assessed using Boundary-Layer and Acoustic Levitation Theories, *J. Pharm. Sci.*, 2007, **96**, 2274–2283.

99 E. H. Trinh and J. L. Robey, Experimental study of streaming flows associated with ultrasonic levitators, *Phys. Fluids*, 1994, **6**, 3567–3579.

100 A. Ashkin, Acceleration and Trapping of Particles by Radiation Pressure, *Phys. Rev. Lett.*, 1970, **24**, 156–159.

101 A. Ashkin, J. M. Dziedzic and T. Yamane, Optical trapping and manipulation of single cells using infrared laser beams, *Nature*, 1987, **330**, 769–711.

102 NobelPrize.org, The Nobel Prize in Physics 2018, https://www.nobelprize.org/prizes/physics/2018/summary/, (accessed 29 October 2019).

103 D. G. Grier, A revolution in optical manipulation, *Nature*, 2003, **424**, 810–816.

104 L. P. Ghislain, N. A. Switz and W. W. Webb, Measurement of small forces using an optical trap, *Rev. Sci. Instrum.*, 1994, **65**, 2762–2768.

105 L. Mitchem, J. Buajarern, R. J. Hopkins, A. D. Ward, R. J. J. Gilham, R. L. Johnston and J. P. Reid, Spectroscopy of growing and evaporating water droplets: Exploring the variation in equilibrium droplet size with relative humidity, *J. Phys. Chem. A*, 2006, **110**, 8116–8125.

106 K. Gorkowski, H. Beydoun, M. Aboff, J. S. Walker, J. P. Reid and R. C. Sullivan, Advanced

aerosol optical tweezers chamber design to facilitate phase-separation and equilibration timescale experiments on complex droplets, *Aerosol Sci. Technol.*, 2016, **50**, 1327–1341.

107 K. Gorkowski, N. M. Donahue and R. C. Sullivan, Emulsified and Liquid-Liquid Phase-Separated States of α-Pinene Secondary Organic Aerosol Determined Using Aerosol Optical Tweezers, *Environ. Sci. Technol.*, 2017, **51**, 12154–12163.

108 D. L. Bones, J. P. Reid, D. M. Lienhard and U. K. Krieger, Comparing the mechanism of water condensation and evaporation in glassy aerosol, *Proc. Natl. Acad. Sci. U. S. A.*, 2012, **109**, 11613–11618.

109 M. D. King, K. C. Thompson, A. D. Ward, C. Pfrang and B. R. Hughes, Oxidation of biogenic and water-soluble compounds in aqueous and organic aerosol droplets by ozone: A kinetic and product analysis approach using laser Raman tweezers, *Faraday Discuss.*, 2007, **137**, 173–192.

110 L. Mitchem and J. P. Reid, Optical manipulation and characterisation of aerosol particles using a single-beam gradient force optical trap, *Chem. Soc. Rev.*, 2008, **37**, 756–769.

111 J. R. Butler, L. Mitchem, K. L. Hanford, L. Treuel and J. P. Reid, In situ comparative measurements of the properties of aerosol droplets of different chemical composition, *Faraday Discuss.*, 2007, **137**, 351–366.

112 S. Ingram, C. Cai, Y. Song, D. R. Glowacki, D. O. Topping, S. O'Meara and J. P. Reid, Characterising the evaporation kinetics of water and semi-volatile organic compounds from viscous multicomponent organic aerosol particles, *Phys. Chem. Chem. Phys.*, 2017, **19**, 31634–31646.

113 J. Popp, M. Lankers, K. Schaschek, W. Kiefer and J. T. Hodges, Observation of sudden temperature jumps in optically levitated microdroplets due to morphology-dependent input resonances, *Appl. Opt.*, 1995, **34**, 2380–2386.

114 S. Corsetti, R. E. H. Miles, C. McDonald, Y. Belotti, J. P. Reid, J. Kiefer and D. McGloin, Probing the Evaporation Dynamics of Ethanol/Gasoline Biofuel Blends Using Single Droplet Manipulation Techniques, *J. Phys. Chem. A*, 2015, **119**, 12797–12804.

115 Y. Y. Su, R. E. H. Miles, Z. M. Li, J. P. Reid and J. Xu, The evaporation kinetics of pure water droplets at varying drying rates and the use of evaporation rates to infer the gas phase relative humidity, *Phys. Chem. Chem. Phys.*, 2018, **20**, 23453–23466.

116 G. Rovelli, R. E. H. Miles, J. P. Reid and S. L. Clegg, Accurate Measurements of Aerosol Hygroscopic Growth over a Wide Range in Relative Humidity, *J. Phys. Chem. A*, 2016, **120**, 4376–4388.

117 J. F. Widmann and E. J. Davis, Evaporation of multicomponent droplets, *Aerosol Sci. Technol.*, 1997, **27**, 243–254.

118 J. Archer, M. Kolwas, D. Jakubczyk, G. Derkachov, M. Woźniak and K. Kolwas, Evolution of radius and light scattering properties of single drying microdroplets of colloidal suspension, *J. Quant. Spectrosc. Radiat. Transf.*, 2017, **202**, 168–175.

119 H.-J. Tong, B. Ouyang, F. D. Pope and M. Kalberer, A new electrodynamic balance design for low temperature studies, *Atmos. Meas. Tech. Discuss.*, 2014, **7**, 7671–7700.

120 E. J. Davis and A. K. Ray, Single aerosol particle size and mass measurements using an electrodynamic balance, *J. Colloid Interface Sci.*, 1980, **75**, 566–576.

121 E. J. Davis and E. Chorbajian, The Measurement of Evaporation Rates of Submicron Aerosol Droplets, *Ind. Eng. Chem. Fundam.*, 1974, **13**, 272–277.

122 K. Y. Li, H. Tu and A. K. Ray, Charge limits on droplets during evaporation, *Langmuir*, 2005, **21**, 3786–3794.

123 W. Li and E. J. Davis, Aerosol Evaporation in the Transition Regime, *Aerosol Sci. Technol.*, 1996, **25**, 11–21.

124 C. Heinisch, J. B. Wills, J. P. Reid, T. Tschudi and C. Tropea, Temperature measurement of single evaporating water droplets in a nitrogen flow using spontaneous raman scattering, *Phys. Chem. Chem. Phys.*, 2009, **11**, 9720–9728.

125 E. J. Davis, A history of single aerosol particle levitation, *Aerosol Sci. Technol.*, 1997, **26**, 212–254.

126 R. A. Millikan, The Isolation of an Ion, a Precision Measurement of its Charge, and the Correction of Stokes's Law, *Science (80-.).*, 1910, **32**, 436–449.

127 H. Fletcher, Brownian Movements, *Phys. Rev.*, 1911, **30**, 81–110.

128 W. Paul and M. Raether, Das elektrische Massenfilter, *Zeitschrift für Phys.*, 1955, **140**, 262–273.

129 H. Straubel, Die Dosierung von Substanzmengen unter 10-6g Mittels Elektrostatischer Aufladung für Zwecke der Mikroanalyse, *Zeitschrift für Elektrochemie*, 1956, **60**, 1033–1036.

130 R. F. Wuerker, H. Shelton and R. V. Langmuir, Electrodynamic containment of charged particles, *J. Appl. Phys.*, 1959, **30**, 342–349.

131 A. K. Ray, R. D. Johnson and A. Souyri, Dynamic Behavior of Single Glycerol Droplets in Humid Air Streams, *Langmuir*, 1989, **5**, 133–140.

132 E. Fischer, Die dreidimensionale Stabilisierung von Ladungsträgern in einem Vierpolfeld, *Zeitschrift für Phys.*, 1959, **156**, 1–26.

133 H. G. Dehmelt and F. G. Major, Orientation of (He4)+ ions by exchange collisions with cesium atoms, *Phys. Rev. Lett.*, 1962, **8**, 213–214.

134 R. F. Wuerker, H. M. Goldenberg and R. V. Langmuir, Electrodynamic Containment of Charged Particles by Three-Phase Voltages, *J. Appl. Phys.*, 1959, **441**, 441–442.

135 A. Müller, Theoretische Untersuchungen über das Verhalten geladener Teilchen in Sattelpunkten elektrischer Wechselfelder, *Ann. Phys.*, 1960, **461**, 206–220.

136 M. O. Fernandez, R. J. Thomas, N. J. Garton, A. Hudson, A. Haddrell and J. P. Reid, Assessing the airborne survival of bacteria in populations of aerosol droplets with a novel technology, *J. R. Soc. Interface*, 2019, **16**, 20180779.

137 J. F. Davies, A. E. Haddrell and J. P. Reid, Time-Resolved Measurements of the Evaporation of Volatile Components from Single Aerosol Droplets, *Aerosol Sci. Technol.*, 2012, **46**, 666–677.

138 R. A. Millikan, On the elementary electrical charge and the avogadro constant, *Phys. Rev.*, 1913, **2**, 109–143.

139 N. Gudris and L. Kulikowa, Die Verdampfung kleiner Wassertropfen, *Zeitschrift für Phys.*, 1924, **25**, 121–132.

140 S. T. Martin, Phase transitions of aqueous atmospheric particles, *Chem. Rev.*, 2000, **100**, 3403–3453.

141 D. J. Woodland and E. Mack, The Effect of Curvature of Surface on Surface Energy. Rate of Evaporation of Liquid Droplets. Thickness of Saturated Vapor Films, *J. Am. Chem. Soc.*, 1933, **55**, 3149–3161.

142 J. L. Shereshefsky and S. Steckler, A study of the evaporation of small drops and of the relationship between surface tension and curvature, *J. Chem. Phys.*, 1936, **4**, 108–115.

143 F. T. Gucker and Ro. L. Rowell, The angular variation of light scattered by single dioctyl phthalate aerosol droplets, *Discuss. Faraday Soc.*, 1960, **30**, 185–191.

144 M. Kolwas, D. Jakubczyk, T. Do Duc and J. Archer, Evaporation of a free microdroplet of a binary mixture of liquids with different volatilities, *Soft Matter*, 2019, **15**, 1825–1832.

145 W. J. Glantschnig and S.-H. Chen, Light scattering from water droplets in the geometrical optics approximation, *Appl. Opt.*, 1981, **20**, 2499.

146 A. P. Olsen, R. C. Flagan and J. A. Kornfield, Single-particle levitation system for automated study of homogeneous solute nucleation, *Rev. Sci. Instrum.*, 2006, **77**, 073901–073908.

147 C. J. Homer, X. Jiang, T. L. Ward, C. J. Brinker and J. P. Reid, Measurements and simulations of the near-surface composition of evaporating ethanol–water droplets, *Phys. Chem. Chem. Phys.*, 2009, **11**, 7780–7791.

148 A. Baldelli, M. A. Boraey, D. S. Nobes and R. Vehring, Analysis of the Particle Formation Process of Structured Microparticles, *Mol. Pharm.*, 2015, **12**, 2562–2573.

149 D. B. Southwell and T. A. G. Langrish, Observations of Flow Patterns in a Spray Dryer, *Dry. Technol.*, 2000, **18**, 661–685.

150 G. Tian, M. Hindle, S. Lee and P. W. Longest, Validating CFD Predictions of Pharmaceutical Aerosol Deposition with In Vivo Data, *Pharm. Res.*, 2015, **32**, 3170–3187.

151 J. Dlouhy and W. H. Gauvin, Evaporation rates in spray drying, *Can. J. Chem. Eng.*, 1960, **38**, 113–120.

152 C. D. Hendricks and S. Babil, Generation of uniform, 0.5-10μm, solid particles, *J. Phys. E.*, 1972, **5**, 905–910.

153 T. M. El-Sayed, D. A. Wallack and C. J. King, Changes in Particle Morphology during Drying of Drops of Carbohydrate Solutions and Food Liquids. 1. Effects of Composition and Drying Conditions, *Ind. Eng. Chem. Res.*, 1990, **29**, 2346–2354.

154 C. G. Greenwald and C. J. King, The Effects of Design and Operating Conditions on Particle Morphology for Spray-Dried Foods, *Food Process Eng.*, 1981, **4**, 171–187.

155 K. Alexander and C. Judson King, Factors Governing Surface Morphology Of Spray-Dried Amorphous Substances, *Dry. Technol.*, 1985, **3**, 321–348.

156 R. M. Sayer, R. D. B. Gatherer and J. P. Reid, A laser induced fluorescence technique for determining the pH of water droplets and probing uptake dynamics, *Phys. Chem. Chem. Phys.*, 2003, **5**, 3740–3747.

157 R. J. Hopkins and J. P. Reid, Evaporation of ethanol/water droplets: Examining the temporal evolution of droplet size, composition and temperature, *J. Phys. Chem. A*, 2005, **109**, 7923–7931.

158 A. Baldelli, R. M. Power, R. E. H. Miles, J. P. Reid and R. Vehring, Effect of crystallization kinetics on the properties of spray dried microparticles, *Aerosol Sci. Technol.*, 2016, **50**, 693–704.

159 H. Jubaer, S. Afshar, J. Xiao, X. D. Chen, C. Selomulya and M. W. Woo, On the importance of droplet shrinkage in CFD-modeling of spray drying, *Dry. Technol.*, 2018, **36**, 1785–1801.

160 R. E. M. Verdurmen, P. Menn, J. Ritzert, S. Blei, G. C. S. Nhumaio, T. S. Sørensen, M. Gunsing, J. Straatsma, M. Vershueren, M. Sibeijn, G. Schulte, U. Fritsching, K. Bauckhage, C. Tropea, M. Sommerfield, A. P. Watkins, A. J. Yule and H. Schønfeldt, *Simulation of agglomeration in spray drying installations: The EDECAD project*, 2004, vol. 22.

161 M. Sommerfeld and M. Kuschel, Modelling droplet collision outcomes for different substances and viscosities, *Exp. Fluids*, 2016, **57**, 187.

162 M. Orme, Experiments on droplet collisions, bounce, coalescence and disruption, *Prog. Energy Combust. Sci.*, 1997, **23**, 65–79.

163 K. H. Al-Dirawi and A. E. Bayly, An experimental study of binary collisions of miscible droplets with non-identical viscosities, *Exp. Fluids*, 2020, **61**, 50.

164 S. G. Bradley and C. D. Stow, Collisions Between Liquid Drops, *Philos. Trans. R. Soc. A*, 1978, **287**, 635–675.

165 Y. J. Jiang, A. Umemura and C. K. Law, An Experimental Investigation on the Collision Behaviour of Hydrocarbon Droplets, *J. Fluid Mech.*, 1992, **234**, 171–190.

166 K. H. Al-Dirawi and A. E. Bayly, A New Model for the Bouncing Regime Boundary in Binary Droplet Collisions, *Phys. Fluids*, 2019, **31**, 027105.

167 J. Qian and C. K. Law, Regimes of coalescence and separation in droplet collision, *J. Fluid Mech.*, 1997, **331**, 59–80.

168 M. Kuschel and M. Sommerfeld, in *ILASS - Europe 2010, 23rd Annual Conference on Liquid Atomization and Spray Systems*, 2010, pp. 1–7.

169 P. Atkins and J. De Paula, *Physical Chemistry*, Oxford University Press, Oxford, 7th edn., 2002.

170 A. Zuend, C. Marcolli, B. P. Luo and T. Peter, A thermodynamic model of mixed organic-

inorganic aerosols to predict activity coefficients, *Atmos. Chem. Phys.*, 2008, **8**, 4559–4593.

171 A. Zuend, Aerosol Inorganic-Organic Mixtures Functional groups Activity Coefficients, http://www.aiomfac.caltech.edu.

172 I. N. Tang and H. R. Munkelwitz, Composition and temperature dependence of the deliquescence properties of hygroscopic aerosols, *Atmos. Environ. Part A, Gen. Top.*, 1993, **27**, 467–473.

173 U. Pöschl, Atmospheric aerosols: Composition, transformation, climate and health effects, *Angew. Chemie - Int. Ed.*, 2005, **44**, 7520–7540.

174 I. N. Tang, Chemical and size effects of hygroscopic aerosols on light scattering coefficients, *J. Geophys. Res. Atmos.*, 1996, **101**, 19245–19250.

175 S. L. Clegg, P. Brimblecombe and A. S. Wexler, Thermodynamic Model of the System H+ - NH4+ - Na+ - SO42- - NO3- - Cl- - H2O at 298.15 K, *J. Phys. Chem. A*, 1998, **102**, 2155–2171.

176 A. S. Wexler and S. L. Clegg, Atmospheric aerosol models for systems including the ions H+, NH4+, Na+, SO42−, NO3−, Cl−, Br− and H2O, *J. Geophys. Res.*, 2002, **107**, 4207–4221.

177 S. L. Clegg, P. Brimblecombe and A. S. Wexler, Thermodynamic model of the system H+-NH4+-SO42-NO 3--H2O at tropospheric temperatures, *J. Phys. Chem. A*, 1998, **102**, 2137–2154.

178 A. Zuend, C. Marcolli, T. Peter and J. H. Seinfeld, Computation of liquid-liquid equilibria and phase stabilities: Implications for RH-dependent gas/particle partitioning of organic-inorganic aerosols, *Atmos. Chem. Phys.*, 2010, **10**, 7795–7820.

179 C. N. Davies, N. A. Fuchs, J. W. Gentry, A. A. Kirsch, T. T. Mercer, J. Pich, K. R. Spurny, I. B. Stechkina and W. Stöber, *Fundamentals of Aerosol Science*, John Wiley & Sons, New York, 1st edn., 1978.

180 A. Fick, On liquid diffusion, *London, Edinburgh, Dublin Philos. Mag. J. Sci.*, 1855, **10**, 30–39.

181 J. C. Maxwell, *The Scientific Papers of James Clerk Maxwell*, Dover Publications, Inc., New York, II., 1890.

182 M. Kulmala, T. Vesala and P. Wagner, An analytical expression for the rate of binary condensational particle growth, *Proc. R. Soc. Lond. A*, 1993, **441**, 589–605.

183 F. R. Newbold and N. R. Amundson, A model for evaporation of a multicomponent droplet, *AIChE J.*, 1973, **19**, 22–30.

184 W. Wagner and A. Pruss, International Equations for the Saturation Properties of Ordinary Water Substance. Revised According to the International Temperature Scale of 1990. Addendum to J. Phys. Chem. Ref. Data 16, 893 (1987), *J. Phys. Chem. Ref. Data*, 1993, **22**, 783–787.

185 I. Langmuir, The constitution and fundamental properties of solids and liquids. Part I. Solids, *J. Am. Chem. Soc.*, 1916, **38**, 2221–2295.

186 J. F. Davies, A. E. Haddrell, A. M. J. Rickards and J. P. Reid, Simultaneous analysis of the

equilibrium hygroscopicity and water transport kinetics of liquid aerosol, *Anal. Chem.*, 2013, **85**, 5819–5826.

187 M. E. Wise, G. Biskos, S. T. Martin, L. M. Russell and P. R. Buseck, Phase transitions of single salt particles studied using a transmission electron microscope with an environmental cell, *Aerosol Sci. Technol.*, 2005, **39**, 849–856.

188 M. Kanakidou, J. H. Seinfeld, S. N. Pandis, I. Barnes, F. J. Dentener, M. C. Facchini, R. van Dingenen, B. Ervens, A. Nenes, C. J. Nielsen, E. Swietlicki, J. P. Putaud, Y. Balkanski, S. Fuzzi, J. Horth, G. K. Moortgat, R. Winterhalter, C. E. L. Myhre, K. Tsigaridis, E. Vignati, E. G. Stephanou and J. Wilson, Organic aerosol and global climate modelling: a review, *Atmos. Chem. Phys. Discuss.*, 2004, **4**, 5855–6024.

189 C. L. Har, N. Fu, E. S. Chan, B. T. Tey and X. D. Chen, In situ crystallization kinetics and behavior of mannitol during droplet drying, *Chem. Eng. J.*, 2018, **354**, 314–326.

190 S. G. Maas, G. Schaldach, E. M. Littringer, A. Mescher, U. J. Griesser, D. E. Braun, P. E. Walzel and N. A. Urbanetz, The impact of spray drying outlet temperature on the particle morphology of mannitol, *Powder Technol.*, 2011, **213**, 27–35.

191 A. Dubbini, R. Censi, V. Martena, E. Hoti, M. Ricciutelli, L. Malaj and P. Di Martino, Influence of pH and method of crystallization on the solid physical form of indomethacin, *Int. J. Pharm.*, 2014, **473**, 536–544.

192 F. Lyu, J. J. Liu, Y. Zhang and X. Z. Wang, Combined control of morphology and polymorph in spray drying of mannitol for dry powder inhalation, *J. Cryst. Growth*, 2017, **467**, 155–161.

193 R. P. Sear, Nucleation: Theory and applications to protein solutions and colloidal suspensions, *J. Phys. Condens. Matter*, , DOI:10.1088/0953-8984/19/3/033101.

194 F. Schüth, P. Bussian, P. Ågren, S. Schunk and M. Lindén, Techniques for analyzing the early stages of crystallization reactions, *Solid State Sci.*, 2001, **3**, 801–808.

195 C. Brandel and J. H. Horst, Measuring induction times and crystal nucleation rates, *Faraday Discuss.*, 2015, **179**, 199–214.

196 R. P. Sear, Quantitative studies of crystal nucleation at constant supersaturation: experimental data and models, *CrystEngComm*, 2014, **16**, 6506–6522.

197 P. G. Vekilov, Nucleation of crystals in solution, *AIP Conf. Proc.*, 2010, **1270**, 60–77.

198 J. Desarnaud, H. Derluyn, J. Carmeliet, D. Bonn and N. Shahidzadeh, Metastability limit for the nucleation of NaCl crystals in confinement, *J. Phys. Chem. Lett.*, 2014, **5**, 890–895.

199 Y. Diao, M. E. Helgeson, Z. A. Siam, P. S. Doyle, A. S. Myerson, T. A. Hatton and B. L. Trout, Nucleation under soft confinement: Role of polymer-solute interactions, *Cryst. Growth Des.*, 2012, **12**, 508–517.

200 S. S. Ma, W. Yang, C. M. Zheng, S. F. Pang and Y. H. Zhang, Subsecond measurements on aerosols: From hygroscopic growth factors to efflorescence kinetics, *Atmos. Environ.*, 2019, **210**, 177–185.

201 D. Knezic, J. Zaccaro and A. S. Myerson, Nucleation induction time in levitated droplets, *J. Phys. Chem. B*, 2004, **108**, 10672–10677.

202 D. Duft and T. Leisner, Laboratory evidence for volume-dominated nucleation of ice in supercooled water microdroplets, *Atmos. Chem. Phys. Discuss.*, 2004, **4**, 3077–3088.

203 M. A. Durán-olivencia and F. Otálora, A Brownian model for crystal nucleation, *J. Cryst. Growth*, 2013, **380**, 247–255.

204 Y. C. Song, A. E. Haddrell, B. R. Bzdek, J. P. Reid, T. Bannan, D. O. Topping, C. Percival and C. Cai, Measurements and Predictions of Binary Component Aerosol Particle Viscosity, *J. Phys. Chem. A*, 2016, **120**, 8123–8137.

205 B. Zobrist, V. Soonsin, B. P. Luo, U. K. Krieger, C. Marcolli, T. Peter and T. Koop, Ultra-slow water diffusion in aqueous sucrose glasses, *Phys. Chem. Chem. Phys.*, 2011, **13**, 3514–3526.

206 B. Adhikari, T. Howes, B. R. Bhandari and V. Troung, Surface stickiness of drops of carbohydrate and organic acid solutions during convective drying: Experiments and modeling, *Dry. Technol.*, 2003, **21**, 839–873.

207 J. Lin and J. W. Gentry, Spray Drying Drop Morphology : Experimental Study, *Aerosol Sci. Technol.*, 2010, **37**, 15–32.

208 D. E. Walton and C. J. Mumford, The morphology of spray-dried particles: the effect of process variables upon the morphology of spray-dried particles, *Chem. Eng. Res. Des.*, 1999, **77**, 442–460.

209 C. S. Handscomb and M. Kraft, Simulating the structural evolution of droplets following shell formation, *Chem. Eng. Sci.*, 2010, **65**, 713–725.

210 A. Haddrell, G. Rovelli, D. Lewis, T. Church and J. P. Reid, Identifying time-dependent changes in the morphology of an individual aerosol particle from their light scattering patterns, *Aerosol Sci. Technol.*, 2019, **53**, 1334–1351.

211 J. F. Davies, R. E. H. Miles, A. E. Haddrell and J. P. Reid, Temperature dependence of the vapor pressure and evaporation coefficient of supercooled water, *J. Geophys. Res.*, 2014, **119**, 10931–10940.

212 A. Marsh, R. E. H. Miles, G. Rovelli, A. G. Cowling, L. Nandy, C. S. Dutcher and J. P. Reid, Influence of organic compound functionality on aerosol hygroscopicity: Dicarboxylic acids, alkyl-substituents, sugars and amino acids, *Atmos. Chem. Phys.*, 2017, **17**, 5583–5599.

213 J. F. Davies, University of Bristol, 2014.

214 W. H. Hartung and C. T. Avedisian, On the electrodynamic balance, *Proc. R. Soc. London. Ser. A Math. Phys. Sci.*, 1992, **437**, 237–266.

215 N. E. Rothfuss, A. Marsh, G. Rovelli, M. D. Petters and J. P. Reid, Condensation Kinetics of Water on Amorphous Aerosol Particles, *J. Phys. Chem. Lett.*, 2018, **9**, 3708–3713.

216 C. Cai, R. E. H. Miles, M. I. Cotterell, A. Marsh, G. Rovelli, A. M. J. Rickards, Y. H. Zhang and J. P. Reid, Comparison of methods for predicting the compositional dependence of the

density and refractive index of organic-aqueous aerosols, *J. Phys. Chem. A*, 2016, **120**, 6604–6617.

217 M. I. Cotterell, B. J. Mason, T. C. Preston, A. J. Orr-Ewing and J. P. Reid, Optical extinction efficiency measurements on fine and accumulation mode aerosol using single particle cavity ring-down spectroscopy, *Phys. Chem. Chem. Phys.*, 2015, **17**, 15843–15856.

218 J. R. Rumble, Ed., CRC Press, Taylor & Francis Group, Boca Raton, 98th edn.

219 A. Marsh, G. Rovelli, R. E. H. Miles and J. P. Reid, Complexity of measuring and representing the hygroscopicity of mixed component aerosol, *J. Phys. Chem. A*, 2019, **123**, 1648–1660.

220 T. Vesala, M. Kulmala and M. Olin, Condensation and evaporation of binary droplets with internal mass transfer, *J. Aerosol Sci.*, 1990, **21**, 7–10.

221 A. Marsh, University of Bristol, 2018.

222 A. Marsh, G. Rovelli, Y. C. Song, K. L. Pereira, R. E. Willoughby, B. R. Bzdek, J. F. Hamilton, A. J. Orr-Ewing, D. O. Topping and J. P. Reid, Accurate representations of the physicochemical properties of atmospheric aerosols: When are laboratory measurements of value?, *Faraday Discuss.*, 2017, **200**, 639–661.

223 K. Waldron, W. D. Wu, Z. Wu, W. Liu, C. Selomulya, D. Zhao and X. D. Chen, Formation of monodisperse mesoporous silica microparticles via spray-drying, *J. Colloid Interface Sci.*, 2014, **418**, 225–233.

224 S. Sharma, M. Srisa-Art, S. Scott, A. Asthana and A. Cass, Droplet-based micro fluidics, *Methods Mol. Biol.*, 2013, **949**, 207–230.

225 F. K. A. Gregson, M. Ordoubadi, R. E. H. Miles, A. Haddrell, D. Barona, D. Lewis, T. Church, R. Vehring and J. P. Reid, Studies of competing evaporation rates of multiple volatile components from a single binary-component aerosol droplet, *Phys. Chem. Chem. Phys.*, 2019, **21**, 9709–9719.

226 C. K. Law, T. Y. Xiong and C. H. Wang, Alcohol droplet vaporization in humid air, *Int. J. Heat Mass Transf.*, 1987, **30**, 1435–1443.

227 A. M. J. Rickards, Y.-C. Song, R. E. H. Miles, T. C. Preston and J. P. Reid, Variabilities and uncertainties in characterising water transport kinetics in glassy and ultraviscous aerosol, *Phys. Chem. Chem. Phys.*, 2015, **17**, 10059–10073.

228 V. Devarakonda and A. K. Ray, Determination of thermodynamic parameters from evaporation of binary microdroplets of volatile constituents, *J. Colloid Interface Sci.*, 2000, **221**, 104–113.

229 R. J. Hopkins and J. P. Reid, A comparative study of the mass and heat transfer dynamics of evaporating ethanol/ water, methanol/water, and 1-propanol/water aerosol droplets, *J. Phys. Chem. B*, 2006, **110**, 3239–3249.

230 M. Kulmala, T. Vesala and P. E. Wagner, An analytical expression for the rate of binary condensational particle growth: Comparison with numerical results, *J. Aerosol Sci.*, 1992, **23**, 133–136.

231 K. P. Mishchenko and V. V Subbotina, Dampfdruck von Ethanol bei Temperaturen von 4 bis 46°C., *Zhurnal Prikl. Khimii*, 1967, **40**, 1156–1159.

232 N. A. Fuchs, *Evaporation and Droplet Growth in Gaseous Media*, Pergamon Press, Inc., New York, 1959.

233 Y. Kita, Y. Okauchi, Y. Fukatani, D. Orejon, M. Kohno, Y. Takata and K. Sefiane, Quantifying vapor transfer into evaporating ethanol drops in a humid atmosphere, *Phys. Chem. Chem. Phys.*, 2018, **20**, 19430–19440.

234 M. Seaver, A. Galloway and T. J. Manuccia, Water condensation onto an evaporating drop of 1-butanol, *Aerosol Sci. Technol.*, 1990, **12**, 741–744.

235 B. Henderson-Sellers, A new formula for latent heat of vaporization of water as a function of temperature, *Q. J. R. Meteorol. Soc.*, 1984, **110**, 1186–1190.

236 V. Majer, V. Svoboda and H. V. Kehianian, *Enthalpies of vaporization of organic compounds : a critical review and data compilation*, Blackwell Scientific, Oxford, 1985.

237 J. M. Coulson, J. F. Richardson, J. R. Backhurst and J. H. Harker, *Coulson & Richardson's Chemical Engineering Vol. 1, Fluid flow, heat transfer and mass transfer*, Butterworth-Heinemann, Oxford, 2009.

238 C. L. Yaws, *Yaws' Handbook of Thermodynamic and Physical Properties of Chemical Compounds*, Knovel, Norwich, 2003.

239 I. S. Khattab, F. Bandarkar, M. A. A. Fakhree and A. Jouyban, Density, viscosity, and surface tension of water+ethanol mixtures from 293 to 323K, *Korean J. Chem. Eng.*, 2012, **29**, 812–817.

240 R. L. Rowley, W. V Wilding, T. A. Knotts IV and N. Giles, *DIPPR Project 801 - Full Version*, Design Institute for Physical Property Research AIChE, 2005.

241 W. J. Massman, A review of the molecular diffusivities of H2O, CO2, CH4, CO, O3, SO2, NH3, N2O, NO, and NO2 in air, O2 and N2 near STP, *Atmos. Environ.*, 1998, **32**, 1111–1127.

242 G. A. Lugg, Diffusion Coefficients of Some Organic and Other Vapors in Air, *Anal. Chem.*, 1968, **40**, 1072–1077.

243 M. J. Tang, M. Shiraiwa, U. Pöschl, R. A. Cox and M. Kalberer, Compilation and evaluation of gas phase diffusion coefficients of reactive trace gases in the atmosphere: Volume 2. Diffusivities of organic compounds, pressure-normalised mean free paths, and average Knudsen numbers for gas uptake calculations, *Atmos. Chem. Phys.*, 2015, **15**, 5585–5598.

244 E. W. Lemmon and R. T. Jacobsen, Viscosity and thermal conductivity equations for nitrogen, oxygen, argon, and air, *Int. J. Thermophys.*, 2004, **25**, 21–69.

245 J. V. Sengers and J. T. R. Watson, Improved International Formulations for the Viscosity and Thermal Conductivity of Water Substance, *J. Phys. Chem. Ref. Data*, 1986, **15**, 1291–1314.

246 A. L. Lindsay and L. A. Bromley, Thermal Conductivity of Gas Mixtures, *Ind. Eng. Chem.*, 1950, **42**, 1508–1511.

247 M. O'Neil, Ed., *The Merck Index - An Encyclopedia of Chemicals, Drugs, and Biologicals*, Royal Society of Chemistry, Cambridge, United Kingdom, 15th edn., 2013.

248 P. Atkins, Chlorofluorocarbon to hydrofluoroalkane formulations: An industry perspective, *J. Allergy Clin. Immunol.*, 1999, **104**, 268.

249 S. W. Stein and P. B. Myrdal, The Relative Influence of Atomization and Evaporation on Metered Dose Inhaler Drug Delivery Efficiency, *Aerosol Sci. Technol.*, 2006, **40**, 335–347.

250 B. Asgharian, A model of deposition of hygroscopic particles in the human lung, *Aerosol Sci. Technol.*, 2004, **38**, 938–947.

251 R. Zhang, X. Song, S. Zhan, J. Hu and W. Tan, Investigation of influence factors on particle size measurement with pMDI, *Biomed. Res.*, 2017, **28**, 2582–2588.

252 A. R. Martin, D. Y. Kwok and W. H. Finlay, Investigating the Evaporation of Metered-Dose Inhaler Formulations in Humid Air: Single Droplet Experiments, *J. Aerosol Med.*, 2005, **18**, 218–224.

253 S. A. Jones, M. L. Reid and M. B. Brown, Determining Degree of Saturation after Application of Transiently Supersaturated Metered Dose Aerosols for Topical Delivery of Corticosteroids, *J. Pharm. Sci.*, 2009, **98**, 543–554.

254 D. F. Moraga-Espinoza, E. Eshaghian, A. Shaver and H. D. C. Smyth, Effect of Inhalation Flow Rate on Mass-Based Plume Geometry of Commercially Available Suspension pMDIs, *AAPS J.*, 2018, **20**, 1–12.

255 A. G. Carr, A. Branch, R. Mammucari and N. R. Foster, The solubility and solubility modelling of budesonide in pure and modified subcritical water solutions, *J. Supercrit. Fluids*, 2010, **55**, 37–42.

256 F. Mason, D. A. Lewis and B. Gavtash, Empirical Equations for Predicting the Vapour Pressure of HFA 134a or HFA 227ea Systems containing Ethanol, *Drug Deliv. to Lungs*, 2013, **2013**, 153–156.

257 A. G. M. Ferreira, A. P. V. Egas, I. M. A. Fonseca, A. C. Costa, D. C. Abreu and L. Q. Lobo, The viscosity of glycerol, *J. Chem. Thermodyn.*, 2017, **113**, 162–182.

258 Y. Liu and P. H. Daum, Relationship of refractive index to mass density and self-consistency of mixing rules for multicomponent mixtures like ambient aerosols, 2008, **39**, 974–986.

259 K. C. Pratt and W. A. Wakeham, The Mutual Diffusion Coefficient of Ethanol-Water Mixtures: Determination by a Rapid, New Method, *Proc. R. Soc. Lond. A. Math. Phys. Sci.*, 1974, **336**, 393–406.

260 M. Davis and G. Walker, Recent strategies in spray drying for the enhanced bioavailability of poorly water-soluble drugs, *J. Control. Release*, 2018, **269**, 110–127.

261 F. K. A. Gregson, J. F. Robinson, R. E. H. Miles, C. P. Royall and J. P. Reid, Drying Kinetics of Salt Solution Droplets: Water Evaporation Rates and Crystallization, *J. Phys. Chem. B*, 2019, **123**, 266–276.

262 A. Utoft, K. Kinoshita, D. L. Bitterfield and D. Needham, Manipulating Single Microdroplets of NaCl Solutions: Solvent Dissolution, Microcrystallization, and Crystal Morphology, *Langmuir*, 2018, **34**, 3626–3641.

263 M. D. Choudhury, T. Dutta and S. Tarafdar, Pattern formation in droplets of starch gels containing NaCl dried on different surfaces, *Colloids Surfaces A Physicochem. Eng. Asp.*, 2013, **432**, 110–118.

264 H. Y. Erbil, Evaporation of pure liquid sessile and spherical suspended drops: A review, *Adv. Colloid Interface Sci.*, 2012, **170**, 67–86.

265 Q. Zhang, Y. Zhang, C. Cai, Y. Guo, J. P. Reid and Y. Zhang, In Situ Observation on the Dynamic Process of Evaporation and Crystallization of Sodium Nitrate Droplets on a ZnSe Substrate, *J. Phys. Chem. A*, 2014, **118**, 2728–2737.

266 Y. Gao, S. B. Chen and L. E. Yu, Efflorescence relative humidity of airborne sodium chloride particles: A theoretical investigation, *Atmos. Environ.*, 2007, **41**, 2019–2023.

267 T. B. Onasch, R. Mcgraw and D. Imre, Temperature-Dependent Heterogeneous Efflorescence of Mixed Ammonium Sulfate / Calcium Carbonate Particles, *J. Phys. Chem. A*, 2000, **104**, 10797–10806.

268 A. Baldelli and R. Vehring, Control of the Radial Distribution of Chemical Components in Spray Dried Crystalline Microparticles, *Aerosol Sci. Technol.*, 2016, **50**, 1130–1142.

269 S. L. Clegg, C. Qiu and R. Zhang, The deliquescence behaviour, solubilities, and densities of aqueous solutions of five methyl- and ethyl-aminium sulphate salts, *Atmos. Environ.*, 2013, **73**, 145–158.

270 T. Lei, A. Zuend, Y. Cheng, H. Su, W. Wang and M. Ge, Hygroscopicity of organic surrogate compounds from biomass burning and their effect on the efflorescence of ammonium sulfate in mixed aerosol particles, *Atmos. Chem. Phys.*, 2018, **18**, 1045–1064.

271 A. Osman, L. Goehring, A. Patti, H. Stitt and N. Shokri, Fundamental Investigation of the Drying of Solid Suspensions, *Ind. Eng. Chem. Res.*, 2017, **56**, 10506–10513.

272 R. J. Han, O. R. Moss and B. A. Wong, Derivation and application of an analytical solution of the mass transfer equation to the case of forced convective flow around a cylindrical and a spherical particle with fluid surface properties, *J. Aerosol Sci.*, 1996, **27**, 235–247.

273 R. M. Power, S. H. Simpson, J. P. Reid and A. J. Hudson, The transition from liquid to solid-like behaviour in ultrahigh viscosity aerosol particles, *Chem. Sci.*, 2013, **4**, 2597–2604.

274 A. P. Lyubartsev and A. Laaksonen, Concentration effects in aqueous NaCl solutions. A molecular dynamics simulation, *J. Phys. Chem.*, 1996, **100**, 16410–16418.

275 S. Sugiharto, T. M. Lewis, A. J. Moorhouse, P. R. Schofield and P. H. Barry, Anion-cation permeability correlates with hydrated counterion size in glycine receptor channels, *Biophys. J.*, 2008, **95**, 4698–4715.

276 I. N. Tang, H. R. Munkelwitz and N. Wang, Water Activity Measurements with Single

Suspended Droplets: The NaCl-H20 and KCl-H20 Systems t, *J. Colloid Interface Sci.*, 1986, **114**, 409–415.

277 G. P. Brewington, The Secondary Structure of X-Ray Absorption Edges from Elements in Certain Cubic Crystals, *Phys. Rev.*, 1934, **46**, 861–864.

278 J. W. Gibbs, Equilibrium of Heterogeneous Substances, *Trans. Connect. Acad. Arts Sci.*, 1876, **3**, 108–248.

279 J. W. Gibbs, On the Equilibrium of Heterogeneous Substances, *Trans. Connect. Acad. Arts Sci.*, 1878, **3**, 343–524.

280 J. F. Robinson, F. K. A. Gregson, R. E. H. Miles, J. P. Reid and C. P. Royall, Drying kinetics and nucleation in evaporating sodium nitrate aerosols, *J. Chem. Phys.*, 2020, **152**, 074503.

281 X. Li, F. Wang, P. Lu, J. Dong, L. Wang and Y. Zhang, Confocal Raman Observation of the Efflorescence / Deliquescence Processes of Individual NaNO3 Particles on Quartz, *J. Phys. Chem. B*, 2006, **110**, 24993–24998.

282 M. P. Tolocka, T. D. Saul and M. V Johnston, Reactive Uptake of Nitric Acid into Aqueous Sodium Chloride Droplets Using Real-Time Single-Particle Mass Spectrometry, *J. Phys. Chem. A*, 2004, **108**, 2659–2665.

283 S. Goldstein and J. Rabani, Mechanism of nitrite formation by nitrate photolysis in aqueous solutions: The role of peroxynitrite, nitrogen dioxide, and hydroxyl radical, *J. Am. Chem. Soc.*, 2007, **129**, 10597–10601.

284 S. Ghorai and A. V. Tivanski, Hygroscopic behavior of individual submicrometer particles studied by X-ray spectromicroscopy, *Anal. Chem.*, 2010, **82**, 9289–9298.

285 I. N. Tang and H. R. Munkelwitz, Water activities, densities, and refractive indices of aqueous sulfates and sodium nitrate droplets of atmospheric importance, *J. Geophys. Res. Atmos.*, 1994, **99**, 18801–18808.

286 M.-. J. Lee, H.-J. Jung, H.-J. Eom, S. Maskey, H. K. Kim and C.-U. Ro, Hygroscopic behavior of individual NaNO3 particles, *Atmos. Chem. Phys. Discuss.*, 2011, **11**, 23203–23229.

287 H. S. Yeh and G. B. Wills, Diffusion Coefficient of Sodium Nitrate in Aqueous Solution at 25° C. as a Function of Concentration from 0.1 to 1.0M, *J. Chem. Eng. Data*, 1970, **15**, 187–189.

288 J. R. Espinosa, C. Vega, C. Valeriani, D. Frenkel and E. Sanz, Heterogeneous versus homogeneous crystal nucleation of hard spheres , *Soft Matter*, , DOI:10.1039/c9sm01142k.

289 T. A. G. Langrish and S. Wang, Crystallization rates for amorphous sucrose and lactose powders from spray drying: A comparison, *Dry. Technol.*, 2009, **27**, 606–614.

290 Z. Ji, Y. Zhang, S. Pang and Y. Zhang, Crystal Nucleation and Crystal Growth and Mass Transfer in Internally Mixed Sucrose / NaNO3 Particles, *J. Phys. Chem. A*, 2017, **121**, 7968–7975.

291 C. G. Golding, L. L. Lamboo, D. R. Beniac and T. F. Booth, The scanning electron microscope in microbiology and diagnosis of infectious disease, *Sci. Rep.*, 2016, **5**, 26516.

292 R. E. H. Miles, M. W. J. Glerum, H. C. Boyer, J. S. Walker, C. S. Dutcher and B. R. Bzdek, Surface Tensions of Picoliter Droplets with Sub-Millisecond Surface Age, *J. Phys. Chem. A*, 2019, **123**, 3021–3029.

293 J. F. Davies and K. R. Wilson, Raman Spectroscopy of Isotopic Water Diffusion in Ultraviscous, Glassy, and Gel States in Aerosol by Use of Optical Tweezers, *Anal. Chem.*, 2016, **88**, 2361–2366.

294 W. Pan, A. B. Kolomeisky and P. G. Vekilov, Nucleation of ordered solid phases of proteins via a disordered high-density state: Phenomenological approach, *J. Chem. Phys.*, 2005, **122**, 174905.

295 S. Lee, H. S. Wi, W. Jo, Y. C. Cho, H. H. Lee, S.-Y. Jeong, Y.-I. Kim and G. W. Lee, Multiple pathways of crystal nucleation in an extremely supersaturated aqueous potassium dihydrogen phosphate (KDP) solution droplet, *Proc. Natl. Acad. Sci.*, 2016, **113**, 13618–13623.

296 D. Erdemir, A. Y. Lee and A. S. Myerson, Nucleation of crystals from solution: Classical and two-step models, *Acc. Chem. Res.*, 2009, **42**, 621–629.

297 P. Vazquez, L. Sartor and C. Thomachot-Schneider, Influence of substrate and temperature on the crystallization of KNO3 droplets studied by infrared thermography, *Prog. Earth Planet. Sci.*, 2018, **5**, 75.

298 E. J. Freney, S. T. Martin and P. R. Buseck, Deliquescence and efflorescence of potassium salts relevant to biomass-burning aerosol particles, *Aerosol Sci. Technol.*, 2009, **43**, 799–807.

299 H. Cachier, C. Liousse, P. Buat-Menard and A. Gaudichet, Particulate content of savanna fire emissions, *J. Atmos. Chem.*, 1995, **22**, 123–148.

300 R. J. Sutton, E. Jewell, J. Elvins, J. R. Searle and P. Jones, Characterising the discharge cycle of CaCl2 and LiNO3 hydrated salts within a vermiculite composite scaffold for thermochemical storage, *Energy Build.*, 2018, **162**, 109–120.

301 I. M. Abdulagatov and N. D. Azizov, Viscosities of aqueous LiNO3 solutions at temperatures from 298 to 573 K and at pressures up to 30 MPa, *Ind. Eng. Chem. Res.*, 2005, **44**, 416–425.

302 J. E. Huheey, *Inorganic Chemistry: Principles of Structure and Reactivity*, Harper & Row Publishers, New York, Third Edit., 1983.

303 D. E. Irish, D. L. Nelson and M. H. Brooker, Quasilattice Features of Concentrated Aqueous LiNO 3 Solutions , *J. Chem. Phys.*, 1971, **54**, 654–657.

304 K. J. Rao and C. N. R. Rao, Crystal Structure Transformations of Alkali Sulphates , Nitrates and Related Substances *: Thermal Hysteresis in Reversible Transformations, *J. Mater. Sci.*, 1966, **1**, 238–248.

305 J. Liu, C. Duan, M. M. Ossowski, W. N. Mei, R. W. Smith and J. R. Hardy, Molecular Dynamics Simulation of Structural Phase Transitions in RbNO3 and CsNO3, *J. Solid State Chem.*, 2001, **160**, 222–229.

306 W. J. Xie, Z. Zhang and Y. Q. Gao, Ion Pairing in Alkali Nitrate Electrolyte Solutions, *J. Phys.*

Chem. B, 2016, **120**, 2343–2351.

307 Y. Marcus and G. Hefter, Ion pairing, *Chem. Rev.*, 2006, **106**, 4585–4621.

308 K. D. Collins, Ions from the Hofmeister series and osmolytes: Effects on proteins in solution and in the crystallization process, *Methods*, 2004, **34**, 300–311.

309 K. Zhang, W. W. Smith, M. Wang, Y. Liu, J. Schroers, M. D. Shattuck and C. S. O'Hern, Connection between the packing efficiency of binary hard spheres and the glass-forming ability of bulk metallic glasses, *Phys. Rev. E - Stat. Nonlinear, Soft Matter Phys.*, 2014, **90**, 1–7.

310 R. E. H. Miles, J. F. Davies and J. P. Reid, The influence of the surface composition of mixed monolayer films on the evaporation coefficient of water, *Phys. Chem. Chem. Phys.*, 2016, **18**, 19847–19858.

311 R. Sorjamaa, B. Svenningsson, T. Raatikainen, S. Henning, M. Bilde and A. Laaksonen, The role of surfactants in Kohler theory reconsidered, *Atmos. Chem. Phys.*, 2004, **4**, 2107–2117.

312 R. C. Fox, An Oil–Wax–Surfactant System for retarding the Evaporation of Water, *Nature*, 1965, **205**, 1004–1005.

313 J. F. Davies, R. E. H. Miles, A. E. Haddrell and J. P. Reid, Influence of organic films on the evaporation and condensation of water in aerosol, *Proc. Natl. Acad. Sci. U. S. A.*, 2013, **110**, 8807–8812.

314 S. J. Richardson, P. A. Staniec, G. E. Newby, J. L. Rawle, A. R. Slaughter, N. J. Terrill, J. M. Elliott and A. M. Squires, Glycerol prevents dehydration in lipid cubic phases, *Chem. Commun.*, 2015, **51**, 11386–11389.

315 A. Nowacka, S. Douezan, L. Wadsö, D. Topgaard and E. Sparr, Small polar molecules like glycerol and urea can preserve the fluidity of lipid bilayers under dry conditions, *Soft Matter*, 2012, **8**, 1482–1491.

316 J. Yu, Y. Zhang, G. Zeng, C. Zheng, Y. Liu and Y. Zhang, Suppression of NaNO 3 Crystal Nucleation by Glycerol: Micro-Raman Observation on the Efflorescence Process of Mixed Glycerol/NaNO 3 / Water Droplets, *J. Phys. Chem. B*, 2012, **116**, 1642–1650.

317 T. Koop, J. Bookhold, M. Shiraiwa and U. Pöschl, Glass transition and phase state of organic compounds: Dependency on molecular properties and implications for secondary organic aerosols in the atmosphere, *Phys. Chem. Chem. Phys.*, 2011, **13**, 19238–19255.

318 H. Y. Zhang, W. W. Zhu, G. L. Qin and Z. Wei, Phase equilibrium of NaNO3/KNO3in glycerol + H2O mixed solvent system at 288.15 K and 298.15 K, *Kem. u Ind. Chem. Chem. Eng.*, 2014, **63**, 345–354.

319 R. A. Halliwell, R. M. Bhardwaj, C. J. Brown, N. E. B. Briggs, J. Dunn, J. Robertson, A. Nordon and A. J. Florence, Spray Drying as a Reliable Route to Produce Metastable Carbamazepine Form IV, *J. Pharm. Sci.*, 2017, **106**, 1874–1880.

320 M. Anyfantakis, Z. Geng, M. Morel, S. Rudiuk and D. Baigl, Modulation of the coffee-ring effect in particle/surfactant mixtures: The importance of particle-interface interactions,

Langmuir, 2015, **31**, 4113–4120.

321 J. Park and J. Moon, Control of colloidal particle deposit patterns within picoliter droplets ejected by ink-jet printing, *Langmuir*, 2006, **22**, 3506–3513.

322 HDK® N20 PYROGENIC SILICA, Wacker Chemie AG, https://www.brenntag.com/media/documents/bsi/product_data_sheets/life_science/wacker_fumed_silica/hdk_n20_pds.pdf, (accessed 8 October 2019).

323 J. Archer, J. S. Walker, F. K. A. Gregson, D. A. Hardy and J. P. Reid, Drying Kinetics and Particle Formation from Colloidal Suspension in Aerosol Microdroplets, Article in Progress.

324 C. O. Metin, R. T. Bonnecaze, L. W. Lake, C. R. Miranda and Q. P. Nguyen, Aggregation kinetics and shear rheology of aqueous silica suspensions, *Appl. Nanosci.*, 2014, **4**, 169–178.

325 S. L. Clegg and A. . Wexler, Densities and Apparent Molar Volumes of Atmospherically Important Electrolyte Solutions. 1. The Solutes H2SO4, HNO3, HCl, Na2SO4, NaNO3, NaCl, (NH4)2SO4, NH4NO3 and NH4Cl from 0 to 50 °C, Including Extrapolations to Very Low Temperature and to the Pure Li, *J. Phys. Chem. A*, 2011, **115**, 3393–3460.

326 F.-M. Wu, N. Wang, S.-F. Pang and Y.-H. Zhang, Hygroscopic behavior and fractional crystallization of mixed (NH4)2SO4/glutaric acid aerosols by vacuum FTIR, *Spectrochim. Acta Part A Mol. Biomol.*, 2019, **208**, 255–261.

327 Q. Liu, B. Jing, C. Peng, S. Tong, W. Wang and M. Ge, Hygroscopicity of internally mixed multi-component aerosol particles of atmospheric relevance, *Atmos. Environ.*, 2016, **125**, 69–77.

328 M. A. Zawadowicz, S. R. Proud, S. S. Seppalainen and D. J. Cziczo, Hygroscopic and phase separation properties of ammonium sulfate/organics/water ternary solutions, *Atmos. Chem. Phys.*, 2015, **15**, 8975–8986.

329 X. M. Shi, F. M. Wu, B. Jing, N. Wang, L. L. Xu, S. F. Pang and Y. H. Zhang, Hygroscopicity of internally mixed particles composed of (NH4)2SO4 and citric acid under pulsed RH change, *Chemosphere*, 2017, **188**, 532–540.

330 J. I. Goldstein, A. D. Romig Jr., D. E. Newbury, C. E. Lyman, P. Echlin, C. Fiori, D. C. Joy and E. Lifshin, *Scanning Electron Microscopy and X-Ray Microanalysis*, Plenum Press, New York, London, 2nd edn., 1992.

331 W. Chrzanowski and F. Dehghani, *Standardisation in Cell and Tissue Engineering, Methods and Protocols*, Woodhead Publishing Limited, Cambridge, United Kingdom, 2013.

332 Bruker, Periodic Table of Elements and X-Ray Energies, https://www.bruker.com/fileadmin/user_upload/8-PDF-Docs/X-rayDiffraction_ElementalAnalysis/HH-XRF/Misc/Periodic_Table_and_X-ray_Energies.pdf, (accessed 16 January 2020).